Attosecond Light Pulses and Attosecond Electron Dynamics Probed using Angle-Resolved Photoelectron Spectroscopy

Cong Chen

B.S., Nanjing University, 2010

M.S., University of Colorado Boulder, 2013

A thesis submitted to the

Faculty of the Graduate School of the

University of Colorado in partial fulfillment

of the requirement for the degree of

Doctor of Philosophy

Department of Physics

2017

This thesis entitled:
Attosecond Light Pulses and Attosecond Electron Dynamics Probed using Angle-Resolved Photoelectron Spectroscopy

written by Cong Chen
has been approved for the Department of Physics

_____
Prof. Margaret M. Murnane

_____
Prof. Henry C. Kapteyn

Date_____

The final copy of this thesis has been examined by the signatories, and we find that both the content and the form meet acceptable presentation standards of scholarly work in the above mentioned discipline.

Chen, Cong (Ph.D., Physics)

Attosecond Light Pulses and Attosecond Electron Dynamics Probed using Angle-Resolved Photoelectron Spectroscopy

Thesis directed by Prof. Margaret M. Murnane

Recent advances in the generation and control of attosecond light pulses have opened up new opportunities for the real-time observation of sub-femtosecond (1 fs = 10^{-15} s) electron dynamics in gases and solids. Combining attosecond light pulses with angle-resolved photoelectron spectroscopy (atto-ARPES) provides a powerful new technique to study the influence of material band structure on attosecond electron dynamics in materials. Electron dynamics that are only now accessible include the lifetime of far-above-bandgap excited electronic states, as well as fundamental electron interactions such as scattering and screening. In addition, the same atto-ARPES technique can also be used to measure the temporal structure of complex coherent light fields. In this thesis, I present four experiments utilizing atto-ARPES to provide new insights into the generation and characterization of attosecond light pulses, as well as the attosecond electron dynamics in transition metals. First, I describe a new method to extend attosecond metrology techniques to the reconstruction of circularly polarized attosecond light pulses for the first time. Second, I show that by driving high harmonics with a two-color linearly polarized laser field, quasi-isolated attosecond pulses are generated because the phase matching window is confined. Third, I present the first measurement of lifetimes for photoelectrons that are born into free-electron-like states compared with those that are excited into unoccupied excited states in the band structure of a material (Ni(111)). The finite excited-state lifetime causes a ≈200 as delay in the emission of photoelectrons. Finally, I describe direct time-domain studies of

electron-electron interactions in transition metals with both simple and complex Fermi surfaces. In particular, I show the influence of electron-electron scattering and screening on the lifetime of photoelectrons.

Dedication

For my family

Acknowledgements

First of all, I would like to thank my advisors, Margaret and Henry for their mentoring, support and encouragement. They have provided me with incredible resources and opportunities in my Ph. D, as well as the connections with some of the best experts in attosecond and surface science community: Martin Aeschlimann (TU Kaiserslautern), Andreas Becker (JILA), Agnieszka Jaron-Becker (JILA), Mark Keller (NIST), Manos Mavrikakis (UW Madison) and Dan Dessau (CU Boulder). I gained lots of invaluable perspectives on science through the collaborations with them. I am also glad to work with the photoemission team in Kapteyn-Murnane group. Tory, thank you for teaching me so that I am able to go on and dive deeply into photoemission. Your optimism kept me motivational and patient during the difficult time of building a new setup. Piotr, thank you for providing so many ideas and new perspectives to the experiment. The discussions with you on physics upgrades my knowledge and help me grow professionally as a scientist. Zhensheng, thank you for working together with me during so many late nights in the lab. Those moments when we felt closer to the explanations to our data are truly unforgettable. Wenjin, thank you for the confidence in turning over the ongoing experiments to you. I am sure there will be more scientific findings to come.

Many thanks to our collaborators in Germany, especially Sebastian Emmerich, Markus Rollinger, Stefan Mathias, Steffen Eich and Martin Piecuch from TU Kaiserslautern, and Moritz

Ploetzing from Jülich. Thank you all for the knowledge and support I gained during my visit to Germany.

I gratefully acknowledge the sample providers and theoretical support to our experiments. Many thanks to Mark Keller and David Miller who fabricated high-quality nickel samples for us and helped us understand the physics of graphene/nickel system and the magnetic properties of nickel. To Justin Shaw who provides us the permalloy sample. To Carlos for the simulations on high harmonic generation that constitutes tremendous theoretical support to our papers. Thanks to Guowen Peng and Tibor Szilvasi for the DFT calculations that help to unravel the magic of materials' bandstructure.

Thanks to the JILA machine shop their technical support, especially Hans Green, David Alchenberger, Blaine Horner, Kim Hagen, Todd Asnicar, and Kels Detra.

To JILA computing group, especially J. R. Raith who made sure the computer well-behaved during the data-taking.

To Ofer Kfir and Oren Cohen from Technion University for the excitement in circularly polarized harmonics.

To Yue Cao for his instructions about ARPES theory and equipment.

To Wei, for his advice on research and life and keeping me from getting lost in the difficult days.

Many thanks to Dan Adams and his family for the wonderful Thanksgiving memories.

To group members, past and present, especially Chengyuan Ding, Bosheng Zhang, Tingting Fan, Ming-Chang Chen, Ronny Knut, Chan La-o-vorakiat, Qing Li, Tenio Popmintchev, and Dimitar Popmintchev.

Finally, and most of all, I thank my parents, my brother, my grandparents and the rest of my family for their great love and never-ending support.

Contents

Figures

Page

Figure

Tables

Page

Table

Chapter 1

Introduction to Ultrafast

1.1 Why Ultrafast

Time is one of the parameters that divides the natural sciences into different fields. To human beings, the most perceivable unit of time is the second, with one second close to the period of the heartbeat that repeats throughout a human's lifetime. However, our universe is filled with a variety of marvelous events and phenomena that take place at different time scales (Figure 1.1). On the one hand, there are processes that are achingly long compared to the lifetime of a human being. For example, the formation of a galaxy takes billions of years while the evolution of biological species on earth happens in millions of years. On the other hand, modern research in physics and chemistry is able to show us the dynamics of phenomena in the other temporal extreme where we can visualize a world in which dynamical changes occur on an ultrafast timescale, i.e., in the femtosecond (fs, 10^{-15} s) to attosecond (as, 10^{-18} s) range (Figure 1.2). These dynamics usually take place in a microcosm and therefore are inherently connected by the laws of quantum mechanics. For example, from quantum mechanics, a particle put in a superposition of two states has a characteristic oscillation period of

$$T_{osc} = 2\pi(\hbar/\Delta W), \tag{1.1}$$

where ΔW is the energy separation between two states. This energy separation is determined by the potential confining the particle motion and the particle's mass. Because the spacing between

vibrational energy levels in molecules is in the milli-eV range, molecular vibrations occur on the time scale of tens to hundreds of femtoseconds. Compared to these vibrational motions, the motion of an individual electron in metals, molecules, and the inner shells of atoms occurs on a faster time scale, usually in range of tens of femtoseconds to less than an attosecond (see Figure 1.1 and 1.2).

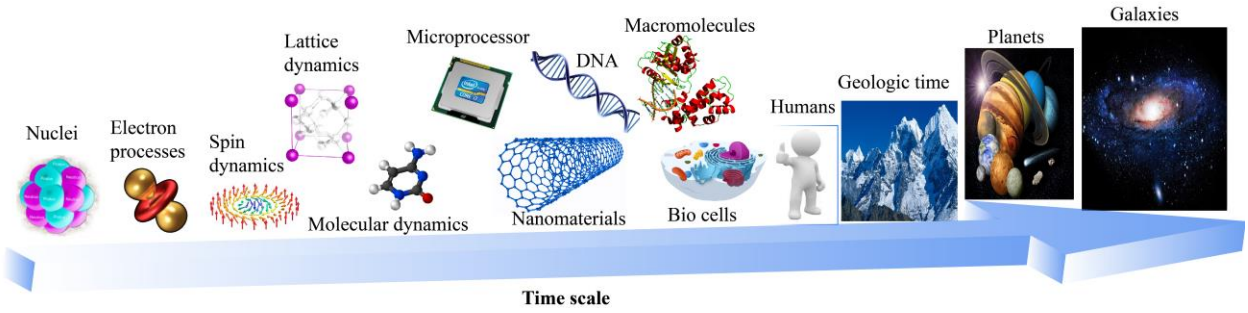

Figure 1.1: Events and phenomena in the universe that take place at different time scales.

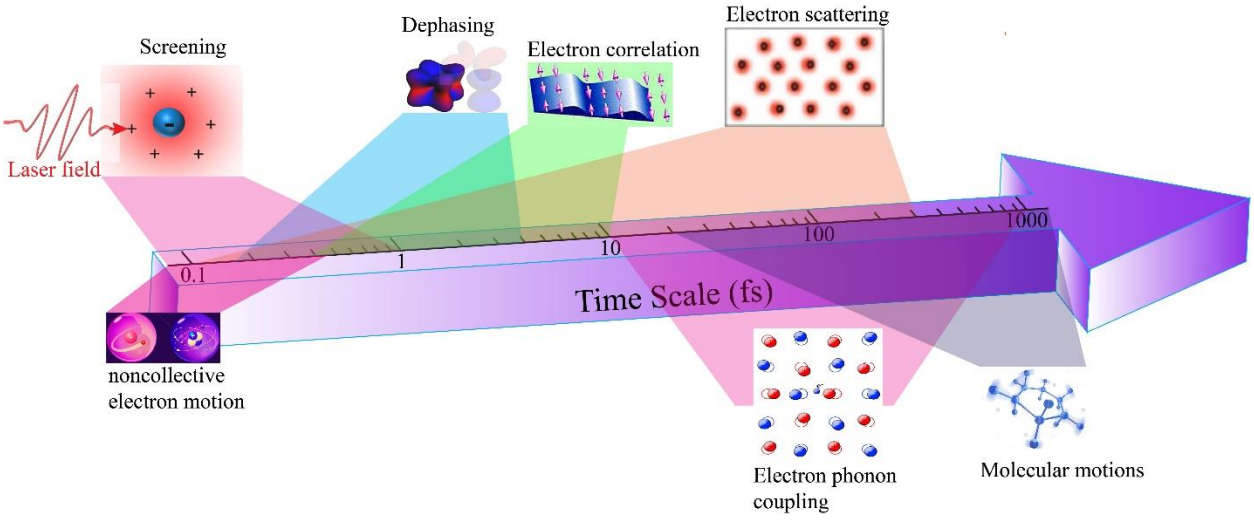

Figure 1.2: Dynamical processes at time scales from 0.1 fs to 1000 fs after laser excitation. Ultrafast time scales are determined through direct time-domain measurements or linewidth analysis. After external excitation, the dynamical screening occurs on the fastest time scale. The screening is followed by the dephasing of coherent excitations. The original nonthermal distribution of excited electrons relaxes to a Fermi-Dirac distribution through electron-electron scattering. The electrons then transfer energy to the lattice through electron phonon coupling.

To give an idea of how short one attosecond is, we know that the age of the Universe, i.e., the time elapsed since the *Big Bang*, is approximately 14 billion years. One attosecond is one billionth of one billionth of a second. The processes of interest at the attosecond time scale are mostly related to the dynamics of electrons. The desire to understand these ephemeral electron dynamics that are invisible to the human eye are of both scientific and practical interest. First, the interrogation of ultrafast electronic motion will provide us answers to fundamental scientific questions of how the microscopic behaviors of electrons and atoms of a material dictate its macroscopic properties. For example, the well-known Ohm's law is a macroscopic description that relates the current $\boldsymbol{J}$ with the applied electric field $\boldsymbol{E}$ through equation $\boldsymbol{J}=\boldsymbol{E}/\rho$, where ρ is the electrical resistivity and has the unit of time. The resistivity of copper is 1.7 $\mu\Omega\cdot$cm, which equals to approximately 2 as. This 2 as is the time for an electronic system in metal to establish Ohm's law-like behavior. During the relaxation time, the electrons first accelerate in the electric field and then slow down because of scattering. The electrons finally reach the ultimate velocity by balancing the two competing mechanisms of acceleration and scattering. This final velocity determines the electric current [1]. There is an abundance of similar macroscopic phenomena dictated by the microscopic motion of electrons. These phenomena include the breakage and reformation of chemical bonds during chemical reactions, charge transfer between atoms and molecules, and phase transitions in materials. A deep understanding of these dynamics will help us steer specific microscopic electron motion for technological applications. Taking the semiconductor industry as an example, during the last several decades this industry had a rapid growth along the pathway of Moore's Law to shrink the transistor size and increase the signal-processing speed. However, the industry has reached a critical barrier point set by the speed at which the electrons can be manipulated. To overcome this speed barrier, attosecond researchers

have discovered light field-driven carrier dynamics oscillating in the petahertz (10^{15} Hz) regime. These dynamics can potentially boost transistor speed by three orders of magnitude compared to current state-of-the-art devices [2,3]. In addition to semiconductor transistors, the potential technological impact of ultrafast sciences lies in many other aspects of modern industry. For example, improvement in the photoconversion efficiency of a solar cell relies on knowledge of charge movement after photoadsorption. The writing-speed limit of a computer disk depends on how fast one can switch the spin state of ferromagnets. Moreover, an understanding of electron dynamics in simple molecules and solids is a building block for manipulating more complicated systems, such as biomolecules to achieve targeted disease treatment.

1.2 Probing into the "Invisible"

Real-time observation of ultrafast electron dynamics requires metrology or spectroscopy tools with sufficient time resolution. The response time of the human eye is one twentieth of a second, precluding us from directly observing many physical and chemical dynamics without the assistance of special techniques. Everything below the limit of naked eyes is "*invisibly fast*". Fortunately, major advance into the "*temporal invisible*" was made with flow tubes in 1923 by H. Hartridge and F. Roughton for resolving solution reactions [4]. In their experiments, the products of chemical reactions were measured at different positions in flow tubes, which could translate into time if the flow speed was known. After that advance, millisecond precision was reached in 1940 by B. Chance with the invention of the stopped-flow method, which is still used in the study of biological kinetics [4].

Around 1950, the invention of flash photolysis enabled microsecond resolution in observing radical intermediates during a chemical reaction via a change in the absorption spectrum

[6]. This technique was later recognized with a Nobel Prize in 1967 that was awarded to R. Norrish and G. Porter and shared with M. Eigen [7]. M. Eigen also developed a series of techniques to investigate chemical reactions with microsecond-to-nanosecond resolution. These experiments were achieved by first disturbing the equilibrium of a solution with energy pulses, either a sound wave or an electric field, and then following the kinetics of the solution. Eigen's techniques indicated that there are two ingredients for overcoming the temporal resolution limit: first, we need the instrumentation to produce ultrafast light pulses or other particle sources, and second, we apply these light and particle sources to create, investigate, and manipulate the short-lived transient states in atoms, molecules, or materials.

1.3 Pump-Probe

To use ultrafast light pulses to create and investigate the evolution of transient states, most of ultrafast experiments employ a pump-probe scheme. In pump-probe experiments, the first energy pulse is injected into the system to induce a dynamical change and the second pulse with a controlled time delay relative to the first one follows the temporal evolution of the system. The pump-probe idea can be traced back to 1864 when Toepler applied photography to investigate microscopic dynamics of a sound wave [8]. In Toepler's experiment, two light sparks were generated with their relative delay controlled electronically. The first one initiated the sound wave, and the second one recorded its motion by taking pictures of the wave. Abraham and Lemoine later (1899) improved Toepler's method by splitting the same spark into the pump and probe arm with an adjustable optical-path length between them. With the pump-probe concept established, subsequent development of time-resolved studies are based upon shorting temporal duration of ultrafast sources, and developing advanced spectroscopy techniques that unravel different aspects

of the dynamical change. In terms of ultrafast light sources, the invention of the pulsed lasers made major breakthroughs in the accessible temporal realm.

1.4 Ultrafast Lasers

The 1960s witnessed several milestones in laser development. In particular, the invention of *laser modelocking* triggered the advancement of ultrafast optics and brought time-resolved studies into the picosecond regime. The first generation of picosecond lasers used solid state materials such as ruby and Nd:glass as the gain media. Modelocking was achieved either actively through an external electrical signal, or passively through loss modulation introduced by a saturable absorber. The latter approach typically generated shorter picosecond pulses. With picosecond resolution achieved, the rotational motion and vibrational modes of polyatomic molecules became accessible in direct time-domain study. Direct temporal study of phonon relaxation in solids and many other nonradiative processes in chemistry were also achieved with picosecond resolution. Pioneering discoveries regarding ultrafast electron motion were made, including studies of photo-induced intramolecular electron transfer. Nevertheless, the response time of organic saturable absorbers limited the further reduction of laser-pulse duration towards the femtosecond regime. Therefore, the mechanisms of many femtosecond excited-state processes, such as electron relaxation in semiconductors, electron transfer in molecules, bond-breaking reactions and photoisomerization, remained out of reach.

The femtosecond barrier was overcome with the invention of organic dye lasers. Organic dye lasers were invented in 1966 by Sorokin *et al*. [9]. Ten years later, subpicosecond pulses from dye lasers were generated, heralding the dawn of the "*femtosecond era*". Compared to previous solid-state lasers, the gain saturation in dye lasers can be significant during pulse formation, and

the response time of the saturable absorber no longer constitutes a limitation to the achievable pulse duration. The momentous development of sub-100-fs pulsed dye lasers revolutionized the field of femtosecond laser spectroscopy in the 1980s, thanks to the discovery of the dispersion-controlled colliding-pulse-modelocking [10] and prismatic pulse-compression techniques [11–13]. Using the latter method, Fork *et al.* demonstrated six femtosecond pulses in 1987 [14].

1.5 Femtosecond Solid-State Lasers

The development femtosecond lasers initially occurred alongside dye lasers until 1990 because it was assumed that passive modelocking in solid state lasers was difficult and usually unsteady because of Q-switching instability. However, breakthrough techniques including semiconductor saturable absorber mirrors (SESAMs) and Kerr lens modelocking (KLM) gave rise to the emergence of femtosecond solid-state lasers.

SESAMs are Bragg reflector mirrors with semiconductor saturable absorbers integrated into them [15]. The light absorption of the mirrors becomes higher for more intense incoming pulses and finally saturates when the available initial states in saturable absorbers are depleted. In these saturable absorbers, different relaxation mechanism in semiconductors with varied time scales from nanosecond (carrier recombination and trapping) to femtosecond (carrier thermalization) can be used for pulse shaping. SESAMs are the essential components to modelock a variety of solid-state lasers and fiber lasers, which now have become the building blocks for many scientific instruments as well as industrial and medical photonic systems. Nevertheless, current SESAMs cannot reach a pulse duration as short as that of Ti:sapphire lasers.

In 1999, the modelocked Ti:sapphire laser surpassed the six femtosecond record set by dye lasers. Along with its other merits [16], this laser is recognized as the best ultrafast laser today.

Historically, the titanium-doped sapphire had already been discovered in the late 1980s as a laser gain medium that possessed a broad bandwidth to support femtosecond pulses. However, researchers assumed that it would be difficult to find a saturable absorber to support stable femtosecond modelocking in such systems. This is why it was very surprising when Sibbett's group demonstrated 60-femtosecond pulses with a Ti:sapphire laser that didn't even use a saturable absorber [17]. Subsequent theoretical and experimental research efforts revealed the responsible mechanism [18,19]. Under the radiation of a laser beam with a radial intensity profile, the Kerr nonlinearity of the Ti:sapphire crystal turns the crystal itself into a focusing lens. This "virtual lens" allows the laser cavity to be designed with a certain aperture to favor the pulsed-lasing mode that has a larger lensing effect as compared to the rivalling continuous-wave mode (Figure 1.3). In other words, the laser crystal itself is an ultrafast saturable absorber for modelocking. This kind of modelocking method is named Kerr lens modelocking (KLM). The KLM Ti:sapphire laser allowed routine generation of pulses with < 20 fs duration. It was quickly used for many kinds of femtosecond time-resolved spectroscopies. Zewail won the Nobel Prize in 1999 for femtochemistry, i.e., the real-time observation of the breakage and formation of chemical bonds by using the short pulse duration of the femtosecond lasers [20].

In addition to its short pulse duration, Ti:sapphire as a solid-state gain medium can achieve high peak power after amplification because of its unique properties including high saturation fluence, excellent thermal conductivity, and broad emission bandwidth. These properties enabled efficient laser-pulse amplification with the development of high-power semiconductor diode-pump lasers and the ingenious invention of the chirp-pulse-amplification technique. The state-of-the-art Ti:sapphire laser systems today can obtain an intensity of $>10^{21}$ W/cm^2 at focus, exceeding the atomic Coulomb field by more than four orders of magnitude [21]. This high intensity field

brings an unprecedented regime of nonlinear optics and strong field physics. The development of strong field physics also brought our temporal resolution into the attosecond regime.

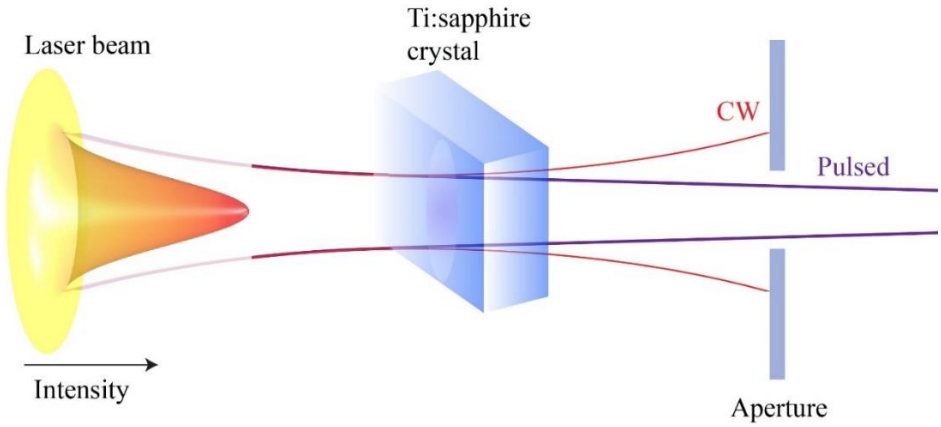

Figure 1.3: Kerr-lens-induced changes in the transmission of laser beam through an aperture. The Ti:sapphire crystal forms a Kerr lens that serves as a saturable absorber with ultrafast response time. The Kerr lens results in a self-focusing effect for the laser field in the pulsed mode. The self-focusing effect results in a higher transmission of the pulsed-laser light through the aperture as compared to CW laser mode and causes mode locking.

1.6 Attosecond

Attosecond science was initiated with the invention of phase-stabilized high power Ti:sapphire lasers. In nonlinear laser-matter interactions, electronic motion can be sensitive to the sub-cycle slopes of the oscillating field rather than exhibiting cycle-averaged dynamics. This dynamical sensitivity to electric field not only gives a way for the direct probing of attosecond charge dynamics but also allows the generation of attosecond light pulses through the process called high harmonic generation (HHG). HHG is the heart of attosecond science. For the past 20 years, the field of attosecond has witnessed substantial progress including pulse generation, pulse characterization, and attosecond spectroscopy of atoms, molecules and solid-state materials. I will briefly discuss the current developments in attosecond science and then give an overview of the attosecond studies performed in this thesis work in chapter 2.

1.7 Beyond Attosecond

In the pursuit of temporal resolution beyond attoseconds, zeptosecond (zs, 10^{-21} second) is the time scale related to the proton and neutron motion inside the nuclei of atoms. Therefore, zeptosecond pulses will grant us the capability to capture nuclear processes in real time and interrogate nuclear dynamics such as quasi-fusion/fission decay. It was demonstrated experimentally that high harmonic generation driven by mid-IR lasers (3.9 μm) could support a huge spectral bandwidth (> 0.7 keV) [22]. Although this broad bandwidth corresponds to single-cycle attosecond pulses in the Fourier transform limit, compensation of the "atto-chip" to actually achieve these short pulses was experimentally challenging. As a result, the exploration of zeptosecond pulse generation remains mainly theoretical. Theory predicted that few-cycle long wavelength driving lasers (9 μm) could generate x-ray pulses with sub-attosecond temporal structure because of the interference of x-ray radiation produced in multiple rescattering of the electron wave packet with the ion [23]. Other theoretical proposals of zeptosecond pulse generation included using nonlinear Thomson back-scattering [24], using the interaction between a muonic hydrogen atom and high power chirped laser pulses [25], and using the reflection of a relativistically intense femtosecond laser from an over-dense plasma [26].

Yoctosecond (10^{-24} second) is a factor of a million faster than the shortest attosecond pulse achieved experimentally this far. In the pursuit of such extreme photon sources, we can still hope for a surprise from highly nonlinear laser-matter interactions. At the same time, we must investigate in systems involving motion at the same time scale. Yoctosecond is the time taken for a quark to emit a gluon. Ipp *et al.* theoretically worked out that the quark-gluon plasma created through heavy-ion collisions could emit zeptosecond pulses when the plasma cools on [27]. A

delayed pulse pair is also possible by taking advantage of the evolution of isotropy during the plasma expansion.

1.8 Conclusion

The expected future evolution of ultrafast science will keep overcoming the limits of temporal resolution and pushing the frontiers of science and technology. This thesis focuses on the dynamics at the attosecond time scale. Therefore, in Chapter 2, I will discuss the current developments of attosecond science and present the overview of the thesis.

Chapter 2

Attosecond Science and Thesis Overview

Electrons bind atoms into molecules and solids. They are carriers of electrical current. Electrons also radiate photons that we can harness to interrogate the microscopic world. The understanding and steering of electron dynamics in the microscopic world are the driving forces of the technological and industrial revolution in the 21st century. One effort of modern computer and information technology is to increase the speed at which electrons can be controlled. To realize this appealing vision of future electronics, we need to achieve the required temporal resolution to capture the real-time evolution of an electronic system during a dynamical change. Attosecond (as) is the fundamental time scale of electron motion and electron-electron interactions. For example, the atomic unit of time is 24.2 as. The period of electron orbiting the nucleus in a hydrogen atom in its ground state is approximately 150 as. The time needed for an electron in the conduction band of a metal with Fermi velocity to travel through a distance equal to the metal lattice constant is near 220 as. These attosecond electron dynamics will impact the subsequent femtosecond-to-picosecond dynamics in materials. Such dynamics include molecular vibration, photodissociation, and phase transitions in solids. The direct time-domain investigation of these extremely fast dynamics relies on the development of attosecond science.

Attosecond science can be categorized into different subfields including attosecond pulse generation [28,29], pulse characterization [30–34], attosecond spectroscopy [33,35–38], and

attosecond control [2,39–41]. These subfields are deeply intertwined. For example, attosecond pulse generation with tailored-temporal structures relies on our knowledge of electron ionization and recombination in a strong laser field, which can be acquired from spectroscopy. This connection extends to attosecond spectroscopy and attosecond control because most time-resolved measurements require the change of a dynamical system in a controlled and reproducible manner on the related time scale. In more than two decades of development, attosecond science has advanced to investigating electron dynamics in a variety of systems ranging from atoms to polyatomic molecules [42,43], to dielectric, metallic, and semiconducting solid-state materials [33,36,44], as well as to nanostructures and quantum dots [45,46]. The spectroscopy methods used in attosecond science include high-harmonic spectroscopy [47–50], above-threshold ionization [51], recollision-based imaging [52,53], transient absorption spectroscopy [2,36], and photoelectron spectroscopy [35,44,54–56]. Each spectroscopy technique interrogates the system from its unique perspective, using different light sources. Therefore, attosecond spectroscopies are performed using waveform-controlled femtosecond pulses [57,58], isolated attosecond pulses [33,40,42,44,56], and attosecond pulse trains [35,54,59,60]. The information we gained from attosecond spectroscopy opens the door to attosecond technology. For example, controlled femtosecond and attosecond light fields permit the manipulation of electric current on the atomic scale at petahertz frequencies, in the same way radio-frequency fields control the mesoscopic currents in semiconductor chips [2,3,40,61].

The work presented in my thesis includes attosecond pulse characterization and attosecond spectroscopy. This chapter first reviews various advances and future developments of attosecond science. Then I introduce how the thesis is organized and briefly describe the content of each chapter.

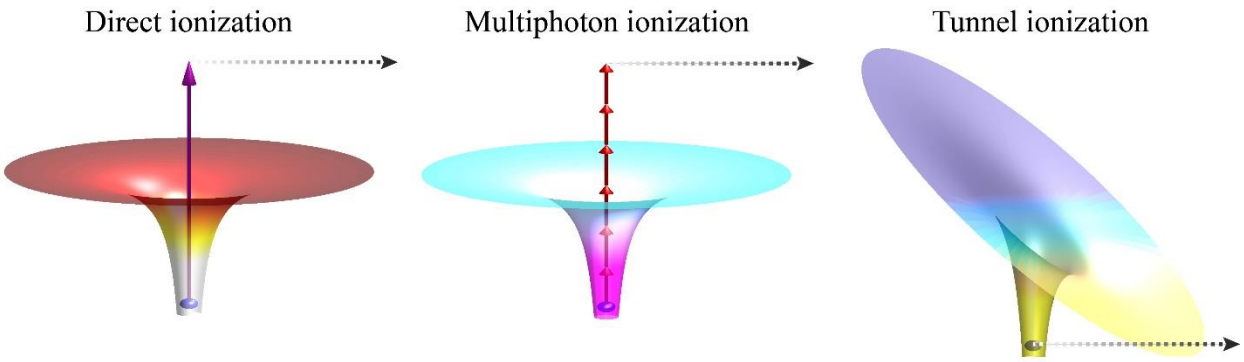

Figure 2.1: Different scenarios of election ionization. When the photon energy is larger than the ionization potential, the electron goes through direct ionization. If the photon energy is smaller than the ionization potential, the electron can be removed through either multiphoton ionization or tunnel ionization, depending on the Keldysh parameter γ.

2.1 Attosecond Dynamics Probed by Femtosecond Pulses

In conventional pump-probe experiments, the temporal resolution is limited by the pulse duration of the pump and probe beams. Therefore, one could assume that attosecond experiments must be performed with attosecond pulses. However, this is not the case. Waveform-controlled femtosecond IR pulses allow the use of sub-cycle gradients of the electric field to initiate and probe subsequent dynamics with attosecond-timing precision. One example is probing the electron ionization in a strong field. Since a strong IR field rivals the interatomic Coulomb force, electrons can be freed from the ion core either through multiphoton ionization or tunneling ionization. These two regimes are categorized via the Keldysh parameter $\gamma = \sqrt{I_P/2U_P}$, where I_P is the ionization potential, and U_P is the ponderomotive energy of electrons in the laser field, defined as $U_P = E_0^2/4\omega_0^2$, where E_0 is the peak-laser electric field, and ω_0 is the laser carrier frequency [62]. For $\gamma > 1$, the electron goes through multiphoton ionization, with the final kinetic-energy distribution depending on the waveform of the driving laser, including the carrier-envelope phase. For the

Ti:sapphire laser systems that are usually used in these experiments, the peak intensity is approximately 10^{13}-10^{14} W/cm^2. In this regime, the laser filled bends the atomic Coulomb potential trapping the electrons and creates a penetrable potential barrier. The electron tunnels through this barrier and starts to accelerate in the laser field. Depending on when the tunnel ionization happens during a laser cycle, the electron undergoes different acceleration, deceleration, recombination, and scattering processes. Studying these sub-cycle dynamics at the attosecond time scale provides information on strong-field electron dynamics, including the process of high harmonic generation (HHG).

2.1.1 High Harmonic Spectroscopy

HHG is a highly nonlinear process caused by electron motion in a strong field. After strong field ionization, a tunneled electron could recombine with the parent hole it left upon ionization and emits an attosecond burst of radiation [63,64]. This unique attosecond EUV/X-ray light source promises many important spectroscopic applications such as resolving the emission time of electrons upon photoionization. In addition, HHG from laser-atom or laser-molecule interactions carries a wealth of information on both the ionization process and the recollision dynamics. For example, HHG is sensitive to electron trajectories and molecular orbital changes as well as the structural evolution of the ionized target [47,49,65]. We can obtain these strong-field electron and ion dynamics by analyzing the properties of the emitted harmonics, e.g., the intensity, phase, and polarization [66]. Since the HHG process is triggered by ionization and terminated by recombination, the time between the two events can be viewed as a time delay. This time delay can be controlled by selecting the electron trajectories or adjusting the driving laser wavelength [48,67].

Most of the experiments on high harmonic spectroscopy only probe the intensity and polarization of the HHG emission. In Chapter 5 and 6, I show that attosecond interferometer technique gives access to the phase of HHG radiation [30]. For manipulating the electron trajectories in HHS, two-color circular or linear high harmonic generation scheme discussed in Chapter 5 and 6 allow us to explore additional degrees of freedom [30,41,48,50,68–74].

2.1.2 Electron Recollision-Based Probe

HHG happens when the ionized electron can recombine with the parent ion. However, in many cases, the recolliding electron diffracts or scatters off the parent ion instead of recombining with it. Since the ionization prior to the recollision creates a nonequilibrium charge distribution that evolves on the attosecond time scale, the diffraction patterns resulting from electrons recolliding at different times can follow the temporal rearrangements of the ion [75–77]. In another intriguing scenario, the interference between the diffracted electrons and undiffracted photoelectron will form a hologram [78,79]. Because of the coherence of the electron wave packets and the subcycle temporal confinement of the process, ångström spatial resolution and attosecond temporal resolution can be achieved.

The laser-induced electron diffraction described above requires the recollision between electron and ion to be a coherent process. In a general term, the electron scatters off the parent ion upon recollision. The scattering can occur either elastically or inelastically. In elastic scattering, the electron's final momentum is sensitive to the IR vector potential at the instant of ionization and the moment of recollision. This dependence has been exploited to trace the subcycle field evolution [80]. For example, this dependence permitted measurement of the carrier-envelope phase of an ultrafast laser pulse [81,82]. In contrast, the laser-induced electron scattering becomes an

inelastic process when back-scattered electrons lose energy via interaction with other particles or quasiparticles. For example, if a back-scattered electron possesses higher energy than the binding energy of the valence electrons, the back-scattered electron may knock off a valence electron upon recollision with the parent ion [83]. This process is called *nonsequential double ionization*. It provides a spectroscopy method for studying the multielectron correlation [84] and the ionization/recollision-induced structural changes in the molecular ion.

2.1.3 Attoclock

Both electron recollision-based probes and HHG begin with the photoionization of electrons. How long photoionization takes is one of the most intriguing problems in strong field physics. One of the techniques used to measure the photoionization time with attosecond resolution is attoclock. Attoclock uses only one femtosecond laser beam. It measures the angle- and energy-resolved spectra of photoelectrons that tunnel out of the rotating barrier created by a nearly circularly polarized laser field in combination with the atomic Coulomb potential [57,58]. In this technique, the rotation of the laser electric field provides a temporal ruler that can be used to determine the tunneling time of the electron by measuring the direction of maximum photoelectron distribution compared to the direction of maximum electric field [58,85]. The temporal resolution of attoclock is determined by the angular resolution of the photoelectron detection i.e., $\delta\tau = \delta\theta/\omega_L$, where ω_L is the angular frequency of the laser field. Experimentally with attoclock, an accuracy of $\delta\theta \sim 1^o$ yields $\delta\tau \sim 10$ as for 800 nm radiation.

Attoclock provides straightforward access to directly probing the ionization process in the time domain. However, it has not settled the long-standing debate regarding electron-tunneling time because of ambiguities in interpreting the measurement. First, the interpretation of an

attoclock measurement requires three assumptions [57,58,85–87]: 1) the highest ionization probability coincides with the electric field peak, 2) the ionization is completed once electrons tunnel through the barrier, and 3) an electron is treated classically after tunneling. Moreover, it is difficult to disentangle the real tunneling delay from the additional delay introduced by the ionic potential, strong IR field, and multielectron effects. For example, Pfeiffer *et al.* found that the interaction with the ionic potential during streaking would cause an angular offset for the freed electrons; the offset is independent of laser intensity in He, but monotonically decreases in Ar because of multielectron and stark-shift effects [57]. A theoretical paper by Torlina *et al.* indicates no tunneling delays associated with one-electron hydrogen atom, while additional delays may be introduced by multielectron excitation by an IR field [87]. One way to better quantify the time delay introduced by multielectron excitation is to perform attosecond chronoscopy using attosecond pules.

2.2 How to Make Attosecond Pulses

Although HHG and attoclock can probe attosecond electron dynamics using only femtosecond pulses, most of attosecond spectroscopy methods require attosecond pulses. A common way to generate attosecond pulses is through HHG. For example, HHG driven by multicycle laser pulse leads to the generation of attosecond pulse trains because the electron repeats the three-step sequence of tunneling-acceleration-recombination every half period of the laser field [63,64]. If the HHG process is phase-matched over the gas medium, the single atom response will add up, leading to an amplified harmonic radiation [88]. The radiated-high-harmonic spectrum is composed of a frequency comb characterized by a flat plateau region extending from below the

atom's ionization threshold to the high harmonic cutoff [89]. This comb structure in the frequency domain corresponds to attosecond pulse trains in the time domain.

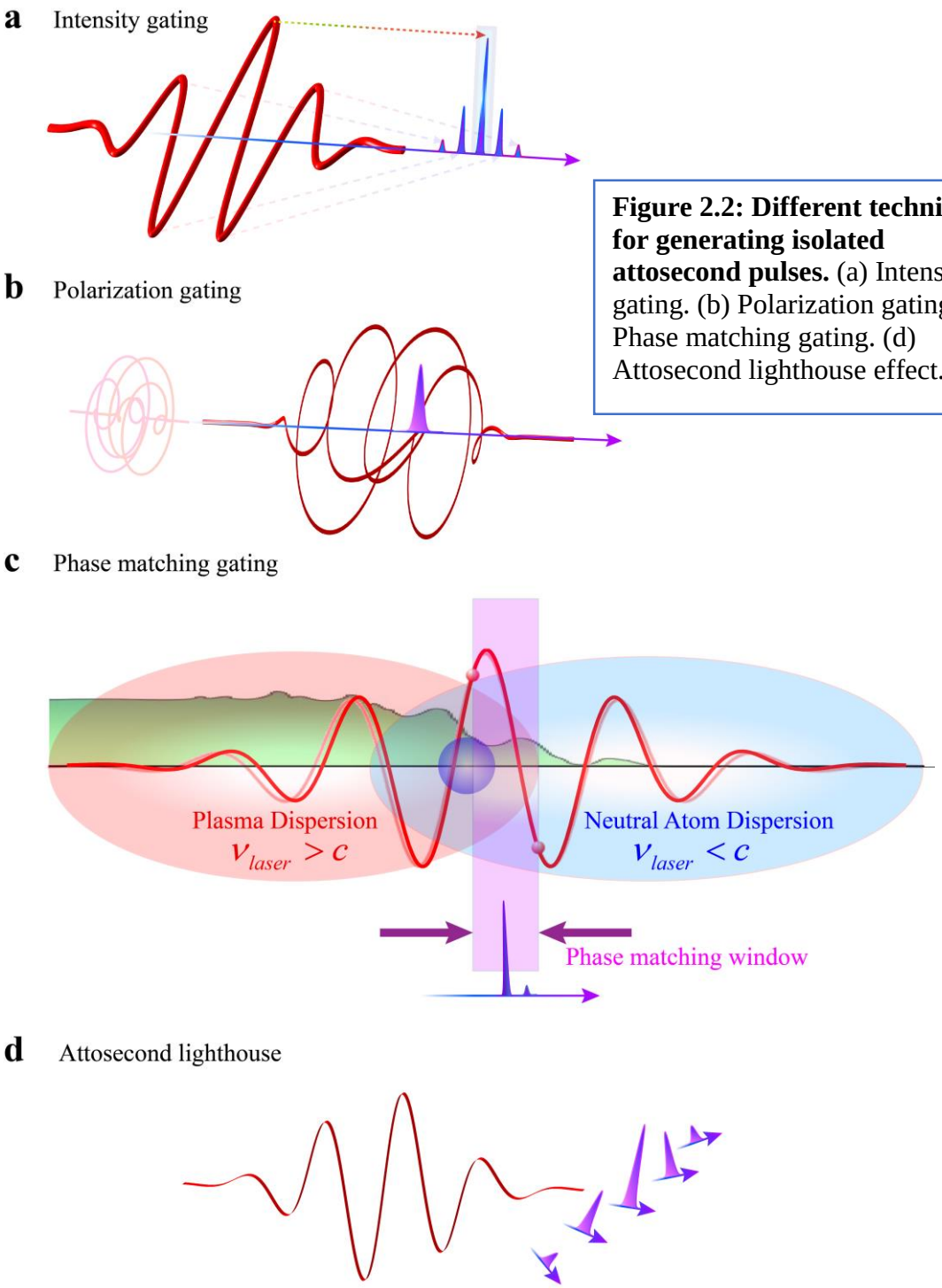

Figure 2.2: Different techniques for generating isolated attosecond pulses. (a) Intensity gating. (b) Polarization gating. (c) Phase matching gating. (d) Attosecond lighthouse effect.

An attosecond pulse train paired with its multicycle driver constitutes a powerful tool for attosecond spectroscopy. When using attosecond pulse trains in spectroscopy to probe electron dynamics, one needs to make sure that the electron dynamics terminate within a half period of the IR field. This termination avoids multiple starts and exposures of the undergoing process and guarantees that each burst in the attosecond pulse train probe the interrogated system in its ground state.

Attosecond pulse trains offer several advantages compared to isolated attosecond pulses in spectroscopy applications such as high energy resolution, easy experimental implementation, and low dressing-field intensity in streaking-type experiments [35]. However, some attosecond experiment requires isolated attosecond pulses. On example of this type of experiment is exciting a coherent superposition of multiple final states in attosecond-beating experiments [2,43]. This excitation is made possible by the super-continuum bandwidth associated with single attosecond pulses. The most intuitive method for achieving a single attosecond pulse is limiting the number of electric field cycles of the driving laser pulse to reduce events of electron recombination. However, this method is difficult to realize because harmonic emission from multiple half cycles cannot be entirely suppressed even with a pulse duration as short as 2.1 fs (corresponding to 0.9 optical cycles). Another difficulty for single attosecond-pulse generation is dispersion control. The dispersion of HHG radiation is different for emission in the plateau and cutoff regions. High-harmonic photons in the plateau region are emitted by electrons returning to the core along both short and long trajectories. These two trajectories have different frequency dispersions and impose a strong chirp on the HHG radiation. The emission in the cutoff region, on the other hand, can be confined within the most intense half cycle of the driving pulse (i.e., *intensity gating*, see Figure 2.2a) and is chirp-free. Therefore, intense waveform-controlled few-cycle laser pulses, combined

with carefully designed bandpass multilayer mirrors to select only the cutoff harmonics, have allowed reproducible generation of isolated attosecond pulses. In this scenario, the harmonic spectrum is usually centered at high energy (> 80 eV). Also, the ultimate pulse duration is limited by the bandwidth of the harmonic cutoff [90].

The generation of isolated attosecond pulses at low EUV photon energies or with ultrabroad bandwidth requires other gating techniques to restrict the HHG process to one single half-cycle of the driving field. For example, the *polarization gating* technique uses two counter-rotating elliptically polarized driving-laser pulses that are properly delayed so that only one half cycle of the two fields overlaps and creates a temporal window with linear polarization [31,91–93]. Outside this window, the tunneled electron cannot return to the parent ion and the harmonic emission is eliminated (Figure 2.2b). Thanks to the polarization-gating approach, isolated single-cycle attosecond pulses with a duration of 130 as and a central photon energy of 36 eV was demonstrated [31,92,93]. Compared to polarization gating, the *double optical gating* technique introduces a second harmonic field in addition to two counter-rotating, elliptically polarized, driving-laser pulses [94–97]. The second harmonic field breaks the symmetry of two consecutive half-cycles of the IR field. This broken-symmetry results in one attosecond pulse being generated within one IR optical cycle. In this way, double optical gating widens the temporal gate by a factor of two compared to polarization gating.

While polarization gating and double optical gating use the microscopic single-atom response to the driving laser fields, *ionization gating* takes advantage of the macroscopic phase-matching effect to confine the HHG emission to the leading half cycle of the driving pulse [98,99]. Therefore, ionization gating can be also called phase matching gating (Figure 2.2c). In ionization gating, phase matching ceases when the time-dependent ionization of the gas medium reaches the

critical ionization level after the first half-cycle of the laser field. This cessation occurs because once the critical ionization level is reached, the negative dispersion of the overly dense free electron in the medium cannot be compensated by the neutral gas atoms any more. Therefore, this critical ionization level sets a temporal window for phase matching. Because the temporal window for phase matching shrinks rapidly with longer driving laser wavelengths [89,100], HHG driven by mid-infrared lasers offers a great advantage for generating isolated attosecond pulses. Another advantage of implementing this phase matching gating using mid-infrared lasers is that because the harmonic cutoff energy increase with increasing λ^2 [89], using long wavelength driving laser fields in HHG can push the isolated attosecond pulse into the soft X-ray regime.

Compared to gating techniques that confine HHG to a single half-cycle of the driving field, the *attosecond lighthouse technique* generates isolated attosecond pulses by emitting each burst in the attosecond pulse train at a different angle and spatially separated in the far field (Figure 2.2d) [101]. This spatial separation is achieved by using a driving field with a rotating wavefront.

2.3 Attosecond Pump-Probe

Attosecond pulses can be used in pump-probe experiments to directly observe attosecond processes in the time domain. In pump-probe experiments, the pump pulse arrives first to initiate the dynamics of interest, the subsequent probe pulse arriving with a variable time delay produces an observable from the interrogated system. The temporal resolution of a pump-probe experiment is determined by the duration of the pump and probe pulses. Because of this requirement, one could decide to use two isolated attosecond pulses for the attosecond pump-probe experiments. However, the low photon fluxes of existing attosecond light sources encumber such a measurement scheme [1,102]. In addition to the flux problem, the cross section of two-photon processes is low

compared to that of a one-photon process. As a result, the EUV/X-ray intensity needs to be > 10^{15} W/cm^2 to obtain a time-resolved signal. This intensity is difficult to realize.

To overcome these difficulties, most of the current attosecond pump-probe experiments use one attosecond pulse and one IR pulse. These two pulses are perfectly synchronized relative to each other because HHG under IR driving field is a coherent process. The temporal-resolution limit imposed by the IR pulse duration can be circumvented by probing dynamics that are sensitive to the instantaneous value of the IR electric field. In this case, the IR carrier frequency imprints a temporal ruler on the dynamical evolution of the system, giving access to the sub-cycle temporal resolution. Although attosecond temporal resolution is obtained, the IR pulses used in experiments add certain difficulties to interpreting the measurement results. For example, intrinsic dynamical changes of the system are coupled with strong-field, light-matter interaction induced by intense IR pulses. To decouple this interaction from intrinsic material dynamics, high-level theoretical work is required to model this interaction. For example, in the measurement of attosecond photoemission time, the Wigner time delay is convolved with a measurement-induced time delay [42,103,104]. Although this measurement-induced delay can be calculated, it requires complex and difficult modeling. Another difficulty of this pump-probe scheme is that the broad bandwidth of attosecond pulses excites a manifold of final states. The excitation is further complicated by state-dependent cross sections and subsequent IR dressing of the final states. Such complications appear in attosecond quantum control of solid-state materials and large polyatomic molecules [43,44,105]. Nevertheless, these complications in attosecond pump-probe experiments provide a rich framework for ultrafast dynamics and strong-field physics.

There are two types of attosecond pump-probe experiments that are categorized by the order in which the attosecond and IR pulses interact with the interrogated system. The order also

determines the information extracted from the system [93,106]. The first type is performed with a conventional pulse sequence, i.e., IR excitation followed with attosecond an EUV/X-ray probe. This scheme can be used to investigate sub-cycle population dynamics of a system excited by the IR pump pulse [107]. The second type employs a less intuitive pulse sequence, i.e., the attosecond pulse precedes the IR pulse. This scheme has found extensive application in attosecond-pulse characterization [28,30,32], the timing of the birth of a photoelectron [42,44,104], and measuring a high-energy photoelectron lifetime [35]. This scheme has also been used to study quantum-pathway interference. For example, quantum beats of multiple bound-excited states launched by isolated attosecond pulses have been observed in neon using the pump-probe scheme just described [108].

2.4 Attosecond Pulse Characterization

The application of attosecond pulses in pump-probe spectroscopy to investigate attosecond dynamics requires knowledge of the time-domain structure of attosecond pulses. Before the advent of attosecond science, the full temporal characterization of ultrafast pulses was achieved primarily by using frequency-resolved optical gating (FROG) technique [109]. FROG applied a temporal gate *G(t)* with a controlled delay τ to decompose the field to be characterized *E(t)* into temporal slices, and then measured the spectrum of each slice. This procedure yielded the so-called FROG trace

$$S(\omega,\tau) = \left| \int_{-\infty}^{+\infty} dt G(t) E(t-\tau) e^{i\omega\tau} \right|^2 . \tag{2.1}$$

Now, various iterative algorithms can be applied to extract *G(t)* and *E(t)* from $S(\omega, \tau)$. In practice, most implementations of FROG use the self-gating method where *G(t)=E(t)*, and the auto-

correlation is achieved via the nonlinear interaction of the pulses with a crystal, *e.g.*, second-harmonic generation. The FROG method cannot be straightforwardly extended to measuring attosecond pulses because of several difficulties. These difficulties include the broad bandwidth of attosecond pulses, difficulty in beam-splitting, and the low nonlinearity of materials in EUV /X-ray regime. Instead, attosecond pulse characterization relies on the combination of an attosecond pulse with a delayed-laser field that acts as a temporal gate. The nonlinear interaction is achieved either using the photoionization process, or the HHG process itself. These two approaches are categorized as *ex-situ* and *in-situ* characterization, depending on whether the characterization is performed at the same location as the attosecond pulse generation [31,41].

2.4.1 *Ex-situ* Characterization of Attosecond Pulses

Ex-situ characterization of attosecond pulses is essentially a pump-probe measurement. Attosecond pulses generated through HHG is focused onto a target to produce photoelectrons. The kinetic momentum spectrum of these photoelectrons is an electron-replica of the attosecond pulse. Also, the spectral phase of each frequency component ω_X of the attosecond pulse is mapped into the time of ionization for photoelectrons with kinetic energy $E_k = \hbar\omega_X - I_p$, where I_p is the ionization potential. To measure the ionization time of the photoelectrons, an IR laser pulse is focused on the target with a controlled time delay relative to the attosecond pulse. The IR field induces perturbations to the liberated photoelectrons. The perturbations depend on the photoelectrons' time of ionization relative to the laser field. Within the strong field approximation, the electron's transition amplitude to the final state with momentum $\boldsymbol{v}$ is given by [34]

$$a(\boldsymbol{v},\tau) = -i\int_{-\infty}^{+\infty} dt e^{i\varphi(t)}\boldsymbol{d}_{\boldsymbol{p}(t)}\,\boldsymbol{E}_X(t-\tau)e^{i(E_k+I_P)t}$$

$$\varphi(t) = -\int_{t}^{\infty} dt' \left[\boldsymbol{v}\cdot\boldsymbol{A}(t') + \frac{\boldsymbol{A}^2(t')}{2}\right], \tag{2.2}$$

where $\boldsymbol{A}(t)$ is the vector potential of the laser field, $\boldsymbol{p}(t) = \boldsymbol{v} + \boldsymbol{A}(t)$ is the canonical momentum of a free electron dressed by the laser field, $\boldsymbol{d_p}$ is the electron transition dipole matrix from the bound-state to the continuum-state, and E_k is the kinetic energy of free electron $E_k = \boldsymbol{v}^2/2$. Equation 2.2 indicates that a phase gate $G(t) = e^{i\varphi(t)}e^{i(E_k+I_P)t}$ is applied to the electron wave packet replica of the attosecond pulse $\boldsymbol{d}_{\boldsymbol{p}(t)}\boldsymbol{E}_X(t-\tau)$. Equation 2.2 constitutes the basis for the *frequency-resolved optical gating for complete reconstruction of attosecond bursts* (FROG-CRAB) technique. Within this general picture, two special schemes are utilized for two specific temporal structures, i.e., the RABBITT technique for attosecond pulse trains and the attosecond streak camera for isolated attosecond pulses. To understand the RABBITT technique, it is easier to start with laser-assisted photoemission.

Laser-assisted photoelectric effect (LAPE). The laser-assisted photoelectric effect is the basis of many advanced attosecond pulse-characterization techniques such as RABBITT and Phase retrieval by omega oscillation filtering (PROOF). The process can be described as [110]:

$$\boldsymbol{A} + \gamma \rightarrow \boldsymbol{A}^+ + (e^- + n\omega) \qquad n = \pm1, \pm2, \pm3 \cdots\cdots, \tag{2.3}$$

where the system $\boldsymbol{A}$ absorbs a high-energy photon γ and emits a bound electron into the continuum (Figure 2.3a). In the presence of a laser field, the continuum electron e^- can exchange an integer number of photons $n\omega$ with the field, forming sidebands corresponding to the absorption or stimulated emission of photons. Since free electrons in vacuum cannot absorb or emit photons, LAPE should also be assisted by the ionic core or the surface to satisfy the both energy and momentum conservation. This conservation can only happen when electron is in close proximity with the ion or surface. This restriction can be exploited to study the evolution of an electron wave function moving away from the ion or surface. The wave function evolution and attosecond pulse

structure can be obtained by studying the intensities of different orders of sidebands as a function of laser wavelength, intensity, pump-probe delay etc.

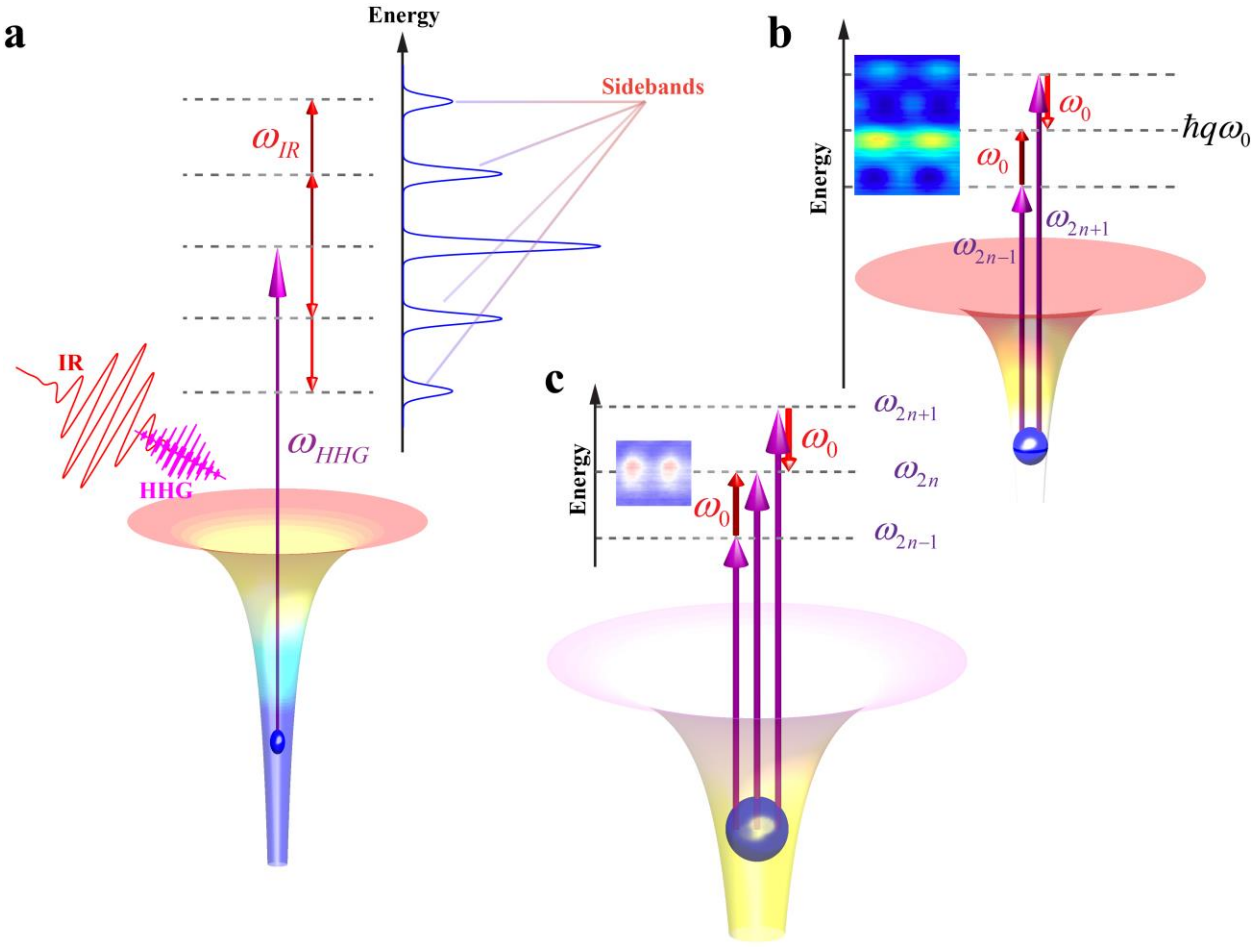

Figure 2.3: Different ex-situ methods of characterizing attosecond pulses. (a) Laser-assisted photoemission (LAPE). (b) Reconstruction of attosecond beating by interference of two-photon transitions (RABBITT). (c) Phase retrieval by omega oscillation filtering (PROOF), adapted from [111].

For simplicity, we can just consider the first and second orders of sidebands. In this case, the LAPE response function can be written as [55,112,113]

$$f(E-E_0) = \frac{1-2A_1-2A_2}{\sqrt{2\pi\sigma^2}} e^{-\frac{(E-E_0)^2}{2\sigma^2}} + \sum_{\pm}\left(\frac{A_1}{\sqrt{2\pi\sigma^2}} e^{-\frac{(E-E_0\pm\hbar\omega)^2}{2\sigma^2}} + \frac{A_2}{\sqrt{2\pi\sigma^2}} e^{-\frac{(E-E_0\pm 2\hbar\omega)^2}{2\sigma^2}}\right), \quad (2.4)$$

where A_1 and A_2 represent the first- and second-order sideband intensities, E_0 is the electron kinetic energy of the photoemission peak, σ is the peak width, and ħω is the peak separation. Both theory and experiment have shown that the sideband intensity for small values of argument x can be modeled by the square of a Bessel function:

$$A_1 = J_n^2(x)$$

$$x = \sqrt{\frac{16\pi\alpha}{m_e\hbar}\frac{IE_0}{\omega^4}}. \quad (2.5)$$

Here, I is the dressing-field intensity. For small x, A_1 can be approximated by $A_1 \approx x^2/4$ leading to

$$A_1 \propto \frac{IE_0}{\omega^4}. \quad (2.6)$$

In this regime, the sideband height depends linearly on the IR laser intensity. This linear relationship forms the basis for EUV+IR cross-correlation measurements with the LAPE technique.

Reconstruction of attosecond beating by interference of two-photon transitions (RABBITT). The LAPE technique measures the overall pulse duration of the attosecond pulse. However, detailed temporal information about attosecond pulses is required for certain experiments. The temporal structure of attosecond pulse trains corresponds to combs in the frequency domain. Therefore, the photoelectron spectrum produced by an attosecond pulse train

consists of discrete peaks with kinetic energies separated by 2ħω. The photoelectron can absorb or emit integer numbers of IR photons in the presence of the laser field, forming sidebands around the main photoelectron peaks (Figure 2.3b). If the IR intensity is properly adjusted so that only first-order LAPE sidebands exists, there are two different quantum paths exciting electrons from the same initial state to the same sideband, nħω: (i) absorbing a lower-order harmonic photon and an IR photon (n-1)ħω+ħω; (ii) absorbing a higher-order harmonic photon while emitting an IR photon (n+1)ħω-ħω. Because of the inference between two quantum paths, the sideband intensity oscillates as a function of delay between the attosecond pulse train and the IR pulse $S_n \propto sin\left[2\omega\left(\tau - \frac{\varphi_{n+1}-\varphi_{n-1}}{2\omega} - \tau_q^{atom}\right)\right]$. The atomic delay τ_q^{atom} can be calculated or ignored when $\tau_q^{atom} \ll \tau_q^{GD}$. This gives access to phase information of harmonics that can be combined with the amplitude information to reconstruct the temporal profile of the attosecond pulse train [32]. This reconstruction technique is called RABBITT.

Attosecond streak camera (atto-streaking). While the RABBITT technique is used to characterize attosecond pulse trains, the attosecond streak camera was developed to characterize isolated attosecond pulses. Similar to RABBITT, the isolated attosecond pulse photoemits the electrons to the continuum in the laser field. The electron ejected into the laser field at the moment t_i with initial velocity $\boldsymbol{v}_i$ has a final drift velocity of $\boldsymbol{v}_f = \boldsymbol{v}_i + \frac{e}{m_e}\boldsymbol{A}(t_i)$. In other words, the laser field modulates ("streaks") the momentum of the photoelectrons in proportion to the laser vector potential at the instant of ionization. Therefore, the laser-modulated electron-momentum distribution can be changed by adjusting the delay between the attosecond pulse and the laser pulse. This time-dependent electron-momentum distribution forms the streaking spectrogram and allows us to retrieve the temporal shape of both fields from the spectrogram [34].

Phase retrieval by omega oscillation filtering (PROOF). The FROG-CRAB technique needs to assume a narrow spectral bandwidth of the attosecond pulse for the retrieval algorithm to be accurately and reliably used. For attosecond pulses with ultrabroad bandwidth, phase retrieval by omega oscillation filtering (PROOF) was developed [31,111]. The PROOF method employs a quantum-path interference scheme similar to RABBITT. However, because of the continuous spectrum, there is an additional quantum path of one-photon direct excitation besides two two-photon pathways to a given photoelectron final state (Figure 2.3c). The quantum-path interference results in three components in the photoelectron momentum spectrum: $I(\boldsymbol{v},\tau) = I_0(\boldsymbol{v}) + I_\omega(\boldsymbol{v},\tau) + I_{2\omega}(\boldsymbol{v},\tau)$, where ω is the frequency of the dressing laser field. $I_0(\boldsymbol{v})$ is the combined transition probability of three paths. $I_\omega(\boldsymbol{v},\tau)$ and $I_{2\omega}(\boldsymbol{v},\tau)$ oscillates with frequency ω and 2ω respectively as a function of delay τ between the attosecond pulse and the laser pulse. The spectral phase of the attosecond pulse can be extracted from I_ω with proper algorithm.

(Ex-situ) tomographic reconstruction of attosecond pulses (TRAP). Most of the existing methods of attosecond pulse characterization are for linearly polarized light. Circularly polarized coherent EUV/X-ray has been demonstrated through several generation schemes including using two counter-rotating circularly polarized driving light [68–70], using below-threshold resonant HHG driven by elliptical laser pulse [114], and using bi-chromatic cross-polarized linearly polarized drivers [115]. Direct reconstruction of the temporal structure of these three-dimensional light pulses not only facilitates their applications to study magnetic matters and chiral materials, but also serves as a sensitive probe of the HHG medium under multi-color ionization or below-threshold tunneling and recombination. I demonstrate the first *ex-situ* tomographic reconstruction of attosecond pulses in chapter 5 [30].

2.4.2 *In-situ* Characterization of Attosecond Pulses

Different from the ex-situ techniques that rely on the photoelectric effect in a downstream setup, the *in-situ* characterization of attosecond pulses employs an additional second harmonic field to directly probe the process of attosecond pulse generation [31,41,116,117]. The added field is too weak to cause electron ionization but can perturb the HHG process. The perturbation modifies the spectral patterns of the HHG radiation. As a result, the HHG pulse duration can be retrieved by measuring the radiation modification as a function of time delay between the second harmonic and fundamental IR field. For HHG under a single-color fundamental-driving field, the electron trajectories in two consecutive subcycles are symmetric with respect to the atom, resulting in a HHG spectrum with only odd-order harmonics. The addition of an orthogonally polarized second harmonic field collinear with the fundamental field breaks the half-cycle symmetry, causing the emergence of even-order harmonics. In the microscopic single-atom picture, a given even-order harmonic appears when the second harmonic field perturbs the electron trajectory during the temporal window between ionization and recombination, and maximizes when second harmonic peak overlaps with the excursion of the electron in continuum. This relationship between electron-trajectory modulation at second harmonic field strength allows the recombination time of the electrons to be extracted, corresponding to the emission time of attosecond pulses. Therefore, the second harmonic field acts as a temporal gate in the in-situ characterization of attosecond pulses.

***(In situ)* space-time reconstruction of attosecond pulses (STRAP).** The in-situ characterization method in principle cannot be applied to an isolated attosecond pulse, because the generation process in this case is confined in only one half-cycle. This difficulty is overcome by introducing the second harmonic field at a small angle relative to the propagation direction of the

fundamental field [31,41]. Because of the noncollinearity, the second-harmonic perturbation modifies the electron trajectories not only in time, but also in space. Spatially, the second-harmonic field changes the near-field wave front of the driving pulse and thus the far-field propagation direction of the attosecond EUV/X-ray pulses. Measurement of the space-dependent EUV/X-ray spectrum as a function of delay between two fields gives the space-time reconstruction of the attosecond pulses. Although in-situ characterization of isolated attosecond pulses including STRAP is an all optical approach and sensitive to the quantum trajectories of electrons, it is also an invasive probing technique and destroys the attosecond pulse structure for downstream applications. On the other hand, it doesn't require a bright attosecond pulse to produce adequate photoelectrons, and offers several advantages compared to the attosecond streak camera.

2.4.3 Applications of Sub-cycle IR Electric Field Characterization

Attosecond pulse-characterization techniques, such as CRAB, not only provide temporal information about attosecond pulses, but also give the full time-domain structure of the ultrafast IR probe pulses. This capability of sub-cycle laser-field characterization is beyond the resolution limit of the conventional FROG method based on nonlinear crystals. In addition, CRAB is not limited by the bandwidth of nonlinear materials. This capability can help us acquire insights into the propagation and modulation of an ultrafast laser field in materials on attosecond time scales and atomic length scales [56,60,118]. For example, the sub-cycle temporal resolution was used to study the attosecond nonlinear polarization and light-matter energy transfer in solids [119,120]. The nonlinear polarization, or light-matter interaction, changes the sub-cycle laser field structure after the laser passes through the sample. The change was measured in the downstream attosecond

streak-camera setup. A similar method was applied to study the near field's temporal response to the ultrafast laser excitation in nanostructured materials [45].

The screening of laser field on material surfaces is another intriguing problem in near field physics. In particular, screening at metal surfaces is a dynamical dielectric response of electrons in materials to the incident laser field. Additionally, the combination of the incident and reflected laser fields on a metal surface can create a dynamical 2D transient grating on the surface. The effect of this grating on electron motion is no longer negligible at attosecond time scales. By using the RABBITT method to measure the photoemission time delay of electrons emitted at different angles into this transient grating, Lucchini *et al.* discovered that, surprisingly, the macroscopic Fresnel equation can still reproduce the spatiotemporal profile of the electromagnetic field under ultrafast electron screening [60,118]. In contrast, atto-streaking results claims that Fresnel equations based on the macroscopic properties of a target cannot be applied at the near-field of metal-vacuum interface [56]. To fully understand the effect of an IR field at a metal-vacuum interface on photoelectrons, we need to achieve enough time, angle and energy resolution to distinguish the laser-field-induced and band-structure-related photoemission time delay as functions of electron kinetic energy and emission angle. This problem is discussed in Chapter 8.

2.5 Attosecond Time-Resolved Spectroscopy in Atoms

The full temporal information of attosecond pulses and IR pulses facilitates their applications in pump-probe spectroscopy to investigate attosecond processes in atoms, molecules and solid-state materials. Atom represents the simplest form of matter. Attosecond spectroscopy starts with atoms. Besides the importance of directly probing atoms, the knowledge gained from studying atoms also guides us in applying similar methods to molecules and solids. One example

is the study of photoemission time delay in atoms, molecules and solids. In atoms, a large contribution to photoemission time delay comes from the scattering of photoelectrons with the Coulomb potential, which is dominant over the time delay caused by electron-electron interactions. For molecules, such scattering-induced delay is observed to be angle-dependent due to the asymmetric stereopotential [121]. For metallic solids, the Coulomb potential-induced delay is very small for valence electrons, allowing us to study the state-specific photoelectron lifetime and the effect of many-body electron-electron interactions [35,122].

2.5.1 Photoemission Time Delay in Atoms

Attosecond streak camera was first used to measure the lifetime of $3d^{-1}$ core hole in krypton during Auger decay [37]. A $3d^{-1}$ core hole was created in a krypton atom by an EUV pulse and subsequently filled by a *4s* electron. The released energy from core-hole filling was transferred to the emission of a *4p* Auger electron. The difference between the emission time of the Auger electron and direct-photoemitted electron is the core-hole lifetime. To measure the core-hole lifetime, an IR pulse was introduced and dressed both the direct-photoemitted *3d* electron and the *4p* Auger electron. The evolution of the electron kinetic-energy spectra as a function of relative delay between two pulses revealed a $3d^{-1}$ core-hole lifetime of 7.9 fs. The localization of the core-hole provides an element-specific probe to investigate the local electronic structure at a given atomic site. However, when a core-hole is created by resonant excitation of a core-level electron to an unoccupied electronic level, the core-hole lifetime can be influenced by localization of the excited core electron. This dependence of core-hole lifetime and core-electron localization can be used to study the charge transfer between adsorbed atoms or molecules and the metal surface. The direct time-domain study of core-hole lifetime of atoms on a metal surface was pioneered by

Miaja-Avila *et al.* through measuring the $4d^{-1}$ core-hole lifetime of xenon on Pt(111). The measurement was enabled by their first observing LAPE on a metal surface [112]. By comparing the LAPE sideband intensity as a function of pump-probe delay for the Pt *d*-band and Xe Auger photoelectrons, the researchers measured the lifetime of the Xe $4d^{-1}$ core-hole to be 7.1 fs. Here, although the measured core-hole lifetime is in the femtosecond regime, the experiments used pulses with attosecond structure.

Attosecond pulses can also be used to investigate attosecond excited-state lifetimes such as the autoionizing states of noble atoms [59,123,124]. Autoionization results from the presence of discrete states above the ionization threshold in atomic or molecular systems. These discrete states are embedded in the continuum and leads to two quantum pathways for electron ionization, i.e., 1) direction ionization to continuum and 2) excitation to discrete states then coupled to the continuum. The interference between two quantum pathways lead to an asymmetric Fano intensity profile as a function of the exciting-photon energy [125]. Direct time-domain study of Fano resonances is a test bed for theories to address many electron interactions.

Fano resonance induces strong phase variations in an electron wave packet. This phase can be regarded as a timing shift. Now the question is: does direct photoionization into the continuum take time? To answer this question, one of the first experiments to measure the attosecond photoionization delay was done in gas-phase neon atoms [42]. An isolated attosecond pulse < 200 as centered at 106 eV photoionized neon atoms and the few-cycle IR pulse streaked the photoelectrons. The streaking trace showed that 2*p* electrons were emitted at a 20 as delay as compared to the 2*s* electrons. These attosecond delays shined light on the scattering of photoelectrons in the ionic potential. The spherical symmetry of the atomic potential facilitated the theoretical calculations to understand the origin this delay. However, multiple efforts were

performed [126–128], and so far they has underpredicted the delay by a factor of two. This discrepancy between experiment and present theory indicates the possible influence of laser-atom interaction, shakeup and many-electron correlation in attosecond photoionization dynamics.

2.6 Attosecond Time-Resolved Spectroscopy in Molecules

2.6.1 Born-Oppenheimer and Single Electron Approximations

Compared to simple atoms, attosecond-photoinduced dynamics in molecular systems have a crucial influence in chemical or biological processes such as photosynthesis, vision and radiation damage of biomolecules. It is well-accepted that the explanation of these ultrafast molecular dynamics involves the breakdown of two conventional approximations [105].

The first one is the Born-Oppenheimer approximation, in which the electronic configuration is assumed to adapt instantaneously to the nuclear motion since the nuclei have much larger masses than the electrons. However, this is true only when the energy difference between electronic states of interest is sufficiently large compared to the energy contained in the nuclear degrees of freedom. For example, it has been accepted in scientific community as a general rule rather than the exception that the Born-Oppenheimer approximation fails during nonadiabatic dynamics when crossing conical intersections where the nuclear and electronic degrees of freedom are strongly coupled and evolve at a few femtosecond-to-attosecond time scale [129]. This ultrafast relaxation at conical intersections is responsible for the extraordinary photo stability of the DNA double helix structure [130].

The second approximation is the independent electron approximation, i.e., the electrons are treated as individual particles in a mean field generated by nuclei plus all other electrons. This approximation is valid if we assume that electron-electron coupling is negligible compared to the

energy difference between relevant electronic states. However, this assumption can become invalid during photoemission [105,131]. In photoemission, the sudden removal of an electron may leave the cation in a non-eigenstate, i.e., a non-stationary state that is a coherent superposition of multiple cationic eigenstates. These superposition states can lead to charge redistribution across the molecule on an attosecond-to-femtosecond time scale. This charge migration can be terminated by an additional IR pulse or the molecular nuclear dynamics. The termination will trap (localize) the hole and determine the subsequent reaction pathways [43]. This hole-localization-determined reaction pathway is an example of how attosecond techniques manipulate the chemical reactions through coherent control. Chemical reaction pathways can also be affected by molecular vibrations. It has been experimentally demonstrated that certain electronic superposition states can be prepared to circumvent the intramolecular vibrational energy dissipation. Thus, coherent control of attosecond charge dynamics is opening the door to engineering nonequilibrium reaction pathways. These pathways can be investigated by pump-probe spectroscopy.

The first attosecond pump-probe experiment studied the intramolecular charge dynamics in the simplest form of molecule, a hydrogen molecule [132]. An EUV pulse ionized H_2 and promoted it into an excited state. An intense few-cycle IR pulse with a controlled delay interacted with the excited molecule and changed the localization of the remaining hole, thereby influencing the emission direction of the neutral and charged fragments (H and H^+) after molecular dissociation. Moving to more complicated large molecules, Calegari *et al.* applied isolated attosecond and IR pulses in a pump-probe geometry to track ultrafast hole migration in the amino acid phenylalanine in the gas phase [43]. In the experiment, a single sub-300-as pulse with a spectrum covering 15 to 35 eV prompted sudden ionization of phenylalanine. A waveform-controlled 4-fs visible/IR pulse ionized the molecule for the second time, causing it to dissociate into –COOH and doubly charged

immonium ($^{++}NH_2$-CH-R) fragments. The yield of $^{++}NH_2$-CH-R oscillated as a function of pump-probe delay with evolving frequencies. This pattern emerged because several beating processes were initiated by the attosecond broad-band excitation. It showed that the attosecond charge dynamics in large molecular systems are more complicated than simple atoms because of the intricate energy levels that are intertwined with the vibrational and rotational motion of molecules.

2.6.2 Photoemission Time Delay in Molecules

Compared to atoms, the photoemission time in molecules has additional complexity originating from the dependence of the photoionization matrix element on the orientation of the molecule. For hetero nuclear molecules, the photoelectron wave packet will accumulate a highly structured scattering phase after travelling through an anisotropic scattering potential, leading to a Wigner delay of $\tau_W = \hbar \frac{\partial \varphi_W}{\partial E}$ depending on the electron emission angle. Cattaneo and coworkers observed this effect in the photoionization time delay of carbon monoxide (CO) by using the RABBITT technique combined with a Cold Target Recoil Ion Momentum Spectroscopy (COLTRIMS) apparatus [121]. In this experiment, the electrons were expected to escape faster on the O-Side compared to C-Side, in accordance with the steeper Coulomb potential on the O side. However, this expectation is only true in experiments at low photon energies, a reversed behavior is observed at higher photon energies. Catraneo *et al.* ascribe this observation to photoemission from different dissociative states of CO at different photon energies [121]. This work by Catraneo et al. shows that electron photoionization time in a molecule is influenced by both its electronic and structural properties.

Photoionization time delay can also be influenced by molecular resonances. These resonances were only characterized in the frequency domain before the advent of attosecond

spectroscopy. For example, shape resonance occurs when the outgoing electron wave packet matches the shape of the potential barrier formed by combining the molecular and centrifugal potential felt by photoelectrons. Recently, this shape resonance was studied in time domain by Huppert *et al.* They discovered through RABBITT measurements that the shape resonance in N_2O molecules can trap the photoelectron for a duration up to 110 as [133].

2.7 Attosecond Time-Resolved Spectroscopy in Solids

As with molecules, the Born-Oppenheimer approximation and the single-electron approximation have been standards for describing the electrons in solid. Based on these two approximations, the well-celebrated Sommerfeld model and Drude model are developed. In spite of the effective determination of band structure and phonon frequencies in a wide range of metallic systems, these approximated models are more a compromise rather than accurate. First, the bandgap is zero in metal. Therefore, the change in nuclear coordination can strongly influence the electronic properties, and vice versa. This coupling between nuclei and electron is manifested in phonon-mediated superconductivity and phonon-induced renormalization of the electronic dispersion. Second, phenomena beyond the single-electron picture occur in metal-to-insulator transitions, charge screening, ultrafast demagnetization, and in high-temperature superconductors. In these material systems, electron-electron many-body interactions play a pivotal role [134]. To directly investigate the these interaction in time domain, attosecond spectroscopies performed above and below transition temperatures may disentangle phonon, charge, and spin, as well as orbital-assisted dynamics and temporally study the process of electron-electron interactions responsible for the exotic electronic properties in solids.

2.7.1 Photoemission Time Delay in Solids

Although attosecond spectroscopy of solids is still in its infancy, impressive discoveries have been made. The first attosecond-streaking experiment in solids was an attempt to determine the escape time of electrons from tungsten (Figure 2.4) [44]. In the experiment, isolated EUV pulses with a duration of ~300 as centered at 91eV were used to initiate electron emission from W(110) surface. In the photoelectron spectrum, the spectral lines from *5d* and *6s* conduction-band electrons are congested because of the broad bandwidth of isolated attosecond pulses (6-eV FWHM). As a result, the photoelectron spectrum consists of two peaks: one at the kinetic energy of 56 eV corresponding to the emission from *4f* core level electrons, and the other at 83 eV corresponding to emission from integrated conduction bands. To time the electron emission, a few-cycle waveform-controlled 5-fs pulse at 750 nm was used to streak the photoelectrons. The measured streaking spectrogram revealed a delay of 110 ± 70 as for the emission of *4f* core-level photoelectrons relative to the conduction-band photoelectrons from the W(110) surface. The paper explained this delay through the variation in transport time of *4f* (~150 as) and conduction-band photoelectrons (~ 60 as) to the surface on the basis of two considerations. First, the mean group velocity of the conduction-band photoelectrons is approximately twice than that of the *4f* core-level photoelectrons. Second, *4f* photoelectrons have a longer inelastic mean free path, originating 1 Å deeper than conduction-band photoelectrons.

This paper triggered multiple theoretical efforts to explain the origin of the measured delay [93,103,135–139]. Two main contradictory interpretations have been proposed. The first explanation suggested that the delay is caused by propagation effects, and is supported by semiclassical calculations [140] and subsequent quantum-mechanical calculations including the interference effects of electron wave packets emerging from different layers [138]. The second

explanation ascribes the observed photoemission delay to the influence of initial-state electron localization, i.e., strongly bound 4f core-level electrons are photoemitted later than delocalized conduction-band electrons [103,141].

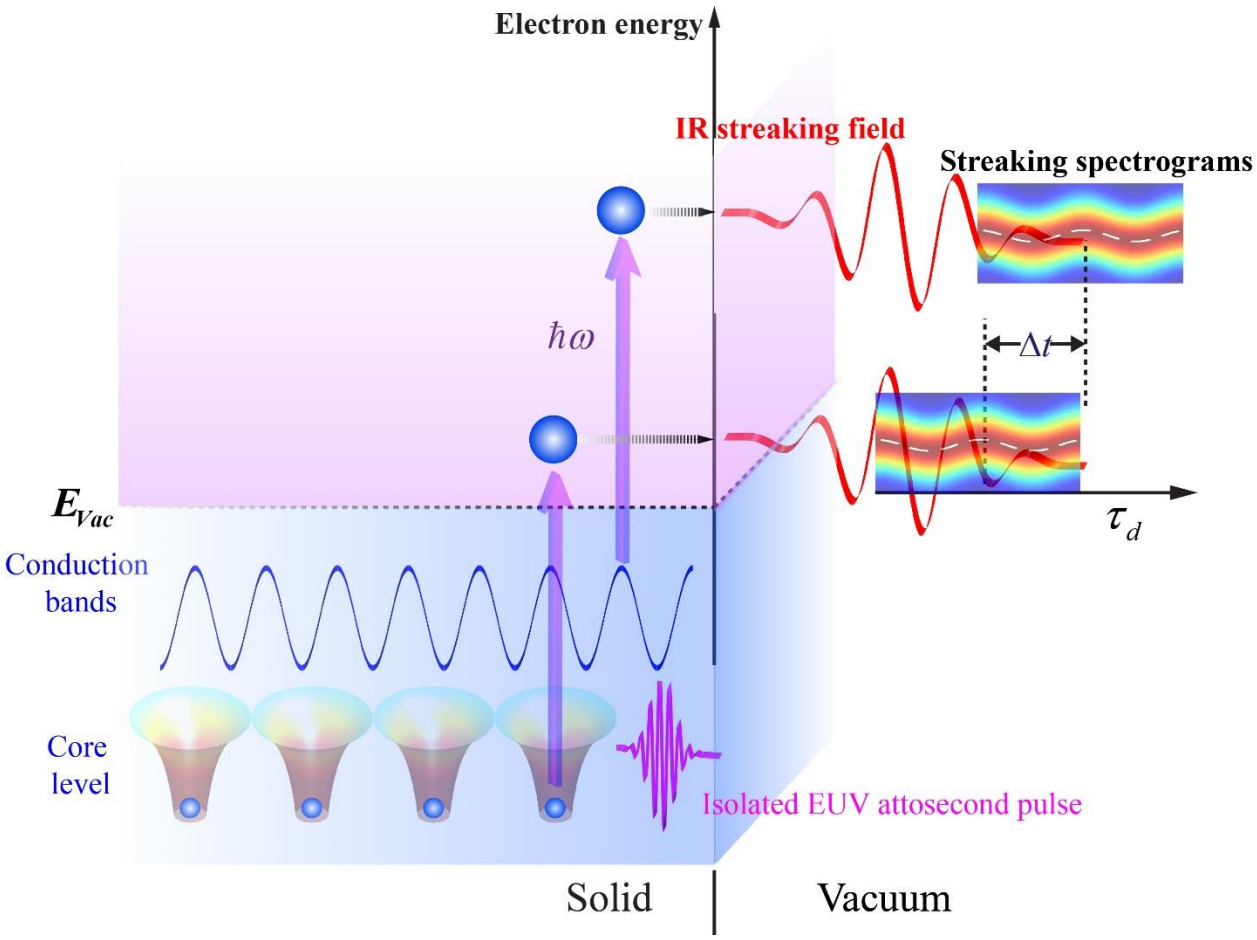

Figure 2.4: Photoemission time delay probed using isolated attosecond pulses. Schematic of the photoemission delay measurements performed by Cavalieri *et al.* [44]. In the experiment, isolated EUV pulses were used to initiate electron emission from solid surface. The broad bandwidth of the EUV pules congested the spectral lines from different conduction-band electrons. A few-cycle IR pulse was used to streak the photoelectrons. They measured the streaking spectrograms for the emission of core-level photoelectrons relative to the conduction-band photoelectrons. The streaking spectrograms revealed a delay for photoemission from core levels compared to conduction bands.

The follow-up experiment was performed in magnesium (Mg) [142]. Two advantageous properties of Mg rendered it a good material to discern different mechanisms responsible for photoemission time delay. First, Mg is a free-electron metal, with the applied IR field effectively screened at the surface, ensuring that the photoelectrons are only streaked after being liberated from the bulk. Second, the conduction-band electrons are much more delocalized than the *2p* core-level states in Mg, creating a greater contrast between conduction-band vs core-level localization than W. One would expect that similar to W(110), the photoemission delay should also be in the ~100 as range. Surprisingly, no discernable relative delay within the experimental error was measured between photoelectrons from the conduction band and from the core level. The paper suggested this result was due to the offsetting effects of escape depth (mean free path) and escape velocity. In Mg, higher (lower) kinetic-energy conduction-band (core-level) electrons are emitted from larger (smaller) depth inside the bulk. Thus, the results of Mg favor the interpretation that photoemission delay originates from the propagation effects rather than initial-state localization [93,142]. In contrast, other theoretical work suggests a difference in photoemission time for resonant interband and nonresonant surface-emission processes [143]. To measure this difference, we need to achieve enough energy resolution to distinguish various valence bands.

The energy resolution in attostreaking experiments is limited by the broad bandwidth associated with isolated-single attosecond pulses. Therefore, multiple conduction bands are treated as a block emission and referenced to core level states [44,142]. The other disadvantage is that photoemission time delay is mostly measured at one photon energy. Both implementations are problematic given that the mean free path of photoelectrons is both band-specific and photon-energy dependent [144]. Finally, the extraction of time delay requires complicated algorithms that may have errors or uncertainties in the retrieval processes [145]. This problem is less severe for

gas atoms, because the photoelectron wave packet is a perfect replica of the incident EUV pulse shifted by the photoemission time [42]. However, in solid-state materials, in addition to photoemission time, the temporal structure of the photoelectron wave packet is modified because of electron transport and dispersion in solids [146]. This influence needs to be taken into account in the retrieval algorithm of attostreaking.

In addition to attostreaking, RABBITT techinique can be used to investigate photoemission time delay. Locher *et al.* first extended the RABBITT technique to study energy-dependent photoemission delays from the noble metal surfaces Ag(111) and Au(111) [54]. The delays were measured at four photon energies from sideband 16 to 22. Emissions from different conduction bands, however, were convolved because the energy resolution was comparable to previous attostreaking experiments. To reference the release time of this convolved photoelectron, Locher *et al.* conducted the RABBITT measurement simultaneously on argon and metal surfaces in two interaction regions. Co-propagating EUV and IR pulses were focused onto the argon gas at the first interaction region where a time-of-flight spectrometer recorded the RABBITT race. The diverging beams were then refocused onto a metal surface at the second interaction region where the hemispherical electron analyzer measured the electron kinetic-energy spectrum. The photoionization time delay of Ar that had been widely investigated before served as a reference for calibrating the spectral phase of the attosecond pulse train. However, the measured delay in Ag and Au cannot be fully accounted for with initial state localization and electron transport. Locher *et al* postulated that a final-state effect may play an important role.

This result has several limitations because of the measurement scheme. First, uncertainty comes from the error bar (~100 as) presented in the time delay results. First uncertainty ocuurs because the results comprise two RABBITT measurements on two different targets (Ar and metal

surfaces). Second uncertainty comes from the complicated-photoemission time delay from Ar. Using Ar gas as the benchmark does not guarantee that the absolute photoemission time delay can be extracted from the results. Recent experiments have shown that in the energy range probed by Locher *et al.*, the photoemission time delay from Ar can have very complicated energy-dependent structures due to various resonance effects [104,147]. Third uncertainty comes from the systematic errors introduced by additional EUV optics, even though the authors attempted to correct the time delay caused by EUV dispersion and Ar through additional experiments and theoretical calculations. Finally, the authors did not specify the momentum range and the integrated angle for their results, which are extremely important for assigning band-structure effects.

2.7.2 Photoemission Delay Reveals Intrinsic Material Properties

The problems of previous attostreaking and RABBITT measurements are carefully considered in Chapter 7 of this thesis work where I measure the time delay using "self-referencing" strategy, i.e., referring the timing of the resonant photoemission to the off-resonant emission from the same metal surface (Figure 2.5) [35]. Using this technique, I unambiguously present the first direct observation of the influence of the final-state band structure on the lifetime of high-energy photoelectrons from multiple valence bands of Ni(111). We carefully investigated the energy-, angle-, and polarization-dependence of measured photoemission time delays. Our results show that photoelectrons experience an abrupt increase in lifetime by $\approx$ 212 as, when the ultraviolet (EUV)-photon-induced direct transition coincides with a final-state resonance in the Ni band structure. Moreover, large angle- (momentum-) dependent variations in photoemission time delay were also observed for the first time. This angle-dependent photoemission time delay are directly

related to the final-state band dispersion. This result represents the shortest final-state lifetime measured directly in the time domain to date.

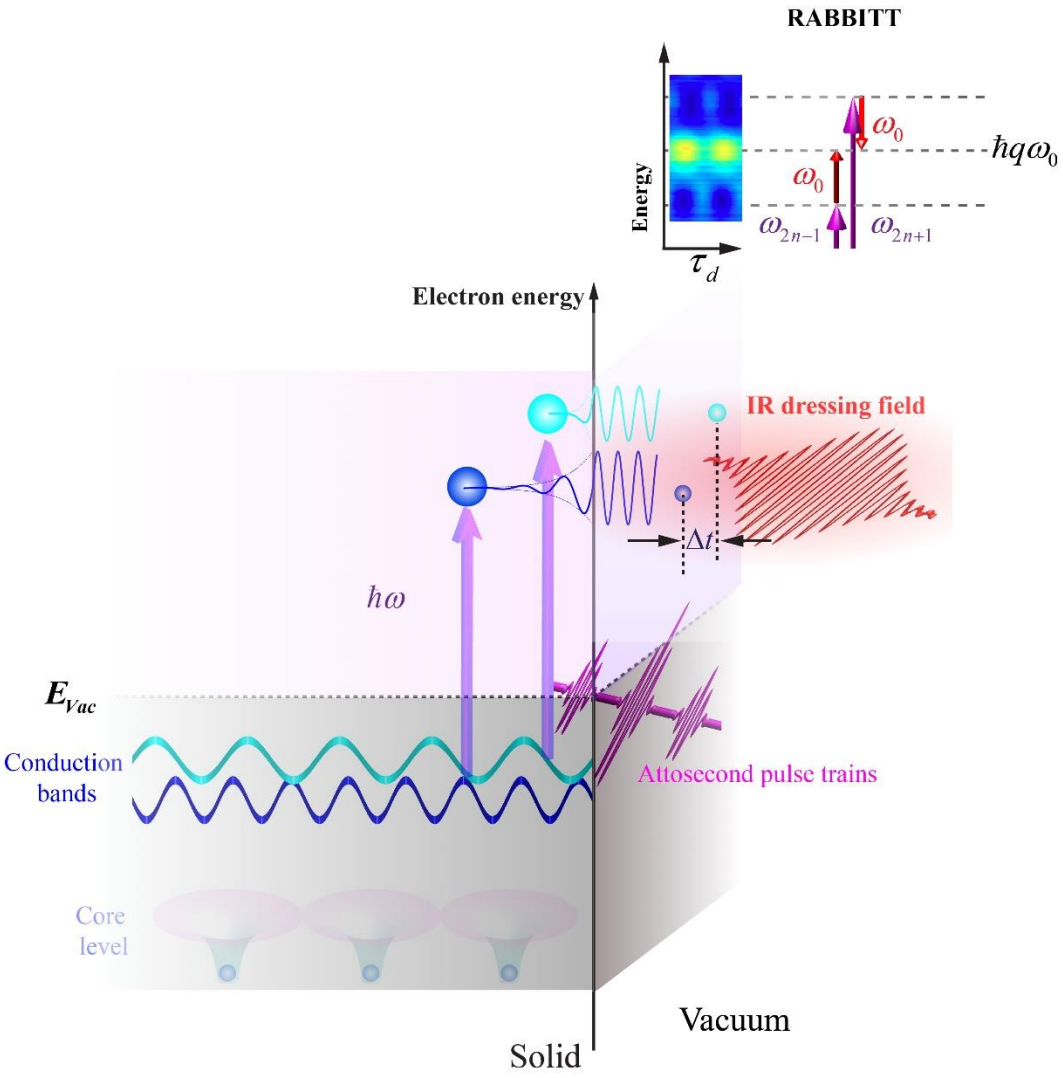

Figure 2.5: Photoelectron lifetime probed using attosecond pulses trains. Schematic of the photoemission delay measurements performed in Chapter 7-8 of this thesis. In the experiment, attosecond EUV pulse trains were used to initiate electron emission from solid surface. The narrow bandwidth of the EUV pulse trains is able to distinguish spectral lines from different conduction-band electrons. A IR pulse was used to dress the photoelectrons. We measured the RABBITT spectrograms for the emission of multiple conduction-band photoelectrons. The measurement revealed the influence on photoelectron lifetime from both unoccupied final states and occupied initial states.

After the final-state effects are taken into account, we can investigate the influence of occupied-band dynamics to photoemission time delay. These dynamics include electron-electron interactions. Electron-electron interactions are among the fastest processes in materials, playing prominent roles in strongly correlated electron systems and quantum materials. In recent years, these interactions have become accessible to direct time-domain studies by using femtosecond lasers in techniques such as time-resolved two-photon photoemission experiments. However, measurements using infrared or visible wavelength light are limited to the electron-electron interactions at the low-energy excited states with femtosecond time scales, while many electron-electron interactions can happen on faster attosecond time scales.

Chapter 8 of the thesis presents the measurement of attosecond electron-electron interactions in metals with time-, energy-, angle-, and polarization-resolved photoemission. In particular, we extract the time delays associated with photoemission from occupied bands in Ni(111) and Cu(111) into free-electron final states. This strategy allows us to demonstrate that photoemission from the occupied *d* band of Cu into free-electron final states is delayed by ~100 as compared to photoemission from the same band of Ni. We attribute this difference to the fact that the d band in Ni is half-filled, resulting in enhanced electron-electron scattering during photoemission. Moreover, we present a unified understanding of electron-electron interactions in transition metals across a broad energy range (0.5~40eV), by comparing attosecond photoemission measurements to the results from previous two-photon photoemission experiments.

2.7.3 Attosecond Control of Charge Dynamics in Solids

Photoemission is a surface-sensitive technique because of the low escape depth of electrons. Complementarily, attosecond transient-absorption spectroscopy is implemented to study the field-

induced subcycle interband transitions in bulk solids. The first experiment was performed on silicon dioxide (SiO_2) where a 72-as isolated-EUV pulse tracks the change in silicon's *L*-edge absorption (*2p* to conduction band) after excitation by <4 fs 780 nm waveform-controlled IR pulse [40]. The experiment reveals both a transient reduction in the *L*-edge absorption and a red shift of the conduction-band edge. Both changes are driven by the instantaneous electric field and therefore oscillate at twice the frequency of the driving field. The variation in *L*-edge absorption follows the transient change in conduction-band population. The shift of the conduction-band edge is identified as a dynamic stark shift resulting from the field-induced polarization in the material. The Stark shift of the bands brings interband transition into resonance with the IR laser excitation and amplified the increase in the conduction-band population.

A similar attosecond transient-absorption experiment was performed on the semiconductor Si, which is different from the dielectric SiO_2 [36]. In Si, an IR pulse excited the valence-band electrons across the bandgap and caused a change in the Si *L*-edge absorption. This change survives the duration of the pulse, indicating that the lifetime of the excited electron is longer than the subcycle duration of the IR pulse. The most fascinating result is the step-like increase in the conduction band population following the doubling of the frequency of the driving field, indicating a carrier-carrier interaction faster than the half period of the driving pulse. These results demonstrated that electron dynamics can be manipulated by a strong field at a frequency corresponding to a half-cycle period (~1.3 fs) up to ~800 THz. In the quest of manipulating the electron dynamics at a faster speed, Mashiko *et al.* later broke the 1-PHz barrier in the ultrafast control of electron motion in solid-state material by using the third-order nonlinearity of a wide band-gap semiconductor GaN. The band gap of GaN is 3.35 eV, requiring three IR photons ($\hbar\omega_L$ = ~1.6 eV) to complete the first resonant interband transition. Therefore, the third-order interband

polarization dominates the IR excitation, leading to a modulation in the absorption of the isolated attosecond pulse with a periodicity of $T_L/3$=860 as, corresponding to triple frequency of the IR field. This process can be described as a quantum beating between two channels coupling valence-band electrons to continuum states. These two channels include 1) direct excitation by isolated attosecond pulse and 2) absorption of three IR photons to complete the interband transition followed by an additional EUV photon absorption.

In addition to interband transitions, attosecond-intraband motion of charges in dielectrics was studied using attosecond transient-absorption technique [33]. The system studied is polycrystalline diamond. First, a waveform controlled 5-fs IR pulse pumped the sample. Second, an EUV single attosecond pulse spanning 30 to 55 eV probed the dynamics through absorption. The absorption features oscillated with twice the frequency of the driving field over the whole bandwidth of the single attosecond pulse, for small values of time delay. The phase of the oscillation was photon-energy dependent and assumed a V-shape with a vertex at 43 eV. Time-Dependent Density Functional Theory (TD-DFT) calculations showed that the oscillation resulted from the pump-induced change in the imaginary part of the dielectric function and hence in the EUV absorption of diamond. Since the V-shaped energy dispersion of oscillation can be reproduced by using two IR-dressed sub-bands, the main IR-induced dynamic in diamond is likely due to intraband rather than interband transitions.

These experiments show that attosecond spectroscopy can be applied to investigate electron dynamics in metals, dielectrics, and semiconductors. These applications provide us valuable insights into electron-electron and electron-phonon interactions as well as allowing us to investigate tunneling or multiphoton processes during IR-excitation.

2.8 Organization of the Thesis

In Chapter 3, the relevant theoretical background will be presented regarding the techniques used in this thesis work: photoelectron spectroscopy and high harmonic generation. Chapter 4 shows the experimental apparatus of attosecond photoelectron spectroscopy. It describes the laser system, EUV/soft x-ray generation setup, monochromator design, and end station. The end station is equipped with a variety of spectroscopic detectors and sample preparation/characterization tools.

Chapters 5-6 present the application of attosecond metrology in characterizing the temporal structure of attosecond pulses. In Chapter 5, 3D attosecond pulse trains of circularly polarized harmonic field are reconstructed by combining the interferometric laser-assisted photoemission technique with the ability to rotate the 3D attosecond field via controlling the high harmonic generation process. Chapter 6 describes the measurement of a linearly polarized attosecond pulse train generated by two-color laser pulses. By controlling the phase delay between the two drivers, the sub-attosecond pulse structure can be manipulated. More importantly, the phase-matching effect can confine most of the EUV emission to one burst, giving rise to quasi-isolated single attosecond pulses.

Chapters 7-8 then discuss the investigations of the attosecond electron dynamics in transition metals including nickel and copper. Here I want to emphasize that even though this is an attosecond experiment, the strong field influence is minimal. The goal is to unravel several central mysteries of photoemission identified since the invention of this technique. What is the lifetime of the highly excited states (>20 eV above Fermi) in solids and how does the resonant excitation of these states influence the photoelectron lifetime? What is the velocity of photoelectrons when they are travelling inside solids before being liberated into space? How does

the many-body interactions like electron screening and scattering influence the photoelectron lifetime? Are the interactions spin dependent? We will consider the first two questions in Chapter 7 with measurements of the dependence of photoelectron lifetime on incident photon energy in nickel. Chapter 8 answers the latter two questions by comparing the photoelectron lifetime in nickel and copper. Chapter 8 also shows how attosecond measurement can inform us about the coupling between initial and final states during photoemission.

Chapter 9 summaries the thesis and describes future work that would take the attosecond metrology to another level.

2.9 Conclusion

The rapid progress in attosecond science over the past decades provide us with access to the fastest electronic dynamics. Understanding the microscopic motion of electrons advances the control over tabletop EUV/X-ray generation and attosecond light sources. Advanced attosecond sources coupled with state-of-the-art spectroscopy techniques reveal electron transport, the lifetime of highly-excited states, and electron-correlation dynamics. Extending attosecond studies to more complicated systems like surface adsorbates and strongly correlated systems may shed light on the central mysteries of photovoltaic and superconductivity. The development of water-window attosecond sources will grant us the capability to study carbon-based organic molecules and ultrafast biology such as DNA damage and repair.

Chapter 3

General Background

This chapter outlines the theoretical and technical background for two common techniques used in this thesis: angle-resolved photoemission (ARPES) and high harmonic generation (HHG).

3.1 Photoemission Spectroscopy

The photoelectric effect was discovered by Hertz in 1887 during experiments with a spark-gap generator (the earliest version of radio receiver). Although the initial observation that the electric sparks were easier to create when electrodes were illuminated with ultraviolet light did not attract much interest, later findings of the so called *"threshold frequency"* failed the classical theory of electromagnetic radiation. In 1905, Einstein provided his revolutionary explanation at the dawn of quantum mechanics. Quantum mechanics, on the other hand, provides the theoretical foundation for the invention of lasers, which are used for time-resolved pump-probe photoemission spectroscopy to study the laser-matter interaction. Again, laser-matter interaction can produce attosecond pulse, which is recently ultilized to interrogate the fundamental timescale of photoemission [35,42,44].

3.1.1 Photoemission: from One-Step to Three-Step Model

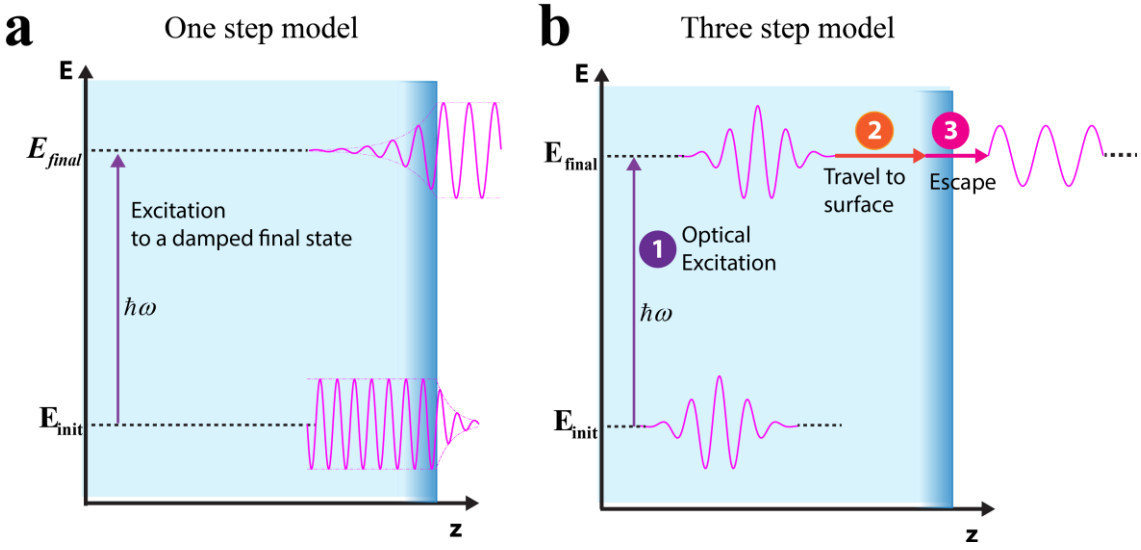

Figure 3.1: Illustration of one-step model and three-step model of photoemission. (a) The one-step model directly calculates the transition dipole from the initial state to final state. The final state wavefunction include all the possible interactions with the rest of the system. (b) In three-step model, the photoemission process is separated into three steps of (1) optical excitation, (2) electron transport to surface, and (3) escape of photoelectron into the vacuum. The *E* axis represents the electron energy and *z* axis denotes the depth into the bulk. Adapted from [148].

The complete description of photoemission in the language of many-body physics should be a one-step process [148]: electrons are excited from the initial state ψ_i^N to the final state $\psi_f^N = \psi_{\mathbf{k},s}^N$ with the transition probability given by *Fermi's golden rule* as a result of perturbation theory in the first order:

$$\omega_{fi}(\boldsymbol{k},\omega) = \frac{2\pi}{\hbar}\sum_s \left|\left\langle \psi_{\mathbf{k},s}^N \middle| H_{int} \middle| \psi_i^N \right\rangle\right|^2 \delta(E_{\mathbf{k}}^N - E_i^N - \hbar\omega), \tag{3.1}$$

where ψ_i^N is one of the possible initial *N*-electron eigenstates characterized by the eigenvalue E_i^N while the final state $\psi_{\mathbf{k},s}^N$ is one of the eigenstates with eigenvalue $E_{\mathbf{k}}^N$ containing the escaping photoelectron and the remain (N-1)-electron system; the index *s* represents a set of quantum numbers that incorporates all possible interactions in the final state of the system, including phonon

absorption, plasmons, electron-hole pair, scattering and multiple excitations. Apparently, this ideal *"one step model"* (Figure 3.1a) matrix element is inherently difficult to solve and an alternative simpler model divides the process into three steps, isolating each event experienced by the electrons [148,149]:

(1) Optical excitation of the electron within the bulk.

(2) Travel of the excited electron to the surface.

(3) Escape of the photoelectron into the vacuum.

Under the *three step model* (Figure 3.1b), the photoexcitation step (1) is isolated from the scattering and transmission processes and the transition probability is calculated between the initial and final Bloch states within the crystal. For the final state, a very central simplification, known as the *sudden approximation*, has to be made. It means the photoexcited electron doesn't interact with the remaining (N-1)-electron solid. With this simplification, Equation 3.1 can be written as

$$\omega_{fi} = \frac{2\pi}{\hbar}\left|\Delta_{fi}\right|^2 A^{<}(\boldsymbol{k},\omega), \tag{3.2}$$

where $\Delta_{fi} = \left|\langle\psi_f|\boldsymbol{A}\cdot\boldsymbol{p}|\psi_i\rangle\right|^2$ is the photoemission matrix element and $A^{<}(\boldsymbol{k},\omega)$ is the one electron spectral function, which is connected to imaginary part of the single-electron Green's function by

$$A^{<}(\boldsymbol{k},\omega) = -\frac{1}{\pi} Im\{G_{\boldsymbol{k}}(E_{\boldsymbol{k}} - i0^{+})\}\cdot f(E,T), \tag{3.3}$$

with $f(E,T)$ being the Fermi-Dirac distribution. The Green function is

$$G_{\boldsymbol{k}}(E_{\boldsymbol{k}}) = \frac{1}{E_{\boldsymbol{k}} - \epsilon_{\boldsymbol{k}} - \sum(\boldsymbol{k},E_{\boldsymbol{k}})}, \tag{3.4}$$

$\epsilon_{\boldsymbol{k}}$ is the electronic dispersion in the absence of many-body interactions and is often termed as the "*bare dispersion*". $\sum(\boldsymbol{k},E_{\boldsymbol{k}})$ is the complex electron self-energy including all the contributions

from many-body processes like electron-electron, electron-phonon or electron-impurity interactions that determine the intrinsic quasi-particle spectrum or photoemission line shape:

$$\sum(\boldsymbol{k}, E_{\boldsymbol{k}}) = Re\{\sum(\boldsymbol{k}, E_{\boldsymbol{k}})\} + Im\{\sum(\boldsymbol{k}, E_{\boldsymbol{k}})\}, \tag{3.5}$$

By plugging Equation 3.4 and 3.5 into Equation 3.3, we get the spectral function

$$A^{<}(\boldsymbol{k}, \omega) = \frac{1}{\pi} \frac{[Im\{\sum(\boldsymbol{k}, E_{\boldsymbol{k}})\}]}{|E_{\boldsymbol{k}} - \epsilon_{\boldsymbol{k}} - Re\{\sum(\boldsymbol{k}, E_{\boldsymbol{k}})\}|^2 + |Im\{\sum(\boldsymbol{k}, E_{\boldsymbol{k}})\}|^2}, \tag{3.6}$$

Step (2) represents the scattering of photoexcited electrons on their way to the surface. As a result, most of the electrons suffer from an energy or momentum loss and cannot make it to the surface. The electrons have an exponentially decaying probability of escaping the solids depending on their distance to the surface

$$P(d) = e^{-d/\lambda_{MFP}}, \tag{3.7}$$

The characteristic length λ_{MFP} is called the escape depth of the electrons, which is also referred to as electron's *inelastic mean free path* mainly dictated by electron-electron scattering. The dependence of λ_{MFP} on electron's kinetic energy is named the "universal curve" [150] and plotted in Figure 3.2. For the high harmonic photons used in this thesis work, the electron kinetic energy is about 20~100 eV and the escape depth is around 5Å. In this case, photoemission is said to be surface-sensitive. On one hand, this can serve as an advantage for probing atomic layer structures like graphene or surface adsorbate system. On the other hand, the photoemission measurements for bulk materials might be a mere a projection of the band structure on the surface and may not reflect the intrinsic bulk properties.

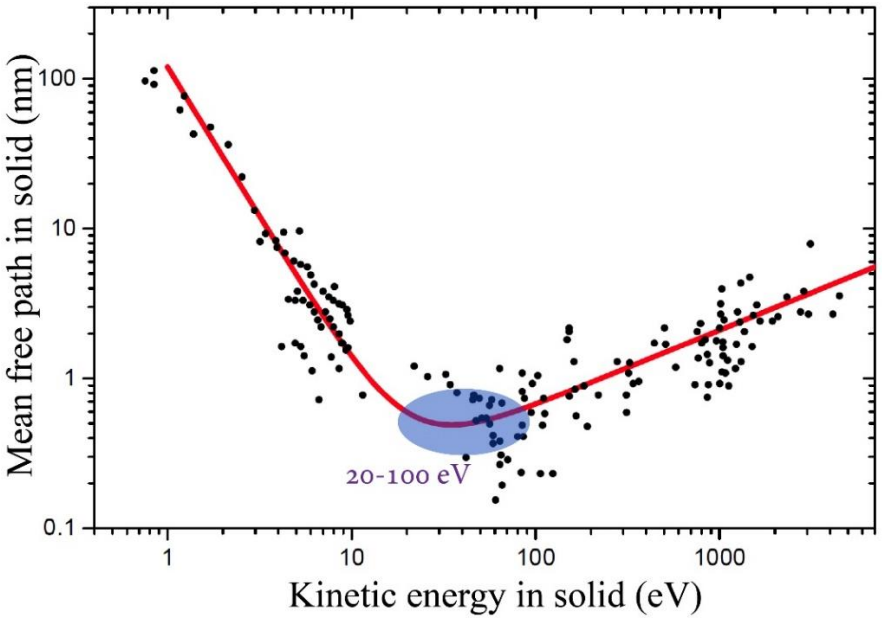

Figure 3.2: "Universal Curve". The curve indicates the relation between the electron mean free path and the kinetic energy of the photoelectrons in the solid. Reproduced from [151], and data originally from [150].

3.1.2 Direct Imaging of Electronic Bands

Energy Conversion. According to energy conservation (*i.e.* the Dirac function in transition probability), the kinetic energy of a photoelectron is related to the photon energy $\hbar v$ via the following equation

$$E_k = \hbar\upsilon - E_B - \Phi_s, \tag{3.8}$$

where Φ_s is the sample work function and E_B is the binding energy, i.e., the energy of the electron in solid relative to the Fermi level. However, the determination of work functions in photoemission spectra is more complicated.

Measurement of the Sample Work Function. During the last two stages of the "three step model", the majority of the generated electrons suffer from inelastic collisions, which result in a decrease in their kinetic energy. Hence photoemission spectra are composed of two main components: (1) the *primary electrons* without suffering inelastic collisions, which is of main

interest in the spectra because they show spectral features directly reflecting the density of states of the sample, and (2) *secondary electrons*, which lose varying amount of energy in collisions and constitute a continuous energy background down to zero kinetic energy. As shown below, a complete characterization of the work function requires the interplay between both features [152].

Since the sample and spectrometer are in good electrical contact hence equilibrates their Fermi levels in practical measurements of electrons' kinetic energy, thus, emitted photoelectrons suffer from the resultant "contact potential ($\Delta\Phi = \Phi_s - \Phi_d$, Φ_d is the detector work function)" and accelerate (or decelerate) on their way to the detector. Therefore, the measured kinetic energy for primary electrons is:

$$E_k^{meas} = \hbar\upsilon - E_B - \Phi_s + (\Phi_s - \Phi_d) = \hbar\upsilon - E_B - \Phi_d. \quad (3.9)$$

The deducted work function for the primary electrons is the one of the electron detector. The high cutoff of the spectra (assuming a metallic sample here) is $E_{k,Hc}^{meas} = \hbar\upsilon - \Phi_d$ from electrons with $E_B = 0$. For the secondary electron continuum, the slowest electrons are those barely made it to the sample surface with $E_{kin} = 0$, and subsequently gain/lose their energy through the "contact potential". Applying a bias voltage between sample and detector allows for the detection of these low-edge electrons even when they are repelled by the contact potential. These electrons form the low cutoff of the spectra with $E_{k,Lc}^{meas} = \Phi_s - \Phi_d$. The sample work function can be calculated from the high and low energy cutoff of the spectra:

$$\Phi_s = \hbar\upsilon - (E_{k,Hc}^{meas} - E_{k,Lc}^{meas}). \quad (3.10)$$

Momentum Conversion. Angle-resolved Photoemission (ARPES) is a leading tool in pushing the frontier of complex phenomenon in solids like High-T_c superconductors and charge-density-wave materials. The addition of angular detection of photoelectrons provides a way of studying the electronic dispersion or taking a "snapshot" of the bandstructure in the solid. Since

the momentum parallel to the sample surface is conserved during photoemission because of translational symmetry:

$$\boldsymbol{k}_{\parallel} + \boldsymbol{k}_{h\upsilon} = \boldsymbol{K}_{\parallel}, \tag{3.11}$$

where $\boldsymbol{k}_{\parallel}$ and $\boldsymbol{K}_{\parallel}$ are momentum component parallel to the sample surface for bound and photoemitted electron, respectively. $\boldsymbol{k}_{h\upsilon}$ is the momentum of the incident photon, which can be neglected for low photon energies used in most of ARPES experiments $(h\upsilon < 100\ eV)$. Then we have:

$$\boldsymbol{k}_{\parallel} = \boldsymbol{K}_{\parallel}. \tag{3.12}$$

The photoelectron momentum $\boldsymbol{K}$ is usually obtained in terms of the polar (θ) and azimuthal (φ) emission angles:

$$\begin{aligned} \boldsymbol{K}_{\parallel} = \boldsymbol{K}_{\mathrm{x}} + \boldsymbol{K}_{\mathrm{y}} &= \frac{\sqrt{2m_e E_k}}{\hbar}\sin\theta \\ K_{\mathrm{x}} &= \frac{\sqrt{2m_e E_k}}{\hbar}\sin\theta\cos\varphi \\ K_y &= \frac{\sqrt{2m_e E_k}}{\hbar}\sin\theta\sin\varphi \\ K_{\mathrm{z}} &= \frac{\sqrt{2m_e E_k}}{\hbar}\cos\theta. \end{aligned} \tag{3.13}$$

Determination of $\boldsymbol{k}_{\perp}$ (Band Mapping). Electron momentum perpendicular to the sample surface $\boldsymbol{k}_{\perp}$ is not conserved because the potential change across the surface breaks translational symmetry. However, the value of $\boldsymbol{k}_{\perp}$ is required for a complete 3D band mapping of the electronic dispersion $E(\boldsymbol{k})$ [153]. There are several specific experimental methods developed for this purpose, which are mostly complicated and/or need other complementary measurements. Alternatively, $\boldsymbol{k}_{\perp}$ can be calculated by knowing the dispersion of the final bulk Bloch states, which can be obtained

either from bandstructure calculations, or more commonly, by just assuming a simple free electron dispersion:

$$E_f(\boldsymbol{k}) = \frac{\hbar^2 \boldsymbol{k}^2}{2m_e} - |E_0| = \frac{\hbar^2(\boldsymbol{k}_\parallel^2 + \boldsymbol{k}_\perp^2)}{2m_e} - |E_0|. \tag{3.14}$$

E_0 corresponds to the bottom of the valence band as indicated in Figure 3.3. Note that both E_0 and E_f are referenced to the Fermi level E_F, while E_k is referenced to the vacuum level E_V. Given $E_f = E_k + \Phi_s$ and $\hbar^2 \boldsymbol{k}_\parallel{}^2 / 2m_e = E_k \sin^2\theta$, we have:

$$\boldsymbol{k}_\perp = \frac{1}{\hbar}\sqrt{2m_e(E_k \cos^2\theta + V_0)}\,, \tag{3.15}$$

where $V_0 = |E_0| + \Phi_s$ is the *inner potential*, which corresponds to the bottom of the valance band referenced to the vacuum level. At normal emission geometry where $\theta = 0$ thus $\boldsymbol{k}_\perp = \frac{1}{\hbar}\sqrt{2m_e(E_k + V_0)}$, the mapping of $E(\boldsymbol{k}_\perp)$ can be achieved by measuring the photoelectrons as a function of incident photon energy. There are three commonly used methods to determine V_0: (1) optimize V_0 to match the experimental measurements with theoretical calculations; (2) set V_0 as the theoretical zero of the muffin tin potential applied in band structure calculations; (3) infer V_0 from the experimentally observed periodicity of the dispersion $E(\boldsymbol{k}_\perp)$ [153].

There are several cases where $\boldsymbol{k}_\perp$ is less relevant. (1) 2D materials like graphene has a vanishing $\boldsymbol{k}_\perp$ component, which can be ignored. (2) Surface state, as opposed to bulk-related states, shows no dispersion in $E_k(\boldsymbol{k}_\perp)$ because one can think of the surface state as being present for all values of $\boldsymbol{k}_\perp$. (3) For 3D materials with large c-axis vector, $\boldsymbol{k}_\perp$ is almost independent of E_B or E_k and it is also reasonable to assume $\boldsymbol{k}_\perp$ is constant and we can focus only on the in-plane electronic behavior.

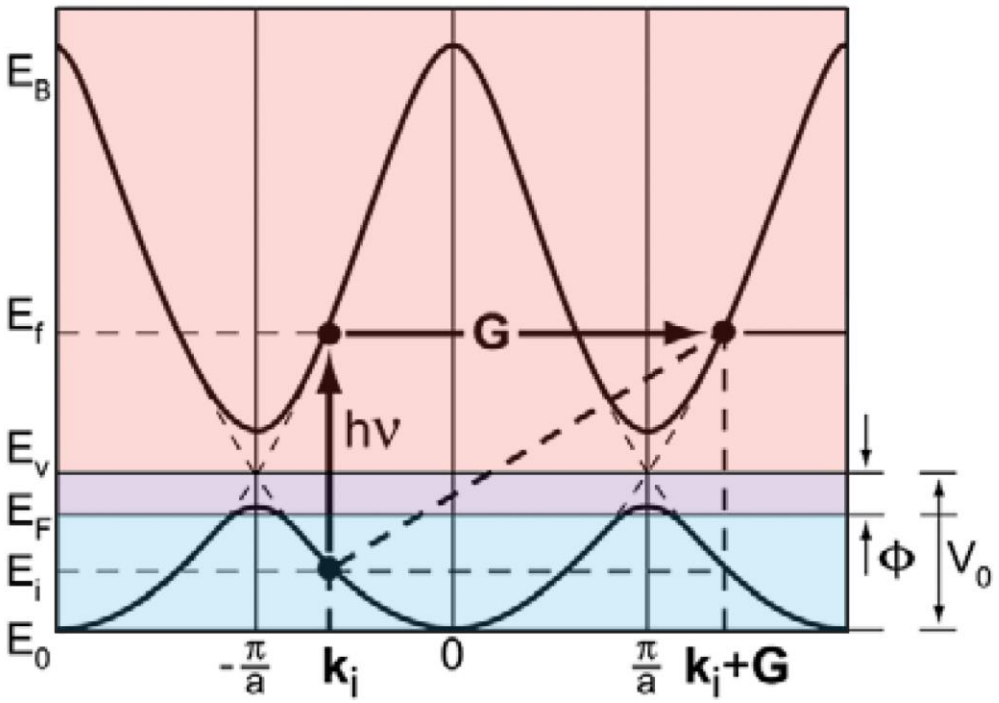

Figure 3.3: Illustration of the inner potential in band mapping. In direct optical excitation from initial state to free-electron final state in vacuum, the lattice supplies the required momentum G. The inner potential V_0 corresponds to the bottom of the valence band E_0 referenced to the vacuum level E_V. Adapted from [153].

3.1.3 The Influence of Brillouin Zone in Photoemission

Except amorphous solids and glasses, most solids have periodic arrays of atoms which form a crystal lattice. The existence of the crystal lattice implies a characteristic symmetry under a combination of one or more translation-, rotation- and inversion- operations. This symmetry can be represented by the *Bravais lattice*, which is an infinite array of discrete points in 3D real space generated by a set of discrete translation operations described by:

$$\boldsymbol{R} = n_1\boldsymbol{a_1} + n_2\boldsymbol{a_2} + n_3\boldsymbol{a_3}. \tag{3.16}$$

where n_i are integers and $\boldsymbol{a_i}$ are *primitive vectors*. ***{R}*** should be closed under vector addition and subtraction. All points of lattice defined by $\boldsymbol{R}(n_1, n_2, n_3)$ are in the same environment.

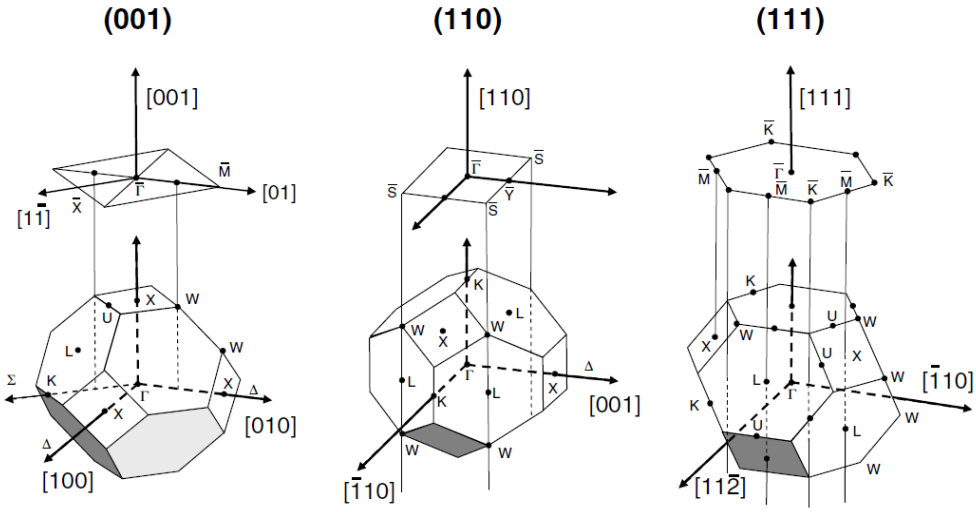

Figure 3.4: Surface Brillouin zone for crystals with face centered cubic (fcc) structure. From [154]**.**

The *reciprocal lattice* is a construction with significant importance for condensed matter physics. It represents the Fourier transform of the real-space lattice to the reciprocal space (or momentum space). Starting with the Bravais lattice, the reciprocal lattice is a group of wave vectors **G** that give plan waves $e^{i\boldsymbol{G}\cdot\boldsymbol{r}}$ with the same translation symmetry as the Bravais lattice:

$$e^{i\boldsymbol{G}\cdot(\boldsymbol{r}+\boldsymbol{R})} = e^{i\boldsymbol{G}\cdot\boldsymbol{r}}. \tag{3.17}$$

The reciprocal lattice can be determined through the formula: $\boldsymbol{G} = m_1\boldsymbol{b_1} + m_2\boldsymbol{b_2} + m_3\boldsymbol{b_3}$, where m_i are integers and $\boldsymbol{b_i}$ are reciprocal primitive vectors defined as:

$$\boldsymbol{b_1} = 2\pi\frac{\boldsymbol{a_2}\times\boldsymbol{a_3}}{\boldsymbol{a_1}\cdot(\boldsymbol{a_2}\times\boldsymbol{a_3})} \qquad \boldsymbol{b_2} = 2\pi\frac{\boldsymbol{a_3}\times\boldsymbol{a_1}}{\boldsymbol{a_1}\cdot(\boldsymbol{a_2}\times\boldsymbol{a_3})}$$
$$\boldsymbol{b_1} = 2\pi\frac{\boldsymbol{a_1}\times\boldsymbol{a_2}}{\boldsymbol{a_1}\cdot(\boldsymbol{a_2}\times\boldsymbol{a_3})}. \tag{3.18}$$

The Wigner-Seitz cell of the reciprocal lattice (constructed as the set of points enclosed by the nearest *Bragg planes*, i.e. the planes perpendicular to a connection line from the origin to each

lattice point and passing through the midpoint) is called the *Brillouin zone*. Photoemission with a fixed photon energy probes a projection of the band structure at the surface Brillouin zone with fixed $\boldsymbol{k}_{\perp}$. The surface Brillouin zone for fcc (face-centered-cubic) lattice structure, which is the crystal structure of the materials mostly used in this thesis work [Cu(111) and Ni(111)], is plotted in Figure 3.4 [154].

Note that no *k*-conversing optical transition along the free-electron parabola is possible in the limit $\boldsymbol{k}_{h\upsilon} = 0$. The periodic lattice can provide the external momentum in bulk transitions. In the *extended Brillouin zone scheme*, the transition is connected by the reciprocal-lattice vector $\boldsymbol{k}_f - \boldsymbol{k}_i = \boldsymbol{G}$, which can be simplified as a vertical transition in the *reduced Brillouin zone scheme* $\boldsymbol{k}_f - \boldsymbol{k}_i = 0$. The problem is different when the surface is taken into account in the *semi-infinite crystal picture*. While the $\boldsymbol{k}_{\parallel}$ is conserved within a reciprocal-lattice vector because of the translational symmetry of the surface, $\boldsymbol{k}_{\perp}$ is not conversed across the surface due to the potential change. Thus, the surface acts like a momentum reservoir delivering the necessary momentum for indirect transitions even in the absence of the crystal potential (i.e., the so-called surface photoelectric effect) [153].

3.1.4 The Matrix Element Effect

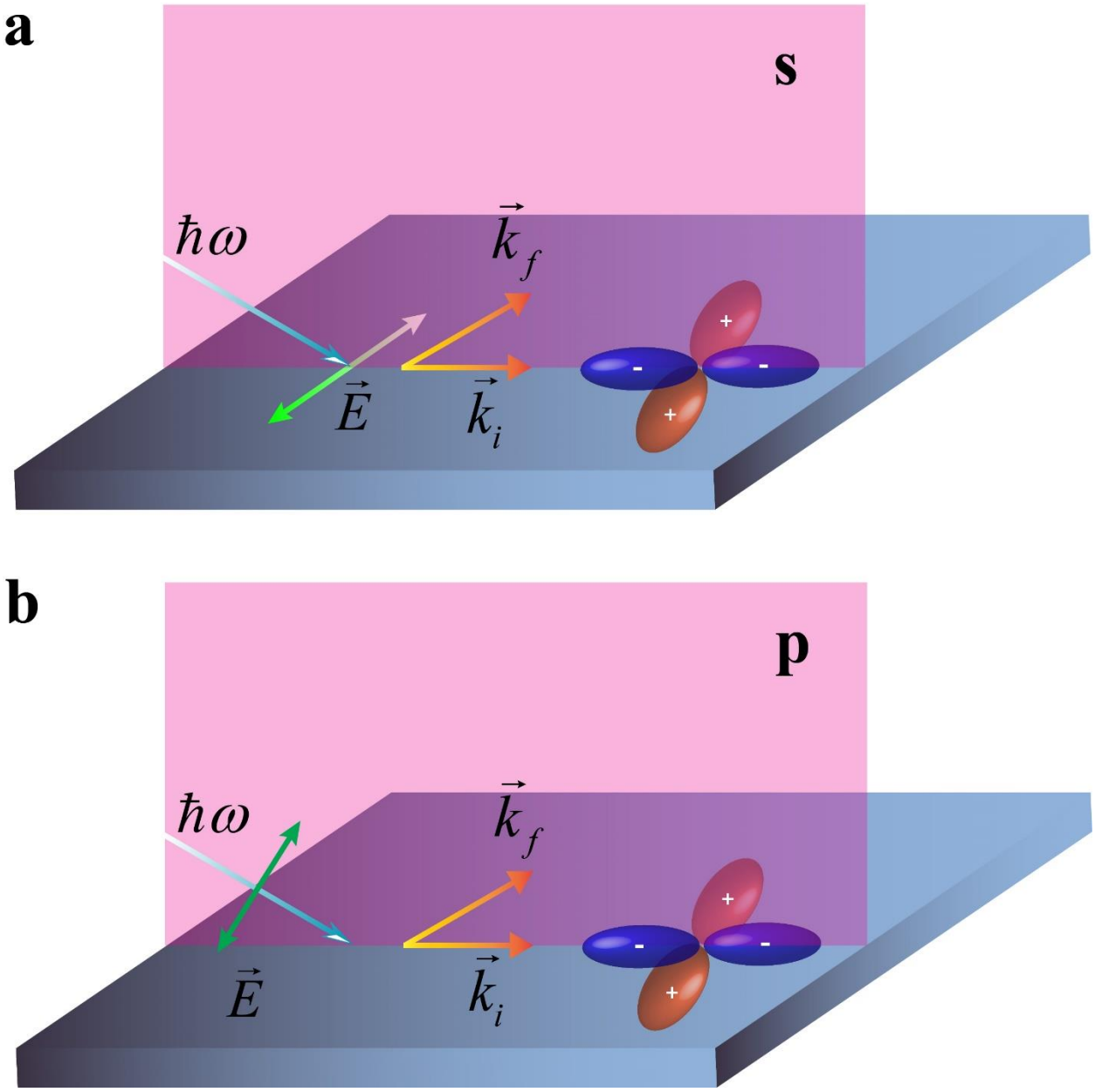

Figure 3.5: Illustration of matrix element effect in photoemission. $\boldsymbol{k}_i$ and $\boldsymbol{k}_f$ are the initial and final state momentum. The pink color indicates the mirror plane that contains $\boldsymbol{k}_i$, $\boldsymbol{k}_f$, and the Poynting vector of the light. The initial-state wavefunction is even relative to the mirror plane. Therefore, (a) when the incident light field is s-polarized, the light field is odd with respective to the mirror plane. In this case, the matrix element $\left|\langle\psi_f|\boldsymbol{A}\cdot\boldsymbol{p}|\psi_i\rangle\right|^2$ vanishes. (b) p-polarized light field is even to the mirror plane and leads to a non-zeros matrix element. Adapted from [155].

The matrix element $\Delta_{fi} = \left|\langle \psi_f | \boldsymbol{A} \cdot \boldsymbol{p} | \psi_i \rangle\right|^2$ represents the transition probability between the electron wavefunction in solid $|\psi_i\rangle$ (or "the initial state") and the photoexcited electron $|\psi_f\rangle$ (or "the final state") [155,156]. $\boldsymbol{p}$ is the electron momentum and $\boldsymbol{A}$ is the electromagnetic gauge, which is related to the electric field $\boldsymbol{E}$ through $\boldsymbol{E} = -\partial \boldsymbol{A}/\partial t$, thus shares the same spatial mirror symmetry as $\boldsymbol{E}$. The initial state wavefunction carries information about the electron's orbital. The final sate wavefunction is usually approximated as a plane wave propagating into vacuum with the photoelectron momentum $\boldsymbol{k_f}$**.** This approximation is usually valid for sufficiently high photon energies at or above tens of eV.

The matrix element is so complicated to calculate that it is mostly treated as a mysteries elf controlling the amount of electrons released into vacuum upon the arrival of light. There are, however, special cases where we can use symmetry analysis to determine whether certain electronic states will contribute to the photoelectron spectra under the illumination of polarized light. Since the matrix element includes integration over all spatial dimensions, it goes to zero if the product $\langle \psi_f | \boldsymbol{A} \cdot \boldsymbol{p} | \psi_i \rangle$ is odd with respect to a particular mirror plane. We demonstrate this symmetry analysis by studying two examples in Figure 3.5. To simply the problem, we deliberately put the momentum of the initial ($\boldsymbol{k_i}$) and final ($\boldsymbol{k_f}$) states in the plane of incidence, which is also chosen as the mirror plane here. The in-plane momentum $\boldsymbol{k}_{\parallel} = \boldsymbol{k}_i$ and the final state wavefunction $|\psi_f\rangle$ are all even to the mirror plane. For s-polarized light, the electric field $\boldsymbol{E}$ (and thus the gauge field $\boldsymbol{A}$) is odd with respect to the mirror plane. if the orbital wavefunction $|\psi_i\rangle$ is odd to the mirror plane, the overall mirror symmetry of $(\psi_f \cdot \boldsymbol{A} \cdot \boldsymbol{p} \cdot \psi_i)$ is odd and the matrix element vanishes. For p polarized light, the electric field $\boldsymbol{E}$ is even with respect to the mirror plane and matrix element is nonzero only when the orbital wavefunction $|\psi_i\rangle$ is even regarding the mirror plane. To sum up:

$$\left|\langle\psi_f|\boldsymbol{A}\cdot\boldsymbol{p}|\psi_i\rangle\right|^2 = 0 \begin{cases} |\psi_i\rangle \text{ even} & \langle+|-|+\rangle \rightarrow \boldsymbol{A} \text{ odd} \\ |\psi_i\rangle \text{ odd} & \langle+|-|+\rangle \rightarrow \boldsymbol{A} \text{ even} \end{cases}$$

Using the symmetry analysis, the dipole-allowed initial states for normal emission from low-index faces of cubic metal are listed in Table 3.1 [157]. The spin-orbit coupling is ignored for simplicity. The z axis the normal to the sample surface. Note that each polarization x, y or z excites only one initial symmetry. This selective excitation of the initial states with different symmetry by changing the light polarization (the so called "*photoemission selection rule*") is heavily used in this thesis work.

Crystal Face	**Coordinate Axes**			**Irreducible Representations**	**Allowed Initial Symmetries**		
	x	**y**	**z**		**E ∥ x**	**E ∥ y**	**E ∥ z**
(001)	<100>	<010>	<001>	$\Delta_1\ \Delta_1'\ \Delta_2\ \Delta_2'\ \Delta_5$	Δ_5	Δ_5	Δ_1
(110)	<001>	$<1\bar{1}0>$	<110>	$\Sigma_1\ \Sigma_2\ \Sigma_3\ \Sigma_4$	Σ_3	Σ_4	Σ_1
(111)	$<\bar{1}10>$	$<\bar{1}\bar{1}2>$	<111>	$\Lambda_1\ \ \Lambda_2\ \ \Lambda_3$	Λ_3	Λ_3	Λ_1

Table 3.1: Dipole-allowed initial state symmetries for transitions in normal emission geometry from low-index cubic metals. Adapted from [157].

3.1.5 EDC and MDC

An example of photoemission spectrum of Na-intercalated graphene on Ni(111) substrate is shown in Figure 3.6a, where the well-celebrated Dirac-cone is shown. The intensity map indicates the normalized (measured) density of states as a function of $k_{//}$ and binding energy. Figure 3.6b shows the bandstructure calculated by density function theory (DFT). This is an illustration that photoemission spectra are not a mere "shift" of the electron density of states in the solid. Matrix element effect can generate an intensity modulation that may change with photon energy and polarization.

There are two useful ways of slicing the 2D photoemission spectra up for analysis. (1) The ARPES spectrum as a function of energy at a fixed momentum or integrated over certain momentum range is called energy distribution curve (*EDC*). The EDCs of the photoemission spectra of Na-intercalated Graphene/Ni(111) are shown in Figure 3.6c. (2) Similar to EDC, Momentum distribution curve (*MDC*) is ARPES spectrum as a function of momentum at a constant kinetic energy or over a certain kinetic energy range.

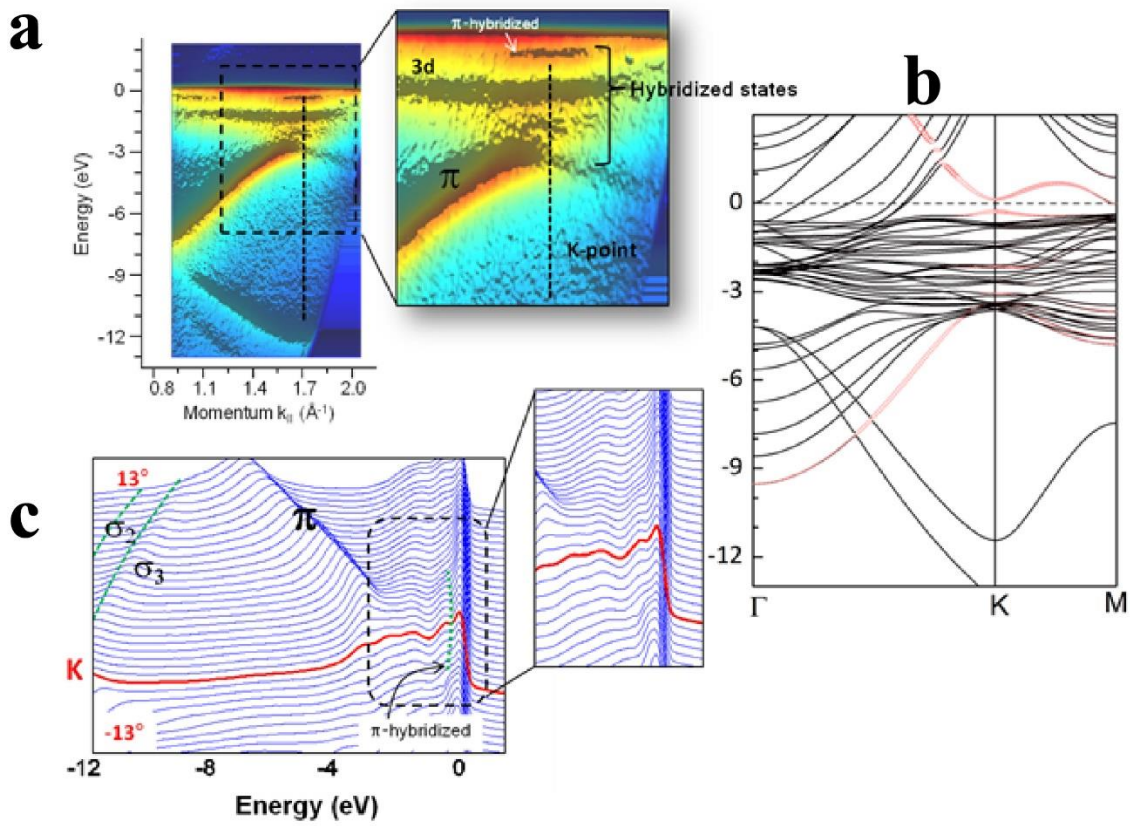

Figure 3.6: Photoemission spectrum of Na-intercalated graphene on Ni(111) substrate. The spectrum is measured along Γ-K direction**.** (a) Hybridization of the π state near the K-point in graphene/Ni(111). Black vertical line (dashed) indicates position of the K-point, as established from the minimum of the σ_3 state of graphene; a manifold of states arising from the hybridization of the Ni 3d and graphene π states is indicated with the bracket. (b)DFT calculated states near the K-point. $2p_z$ states of graphene are highlighted in red. (c) Corresponding EDC lineouts of (a). Graphene states are indicated with symbols and the EDC lineout at the K-point is indicated as red. Weak feature near the Fermi level is a hybridized state between Ni and graphene, which is also visualized in (b).

3.2 Theory of High Harmonic Generation

High harmonic generation (HHG) takes place when intense linearly polarized laser pulse is focused onto a target of noble gas. During the process, the driving laser light at a given frequency is converted into odd integer multiples of this fundamental frequency. In HHG spectrum, following the rapidly decreasing low-order harmonics, there exists a plateau region where higher order harmonics are produced with almost equal intensity extending to the so called cut-off region, where harmonic intensity drops sharply again [158].

The occurrence of a "plateau region" was not immediately understood with the birth of HHG [159,160] because under the scope of the established perturbation theory that well described the low-order harmonic generation, the probability of a n-photon excitation decreases exponentially with its order n. This unexpected highly nonlinear behavior was realized later to be related to the enormous applied laser strength comparable to the binding energy of electrons inside the atom. A generic intensity scale for laser-atom interactions is the so called atomic unit of intensity: $I_{atom}=3.5\times10^{16}$ W/cm^2. The laser source commonly used to drive HHG are Ti:sapphire laser system operating at $I_L\approx 10^{14}$ W/cm^2 therefore cannot be treated as small perturbation to the system [161].

3.2.1 Three-Step Model

Although a complete quantum description of HHG is based on numerically solving the time dependent Schrödinger equation (TDSE), a more convenient semi-classical theory proposed by Kulander and Corkum explained the mechanism of the process via the celebrated "three step model" [63,64]:

(1) Ionization. A bound electron is driven away from the atomic Coulomb potential of the nucleus when the electric field is close to its peak during an optical cycle, and tunnel into the continuum.

(2) Acceleration in the laser field: once freed, the electron is first accelerated away from the nucleus in the laser field like a classical particle. When the oscillating electric field switches its direction about a quarter of a period after electron ionization, the electron decelerates and then re-accelerates back towards its parent ion.

(3) Recombination: There is a small probability for the ionized electron to recombine with its parent ion. Upon relaxation to the ground state, the kinetic energy the electron gains during its excursion in the laser field plus the ionization potential can be released in the form of high energy photons, much larger than the fundamental photon energy.

A detailed analysis of the electron trajectory in the laser field shows that the maximum energy $3.17U_p$ can be transferred from the laser field to the electrons when they are ionized at ω_t=17° after the field peak, where U_p is the ponderomotive potential of the laser field, which is

$$U_p = \frac{e^2 E_0^2}{4 m_e \omega_L^2}, \tag{3.19}$$

where e and m_e are the electron charge and mass separately and E_0 and ω_L are the amplitude and angular frequency of the electric field. This dictates the highest photon energy, i.e. the harmonic cut-off, generated when electron reencounters its parent ion:

$$h\upsilon_{max} = I_p + 3.17U_p. \tag{3.20}$$

Here I_p is the ionization potential of the atom. For harmonics in the plateau region, each kinetic energy of electrons can be produced by two different electron trajectories, differentiated the time they spent in continuum. The one in which electrons are ionized at a smaller phase of the electric

field and spend longer time in continuum is called long trajectory and the second one is called short trajectory. Macroscopic phase-matching is able to eliminate the long-trajectory contribution and this is important for the generation of attosecond pulses [162].

3.2.2 Phase Matching and Absorption

The coherent buildup of the harmonic field requires that the light generated in different portions of the gas across the interaction region are in phase with each other, i.e., phase-matched. This can be accomplished by forcing the phase velocities $c_p = \frac{\omega}{k}$ of both two participating fields (the fundamental driving field and generated harmonic field) to be equalized, where ω is the angular frequency and k is the magnitude of the wavevector. This corresponds to:

$$\frac{\omega_f}{k_f} = \frac{\omega_q}{k_q} = \frac{q\omega_f}{k_q}. \tag{3.21}$$

where f refers to the fundamental driving laser and q is the harmonic order. The best-case scenario of complete phase matching is:

$$\Delta k = qk_f - k_q = 0. \tag{3.22}$$

For nonzero Δk, it is convenient to define coherence length $L_c = \pi/\Delta k$, the characteristic length in which a π phase shift is developed for harmonics generated at two positions along the propagation direction. Beyond π phase shift, the energy starts to flow back to the driving field. Another characteristic parameter is the absorption L_a length of medium, in which the harmonic intensity drops by a factor of e. The on-axis harmonic intensity as a function of interaction length L_i is given by [163]:

$$I_q \propto L_a^2 \frac{1+\exp\left(-\frac{L_i}{L_a}\right)-2\exp\left(-\frac{L_i}{2L_a}\right)\cos\left(\frac{\pi L_i}{L_c}\right)}{\left(2\pi\frac{L_a}{L_c}\right)^2+1}. \tag{3.23}$$

The intuition of how L_a and L_c influence the build-up of the high-harmonic beam can be gained by reviewing several limiting cases: (1) the ideal case is when there is neither absorption nor phase mismatch (L_a, $L_c \to \infty$). In this case, the harmonic field I_q grows continuously over the interaction region:

$$\lim_{L_a,\, L_c \to \infty} I_q \propto L_i^2. \tag{3.24}$$

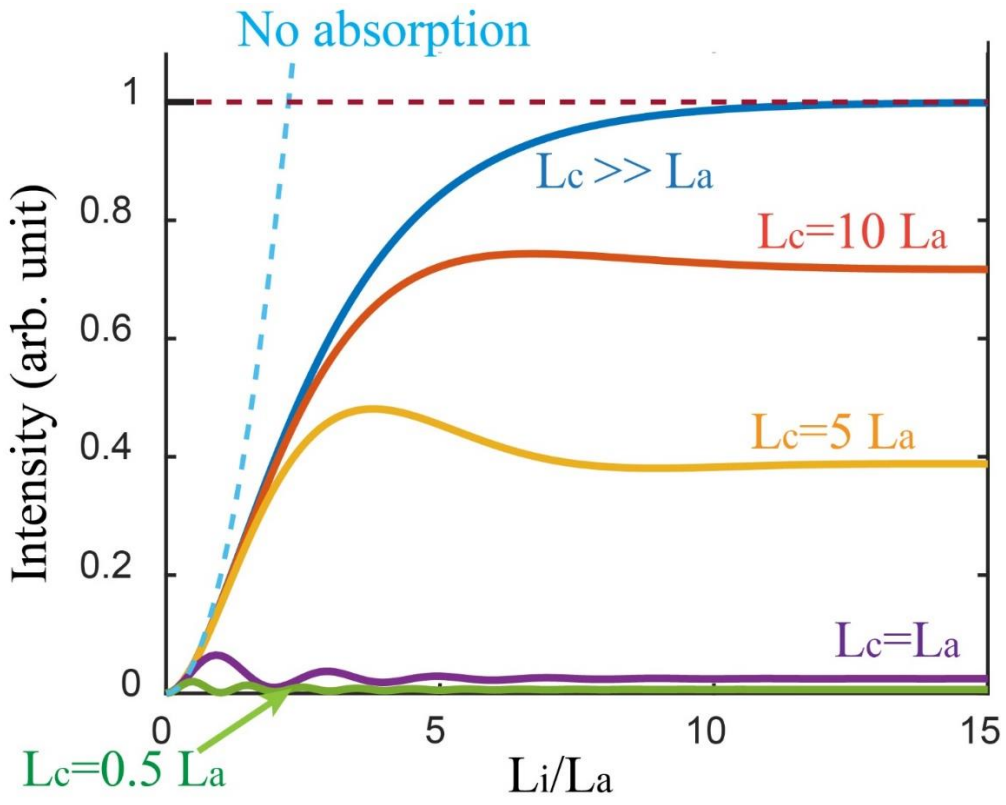

Figure 3.7: The on-axis intensity of HHG radiation as a function of medium length. The curves are calculated from Equation 3.23. It is shown that the radiation intensity oscillation as a function of medium length is suppressed when Lc > La, leading to an enhanced HHG emission intensity. When Lc >> La, the HHG radiation intensity can be maximized by increasing the medium length to longer than 10 times the absorption length, approximately. Phase-matched growth in the absence of absorption is plotted in blue dash line for reference. Figure adapted from [163].

(2) When there is no absorption ($L_a \to \infty$), Equation 3.23 reduces to:

$$\lim_{L_a \to \infty} I_q \propto \left[\frac{L_c}{\pi} sin\left(\frac{\pi L_i}{2L_c}\right)\right]^2. \tag{3.25}$$

Equation 3.25 means the HHG output oscillates into and out of constructive interference during the propagation, with the maximum achievable intensity proportional to the square of the coherent length.

(3) When the coherence length is long ($L_c \to \infty$), Equation 3.23 can be written as:

$$\lim_{L_c \to \infty} I_q \propto L_a^2 \left[1 + exp\left(-\frac{L_i}{L_a}\right) - 2exp\left(-\frac{L_i}{2L_a}\right)\right]. \tag{3.26}$$

The harmonic intensity saturates with sufficiently long interaction length and the maximum is proportional to the square of the absorption length. The intensity dependence on medium length for different cases is also illustrated in Figure 3.7. It is clear that the key to generate bright harmonic field is to maximize both the absorption length and coherence length. Since the absorption is entirely medium-dependent can be barely controlled in experiment, the harmonic emission efficiency is usually improved by optimizing the phase matching and medium length. According to Equation 3.26, the following conditions typically ensure the macroscopic response is more than half the maximum response:

$$\begin{aligned} L_i &> 3L_a \\ L_c &> 5L_a. \end{aligned} \tag{3.27}$$

Phase Matching in Capillary Waveguide. HHG by propagating the driving lasers in a gas filled hollow waveguide offers several advantages for efficient phase matching. First, a non-diverging plane wave geometry is maintained over the entire interaction region, eliminating the Gouy phase shift introduced by focusing the beam into a gas jet/cell [164]. Second, it is straightforward to tailor the gas pressure profile inside the waveguide for optimal phase matching. The phase mismatch, Δk, for the *qth* harmonic can be written as [165,166]:

$$\Delta k \approx q\left\{\frac{u_{11}^2\lambda_L}{4\pi a^2} - P\left[(1-\eta)\frac{2\pi}{\lambda_L}(\Delta n + n_2) - \eta N_{atm} r_e \lambda_L\right]\right\}, \quad (3.28)$$

where q is the harmonic order, u_{11} is the lowest-order waveguide mode factor, λ_L is the central wavelength of the fundamental driving laser, a is the inner radius of the hollow waveguide, P is the gas pressure, η is the ionization fraction, Δn is the difference in indices of refraction of the neural gas between the fundamental and harmonic wavelength, n_2 is the nonlinear index of refraction per atmosphere at λ_L. N_{atm} is the number density of the gas at one atmosphere and r_e is the classical electron radius. Since the phase velocity of EUV can be assumed to be the speed of light in vacuum, the phase matching condition, or $\Delta k \rightarrow 0$, is achieved by varying the gas pressure inside the waveguide, because neutral gas and laser ionized plasma have opposite dispersions.

3.3 High Harmonics for Photoemission

There exists a variety of light sources for photoemission spectroscopy. Compared to traditional ones like plasma discharge lamp and 10-100 ps pulse-length synchrotron facilities, the clearest advantage of implementing HHG in photoemission spectroscopy is the temporally short EUV beam coexisting with a phase locked IR beam, which can also go through frequency conversion in nonlinear crystal to change color. This allows us to investigate the femtosecond to even attosecond dynamics in materials. Although the newly-developed Free Electron Laser (FEL) facilities offers shorter pulse down to ~10 fs and has done successful work with it, tremendous work is needed to suppress temporal jitter in pump-probe and it is also not quite available for photoemission application because of its low repetition rate resulting in extensively bright single pulses causing severe space charge effect [167,168]. Tunable 6 eV radiation generated by quadrupled Ti: Sapphire laser beam started the era of high resolution ARPES with bulk sensitivity and has also demonstrated its time-resolved capability [169]. In comparison, besides the

complementary surface sensitivity, harmonic radiation holds the advantage of possessing higher energy to reach deep core levels and the larger Brillouin zone in solids. Furthermore, by using higher energy incident photons, primary electrons are better separated from the secondary electrons and IR-induced above threshold ionization (ATI) background. This spectral separation allows for a more intense pump beam to promote the electrons to a far non-equilibrium state in phase transition and photochemistry investigations [170].

3.3.1 Tailoring HHG for Photoemission Spectroscopy

Depending on the interrogated sample and dynamics, photoemission spectroscopy benefits from a light source that is easily tunable in bandwidth, energy and polarization state. For example, typical photoemission experiments require monochromated photons while atto-streaking and RABITT measurements requires broadband harmonics to support attosecond temporal structure [35,44]. Although photons with higher energy are able to access larger Brillion zone in k space and deeper core-level states, consideration of other factors such as photoemission cross section, resonant excitation and final state effect add the complication of selecting the optimal wavelength for specific materials [144]. Recently developed circularly polarized harmonics have the advantage to unravel the spin and orbital related dynamics in magnetic materials and graphene [30,68–70]. Here we present our capability of tailoring the high harmonic source to offer the highest experimental power possible.

3.3.2 1ω, 2ω or 1ω+2ω

The cutoff-law (equation 3.20) dictates that harmonics with higher photon energy can be generated by increasing the wavelength of the driving laser. It was demonstrated in experiment

that keV harmonics can be achieved using 4μm lasers [22]. However, the laser system used within the work of this thesis (2mJ, 4 kHz, <30fs) doesn't reached the point at which mid-infrared (1.3 or 2 μm) pulses of sufficient energy are practical through optical parametric amplifier (OPA). Thus, the driving light fields implemented in our EUV beamline are fundamental Ti: sapphire beam - 1ω (centered at 780 nm), its frequency-doubled beam - 2ω (centered at 390 nm) or a mix of both in two-color linear HHG (Chapter 6) and circularly polarized HHG (Chapter 5).

1ω (780nm) driven HHG. 1ω-driven harmonic emission is the most straightforward way to obtain EUV light. In the spectral domain, the harmonic peaks are separated by ~3eV from the neighboring ones, allowing us to design the multilayer mirrors with certain bandwidth to select particular harmonic while maintaining moderate efficiency. In attosecond RABBITT experiment, the entire bandwidth is ultilized by using a toroidal mirror with carefully designed coating.

2ω (390nm) driven HHG. High harmonic radiation generated by frequency doubled Ti:Sapphire laser possesses several advantages in photoemission spectroscopy compared to 1ω (780nm) drivers [171,172]. (1) It eliminates the use of EUV multilayer mirrors or grating based monochromators. (2) The photon flux is higher because of (1) and higher quantum efficiency in HHG, which scales with driving wavelength at λ^{-5} to λ^{-9}. [63,89,173,174]. (3) The intensity of the driving field is moderate and avoids the damage of the waveguide and EUV optics. It also makes the harmonics more stable. (4) It offers better energy resolution (<150 meV) while preserving the temporal resolution (<30 fs) because the blue drivers are longer in duration after the BBO crystal but still preserve sufficient peak intensity to produce bright harmonic radiation [171].

Although bright and narrow harmonic of 60 eV has been demonstrated using 2ω driver in Neon, the laser system used in this thesis work only allows the 7^{th} harmonics in Krypton (~22 eV) with flux high enough for photoemission use.

Two color (1ω+2ω) HHG. Two-color laser field can increase the spectral coverage and minimize the low-flux regions between odd harmonics. This is because the addition of the 2ω field breaks the inversion symmetry and allows both the odd the even harmonics to be generated. This spectral shape is found to be beneficial for transient absorption experiments [175]. In terms of attosecond photoemission spectroscopy, combined two-color field reduces the requirement on driving pulse duration in the generation of supercontinuum or isolated attosecond pulse [176].

Circular HHG. It is not straightforward to generate circularly polarized harmonics because the liberated electron cannot recombine with its parent ion under circularly polarized driving field. There are several ways to overcome this limitation. The brute force method is converting the linear HHG to circular using EUV optics (usually achieved using multiple reflections on surfaces, which possess a different complex reflectivity/transmission for s and p polarized light thus result in a phase shift between the two) [177,178]. The disadvantage is that the EUV optics are difficult to fabricate, low in efficiency (~1%) and limited in bandwidth. Therefore, there are multiple efforts in the direct generation of circular harmonics with high efficiency.

One way to obtain circular harmonic is through molecular HHG. It was reported that the harmonics generated from N_2 molecules can reach an ellipticity of 40% when the molecules are aligned at 60^o from the polarization direction of the linear driving field [179]. However, this scheme is cumbersome to implement due to the pre-alignment of molecules and complicated revival dynamics.

An alternative way is using resonant HHG in elliptical laser fields. Different types of below- or above-threshold resonances in atoms and molecules can be utilized for this purpose, covering a broad spectral range. For example, Ferré *et al.* achieved highly-elliptical (0.6~0.8) harmonic radiation up to 49 eV by using the shape resonance in the ionization continuum of SF_6

[114]. Nevertheless, this method cannot generate a continuously tunable EUV source because circular harmonic emission is only emitted under the influence of resonance.

A universal way of circular harmonic generation is using bi-chromatic counter-rotating circularly polarized driving lasers in a collinear geometry. The harmonic spectrum consists of double peaks with alternating left and right circular polarization [68,69]. The first experimental demonstration of this method is by combing 0.8 μm Ti:sapphire laser and its frequency doubled beam at 0.41 μm. In a later work, photon energies >160 eV is obtained by mixing 0.79 μm and 1.3 μm beams in this counter-rotating scheme [70]. Another work shows that efficient generation of elliptical high harmonics can be achieved by simply using orthogonally polarized two-color (800nm+400nm) laser field [115].

One particularly interesting scheme for circular harmonic generation is by using counter-rotating circularly polarized lasers in non-collinear geometry [180]. The advantage of this scheme is that harmonics of different orders are angularly separated. Therefore, it is easy to select one harmonic for photoemission spectroscopy.

Chapter 4

Experimental Apparatus

This chapter focuses on discussion of the laser system, beamline layouts, EUV focusing optics and monochromators, as well as the UHV end station used in the thesis work.

4.1 Laser System

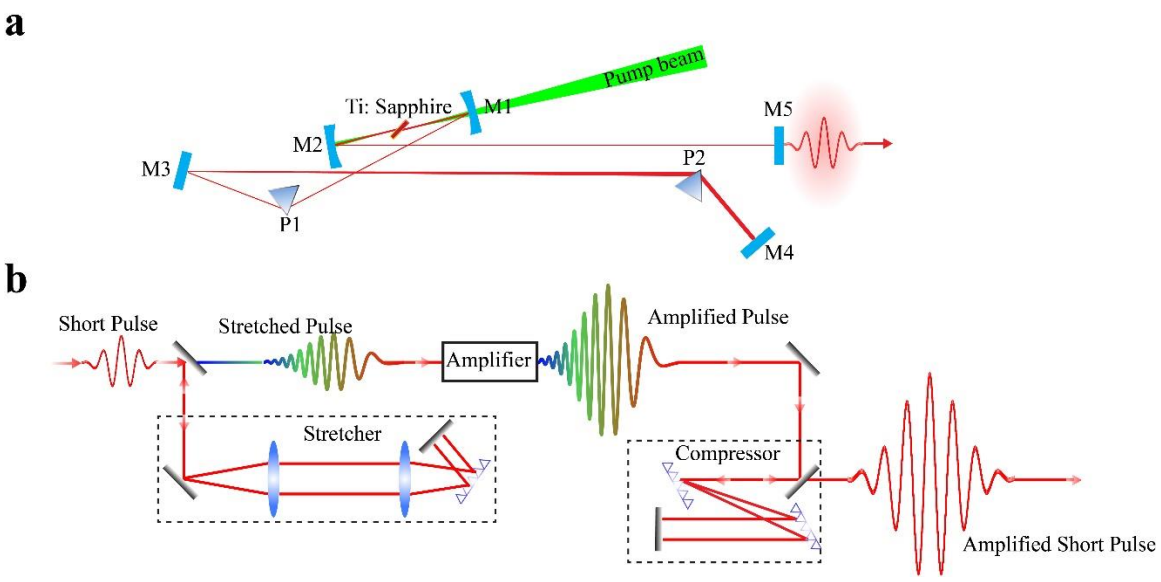

Figure 4.1: Schematic of Ti:sapphire oscillator and amplifier systems. (a) Ti:sapphire oscillator. M1 and M2 are concave mirrors with 10-cm radius of curvature, between M1and M2 is a Ti:sapphire crystal, M3 is a fold mirror, M4 is an end mirror, M5 is an output coupler, P1 and P2 are fused silica prisms. A green pump laser beam (532 nm) is focused onto the Ti:sapphire to induce population inversion for lasing. (b) Layout of a Ti:sapphire amplifier system using chirp pulse amplification technique, figure adapted from [161].

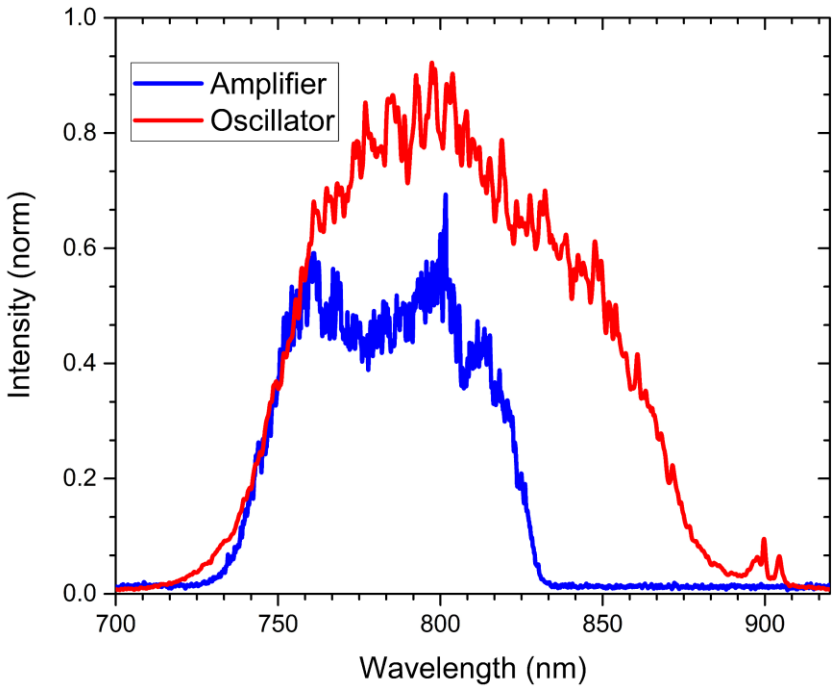

Figure 4.2: Typical spectrum of Ti:sapphire oscillator (red) and spectrum after chirped pulse amplification (blue).

Efficient HHG in noble gas requires the laser field strength to be $>10^{13}$ W/cm^2. This is often achieved by Ti:Sapphire ultrafast laser system operating at a wavelength ~0.8 μm. To reach the necessary intensity, ultrafast laser pulses produced in Ti:Sapphire oscillator (~80 MHz with 6 nJ, ~10 fs, see Figure 4.1a) are amplified at a reduced repetition rate (3-5 kHz) using chirped pulse amplification (CPA) techinique. Figure 4.1b shows the schematic layout of CPA. The output from the oscillator is first sent through a stretcher with positive-dispersion before amplification to avoid damage or nonlinear distortions of optical components. The stretcher chirps the pulses to roughly 150 ps via two reflections on the same grating. The pulses are then picked at the selected repetition rate in the Pockels cell and amplified in a Ti:Sapphire crystal. The crystal is pumped by a frequency-doubled Nd:YAG laser at 532nm (Lee Laser LDP-200MQG-HP) with the repetition rate and output timing synched to the Pockels cell. To reduce the thermal lensing effect, the crystal is cryo-cooled with a closed-loop liquid helium system (Cryomech PT90). Laser pulses are

amplified according to the number of passes through the crystal. They are then re-compressed in the grating compressor with negative dispersion to compensate for the chirp introduced in the stretcher and crystal. A typical laser spectrum before and after amplification is shown in Figure 4.2. The spectrum is narrower after amplification due to gain narrowing, which corresponds to a longer pulse. Higher order dispersion that cannot be compensated by compressor also contributes to the elongation of laser pulses.

The laser system used in this thesis work is a single stage multi-pass amplifier. The output pulse duration is in the range of 25 fs to 30 fs. Although the repetition rate and the corresponding energy per pulse of the laser can be varied according to the ionization potential of the noble gas used in HHG, the typical setting we use is 4 kHz in repetition rate and 2 mJ/pulse. If we assume a Gaussian spatial and temporal distribution and the beam is focused to 100 μm in diameter (~60% of the fiber diameter) to couple into a 150 μm diameter fiber, the resulting electric field amplitude is ~1.2×10^{11} V/m, which is enough to distort the Coulomb potential trapping the electrons in noble gas atoms to allow tunnel ionization.

4.2 Beamline

After the laser system, the IR pulses are guided to the beam splitter and divided into two beams. The majority of the pulse energy (~95%) goes through the HHG capillary waveguide to generate the EUV beam and the rest is used to pump the material or dress the photoelectrons (Figure 4.3). The pump beam is focused by a concave silver mirror that has a radius of curvature of 2 meters. A computer interfaced delay stage (Aerotech ANT130-1110-L-25DU-MP) is used to control the relative pump-probe delay with a resolution approaching 100 as. The EUV probe beam is focused and monochromated according to the requirements in experiments.

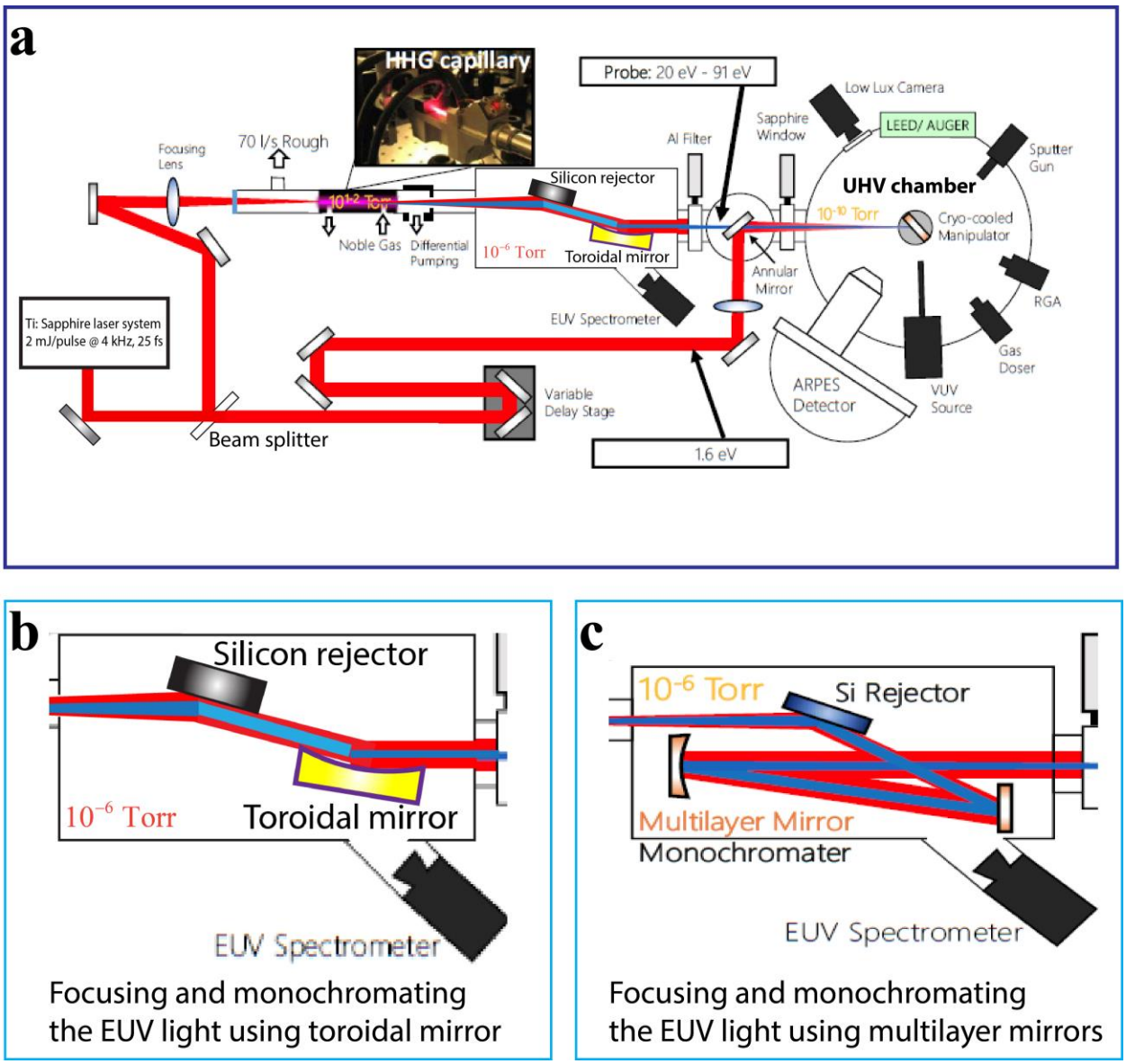

Figure 4.3: Simplified schematics of the beamline layout for tabletop EUV based photoelectron spectroscopy system. (a) the laser beam from a Ti:sapphire laser system is separated into two arms. The majority of the beam is focused into a noble gas-filled capillary waveguide to produce EUV light. The EUV light is then focused by the EUV optics in the mirror chamber onto a sample in the UHV chamber to generate photoelectrons. The rest of the Ti:sapphire beam that transmits through the beam splitter is used to pump the sample or to dress the photoelectrons. (b) Zoom-in view of the mirror chamber. The silicon rejector reduces the intensity of the residual laser beam after HHG. The toroidal mirror focuses the EUV light onto the sample surface. (c) Layout of the mirror chamber when multilayer mirrors are used.

4.3 EUV Focusing Optics and Monochromator

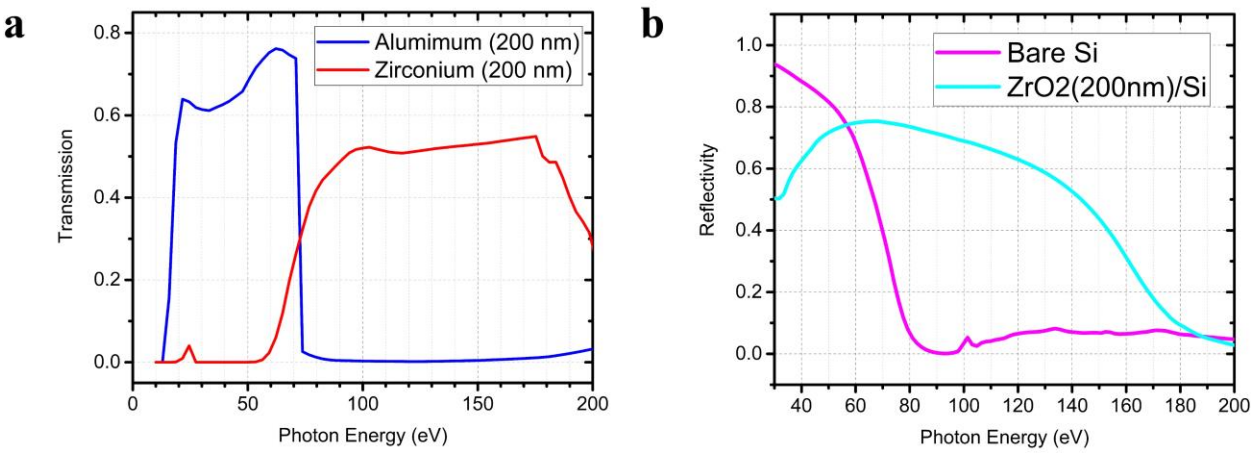

Figure 4.4: EUV transmission of metal foils and EUV reflectivity of rejector mirrors. (a) Transmission curves of aluminum and zirconium filters with 200 nm thickness. (b) Reflectivity curves for bare and ZrO_2 coated rejector mirrors under grazing incidence angle of 10 degrees. Reflectivity and transmission data are acquired from CXRO database.

Spectral selection and beam focusing are essential during the propagation of generated harmonics to the sample surface. These are achieved with the EUV optics. Firstly, because of the low conversion efficiency of the high harmonic process, the residual IR light co-propagating with the EUV beam needs to be filtered to avoid its effect (electron excitation and dressing) on sample. Different metal thin films (thickness=200~300 nm) are chosen depending on their transmission at the desired photon energy. Aluminum (Al) filters are commonly used for low photon energies (20 eV < hυ < 70 eV), and zirconium (Zr) filters for higher photon energies (70 eV < hυ < 150 eV). Their transmission curves are plotted in Figure 4.4a. Additionally, these filters maintain a pressure differential between the UHV chamber (10^{-10} Torr) and the HV environment (10^{-6}-10^{-5} Torr) after HHG capillary. When residual IR intensity exceeds the damage threshold of the filters, an additional “rejector” mirror (superpolished silicon substrate) is placed after the HHG fiber at a

grazing angle to reflect the EUV light and absorb the majority of the IR light. A 200 nm ZrO_2 layer is coated on silicon for its use at high photon energies. Their difference in reflectivity is plotted in Figure 4.4b. The “rejecter” mirror also protects the downstream EUV optics if they are sensitive to intense IR. It also maintains the beam propagating direction when paired with the toroidal mirror in beam focusing (as shown below).

The design of the focusing geometry in EUV beamline is to construct a 1:1 imaging system from the end of the HHG capillary to the sample surface. For blue (390nm) driven harmonics, not only the 7th harmonic (22.26 eV) is dominant over the entire harmonic spectra but also the energy spacing between adjacent harmonics is 6.36 eV, which is large enough to avoid the overlap of spectral features for most materials. Therefore, a focusing toroidal mirror after the rejecter mirror at grazing incidence (Figure 4.3a-b) is used to focus the EUV beam onto the sample. All the attosecond metrology experiments presented in the thesis require the maximum bandwidth of the harmonic pulse train to be utilized. Therefore, the same focusing geometry is used. For experiments requiring monochromated high energy harmonics (42 eV, 65 eV, and 90 eV) driven by IR light, one pair of multilayer mirrors (one flat, one with radius of curvature R=1 m) with precisely manufactured multilayer coatings are used to isolate the desired harmonics (Figure 4.3c). Mg/SiC coatings are used for low photon energies <45 eV; Al/Zr in middle-range from 45 eV to 65 eV and Mo/Si for high energies from 65meV to 95 eV. Further details for designing the coatings for these multilayers can be found in reference.

4.4 The Surface Science End Station

The end station is a μ-metal chamber pumped with 700 l/s magnetically-levitated turbo pump (Pfieffer Hi Pac 700 M) and 270 l/s ion pump (Varian VacIon Plus). The chamber is also

equipped with a titanium sublimation pump (TSP). The chamber base pressure is 2.5×10^{-10} Torr but operates at 3.5×10^{-10} Torr during measurements with harmonics because of small pinholes in the pressure differential aluminum filter. All the sample preparation, characterization and measurement tools are integrated in the same chamber, offering great convenience in experiment. We divide the vacuum ports of the chamber into three categories: vacuum pumps, surface preparation tools and surface characterization tools. Surface preparation tools include: an ion sputter gun, an alkali metal deposition system (SAES Getter source) and a gas dosing system composed of a capillary doser attached to a gas leak value for flow control.

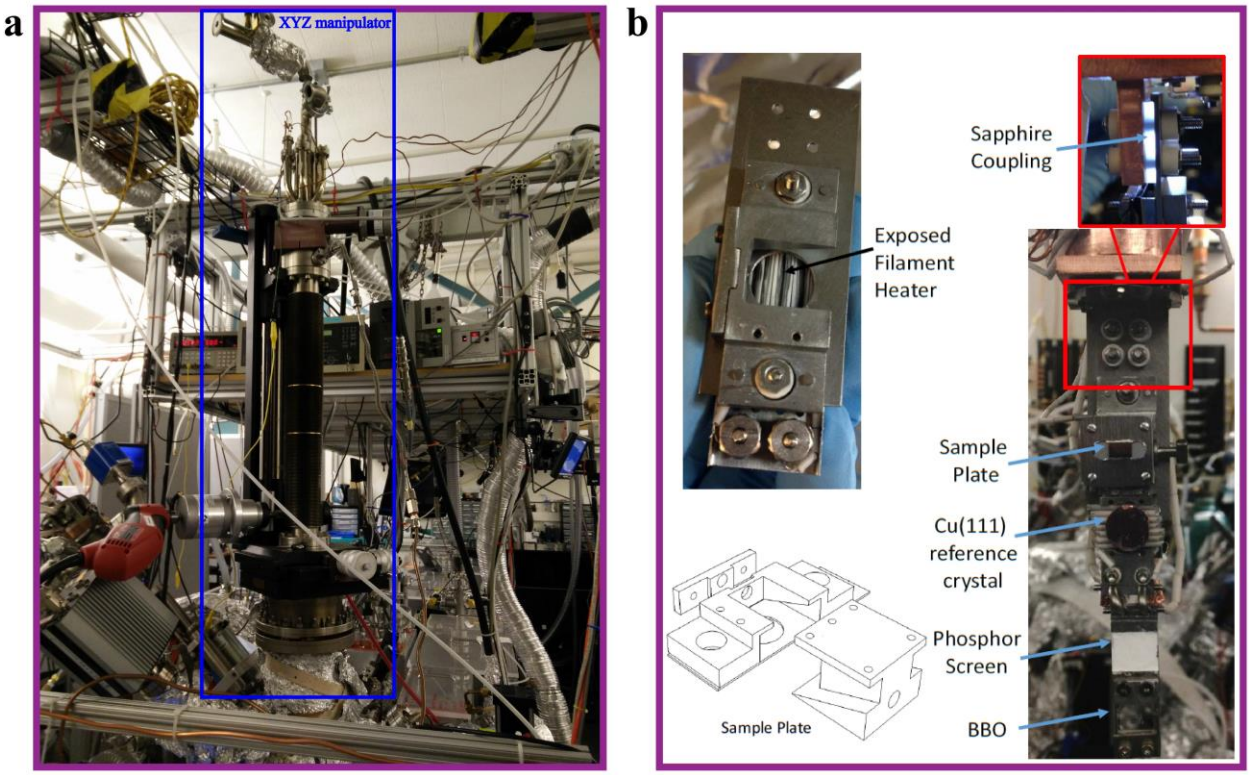

Figure 4.5: XYZ manipulator and sample holder. (a) The blue square highlights the manipulator in the photoelectron spectroscopy setup. (b) schematics of the sample holder.

The solid-state samples are mounted on a screw-fastened transferable sample plate attached to the head of a xyz-manipulator (Figure 4.5a). A differentially pumped feedthrough at the top of the manipulator enables 360^{o} rotation of the sample around the z-axis. The transfer of the sample from atmosphere to UHV chamber is achieved by a load-lock system. The sample temperature can be controlled continuously from 50 K to 1250 K by thermal contact of the sample holder to the cold finger of an open loop continuous flow cryostat integrated inside the manipulator, and by tungsten wire radiative heating plate, respectively. Type-N thermocouple mounted to the side of the sample plate monitors the temperature profile and provides a feedback to a home-developed proportional-integral-derivative (PID) software driving the heater power supply. A Residual Gas Analyzer (RGA, Leybold Inficon Transpector 2) was used to monitor the species and content of gas molecules inside the chamber during sample preparation.

The surface characterization level of the chamber accommodates a Low Energy Electron Diffraction (LEED) system (OCI BDL800IR), home-built Time-Of-Flight (TOF) spectrometer, a Hemispherical Electron Analyzer (HEA, SPECS PHOIBOS 100) equipped with a CCD detector, a EUV source of duo plasmatron discharge lamp (SPECS UVS300) that generates bright plasma radiation (He I: 21.2 eV or He II: 40.8eV) for standard static photoemission measurement.

The IR and EUV beam enter the end station collinearly through one fixed port on the sample characterization level (Figure 4.3a). The collinear geometry is achieved by an annular mirror located right before the UHV port: the EUV beam passes through the central hole in the mirror and the IR beam reflects off it at 45^{o} incidence angle with beam centered on the mirror.

Temporally and spatially overlapping the EUV and the IR pulses on the surface of the sample is crucial for successful pump-probe (especially attosecond metrology) experiments. First, a gross adjustment is obtained by finding the overlap between the IR pump beam and residual red

beam from HHG in the EUV beamline (referred to as IR probe). For this purpose, the Al foil is retracted and a sapphire window is inserted to pass the IR and maintain the pressure differential. The sample is translated up from the measurement position and a BBO crystal underneath is lifted to the beam height. By focusing both IR beams on the BBO crystal, overlap is determined by observing the optical interference between two frequency-doubled beams. Pump-probe collinearity is achieved by optimizing the beam pointing to make the interference fringes as symmetric and uniform as possible. A more accurate IR-pump and IR-probe overlap is determined through the enhancement in multiphoton photoemission in cross correlation of two beams on sample surface.

Fine tuning of the spatial overlap between IR pump and EUV probe is by shooting both beams on the phosphor screen where EUV beam can induce a visible fluorescence. The phosphor screen is right underneath the sample plate (Figure 4.5b). Zero-of-time between EUV and IR is determined with Laser Assisted Photoemission (LAPE).

Chapter 5

Tomographic Reconstruction of Attosecond Pulse Trains with Circular Polarization

This chapter is adapted, with permission, from:

C. Chen, Z. Tao, C. Hernández-García, P. Matyba, A. Carr, R. Knut, O. Kfir, D. Zusin, C. Gentry, P. Grychtol, O. Cohen, L. Plaja, A. Becker, A. Jaron-Becker, H. Kapteyn, M. Murnane, Tomographic reconstruction of circularly polarized high-harmonic fields: 3D attosecond metrology. *Sci. Adv.* **2**, e1501333 (2016).

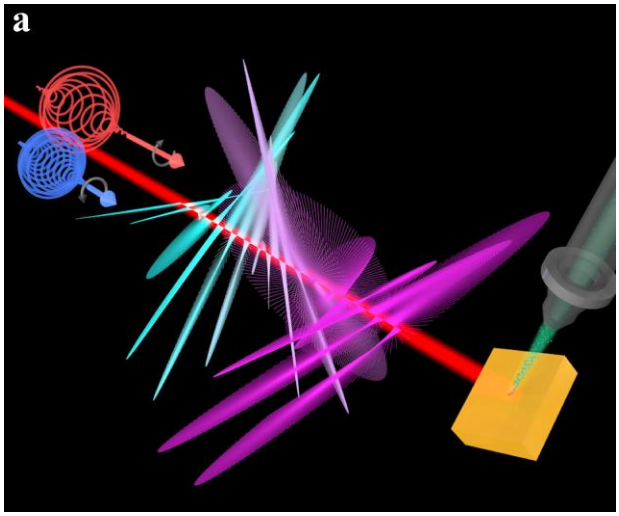

Figure 5.1: Illustration of the 3D reconstruction of circularly polarized harmonics. (a) By simultaneously illuminating a copper surface with circularly polarized extreme ultraviolet (EUV) light and an infrared laser beam that is perfectly synchronized with the EUV light, we are able to reconstruct the most complex light field to date. Art by Steve Burrows, JILA.

5.1 Abstract

Bright, circularly polarized, extreme ultraviolet (EUV) and soft X-ray high harmonic beams can now be produced using counter-rotating circularly polarized driving laser fields. Although the resulting circularly polarized harmonics consist of relatively simple pairs of peaks in the spectral domain, in the time domain, the field is predicted to emerge as a complex series of rotating linearly polarized bursts, varying rapidly in amplitude, frequency and polarization. Here, we extend attosecond metrology techniques to circularly polarized light for the first time by simultaneously irradiating a copper surface with circularly polarized high harmonic and linearly polarized infrared laser fields. The resulting temporal modulation of the photoelectron spectra carries essential phase information about the EUV field. Utilizing the polarization selectivity of the solid surface and by rotating the circularly polarized EUV field in space, we fully retrieve the amplitude and phase of the circularly polarized harmonics, allowing us to reconstruct one of the most complex coherent light fields produced to date.

5.2 Introduction

5.2.1 Circularly Polarized High Harmonic Generation

Tabletop EUV and soft X-ray radiation from high-harmonic generation (HHG) process is a unique light source for uncovering new fundamental understanding of dynamics in atoms [104,112], molecules [181] and materials [44,171]. Until very recently however, most experiments used linearly polarized harmonics which can easily be produced using single-color driving lasers. In this case, HHG emerges when an electron that is ionized by the laser field is driven back and recombines with its parent ion [63,64]. When implemented in a phase matched geometry, the dipole emission from each atom interferes constructively to generate a bright HHG

beam [88]. However, until recently, it was not possible to generate bright, circularly polarized HHG for probing magnetic materials [182] or chiral molecules [183]. This is because although atoms still undergo strong-field ionization in circularly polarized fields, the probability for an electron to recombine with its parent ion to emit a HHG photon is greatly suppressed [63,184,185].

Fortunately, high-brightness circularly polarized harmonics can now be produced in the EUV and soft X-ray regions by driving HHG with bi-chromatic circularly polarized counter-rotating fields [68–71,73,186–189]. In this scheme, a unique HHG spectrum is generated, consisting of pairs of peaks, each with opposite circular polarization. Theory predicts that for counter-rotating ω and 2ω laser fields, the circular harmonics are generated as a superposition of three bursts of linearly polarized EUV light per optical cycle in the time domain, where the polarization of each burst is rotated by 120^{o} from its predecessor [71,187]. Experimentally, the electron trajectories have been shown to predominantly move in a two-dimensional plane [71,190].

5.2.2 Direct Temporal Characterization of Circularly Polarized Harmonics

Despite of the promising applications of circular harmonic, no direct measurement of the temporal characteristics of circularly polarized HHG exists, that could be used to inform and validate advanced theory, and to harness the enormous potential of extreme nonlinear optics to generate arbitrary spectral-temporal-polarization-shaped light fields spanning the EUV and soft X-ray regions. This is due to the novelty of high-brightness circularly polarized HHG, their complex temporal structure, and the fact that conventional methods [28,29,32,34,111,191] for pulse characterization are not directly applicable. Moreover, it was recently proposed that by using crossed beams of circularly-polarized lasers, or taking into account the orbital angular

momentum of the initial state, either isolated circularly polarized single attosecond pulses can be produced [180,192] or else highly elliptical attosecond pulse trains [193,194]. Therefore, the ability to directly characterize the temporal structure of circularly polarized harmonics would benefit a whole new area of polarization-shaped x-ray attosecond science.

In this work, by using laser-dressed angle-resolved photoemission from solids, we extend attosecond metrology techniques to circular polarization for the first time. By simultaneously irradiating a copper surface with circularly polarized HHG and linearly polarized infrared laser fields, the resulting modulation of photoelectron spectra caused by quantum-path interference carries essential phase information about the EUV field. Utilizing the strong polarization selectivity in photoemission from solid surfaces, as well as the ability to rotate the circularly polarized EUV field in space, we retrieve the full waveform of circularly polarized high harmonic fields. This represents the first direct measurement of circularly-polarized HHG in the time domain, enabling us to fully characterize one of the most complex coherent light fields to date, where the spectral, temporal and polarization states are rapidly changing on attosecond timescales.

5.3 Experimental Setup

Figure 5.2 illustrates the circular high harmonic generation (HHG) beamline as well as the linearly and circularly polarized laser fields for our experiment. We used a multi-pass Ti:Sapphire laser system to generate 30 fs IR pulses of 780 nm ($\hbar\omega$=1.60 eV) light, with pulse energy of 2.4 mJ, and at a repetition rate of 4 kHz. The laser output is then split: most of the energy (95%) is used to generate fundamental (ω) and second harmonic (2ω) circularly polarized and counter-rotating driving beams for HHG, while a smaller portion (5%, linear polarization) is used to probe (dress) the photoelectrons generated by the circularly polarized harmonics. The 2ω light is

generated using a 200 μm thick β-phase barium borate crystal, which produces 33 fs pulses at a wavelength of 390 nm and with pulse energy of 0.7 mJ. The 2ω light and the co-propagating residual ω light (pulse energy 1.2 mJ) are separated using a dichroic mirror, and sent into two different arms of a Mach-Zehnder interferometer. The polarizations of the ω and 2ω beams are then converted to right and left circular polarization using a combination of λ/2 and λ/4 waveplates. The relative time delay between the 2ω and ω pulses (τ_{RB}) is adjusted using a closed-loop piezo-stage with sub-femtosecond scanning resolution.

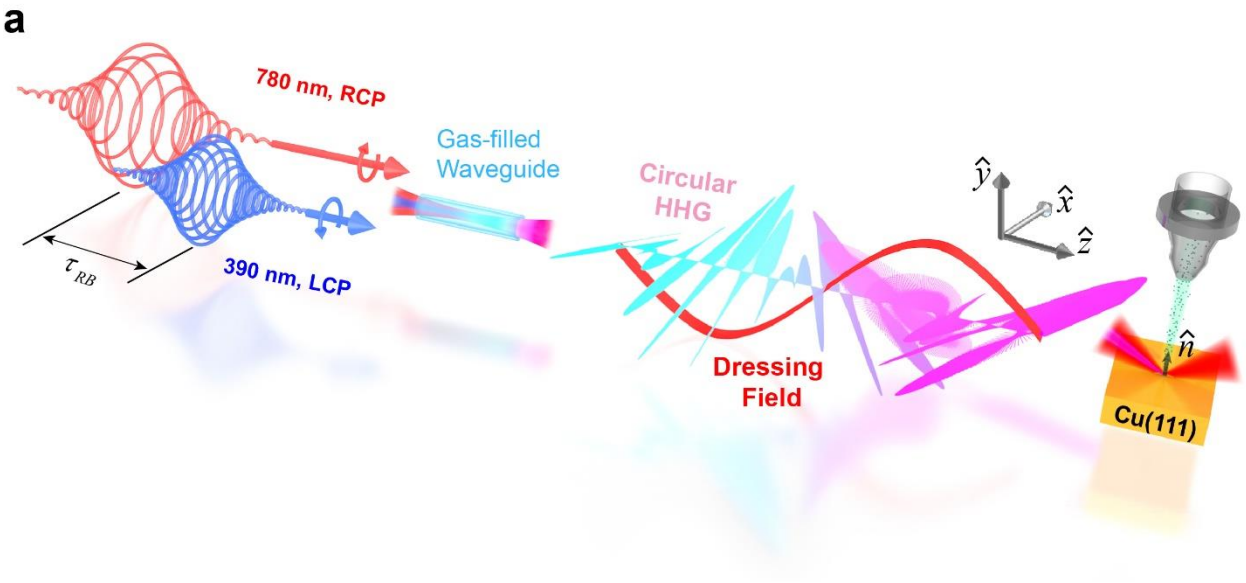

Figure 5.2: Characterization of circularly-polarized HHG fields. (a) counter-rotating ω [780nm, right-circularly polarized (RCP)] and 2ω [390nm, left-circularly polarized (LCP)] beams from a Ti:Sapphire laser are focused into an Ar-filled hollow waveguide. The generated circular HHG and a time-delayed linearly polarized 780nm dressing field are focused onto a clean Cu(111) surface. Here, a specific geometry is plotted for illustration purpose, where the $\hat{y}$ -pol component of circular HHG field is aligned with the normal direction of sample ($\hat{n}$). In experiments, the orientation of the circular HHG field can be rotated by adjusting the temporal delay between the ω and 2ω driving fields, τ_{RB}.

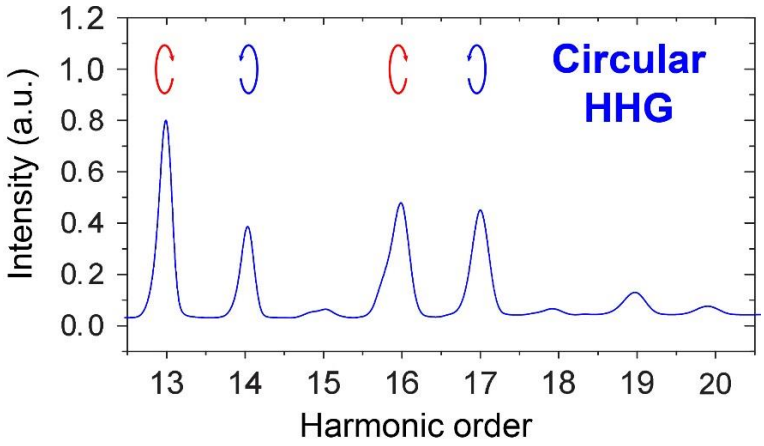

Figure 5.3: Circularly-polarized HHG spectrum recorded by an EUV spectrometer. The 13th and 16th harmonic orders are right circularly polarized (RCP) and 14th and 17th orders are left circularly polarized (LCP).

To generate circularly polarized high harmonics, the ω and 2ω beams are focused using lenses of focal length 50 cm (ω) and 75 cm (2ω), and recombined with a dichroic mirror, before propagating into a 1-cm-long capillary waveguide. The waveguide has an inner diameter of 150 μm and is filled with Argon at a pressure of 30 Torr [69]. To measure the spectrum of circularly polarized HHG, a toroidal Au mirror is inserted temporarily into the beamline at a grazing angle, to reflect the harmonics into an EUV spectrometer. For angle-resolved photoemission experiments, the HHG beam is then focused onto an atomically clean Cu (111) sample using a second toroidal Au mirror, to a spot size of ≈100 μm FWHM. Any residual driving laser light is blocked by a 200 nm thick polycrystalline Al filter.

The linearly polarized IR probe (dressing) beam is recombined collinearly with the circular HHG beam using an annular silver mirror. The FWHM of the IR beam on the sample is ≈250 μm, which is larger than the harmonic beam to ensure efficient dressing of the photoelectrons. The relative delay between the HHG and IR beams is controlled using an interferometrically stabilized

stepper-motor delay stage (with sub-femtosecond resolution). The intensity of the probe IR light on the sample is adjusted to ≈3.75 μJ/pulse (peak intensity: 2.8×10^{11}W/cm^2) using a half wave plate and a linear polarizer. The low intensity of the IR dressing light ensures that contributions from higher-order sidebands (>1st order) are negligible. The IR dressing field is p-polarized, i.e., perpendicular to the sample surface for all the measurements.

5.4 Spectrum of Circularly Polarized Harmonics

The spectrum of circular harmonics consists of three pairs of harmonic orders [(13ω, 14ω), (16ω, 17ω), (19ω, 20ω) in Figure 5.3], each with right and left helicity, which is a consequence of photon energy and spin-angular momentum conservation rules [68,69]. Consistent with experiment and theory [68,69], the intensities of the 3mth orders (15ω and 18ω) are strongly suppressed, because they do not conserve parity and spin angular momentum in the case of perfectly circularly-polarized driving lasers. They are not completely suppressed however, because a slight ellipticity was introduced into the 2ω driving field to serve the characterization purposes.

5.5 Cu(111) Sample Preparation and Band Structure

To measure the phase of circularly polarized harmonics, a Cu(111) single crystal is used as the photoemission target. An atomically clean Cu(111) surface is obtained using repeated cycles of Argon ion sputtering (0.7 keV, incidence angle of 60^o) at room temperature (300 K) in UHV chamber (base pressure $<5\times10^{-10}$ Torr), followed by annealing to 820 K for 10 minutes. The sample is grounded during all static and dynamic measurements. The sample surface quality

is confirmed by monitoring the low energy electron diffraction (LEED) patterns and the Shockley surface state in static photoemission spectra, as shown in Figure 5.4a.

The static photoemission spectra are measured using Helium Iα line radiation at 21.2 eV from a discharge lamp (Specs UVS300), and recorded by an angle-resolved photoelectron spectrometer (ARPES, Specs Phoibos 100, acceptance angle is ±15° under wide angle mode), with an analyzer work function of 4.2 eV. The Cu(111) single crystal features a Shockley surface state at 0.4 eV below the Fermi level, and two conduction bands: an upper band (at 2.8 eV below the Fermi level) and a lower band (at 3.7 eV below the Fermi level). The upper band (*d* band) exhibits Λ_3 symmetry while the lower band (*sp* band) consists of a dominant state with Λ_1 symmetry and a minor contribution from a Λ_3 symmetry state.

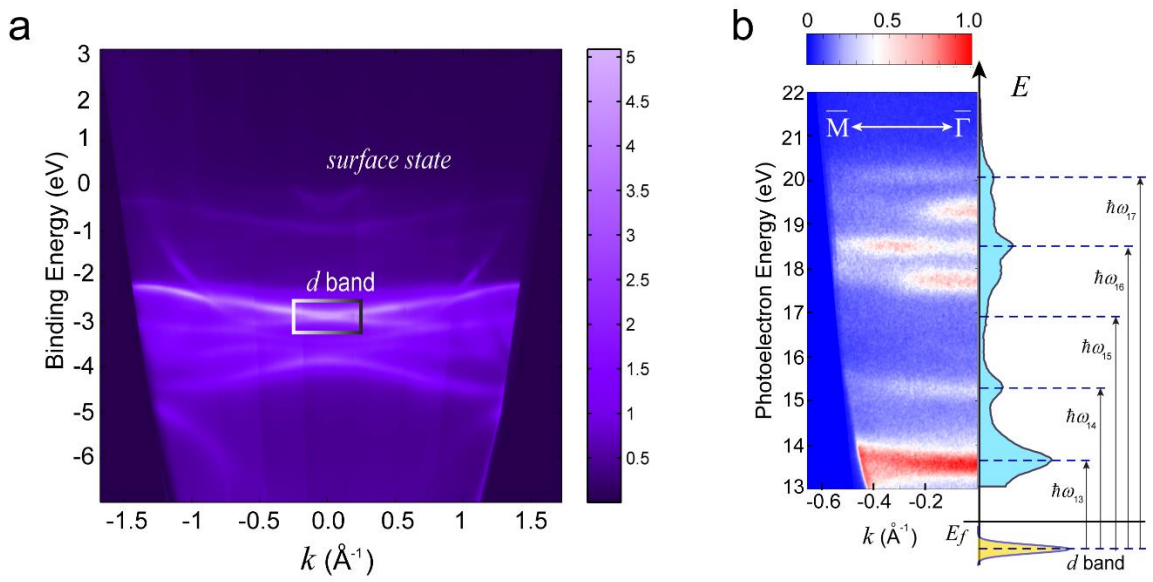

Figure 5.4: Photoelectron spectrum of Cu(111). (a) ARPES spectrum along the $\overline{\Gamma M}$ direction taken using the He Iα (21.2 eV) line from a He discharge lamp. (b) ARPES spectrum of Cu(111) excited by the circularly-polarized HHG. The spectrum with momentum span is recorded by a hemispherical electron analyzer. The analyzer work function is 4.2 eV, which correlates the photoelectron energy with photon energy. The direct photoemission pathways from Cu *d* band excited by the corresponding harmonic orders are labeled in the right panel.

5.6 Static ARPES Spectra of Cu(111) Excited by Circularly Polarized Harmonics

When excited by circularly polarized HHG, the photoemission spectrum from Cu(111) is comprised of a manifold of modulated peaks ranging from 13 to 22 eV, as shown in Figure 5.4b. Due to the complex spectra of circularly polarized HHG, consecutive ARPES peaks from the same electronic state are separated by 1.60 eV ($\hbar\omega_L$). Two sets of strong photoelectron bands can be seen, corresponding to direct photoemission induced by circular harmonic pairs (13ω, 14ω) and (16ω, 17ω) from the *sp* and *d* bands. The photoelectron bands excited by harmonic pair (19ω, 20ω) are too weak to stand out from the secondary background, because of the low intensities of these harmonics. The 3*m*th (*m* is an integer) order harmonics (15ω and 18ω) are also strongly suppressed. However, their presence can be detected from oscillations at a frequency of ω in the photoelectron interferogram at photoelectron energies 17 eV and 21.8 eV, which is discussed in section 5.7.3.

The photoemission cross-section of the *sp* band is very low when excited by 13ω and 14ω, but increases for higher orders (16ω and 17ω). At the same time, photoelectrons from the *sp* bands overlaps with photoelectrons from the surface states excited by lower order harmonics because the binding energy difference between the two states (~3.3 eV) is very close to twice of the energy spacing between consecutive harmonics (3.2 eV). These parasite photoelectrons from *sp* and surface states are spectrally well-separated from *d* band photoelectrons.

5.7 Measuring the Spectral Phase of Circularly Polarized Harmonics

5.7.1 Overview

Full characterization of the amplitude and phase of linearly polarized HHG fields has been demonstrated using many approaches based on an electron-phase modulator [191], including atto-streaking [28], RABBITT (resolution of attosecond beating by interference of two-photon

transitions) [32,195], CRAB (complete reconstruction of attosecond bursts) [34], and PROOF (phase retrieval by omega oscillation filtering) which was successfully used to retrieve the phases associated with isolated attosecond pulses necessarily with an ultrabroad spectrum [111]. In these measurement schemes, the harmonic phases are imprinted as modulations on the photoelectron energy-momentum spectrum in the presence of a dressing (or streaking) IR laser field [191].

In our work, photoelectrons ejected from the Cu(111) surface by the circularly-polarized harmonics are simultaneously dressed by a linearly polarized IR field (780 nm, $\hbar\omega_L$=1.6 eV). The interference between different quantum pathways induces a modulation of the photoelectron yield, which was recorded as a function of temporal delay (τ_d) between the HHG and IR dressing fields using a hemispherical electron analyzer. Because of a dramatic difference in the photoemission cross-section of the Cu(111) surface for s- and p- polarized EUV light, photoelectrons ejected by a s-polarized field dominate the signal, i.e., HHG polarization parallel to the sample surface (section 5.7.2 (a)). This not only eliminates ambiguities resulting from the entanglement of harmonic phases from two orthogonal polarizations ($\hat{x}$ and $\hat{y}$ shown in Figure 5.2) in the electron interferogram, but also eliminates the use of EUV multilayer polarizers, which have very low efficiency and narrow bandwidth in this photon energy range. Moreover, a major advantage of our scheme is that a simple rotation of the HHG field (achieved by varying the delay between the ω and 2ω driving fields) allows us to record the perpendicular component of the HHG polarization (section 5.7.6).

5.7.2 PROOF Algorithm

(a) Polarization dependent photoemission cross section

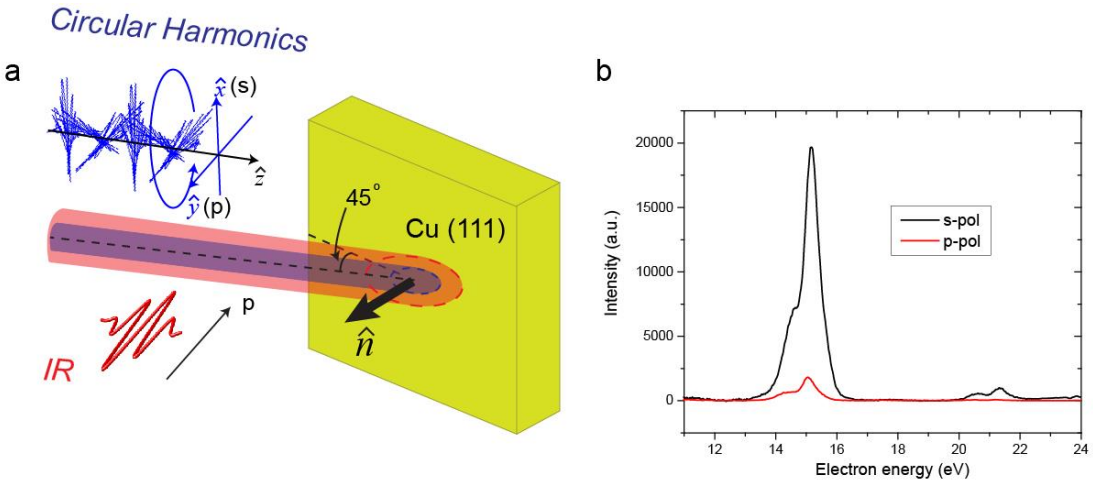

Figure 5.5: Photoelectron yields depend on the HHG polarization. (a) Experimental geometry. The circular HHG and IR dressing fields arrive at Cu(111) surface collinearly with a 45° incidence angle. $\hat{n}$ is the vector normal to sample surface. The IR dressing field is linearly p-polarized, along the surface normal $\hat{n}$. The $\hat{x}$ and $\hat{y}$ axes define two orthogonal linear components of the circularly polarized HHG light, which rotate with the orientation of the HHG light. Here, a situation where the $\hat{x}$-pol HHG component aligns parallel to sample surface is plotted. (b) Photoelectron spectra of Cu(111) excited using linearly polarized equal-intensity HHG beams with s- and p- polarizations.

We will first derive the probability of strong-field ionization from solid surface excited by circularly polarized EUV light in the presence of a linearly polarized dressing IR field. We use the atomic units except where stated otherwise. The photoelectron transition dipole is given by Ref [195] and Ref [138]

$$b(\tau_d) = -i\int_{-\infty}^{+\infty} dt \left\langle \Psi_f(\vec{r},t) \middle| \vec{r}\cdot\vec{E}^X(t-\tau_d) \middle| \Psi_i(\vec{r},t) \right\rangle, \tag{5.1}$$

where $\Psi_i(\vec{r},t)$ is the initial-state wavefunction of electrons inside the material, $\vec{E}^X(t)$ the EUV field, τ_d the time delay between the EUV and dressing IR fields and $\Psi_f(\vec{r},t)$ the final-state

wavefunction of the photoelectrons. Polarization-dependent photoemission cross-section can be determined by the selection rules. The *d* band of Cu(111), which is used for phase retrieval in our experiments, is of Λ_3 symmetry and can only be excited by EUV field parallel to the sample surface. As a result, we can selectively study the spectrum and phase of $\hat{x}$- or $\hat{y}$ -pol component by aligning it parallel to the sample surface (s-polarization). The experimental geometry is plotted in Figure 5.5a. This conclusion is supported by the large difference in photoelectron yields excited by HHG light of the same intensity, but linearly polarized harmonic fields either along s- and p-polarizations, as shown in Figure 5.5b. Since circularly polarized HHG were used to eject photoelectrons, we write down the EUV field $\vec{E}^X(t)$ as

$$\vec{E}^X(t) = E_x(t)\hat{x} + E_y(t)\hat{y}, \tag{5.2}$$

where $E_x(t)$ and $E_y(t)$ are two orthogonal linear components of the circularly polarized EUV field. In our experiments, the orientation of the circularly polarized HHG field can be rotated by adjusting the relative delay between the fundamental IR (ω) and its second harmonic (2ω) driving fields. The incidence-angle of the HHG light (45°) only affects the photoelectron yields, but does not affect the measurement of the harmonic phases.

(b) Amplitude of transition dipole under the strong-field approximation

After considering the geometrical projection of the dipole matrix element, we reduce Equation 5.1 to a form only depending on $E_x(t)$

$$b(\tau_d) = i\frac{\sqrt{2}}{2}\int_{-\infty}^{+\infty} dt \left\langle \Psi_f(\vec{r},t) \middle| s \cdot E_x(t-\tau_d) \middle| \Psi_i(\vec{r},t) \right\rangle. \tag{5.3}$$

Here *s* represents an unit vector parallel to the sample surface. The initial-state wave function is

$$\Psi_i(\vec{r},t)=\psi_i(\vec{r})e^{-iE_it}, \tag{5.4}$$

with binding energy E_i. The final-state wavefunction $\Psi_f(\vec{r},t)$ can be expressed in Volkov-wave

$$\Psi_f(\vec{r},t)=\psi_f(\vec{r})\psi_{\vec{k}}(\vec{r},t), \tag{5.5}$$

where $\psi_f(\vec{r})$ is the spatial wavefunction of the ionic state of the material, $\vec{k}$ is the final state electron wavevector and $\psi_{\vec{k}}(\vec{r},t)$ describes the "dressed" photoelectron state (Volkov-wave function) in the laser field [138]

$$\psi_{\vec{k}}(\vec{r},t)=\frac{1}{(2\pi)^{3/2}}e^{i\left[\vec{k}+\vec{A}_L(t)\right]\vec{r}}e^{i\Phi\left(\vec{k},t\right)}, \tag{5.6}$$

where $\Phi\left(\vec{k},t\right)$ is the Volkov phase, defined as

$$\Phi\left(\vec{k},t\right)=-\frac{1}{2}\vec{k}^2t-\frac{1}{2}\int_t^\infty dt'\left[2\vec{k}\cdot\vec{A}_L(t')+\vec{A}_L^2(t')\right]. \tag{5.7}$$

By plugging Equation 5.4-5.7 into Equation 5.3 and separating the spatial and temporal integration, we can get

$$b(\tau_d)=i\frac{1}{8\pi^{3/2}}\int_{-\infty}^{+\infty}e^{-i\Phi\left(\vec{k},t\right)}e^{-iE_it}E_x(t-\tau_d)D(t)dt. \tag{5.8}$$

Here, we define the canonical momentum $\vec{p}(t)=\vec{k}+\vec{A}_L(t)$ and the transition dipole matrix element $D(t)=\left\langle\psi_f(\vec{r})e^{i\vec{p}(t)\cdot\vec{r}}\middle|s\middle|\psi_i(\vec{r})\right\rangle$. Strictly speaking, $D(t)$ is time-dependent, imprinting additional phases related to the material initial states and the photoemission time delay. In our experiments, only the *d* band of Cu(111) is taken into account, which eliminates its dependence on the initial states. The photoemission time delay in atomic systems can be calculated accurately by theory [32]. However, this is much more challenging for a solid-state system. RABBITT measurements have been performed on Cu(111) surface using similar HHG photon energies. It

was found that the photoemission delay varies approximately linearly with a slope of ~15 as per harmonic order, corresponding to ~0.36 rad in phase. As we will show later, this small correction is within the uncertainty of our phase retrieval algorithm. So, for simplicity, we assume *D(t)* is constant at D_o.

Assuming the dressing laser field is $E_L(t) = E_0(t)\cos(\omega_L t)$, where $E_0(t)$ is the envelope function, the term with the Volkov phase, $\Phi(\vec{k},t)$, can be simplified following Ref [34]

$$e^{-i\Phi(\vec{k},t)} \approx e^{i\frac{1}{2}\vec{k}^2 t} e^{-i\varphi_1} e^{-i\frac{kE_0(t)}{\omega_L^2}\cos(\omega_L t)}, \tag{5.9}$$

where φ_1 is a static phase shift which does not contribute to temporal modulations [34].

Using the properties of Bessel function expansion [110]: $\sum_{n=-\infty}^{\infty} e^{in\phi} J_n(u) = e^{iu\sin(\phi)}$, we can simplify Equation 5.9 to

$$e^{-i\Phi(\vec{k},t)} \approx e^{i\frac{1}{2}\vec{k}^2 t} e^{-i\varphi_1}\left[J_0\left(\frac{kE_0}{\omega_L^2}\right) + iJ_1\left(\frac{kE_0}{\omega_L^2}\right)\left(e^{i\omega_L t} + e^{-i\omega_L t}\right)\right]. \tag{5.10}$$

Here, only the terms with *n* = -1, 0, 1 are taken into consideration [$J_{-1}(x) = -J_1(x)$], because higher order sidebands can be neglected due to the relatively low peak intensity of the IR dressing field (1.25 x10^{11} W/cm^2). On the other hand, the EUV field can be described by Fourier transform

$$E_x(t) = \int_{-\infty}^{+\infty} A_x(\omega) e^{i\phi_x(\omega)} e^{-i\omega t} d\omega, \tag{5.11}$$

where $A_x(\omega)$ and $\varphi_x(\omega)$ are the amplitude and phase spectra of the $\hat{x}$-component of the circularly polarized field, respectively. By plugging Equation 5.10 and 5.11 into Equation 5.8, we find that only the terms with phase terms $e^{-i\omega_n \tau_d}$, $e^{-i(\omega_n+\omega_L)\tau_d}$ and $e^{-i(\omega_n-\omega_L)\tau_d}$ contribute to the temporal

modulations. Here we will ignore the pre-factors for simplicity and use the fact that $\omega_n + \omega_L = \omega_{n+1}$ and $\omega_n - \omega_L = \omega_{n-1}$

$$b(\tau_d) \propto \underbrace{J_0\left(\frac{kE_0}{\omega_L^2}\right)A_x(\omega_n)e^{i\phi_x(\omega_n)}e^{-i\omega_n\tau_d}}_{(ii)} + iJ_1\left(\frac{kE_0}{\omega_L^2}\right)\left[\underbrace{A_x(\omega_{n+1})e^{i\phi_x(\omega_{n+1})}e^{-i(\omega_n+\omega_L)\tau_d}}_{(iii)} + \underbrace{A_x(\omega_{n-1})e^{i\phi_x(\omega_{n-1})}e^{-i(\omega_n-\omega_L)\tau_d}}_{(i)}\right] \quad . (5.12)$$

The three components in Equation 5.12 represents the transition amplitudes of three quantum paths initiated from a same initial state and ending up with a same final state: (i) absorbing an HHG and an IR photon ($\hbar\omega_{n-1}+\hbar\omega_L$); (ii) direct photoemission by a single HHG photon ($\hbar\omega_n$); and (iii) absorbing an HHG photon and emitting an IR photon ($\hbar\omega_{n-1}-\hbar\omega_L$), as shown and labeled in Figure 5.6.

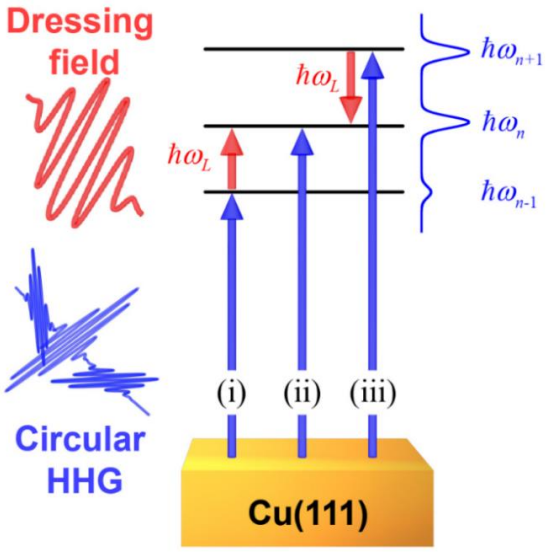

Figure 5.6: Schematic of the quantum paths that give rise to photoelectron interferences.

(c) Quantum-path interference

The modulations on the photoelectron counts as a function of τ_d can be obtained by calculating $S(\tau_d) = |b(\tau_d)|^2$. The interference between (i) and (iii) yields oscillation of frequency $2\omega_L$, while interference between (i) and (ii) or (ii) and (iii) can give oscillation with frequency ω_L:

$$S_{2\omega_L} \propto 2\left[J_1\left(\frac{kE_0}{\omega_L^2} \right) \right]^2 A_x(\omega_{n+1}) A_x(\omega_{n-1}) \cos\left[2\omega_L \tau_d + \phi_x(\omega_{n-1}) - \phi_x(\omega_{n+1}) \right]; \tag{5.13}$$

$$\begin{aligned} S_{\omega_L} \propto J_0\left(\frac{kE_0}{\omega_L^2} \right) J_1\left(\frac{kE_0}{\omega_L^2} \right) \Bigg\{ & A_x(\omega_n) A_x(\omega_{n+1}) \cos\left[\phi_x(\omega_n) - \phi_x(\omega_{n+1}) + \omega_L \tau_d - \frac{\pi}{2} \right] \\ & + A_x(\omega_n) A_x(\omega_{n-1}) \cos\left[\phi_x(\omega_{n-1}) - \phi_x(\omega_n) + \omega_L \tau_d + \frac{\pi}{2} \right] \Bigg\} \end{aligned}. \tag{5.14}$$

With our experimental parameters, we estimate $J_1\left(\frac{kE_0}{\omega_L^2} \right) \Big/ J_0\left(\frac{kE_0}{\omega_L^2} \right) \approx 0.2$, which is in good agreement with the observed amplitude ratio between $2\omega_L$ and ω_L components (see Figure 5.7c). At the energy corresponding to harmonics of (3*m*-1)th or (3*m*+1)th orders, the $2\omega_L$ oscillation diminishes as a result of the low intensity contributed by its suppressed neighboring 3*m*th harmonic order.

As shown in Equation 5.14, the phase differences of consecutive harmonics are imprinted in the oscillation with ω_L frequency. To further extract this relationship, we write down the oscillation with ω_L frequency at the energy corresponding to the direct photoexcitation with n^{th} harmonic in a general form, in a way similar to the PROOF method [111].

$$S_n(\tau_d) = \kappa(\omega_n) \sin\left[\omega_L \tau_d + \alpha(\omega_n) \right], \tag{5.15}$$

where $\kappa(\omega_n)$ and $\alpha(\omega_n)$ are the energy-dependent intensity and phase of the oscillation, respectively, which are defined as

$$\kappa(\omega_n) = \frac{kE_0}{\omega_L^2} I_0(\omega_n) \sqrt{\frac{I_0(\omega_{n+1}) + I_0(\omega_{n-1}) - 2\sqrt{I_0(\omega_{n+1}) I_0(\omega_{n+1})} \cos(\phi(\omega_{n-1}) - \phi(\omega_{n+1}))}{I_0(\omega_n)}}, \quad (5.16)$$

and

$$\tan[\alpha(\omega_n)] = \frac{\sqrt{I_0(\omega_{n+1})} \sin[\phi(\omega_n) - \phi(\omega_{n+1})] - \sqrt{I_0(\omega_{n-1})} \sin[\phi(\omega_{n-1}) - \phi(\omega_n)]}{\sqrt{I_0(\omega_{n+1})} \cos[\phi(\omega_n) - \phi(\omega_{n+1})] - \sqrt{I_0(\omega_{n-1})} \cos[\phi(\omega_{n-1}) - \phi(\omega_n)]}. \quad (5.17)$$

Here, $I_0(\omega_n)$ and $\phi(\omega_n)$ are the power and phase spectra of the harmonics, respectively.

5.7.3 Electron Interferogram

The $\hat{x}$-polarization ($\hat{x}$-pol) of the circular harmonics was first aligned parallel to the sample surface. The temporal interferogram of photoelectrons, for τ_d in range of -5 to 5 fs, is plotted in Figure 5.7a. These data were obtained by integrating the photoelectron spectra over the entire momentum range and subtracting the background photoelectron spectrum obtained well before time-zero. To eliminate photoelectrons originating from different states in the material [44,104], the angle-resolved spectra were filtered before integration (as illustrated in Figure 5.7b), so that photoelectrons only from the Cu *d* band contributed to the interferogram, which have an almost constant photoemission cross-section in the energy range of our experiments [196]. Any residual contribution from *sp* band to the interferogram phases are not expected to influence the HHG pulse train reconstruction, because they are only involved when retrieving phases in regions between the major harmonic, where the spectral intensity of circularly polarized HHG is low.

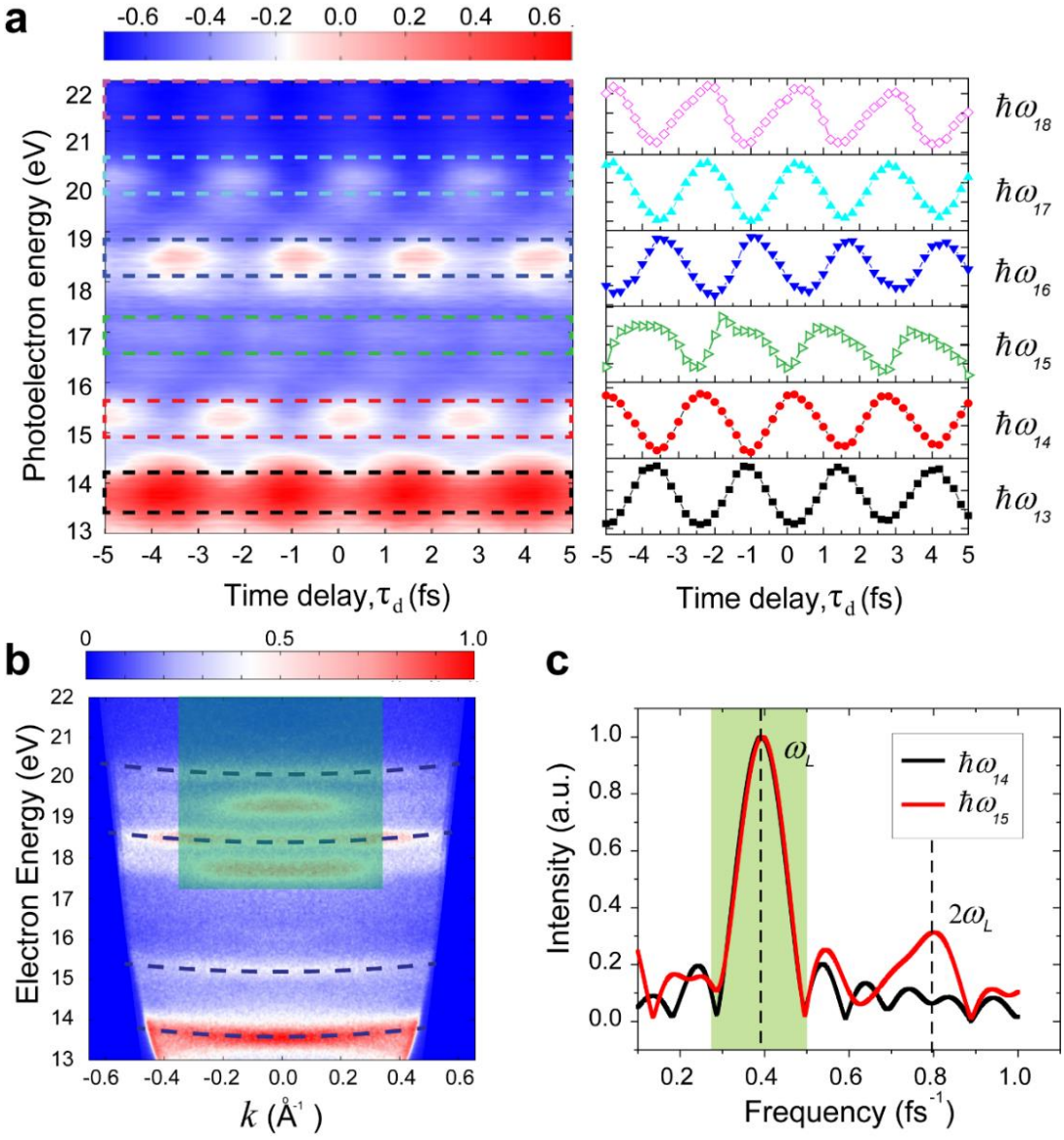

Figure 5.7: Photoelectron interferogram as a function of time delay between the circular HHG and linear IR field. (a) 2D map of photoelectron yields as a function of photoelectron energy and pump-probe time delay. The selected lineouts on the right panel represent the photoelectron-intensity modulation at the photoelectron energies corresponding to direct photoemission from Cu(111) *d* band excited by labeled HHG orders. (b) ARPES spectrum along the same direction of Figure 5.4(a) using circularly polarized HHG. The pink area represents the spectral mask applied in the data analysis to remove the contributions from the *sp* band and the surface state. The photoelectron bands corresponding to direction photoemission from Cu *d* band are labeled by dashed lines. (c) Fourier analysis of the photoelectron-yield oscillations at energies corresponding to direct photoemission by 14ω and 15ω. The green area marks the frequency mask used to extract the phases of the ω_L oscillations in (a).

As can be seen in Figure 5.7a, the photoelectron yields as a function of τ_d oscillate with a frequency of ω_L (periodicity of 2.6 fs), which can be understood through quantum-path interferences (Figure 5.6). Since the energy spacing between consecutive circularly polarized harmonics is $\hbar\omega_L$ (Figure 5.3), there are three distinct quantum pathways for exciting electrons from a given initial state to the same final state (path (i-iii) in Equation 5.12 and Figure 5.6). The photoelectron yield oscillates with frequency ω_L because of one-IR-photon-assisted interference between quantum paths (i) and (ii), and (ii) and (iii). This cross section is much larger than that of two-IR-photon-assisted interferences between (i) and (iii), which cause oscillations with frequency $2\omega_L$, as used in RABBITT characterizations [32]. This conclusion is also supported by a Fourier analysis of the photoelectron-yield oscillations (Figure 5.7c), where the amplitude of $2\omega_L$ component is very weak for the 15^{th} order, and is almost completely absent for the 14^{th} order.

5.7.4 Extraction of the Interferogram Phase

To implement a phase retrieval algorithm to acquire the harmonic phases from the photoelectron interferogram, we first need to extract the interferogram phases. To do this, we bin the interferogram data into 100 meV wide electron energy regions and integrate the photoelectron counts in each region to obtain a series of plots of the photoelectron yield versus relative time delay between the HHG and IR dressing fields. Then, we apply a Fourier analysis to calculate the relative phases between the oscillations of different photoelectron energies.

In the Fourier analysis, we determine the relative phase between two energy-dependent oscillation curves [$x(E_1,t)$ and $x(E_2,t)$] by calculating their cross-correlation function

$$C(E_1, E_2, \omega) = \tilde{x}^*(E_1, \omega)\tilde{x}(E_2, \omega), \tag{5.18}$$

where E_1 and E_2 are the corresponding electron kinetic energies for these two oscillation curves, $\tilde{x}(\omega)$ is the Fourier transform of $x(t)$ and $\tilde{x}^*(\omega)$ is the complex conjugate of $\tilde{x}(\omega)$. The peak frequency of $|C(E_1, E_2, \omega)|$ is the oscillation frequency shared by both curves, which equals to the frequency of the IR dressing laser ω_L, as shown in Figure 5.7c. The averaged phase of $C(E_1, E_2, \omega)$ at this peak frequency corresponds to the relative phase difference between the two oscillations [197]. To improve the signal-to-noise ratio, the measurement of interferogram is repeated 30 times, which yields consistent phase relations. The averaged interferogram phases are used in the phase retrieval algorithm, which are shown as solid lines in Figure 5.8.

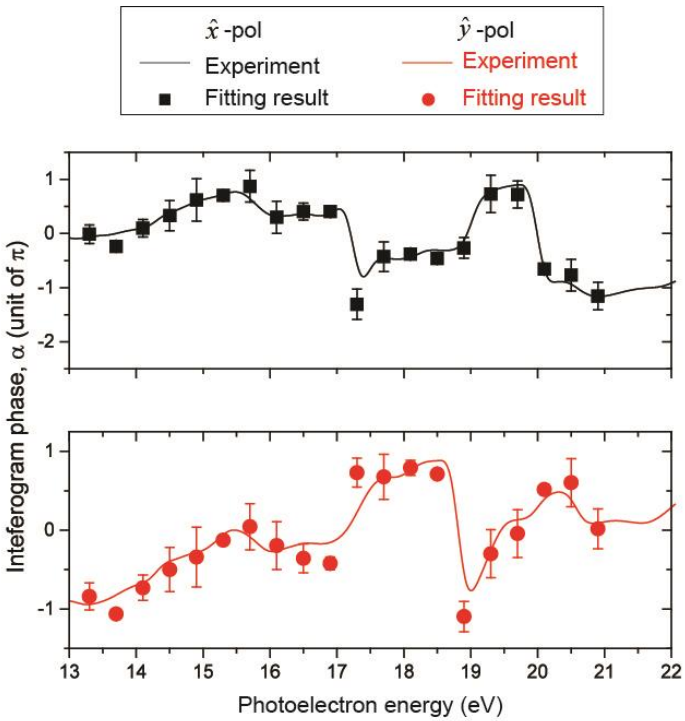

Figure 5.8: Reproducing photoelectron interferogram phase using retrieved HHG phase. The solid lines represent the extracted interferogram phases from the experimental data. The symbols are the reproduced interferogram phases using the retrieved harmonic phases. The error bars represent the standard deviation from multiple trials using the genetic algorithm.

5.7.5 Retrieve Harmonic Phase from Interferogram Phase

To sum the derivation of equations in Section 5.7.2, the phases of the harmonics are encoded in the ω_L oscillations of the photoelectron-yield interferogram. At the electron kinetic energy corresponding to direct photoemission by the n^{th} order harmonics ($\hbar\omega_n$), the oscillating spectral intensity as a function of τ_d can be written in the general form: $S_n(\tau_d) = \kappa(\omega_n)\sin\left[\omega_L\tau_d + \alpha(\omega_n)\right]$, where $\kappa(\omega_n)$ is the energy-dependent oscillation amplitude and $\alpha(\omega_n)$ the phase spectrum of the interferogram, which is related to the phase spectrum of HHG $\phi(\omega_n)$ by -

$$\tan[\alpha(\omega_n)] = \frac{\sqrt{I_0(\omega_{n+1})}\sin[\phi(\omega_n)-\phi(\omega_{n+1})] - \sqrt{I_0(\omega_{n-1})}\sin[\phi(\omega_{n-1})-\phi(\omega_n)]}{\sqrt{I_0(\omega_{n+1})}\cos[\phi(\omega_n)-\phi(\omega_{n+1})] - \sqrt{I_0(\omega_{n-1})}\cos[\phi(\omega_{n-1})-\phi(\omega_n)]}. \quad (5.19)$$

$I_0(\omega_n)$ is the power spectrum. Equation (5.19) bridges the interferogram phase [$\alpha(\omega_n)$] and the phase differences of corresponding neighboring harmonics [$\phi(\omega_n)-\phi(\omega_{n+1})$] and [$\phi(\omega_{n-1})-\phi(\omega_n)$], allowing us to retrieve the harmonic phases from the interferogram in an iterative way. Here, the full interferogram phase spectra were fed into a genetic algorithm [198] to retrieve the harmonic phases by minimizing the ranking function: $R = \sqrt{\sum_{\omega_n} I(\omega_n)\left[\alpha^{\text{calc}}(\omega_n) - \alpha^{\text{expt}}(\omega_n)\right]^2}$, where $\alpha^{\text{calc}}(\omega_n)$ and $\alpha^{\text{expt}}(\omega_n)$ are the interferogram phases obtained from the retrieval algorithm and the experiment, respectively.

In the phase retrieval algorithm, the harmonic phases are represented by an array of numbers ranging from $-\pi$ to π. To minimize the ranking function *R*, a population of random arrays are first assigned as the harmonic phases, covering harmonics of 12th-19th orders (on either side, a redundant harmonic order with zero intensity is included as the boundary conditions). In

the genetic algorithm, reproduction is carried out using Roulette-Wheel selection. Cloning, mutation and crossover operations are used to increase the diversity of population and to prevent stagnation. To ensure uniqueness of the solution, the phase of 13th harmonic in $\hat{x}$- pol is set to be zero, including the phases in its adjacent area. To improve the convergence of the phase retrieval for $\hat{y}$ - component, proper helicities of harmonics are taken into consideration. The solution searching for the phases of $\hat{y}$ -pol component is confined in proper regions related to $\hat{x}$-pol phases, i.e., $\phi_y^{13} \in \phi_x^{13} - \frac{\pi}{2} + \left[-\frac{\pi}{4}, \frac{\pi}{4}\right]$, $\phi_y^{14} \in \phi_x^{14} + \frac{\pi}{2} + \left[-\frac{\pi}{4}, \frac{\pi}{4}\right]$, etc. , where $\phi_{x(y)}^n$ is the phase of n^{th} harmonic order in $\hat{x}$ ($\hat{y}$) –pol, allowing the genetic algorithm to find the best fit to the experimental data in these regions. In Figure 5.8, we plot the reproduced interferogram phases compared with the experimental phases for $\hat{x}$- and $\hat{y}$ - pol. The phases for major harmonics are listed in Table 5.1. The robustness of the algorithm is tested by repeating the phase retrieval processes for more than 50 times. The error bars are determined by the standard deviations of retrieval results from multiple trials.

	Phases of the harmonics (rad)				
Polarization	13^{th}	14^{t}	15^{th}	16^{th}	17^{th}
$\hat{x}$	0.0	0.57± 0.29	0.23 ± 0.58	0.97± 0.30	-0.19± 0.30
$\hat{y}$	-1.65± 0.58	1.88± 0.44	-2.32± 0.91	-0.37± 0.56	2.31± 0.50

Table 5.1: Phases of circular harmonics. The phases along $\hat{x}$- and $\hat{y}$ -pol (see Figure 5.2) are obtained using a phase retrieval algorithm. The uncertainty is determined as the standard deviation of phase values retrieved from multiple trials.

5.7.6 Rotation of Circularly Polarized Harmonic Field

In our experiments, the two orthogonal linear components of the complex circularly polarized HHG field are characterized by rotating the driving laser field with the three-fold-symmetry by 90^o and aligning the component of interest parallel to the sample surface. The successful reconstruction relies on the fact that, except their orientation, the $\hat{x}$ - or $\hat{y}$ -pol components of the EUV field are mostly unchanged throughout the rotation. In practice, the rotation of the driving field is achieved by delaying the fundamental IR (ω) field relative to the second harmonic (2ω) field by 3/8 of the fundamental IR wavelength (292 nm in space or 0.973 fs in time), which is controlled by a closed-loop piezo-stage (position error ±5 nm). As a result, the orientation of the combined driving field (with three-fold symmetry) [190], and hence the circularly polarized HHG field, is rotated by 90^o. Although this rotation has a negligible influence on the HHG spectrum and flux, it has a significant impact on the photoelectron interferogram and the corresponding harmonic phases, allowing us to reconstruct the temporal profile of the $\hat{y}$ -pol HHG field.

In Figure 5.9a, we plot the calculated 3D profile of the combined driving laser field, before and after the ω field is delayed by 0.973 fs. A rotation of the combined laser field can be clearly resolved. The corresponding 2D projections of the combined laser fields are shown in Figure 5.9b. We note that when the temporal delay between ω and 2ω fields is changed, in addition to the rotation of the driving field, a temporal shift (phase change) of the EUV field is also induced, as illustrated by Figure 5.9c, which is taken into account in the phase retrieval algorithm. A 90^o rotation of the combined 2-color laser field can lead to a corresponding rotation of the circular HHG by the same angle, which is confirmed by our numerical simulation (section 5.9) with both driving fields are perfectly circular (ε_1=ε_2=1.0), as shown in Figure 5.10(a-d).

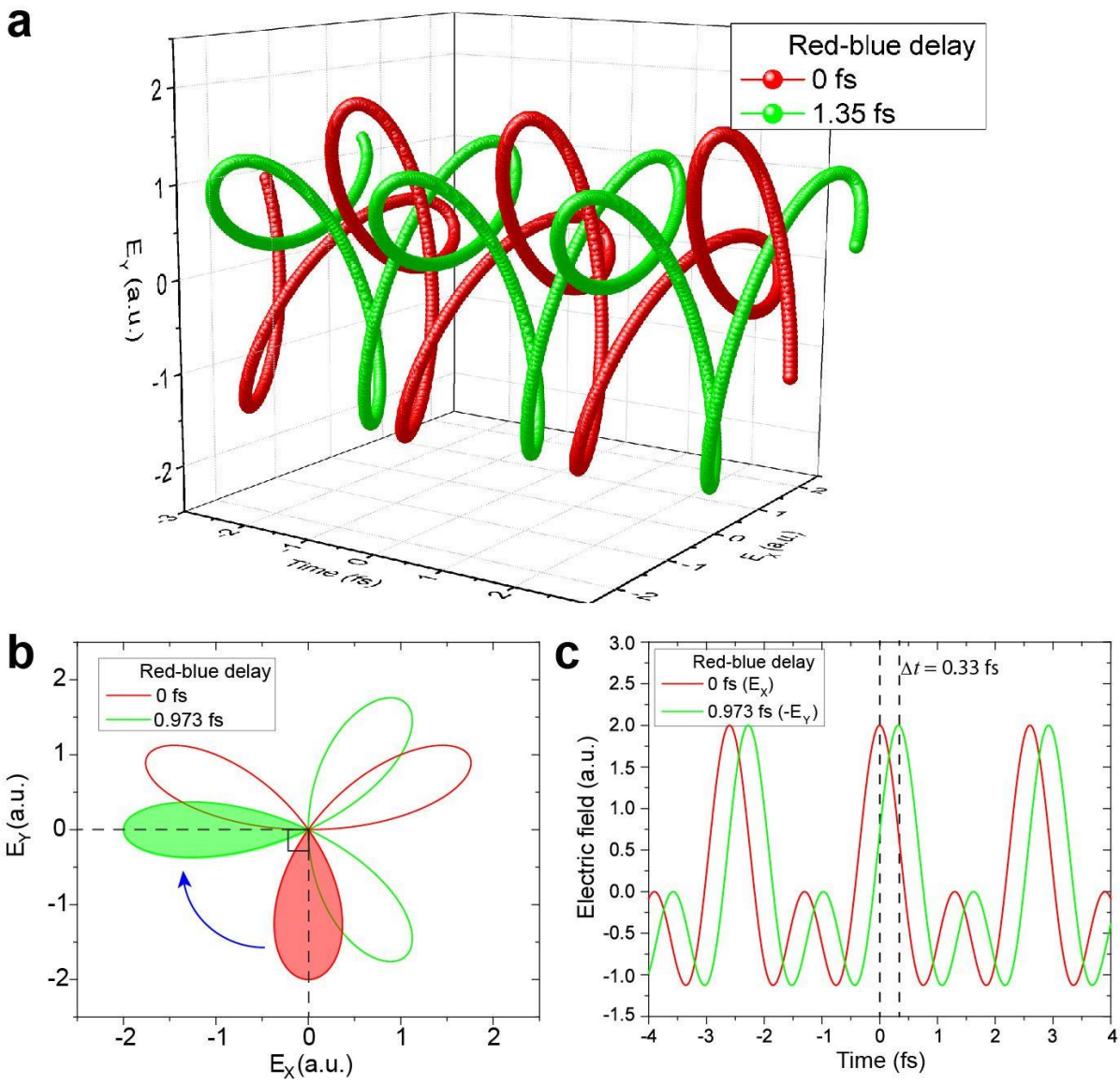

Figure 5.9: Rotation of the clover-leaf-shaped driving field. (a) 3D plot of the combined electric fields of counter-rotating 780 nm (RCP) and 390 nm (LCP) fields. The red and green symbols represent the combined field before and after delaying the IR field by 0.973 fs. (b) E_x-E_y 2D projection of (a), where the red and green curves represent the field before and after the delay. The colored area marks the same section of driving field so that a clear 90° rotation can be resolved. (c) Electric field intensities along $\hat{x}$ and $\hat{y}$ before and after delay, plotted as a function of time. The two fields are identical except for a delay of 0.33 fs.

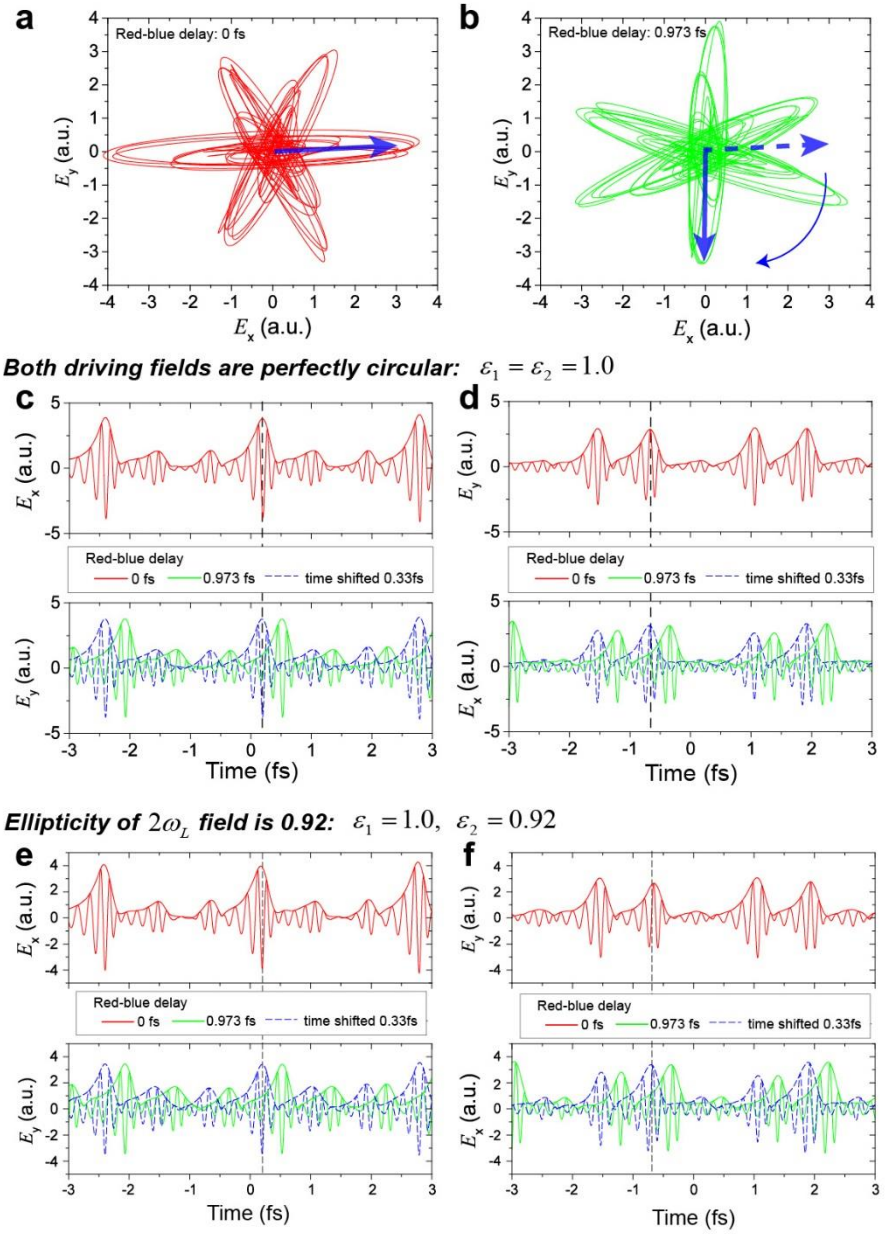

Figure 5.10: Simulation of the EUV field rotation. (a) and (b) Projection views of the circular HHG field before and after delaying the fundamental IR relative to second harmonic field by 0.973 fs. These results are obtained through our numerical simulation in Ar gas with both driving fields perfectly circular. A clear rotation of the HHG field can be observed. (c) and (d)The $\hat{x}$ and $\hat{y}$ components of the EUV field before and after delaying ω field with respect to 2ω field by 0.973 fs. The two components are identical (comparing red solid and blue dashed lines), apart from a time delay of 0.33 fs. The ellipticity of both driving fields are 1.0 ($\varepsilon_1 = \varepsilon_2 = 1.0$, as defined previously). (e) and (f) The $\hat{x}$ and $\hat{y}$ components of the simulated EUV field with the same delay of ω field, but with the ellipticity of 2ω field to be 0.94 ($\varepsilon_1 = 1.0,\ \varepsilon_2 = 0.92$).

We note that the rotation of circularly polarized HHG field can be affected by the ellipticity of the driving fields. In order to test validity of our method when the driving field is slightly elliptical, we simulated the circularly polarized HHG from Ar with the ellipticity of 2ω field (ε_2) to be 0.92. In Figure 5.10(e-f), the $\hat{x}$ - and $\hat{y}$ - components of the simulated HHG field are plotted before and after the ω field is delayed. Similar to Figure 5.10(c-d) where the driving fields are perfectly circular, E_x (E_y) after rotation is almost identical to E_y (E_x) before with a proper time shift, which is a clear evidence of the 90^o rotation of EUV field, even with a slight ellipticity ~0.92 of the driving laser fields.

Using the same procedure in Section 5.7, we characterized the perpendicular polarization component) by aligning it parallel to the sample surface. Our approach therefore extends the RABBITT [32] and PROOF [111] characterization approaches to be able to extract the 3D temporal-polarization structure of an arbitrary polarized attosecond pulse train.

5.8 Reconstruction of Attosecond Pulse Train with Circular Polarization

With the knowledge of both the amplitude and phase, the temporal structure of the circularly polarized harmonics can be uniquely determined. For the HHG pulse train reconstruction, the harmonic phases are interpolated from the retrieved results to provide an enough temporal span. To properly account for the effects of harmonic phase errors from retrieval process, the reconstruction calculation is repeated 100 times, in which a random number generator is applied to vary the harmonic phases within the error bar region.

The 3D electric field of the experimentally reconstructed circular HHG pulse train is plotted in Figure 5.11. In different retrieval processes within experimental error bar, the three-burst structure of the pulse train similar to the one presented in Figure 5.11 can be consistently

reproduced, with some variations in the burst orientation and intensity. Three linearly polarized bursts of the EUV fields with different orientations can be clearly distinguished in each IR optical cycle (2.6 fs), in excellent agreement with the pulse-train structure generated by our numerical simulations [199]. A typical duration of the EUV bursts is ~600 as, as shown in Figure 5.12.

The field orientation of each burst is obtained by averaging throughout each burst, weighted by local field intensity. The deviations from different reconstruction trials are also taken into account, providing the error bar. As shown in Figure 5.12, the field orientation of the EUV bursts rotates approximately 120^{o} from one to the next, which is a consequence of the three-fold symmetry of the combined driving field, directly validating previous theory [71].

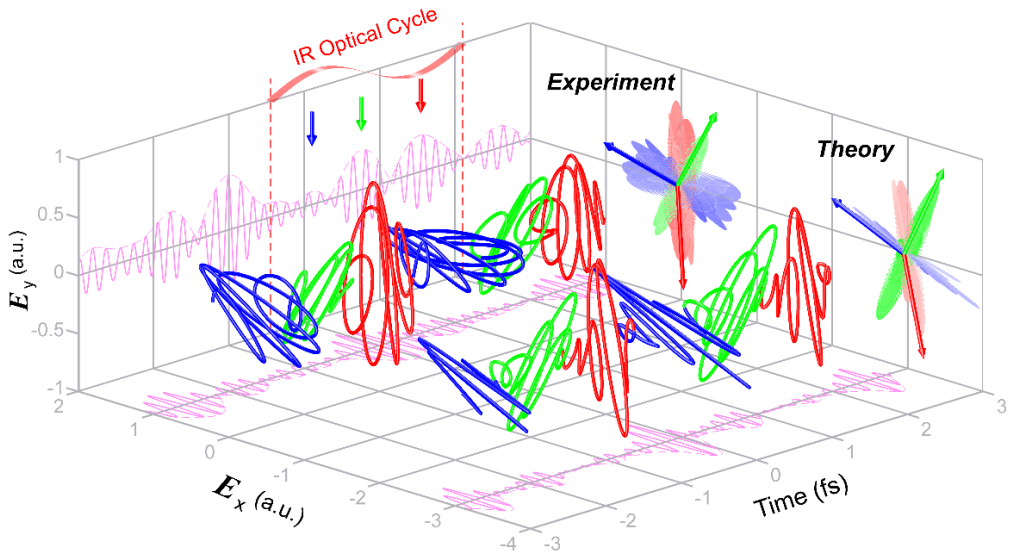

Figure 5.11: Experimental reconstruction of the circular HHG pulse train. Three-dimensional field plot of the experimentally reconstructed pulse train of circular HHG, in direct comparison with our numerical simulation. The pulse train from theory is offset by -3 units along the E_x axis for illustration purpose. Different colors (red, blue and green) highlight the three linear bursts with different field orientations within each fundamental IR optical cycle (2.6 fs). The structure of three bursts and IR optical cycle are also labeled on the $\hat{y}$-projection of the electric field. The carrier field of the experimental pulse train is reconstructed by assuming the phase of the $\hat{x}$ component of the 13th harmonic to be zero.

5.9 Numerical Simulation of Circular Harmonic Generation

The single source HHG has been computed in the dipole approximation using the Strong-Field Approximation (SFA) method, without resorting to the saddle point approximation [199]. The harmonic spectrum is computed from the acceleration by integrating the momentum-space contributions of the Volkov waves. This method allows us to tackle the circular polarization problem without the need of identification of the relevant semiclassical trajectories. Coulomb corrections are introduced using the corresponding pre-factor [200]. The argon wave functions are described as superpositions of Slater-type orbitals resulting from the Rothaan-Hartree-Fock method [201]. We take into account the electrons in the three valence orbitals, adding their contributions to the HHG spectrum coherently.

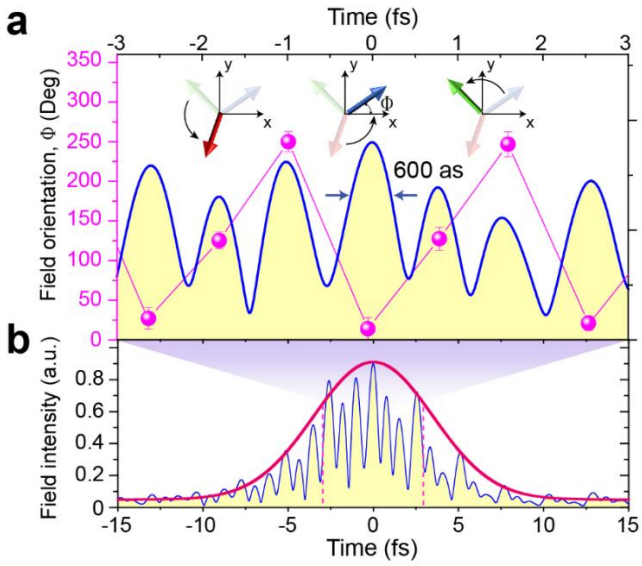

Figure 5.12: Field orientation of circular HHG from Ar. (a) Field orientation and intensity profile of the experimentally reconstructed circular HHG pulse train. The orientation of each EUV burst, Φ, is defined as the angle of the electric field relative to the $\hat{x}$ axis, as shown in the inset of (a). Φ is extracted by averaging the field orientation throughout each burst. (b) The overall field-intensity profile of the pulse train between -15 and 15 fs. Three-burst structure per IR optical cycle (2.6 fs) can be distinguished throughout the entire pulse train. The red curve represents the envelope of the pulse train with a FWHM of ~8 fs. A zoom-in view between -3 and 3 fs is presented in a).

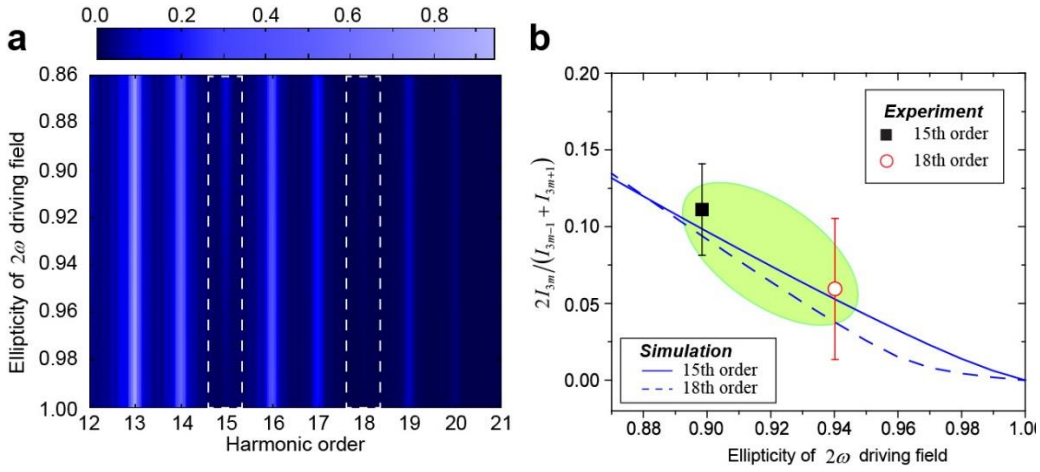

Figure 5.13: Normalized 3mth order harmonic intensity compared with numerical simulation. (a) 2D map of harmonic intensity as a function of harmonic order and the ellipticity of the 2ω driving field. The 15th and 18th orders are highlighted. (b) The normalized 3mth order intensity is plotted as a function of 2ω driving field ellipticity. The solid and dashed lines represent the results from simulation, with solid lines for 3m = 15 and dashed lines for 3m = 18. The symbols are experimental results with the filled black square for 3m = 15 and the open red circle for 3m = 18. The green area represented the estimation of the ellipticity of driving field in our experiment.

The driving field is described as a superposition of two counter-rotating elliptically polarized laser pulses in the form of $\boldsymbol{E}(t) = \sum_{i=1,2} \frac{A_i(t)E_i}{\sqrt{1+\epsilon_i^2}} [cos(\omega_i t)\hat{x} + \epsilon_i sin(\omega_i t)\hat{y}]$ where ϵ_i is the ellipticity. The driver frequencies, ω and 2ω, correspond to laser wavelengths of λ_1 =0.78 μm, and λ_2 =0.39 μm respectively. The temporal envelope, $A_i(t)$, has as a trapezoidal shape with 3 cycles of linear turn-on, 6 cycles of constant amplitude (16 fs) and 3 cycles of linear turn-off (in terms of cycles of λ_1). The electric field amplitudes (E_i) have associated intensities of $I_1 = 7.6\times10^{13}$ W/cm^2 and $I_2 = 3.8\times10^{13}$ W/cm^2 which preserves the ratio between two driving fields (2:1) used in our experiments. The field intensities are adjusted to match the cutoff energy observed in the experiments. In the calculations present in this work, the relative carrier-phase between the pulses is zero at the peak of the envelope.

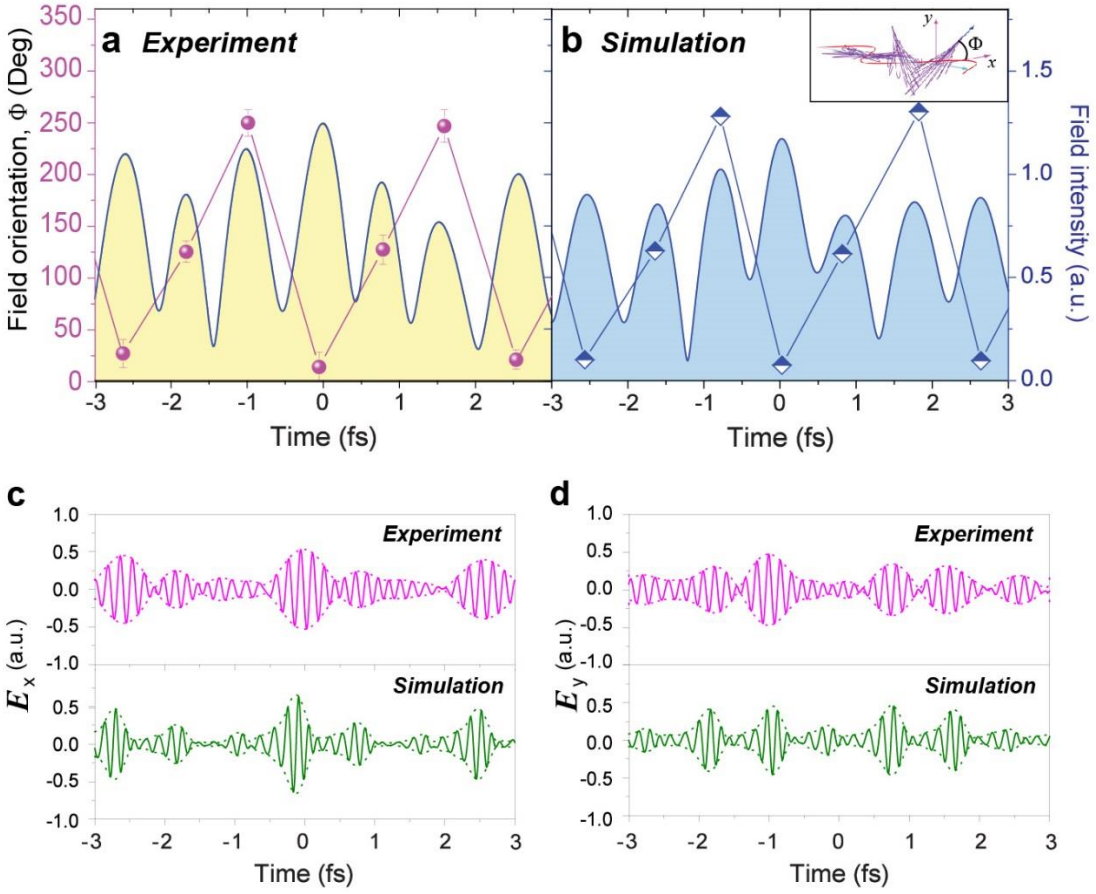

Figure 5.14: Experimental reconstruction of circularly polarized harmonics in comparison with numerical simulation. (a) Experimentally reconstructed field intensity envelope of the circular HHG pulse. The orientation of each EUV burst, Φ, is extracted by averaging the angle of EUV field in each burst relative to the x-axis. (b) The results from our numerical simulation with the ellipticity of 2ω driving field to be 0.94. A Gaussian envelop with 8 fs FWHM is applied on the simulation result for comparison. (c-d) Comparison of the E_x and E_y components from experiments and simulations.

From Equation (5.19), we note that contributions from quantum pathways involving the suppressed $3m^{th}$ order harmonics are essential for retrieving the harmonic phases, because they allow us to bridge the neighboring pairs of strong harmonics that are separated by $2\omega_L$. The appearance of $3m^{th}$ order harmonics is a direct consequence of a slight ellipticity in the driving laser fields, which was intentionally introduced into the 2ω driving beam.

In order to extract the ellipticity of the driving fields, we perform HHG simulations for different ellipticities of 2ω driving field (ε_2). As shown in Figure 5.13a, the intensities of 15th and 18th harmonic increase monotonically as a function of the ellipticity of the 2ω driving field. Here we define the normalized $3m^{th}$ order intensity as $\frac{2I_{3m}}{I_{3m-1}+I_{3m+1}}$. By comparing with our experimental results (symbols in Figure 5.13b) with the simulation results, we can determine that the ellipticity of 2ω driving field in our experiments is 0.92±0.04. In Figure 5.14, we plot the experimentally reconstructed field-intensity envelop in direct comparison with the results from our numerical simulations. The agreement between them is excellent.

5.10 Ellipticity of Circularly-Polarized High Harmonic Field

With the knowledge of intensity and phase of both $\hat{x}$ and $\hat{y}$ linear components, the ellipticity of the circular harmonics can be uniquely determined. The ellipticity of a circular field is given by [68]

$$\varepsilon^2 = \frac{|E_x|^2 + |E_y|^2 - \sqrt{\left(|E_x|^2 - |E_y|^2\right)^2 + 4|E_x|^2|E_y|^2\cos^2\left(\phi_x - \phi_y\right)}}{|E_x|^2 + |E_y|^2 + \sqrt{\left(|E_x|^2 - |E_y|^2\right)^2 + 4|E_x|^2|E_y|^2\cos^2\left(\phi_x - \phi_y\right)}}, \tag{5.20}$$

where $|E_x|$ ($|E_y|$) and ϕ_x (ϕ_y) are the amplitude and phase of $\hat{x}$ ($\hat{y}$) component of the electric field respectively. Here ε =+1/-1 corresponds to full right/left circular polarizations, respectively.

Previously, the ellipticity of circular HHG from Ne was characterized using X-ray magnetic circular dichroism (XMCD) [69]. Using our novel approach to access the harmonic amplitudes, phases and polarization direction, we can analyze the chiral properties of HHG in any spectral region, even when the photon energy does not overlap a characteristic absorption edge of a magnetic material.

The ellipticity ε_X of the circular harmonics is plotted in Figure 5.15 and is also directly compared with our numerical simulations. We find that the 3m+1th and 3m-1th orders are mostly circularly polarized, while the 3mth (i.e., 15th) orders are strongly elliptical, consistent with previous studies and theory [68,69]. Importantly, a reduction in the degree of HHG circularity can be observed in the cutoff region for 3m+1th and 3m-1th orders, which is also quantitatively confirmed by our numerical simulations.

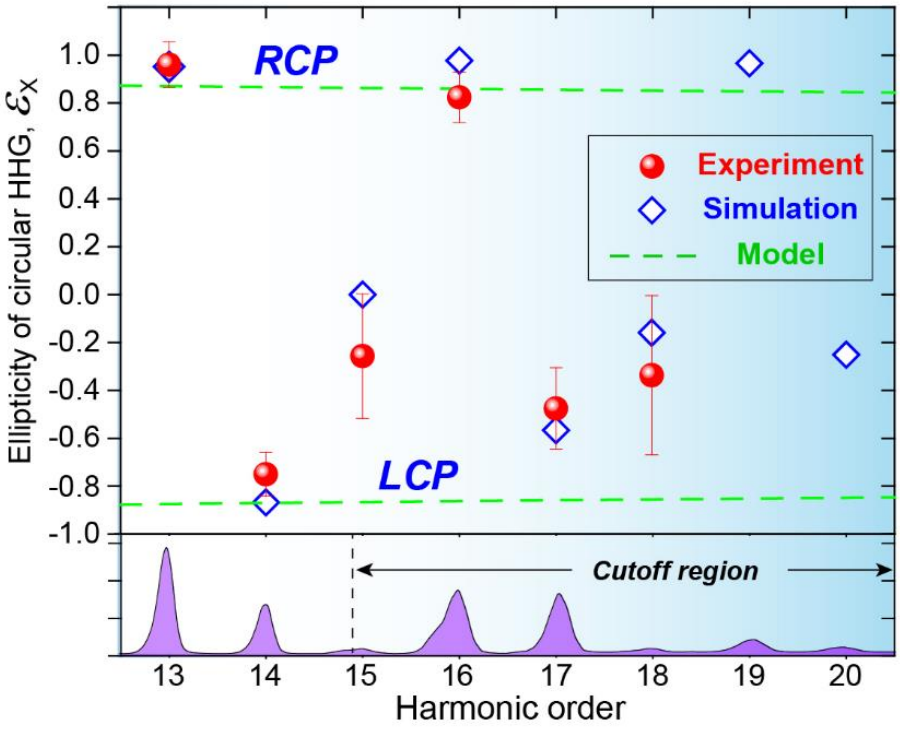

Figure 5.15: Ellipticity of circular HHG from Ar. The experimentally measured and theoretically calculated ellipticity of circular HHG from Ar. The open blue diamonds are the simulation results with $\varepsilon_1 = 1.0$ and $\varepsilon_2 = 0.92$, where ε_1 and ε_2 are the ellipticity of 780 nm and 390 nm driving fields, respectively. The green dashed lines represent the results considering spin-angular momentum conservation under a perturbative model in Ref. [68] and in Ref. [202]. The HHG spectrum obtained from experiment is plotted in the lower panel.

Previously, the ellipticity of circularly polarized HHG has been described under a perturbative-optics models [68,202,203]. In Ref. [68], the spin of HHG photon is simply the sum of averaged spins of RCP and LCP photons involved in each harmonic channel [68]. However, as pointed out in Ref. [202], this model has unphysical discontinuities, when describing the circularly polarized HHG with some ellipticity. This problem was solved in Ref. [202] by considering an ensemble of ω and 2ω photons with definite spin σ=±1, and their contributions to the HHG photon spin are dealt with statistically, by considering different combinations of ω and 2ω photons in each HHG channel when the light carries some ellipticity.

Here, ignoring the discontinuities from the first model [68], we note that both models [68,202] give same estimation on the HHG ellipticity as a function of harmonic order, as shown by the green dashed lines in Figure 5.15. This result is not surprising, since both models treat the problem in a perturbative way. However, comparing the estimation from perturbative models with our experimentally measured HHG ellipticity and numerical simulations, we find obvious deviation at the cutoff region. For linear HHG, it is known that the high-energy harmonics in the cutoff region are generated in a narrow temporal window, within one or two optical cycles at the peak of the driving laser pulse [204,205]. For the same reason, we believe that the large deviation from circularity in the cutoff region can be attributed to the unequal intensity contributions from the linear EUV bursts and the breaking of the three-fold symmetry, due to the narrow temporal emission window and slight ellipticity in the driving fields.

5.11 Conclusion

In summary, we completely characterize the temporal, spectral and polarization states of circularly polarized harmonics generated by counter-rotating bi-chromatic driving fields. Using

this novel generation scheme, we demonstrate that the circular harmonics consist of a superposition of three linear EUV bursts with alternating polarization directions, repeating each optical cycle, which validates theory in the time domain for the first time [71]. We note that although some ellipticity has been intentionally introduced in the driving laser field to induce weak $3m^{th}$ order harmonics, which is necessary to bridge neighboring harmonic pairs in our current phase retrieval algorithm, this limitation can be removed by implementing a more complicated algorithm such as FROG-CRAB [34]. With this implementation, our approach can be applied to fully characterize the properties of both attosecond pulse trains and broadband isolated attosecond pulses from arbitrary HHG fields, which is essential for investigations of coherent attosecond chiral and magnetic dynamics [206], where knowledge of the full temporal structure of the EUV field is important.

Chapter 6

Influence of Microscopic and Macroscopic Effects on Attosecond Pulse Generation Using Two-Color Laser Fields

6.1 Abstract

Attosecond pulses and pulse trains generated by high-order harmonic generation are finding broad use for attosecond spectroscopies and imaging, enabling sub-femtosecond electron dynamics to be probed in atomic, molecular and material systems. To date, isolated attosecond pulses have been generated either by using very short few-cycle driving pulses, or by using circularly polarized driving pules to enforce temporal gating, or by taking advantage of phase matching gating. Here I show that by driving the HHG with a two-color linearly polarized laser field, the temporal window for phase matching is shorter than that for equivalent singe-color driving laser. As a result, even when relatively long 25-femtosecond pulses are used to drive high harmonic generations, we can nevertheless generate *quasi-isolated* attosecond pulses with a peak width of ~450 as. Our theoretical simulations are in good agreement with our experimental measurements, showing that the phase matching window decreases by a factor of 4 from four optical cycles in the case of the single-color fundamental driver to one optical cycle in the case of two-color (ω-2ω) laser drivers. Finally, I also show changing the relative delay between two-color driving fields modulate the duration of attosecond bursts from 450 as to 1.2 fs.

6.2 Introduction

6.2.1 Generation of Isolated Attosecond Pulses

Coherent attosecond pulses spanning the extreme ultraviolet (EUV) and soft X-ray spectral range can be produced via high-order harmonic generation (HHG) of an intense driving laser field in a gas medium [22,207]. Creation of such pulses have attracted extensive attentions, because they open the possibilities to study the ultrafast dynamics in atoms and materials with unprecedented time resolution. Indeed, coherent tabletop HHG sources were recently used to capture chemical reactions in real time [181], to reveal correlated charge, spin and phonon dynamics in materials with femtosecond time resolution [208], and to perform coherent imaging on nanostructures beyond the wavelength limit [209]. Moreover, attosecond HHG pulses were also implemented to track the fastest motion of electrons when they approach the atomic [59,124] or material-final-band resonances [35], revealing the most intriguing observations on the attosecond time scales.

The temporal structure of the HHG pulse trains is determined by the nontrivial electron motion under the influence of the driving field. When driven by a monochromatic laser field, an electron is tunnel ionized near the peak of the laser field and is driven away from its parent ion. A EUV photon is emitted in the recombination step, when the laser field changes its direction and drives the electron back to recollide with its parent ion [64,210]. When driven by a single-color laser field, this process repeats twice every optical cycle at both the positive and negative peaks of the electric field. Therefore, the most straightforward way to achieve single attosecond pulse is by reducing the number of electric field cycles to confine the recombination events to the most intense half cycle of the driving field (i.e., intensity gating). In this scenario, the harmonic spectrum is usually centered at high energies (> 80 eV). The generation of isolated attosecond pulses with

ultrabroad-bandwidth or at low EUV photon energy regime require other gating techniques to restrict HHG process to one single half cycle of the driving field. The polarization gating technique takes advantage of the dependence of HHG efficiency on the circularity of the driving fields by using two overlapping circular fields to create a temporal window with linear polarization. The phase matching gating, on the other hand, utilize the macroscopic phase matching effect to balance the negative dispersion of the ionized plasma and the positive dispersion and the neutral gas atoms in the medium.

6.2.2 HHG under Two-Color Driving Fields

It has been long realized that the HHG emission can be controlled by introducing a second driving field with different wavelength, which breaks the symmetry of the electron dynamics. Two-color driven HHG has been shown to be useful in manipulating the temporal profile and polarization state of the emitted attosecond pulses, as well as relaxing the conditions for single attosecond pulse generation. For example, double optical gating technique introduces a second-harmonic pulse in addition to polarization gating, which allows to generate isolated attosecond pulses [96]. Recently, circularly polarized attosecond pulses have been generated by mixing bi-chromatic circularly polarized driving fields with opposite helicities [30,69]. When driven by the combination of an linearly polarized fundamental IR field and its second harmonic field with a comparable intensity, the harmonics were found to be stronger than those obtained in the fundamental field alone in both parallel and orthogonal configurations [211]. Moreover, when the polarization of the two fields is the same the attosecond pulses are emitted once per IR optical cycle and hence are carrier-envelop phase stabilized [72]. Nevertheless, there is no measurement about the detailed temporal structure generated in this configuration so far, for which the direct

measurement of the HHG phases is required. At the same time, macroscopic phase matching under the two-color scheme could also affect the intensity and temporal structure of the emitted attosecond pulses by tailoring the ionization fraction of the gaseous medium through the change of gas pressure and the confocal parameters [88,100]. Such information could bring insight to the way of coherently engineering the attosecond pulses using the two-color driving fields.

In this chapter, by using interferometric laser-assisted photoemission to measure the full temporal profile of the HHG radiation, I show that quasi-isolated attosecond pulse with a peak width of ~ 450 as can be generated by mixing a multicycle 780 nm driving field with its second harmonic field. In tandem with the numerical simulation, we demonstrate that it is caused by the reduction of the temporal window of HHG phase matching in the two-color (ω-2ω) configuration when compared to that obtained by the equivalent single-color driving laser. Our theoretical calculations show that the phase matching window decreases by a factor of 4 from four optical cycles in the case of the single-color fundamental driver to one optical cycle in the case of two-color laser drivers. In the sub-cycle temporal regime, we also demonstrate the direct coherent control of the attosecond pulses by changing the relative phase between the 390 nm and 780 nm driving fields (φ_{RB}). Our results show that when φ_{RB} gives the maximum HHG yield, the FWHM (full width at half maximum) of the attosecond bursts in a pulse train reaches its minimum value of ~450 as, which is close to the transform-limited width. In contrast, when φ_{RB} is adjusted away from the optimum HHG yields, the peak FWHM is significantly increased due to the emergence of additional temporal structures. By comparing the experimental results with the numerical simulations and semiclassical calculations of the driving-field structure and electron trajectories, I find this observation is a direct consequence of the broken symmetry introduced by the intense second harmonic field, which strongly modifies the electron ionization, propagation and

recombination dynamics during the HHG process. In the spectral domain, this corresponds to the dependence of the HHG phases on φ_{RB}.

6.3 Experimental Setup

The setup of our experiments is illustrated in Figure 6.1a. The linearly polarized HHG beam is generated by mixing a near-infrared field (ω, 780 nm, IR) with its second harmonic field (2ω, 390 nm, blue) in a Mach-Zehnder interferometer. The pulse duration of the IR pulse is 26 fs. The polarizations of the two driving fields are adjusted to be parallel to each other through the λ/2 waveplate in each interferometer arm, before they are collinearly focused into a 10-mm-long waveguide filled with Argon gas at a pressure of ~30 torr. As a result, the HHG beam inherits the polarization of the combined driving fields. In our experiments, the two-color driving fields can be described as $E(t) = A\sin(\omega t) + B\sin(2\omega t + \varphi_0 + \varphi_{RB})$, where A and B are the amplitudes of the IR and blue driving fields, respectively. φ_0 is the relative phase corresponding to the highest HHG yields. In the experiments, the relative phase φ_{RB} can be adjusted using a delay stage with sub-femtosecond scanning precision as shown in Figure 6.1a. The peak intensity of the IR driving field is ~1.5x10^{14} W/cm^2. To enhance the symmetry breaking between neighboring cycles in HHG, we apply a strong (non-perturbative) blue driving field in our experiments with a field intensity approximately half of the IR.

The HHG spectra are measured directly using a EUV spectrometer after travelling through a 200 nm Aluminum filter to block the residual driving fields. The spectra plotted in Figure 6.1b are corrected by considering the transmission of the Al filter reported in Ref. [212]. As shown in Figure 6.1b, the spectra comprise both odd and even orders of harmonics with comparable intensity, consistent with previous studies [72,213]. By adjusting φ_{RB}, we can control the total HHG yield

with high precision, showing a modulation of the total yield with a periodicity corresponding to half optical cycle of the blue light field [72,213] (Figure 6.1b). This is a clear evidence that the harmonics are indeed generated by the two-color laser field. Notably, The HHG spectra show a strong continuum background, suggesting that the harmonic radiation is emitted in the form of an isolated pulse [90,92,205,214] – though quasi-continuum radiation can be emitted through adequate phase relationship between several pulses [215].

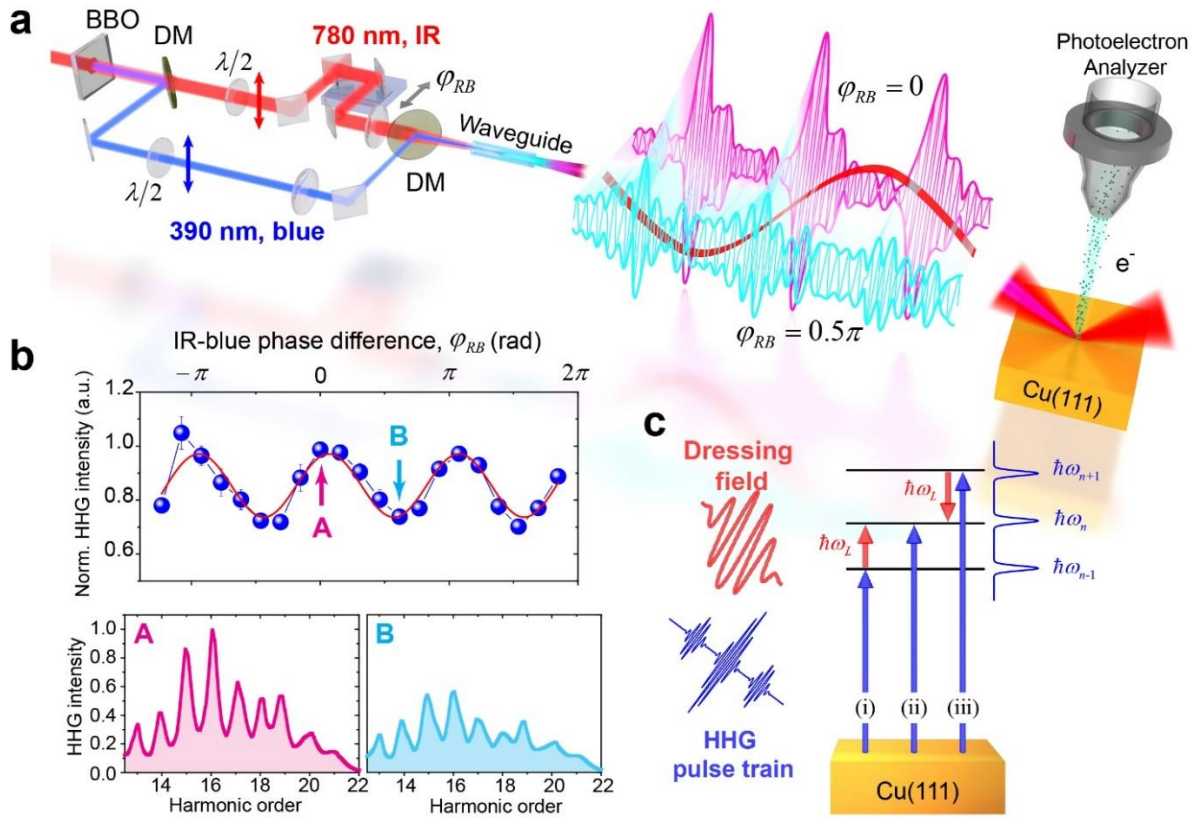

Figure 6.1: Characterizing the high-order harmonics using interferometric laser-assisted photoemission method. (a) Linearly polarized ω (780nm) and 2ω (390nm) beams from a Ti:Sapphire laser are focused into an Ar-filled hollow waveguide. The generated linearly polarized HHG and a time-delayed p-polarized 780nm dressing field are focused onto a clean Cu(111) surface. In experiments, the temporal structure of the attosecond bursts can be adjusted by the relative phase between the ω and 2ω driving fields, φ_{RB}. (b) Upper panel: modulation of the total HHG intensity as a function of φ_{RB}. Lower panel: The HHG spectra measured at the maximum (A) and the minimum (B) HHG intensities. The spectra were de-convoluted by considering the transmission rate of 200 nm Al filter [212]. (c) Illustration of the quantum path interference of the interferometric laser-assisted photoemission with HHG field generated by ω-2ω driving fields.

To fully reconstruct the temporal structure of the HHG pulse trains, I measure the spectral phases of the generated linearly-polarized HHG beam by attosecond metrology techniques. To achieve this, I focus the HHG beam onto a clean Cu(111) surface to induce photoemission. The photoelectrons are simultaneously modulated by a linearly-polarized IR field (780 nm, $\hbar\omega_L$=1.6 eV), which propagate collinearly with the HHG beam. The relative time delay between the HHG pulse and IR dressing pulse (τ_d) can be adjusted by a second delay stage in our experiments. Both the HHG and the dressing IR fields are adjusted to be p-polarized relative to the sample surface. Due to the existence of both even and odd harmonics, the photoelectron yield at the kinetic energy corresponding to the direct excitation by n^{th} order harmonics ($\hbar\omega_n$) is modulated due to the interference (Figure 6.1c) between three quantum paths: (i) absorbing an HHG and an IR photon ($\hbar\omega_{n-1}+\hbar\omega_L$); (ii) direct photoemission by a single HHG photon ($\hbar\omega_n$); and (iii) absorbing an HHG photon and emitting an IR photon ($\hbar\omega_{n-1}-\hbar\omega_L$). The photoelectron yields as a function of τ_d are recorded using a hemispherical photoelectron analyzer, which gives rise to the interferograms as shown in Figure 6.2a. This method was recently implemented to successfully reconstruct the circularly polarized HHG beam [30].

6.4 Numerical Simulation

In order to understand the HHG driven by the two-color (ω-2ω) laser fields, numerical macroscopic HHG simulations were performed using a combination of the strong field approximation with the electromagnetic field propagator [216], where the harmonics are assumed to propagate at the speed of light, and propagation effects in the driving fields such as the dispersion of neutrals and plasma, and group velocity mismatch [217] are taken into account. Note that the time-dependent ionization population (computed via the ADK rates [218]) is taken into

account, thus including the nonlinear phase shifts in the driving field, whereas the nonlinear spatial effects are not included. In the simulation, the driving pulses are modelled as a $\sin^2$ envelope with the FWHM pulse duration of τ_R = 25 fs and τ_B = 35 fs for fields with wavelengths λ_1=775 nm (ω) and λ_2=387.5 nm (2ω), respectively. The peak intensities are $1.17\text{x}10^{14}$ W/cm^2 for the λ_1 field and the intensity of the λ_2 field is half of that of the λ_1 field, which are selected to be similar to the experimental conditions.

6.5 Quasi-Isolated Attosecond Pulses

In Figure 6.2a, we plot the interferogram of photoelectrons excited by HHG beam at $\varphi_{RB} \approx 0$, which gives the highest HHG yield. The yields of the photoelectrons excited by different harmonic orders from the same *d* band of Cu(111) oscillate with a frequency of ω_L as a function of τ_d. The time delay associated with the photoemission process is negligible as shown in recent studies [30]. The information of the harmonic phases [$\phi(\omega_n)$] is encoded in the phases of the modulations in the interferogram [$\alpha(\omega_n)$], which is given by [30,111]

$$\tan[\alpha(\omega_n)] = \frac{\sqrt{I_0(\omega_{n+1})}\sin[\phi(\omega_n)-\phi(\omega_{n+1})]-\sqrt{I_0(\omega_{n-1})}\sin[\phi(\omega_{n-1})-\phi(\omega_n)]}{\sqrt{I_0(\omega_{n+1})}\cos[\phi(\omega_n)-\phi(\omega_{n+1})]-\sqrt{I_0(\omega_{n-1})}\cos[\phi(\omega_{n-1})-\phi(\omega_n)]}, \quad (6.1)$$

where $I_0(\omega_n)$ is the power spectrum. Using the genetic algorithm (details are described in Ref. [30]), I retrieve the harmonic phases that best fit the measured interferogram phases. The fitting results are plotted in the right panel of Figure 6.2a for $\varphi_{RB} \approx 0$. The measured HHG phases are plotted in Figure 6.2b for both $\varphi_{RB} \approx 0$ and $\varphi_{RB} \approx 0.5\pi$. It was found that the HHG phases as a function of harmonic orders gradually evolve from its originally linear shape to a more complicated "S" shape as φ_{RB} changes from 0 to 0.5π. This trend can be successfully captured by the numerical simulation considering the single-atom response as shown in the inset of Figure 6.2b.

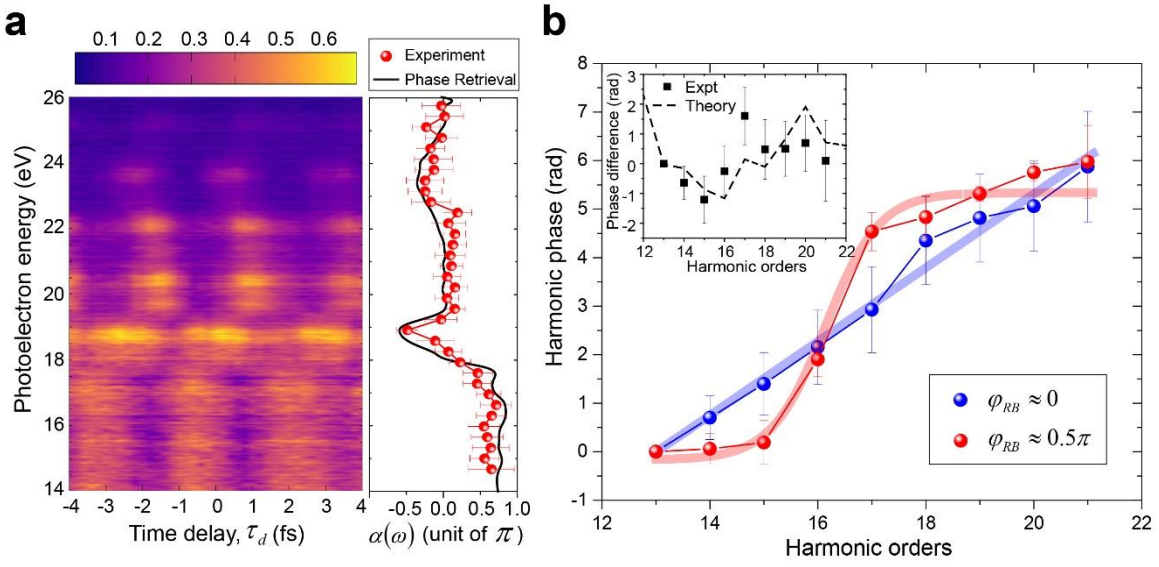

Figure 6.2: Measuring harmonic phases. (a) 2D map of photoelectron yields at $\varphi_{RB} \approx 0$ as a function of photoelectron energy and pump-probe time delay (τ_d). The experimentally measured interferogram phase $\alpha(\omega)$ as a function of photoelectron energy is plotted in the right panel, in comparison with the reconstructed phases obtained from phase retrieval program (black solid line). The good agreement between the two indicates that the correct harmonic phases are retrieved from the experimental results. (b) Phases of major harmonic orders measured at $\varphi_{RB} \approx 0$ and $\varphi_{RB} \approx 0.5\pi$. The uncertainty is determined as the standard deviation of phase values retrieved from multiple trials. For the convenience comparison, the harmonic phases for both cases are offset so that the phase of the13th harmonic is zero. The solid lines highlight the variation of the harmonic phases and serve the purpose of guiding the eyes. The difference of harmonic phases between $\varphi_{RB} \approx 0.5\pi$ and $\varphi_{RB} \approx 0$ is plotted in the inset. The phase difference obtained by the numerical simulation is also plotted for comparison (dashed line).

With HHG spectra and phases measured, the time-domain structure of the HHG pulse train can therefore be reconstructed. The temporal profile of HHG pulse train corresponding to $\varphi_{RB} \approx 0$ is plotted in Figure 6.3a. The profile is observed to be a *quasi-isolated* attosecond pulse with a peak width of ~ 450 as (FWHM), accompanied by two much weaker attosecond bursts separated by one optical cycle of the fundamental IR field. The peak width is very close to the transform-limited value (dashed line in Figure 6.3a), which is consistent with the linear dependence of HHG phases to the harmonic orders as shown in Figure 6.2b. When φ_{RB} is changed to 0.5π, we observe additional attosecond bursts in the temporal domain (Figure 6.3b). I note that the observation here

is distinctively different from several of previous time-domain studies of HHG driven by two-color laser fields, where the attosecond pulses were found to be generated twice per IR-light cycle [219,220]. In those experiments, the blue-field intensity was <0.5% of the IR and therefore only constitute a small perturbation onto the IR driving field [219,220].

Obviously, the generation of the quasi-isolated attosecond pulses driven by multicycle laser fields cannot be explained by the single-atom response during the HHG process. In order to understand the results, I resort to the theory by considering the macroscopic response through the time-gated phase matching [100,165,173,221] under the two-color configuration. In a hollow waveguide fiber, the phase mismatch for q^{th} order harmonics ($\Delta k_q^{\omega-2\omega}$) is given by considering the phase mismatches contributed by 1) waveguide dispersion, 2) free-electron plasma dispersion and 3) neutral atom dispersion. When including the second harmonic field (λ_2), the phase mismatch is:

$$\begin{aligned}\Delta k_q^{\omega-2\omega}(t) &\approx \Delta k_q^{waveguide} + \Delta k_q^{plasma} + \Delta k_q^{neutral} \\ &\approx \left\{ n_1 \frac{\lambda_1 u_{11}^2}{4\pi a^2} + 2n_2 \frac{\lambda_2 u_{11}^2}{4\pi a^2} \right\} + \left\{ n_1 P \frac{\lambda_1 e^2}{m_e c^2} \eta(t) + 2n_2 P \frac{\lambda_2 e^2}{m_e c^2} \eta(t) \right\} \\ &- \left\{ n_1 P \frac{4\pi^2 \chi_0}{\lambda_1} [1-\eta(t)] + 2n_2 P \frac{4\pi^2 \chi_0}{\lambda_2} [1-\eta(t)] \right\}\end{aligned} \quad , \tag{6.2}$$

where $\eta(t)$ is the time-dependent ionization rate, χ_0 is the linear susceptibility of the gas due to the neutrals and P is the gas pressure inside the waveguide. The harmonic generation process $n_1(n_2)$ photons were absorbed from the $\lambda_1(\lambda_2)$ field, so it gives $q=n_1+2n_2$. In Equation (6.2), I have calculated the waveguide dispersion term where a is the radius and $u_{11} = 2.405$ is the first zero of the Bessel function J_0 [100,165]. One can also define the coherence length as $L_{coh}^{\omega-2\omega,q}(t) = \pi / \Delta k_q^{\omega-2\omega}(t)$. The perfect phase matching occurs when the three terms in Equation (6.2) are compensated ($\Delta k_q^{\omega-2\omega}(t) = 0$), which happens at a critical ionization rate. This condition is

achieved during a finite temporal window in which the harmonic signal builds up constructively, giving rise to a selection of the number of attosecond pulses that are efficiently emitted.

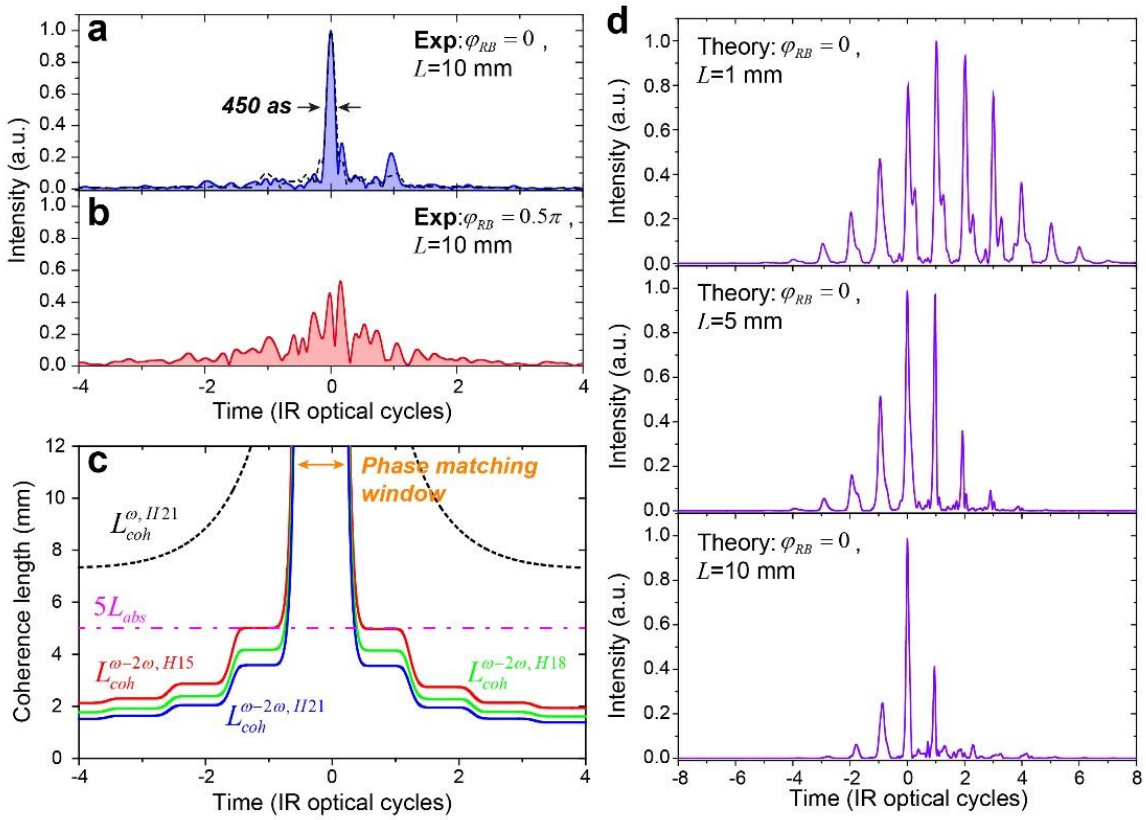

Figure 6.3: Quasi-isolated attosecond pulses generated through macroscopic phase matching. (a) The quasi-isolated attosecond pulses reconstructed using experimentally measured spectra and phases for $\varphi_{RB}\approx 0$. (b) same as (a) for $\varphi_{RB}\approx 0.5\pi$. (c) Time-dependent coherence length for a one-color (λ_1=775 nm, dashed line) and two-color (λ_1=775 nm, λ_2=387.5 nm, solid lines) HHG driven in a 30 torr Ar-filled waveguide. In the one-color case I present the coherence length of the 21st harmonic (33.6 eV, dashed black), whereas in the two-color case we have selected the 15th harmonic (24 eV, red solid, corresponding to n_1=n_2=5), the 18th harmonic (28.8 eV, green solid, n_1=n_2=6), and the 21st harmonic (33.6 eV, blue solid, n_1=n_2=7). The dot-dashed line represents $5L_{abs}$, where the absorption length is L_{abs} =1 mm for 33.6 eV harmonics [222]. (d) The attosecond pulse trains obtained from numerical simulation with two-color driving fields at φ_{RB}=0. The results are calculated by considering the 1D propagation in an Ar-filled waveguide with different interaction length (L= 1mm, 5mm and 10mm). It is clear that the number of attosecond bursts decreases as L increases, as a result of the reduction of phase matching window, consistent with the analytical representation in (c). When L=10mm, only three attosecond pulses are isolated for HHG emission, which is consistent with the experimental results shown in (b).

In Figure 6.3c, I compare the time-dependent coherence length for a one-color (λ_1=775 nm, dashed line) and two-color (λ_1=775 nm, λ_2=387.5 nm, solid lines) driving schemes in a 30 torr Ar-filled waveguide (a=75 μm). The peak intensity of the one-color driving field is 1.3x10^{14} W/cm^2. The peak intensities for the two-color configuration are the same as those used in the numerical simulation as previously described. As shown in Figure 6.3c, I plot the time-dependent coherence length of the 21st harmonic ($L_{coh}^{\omega, H21}$, dashed black) in the one-color configuration, whereas in the two-color case I have selected the 15th harmonic with n_1=n_2=5 ($L_{coh}^{\omega-2\omega, H15}$, solid red), the 18th harmonic with n_1=n_2=6 ($L_{coh}^{\omega-2\omega, H18}$, solid green) and the 21st harmonic with n_1=n_2=7 ($L_{coh}^{\omega-2\omega, H21}$, solid blue). Note that there are many different photon combinations, but for simplicity I have plotted those where n_1=n_2. The appearance of different absorption channels in phase-matching would be similar to that occurring in non-collinear [117,180] or vortex-combination [223] HHG schemes, but its analysis lies beyond the scope of this paper. The optimal phase-matching conditions are achieved if $L_{coh} > 5L_{abs}$ (pink dot-dashed line) where L_{abs} is the absorption length [163]. One can clearly observe that introducing the second-harmonic driver significantly reduces the phase-matching window from ~4 optical cycles of the fundamental IR field in the one-color configuration to less than one optical cycle in the two-color configuration, allowing for the generation of few attosecond bursts driven by multicycle laser fields. Numerical macroscopic HHG simulations by considering different propagation lengths (L) in the gas-filled waveguide are plotted in Figure 6.3d. Indeed, the harmonic emission is narrowed to few attosecond bursts as the medium length is increased to L=10 mm, in very good agreement with the analytical representation presented in Figure 6.3c and the experimental results.

6.6 Controlling the Sub-Cycle Temporal Structure of Attosecond Pulses

By varying the relative delay between two drivers φ_{RB}, I directly control the temporal structure of the emitted HHG pulse train. This is clearly shown by the variation of the pulse train structures (Figure 6.3a-b) and the HHG phases (Figure 6.2b) for different values of φ_{RB}. In Figure 6.4a, I plot the evolution of the FWHM duration of attosecond bursts as a function of φ_{RB}, while the results obtained from numerical simulation are plotted in Figure 6.4b. Because of the complicated pulse train structure in the time domain, especially when $\varphi_{RB} = 0.5\pi$, I calculate the duration of the attosecond bursts (σ) obtained in experiments and simulations in a statistical way by defining the mean square weighted deviation (MSWD) within one IR-light cycle (T_{IR}): $\sigma^2 = \frac{\int_0^{T_{IR}} w(t)(t-t_0)^2 \mathrm{d}t}{\int_0^{T_{IR}} w(t)\mathrm{d}t}$, where $w(t)$ is the pulse-train envelope intensity and $t_0 = \frac{\int_0^{T_{IR}} w(t)\times t\ \mathrm{d}t}{\int_0^{T_{IR}} w(t)\mathrm{d}t}$ is the center-of-mass (COM) of the attosecond pulse. For an ideal Gaussian pulse, σ is the RMS width. Figure 6.4a shows that the attosecond burst reaches its shortest duration ($\Delta t \approx 450$ as) when the HHG efficiency is highest at $\varphi_{RB} \approx 0$, while the peak width gradually increases when the spectral intensity approaches its minimum at $\varphi_{RB} \approx 0.5\pi$. This result can be consistently reproduced by the numerical simulation regardless of the macroscopic propagation distances (Figure 6.4b), indicating that it originates from the single-atom response to the two-color driving fields. To my best knowledge, this represents the first direct measurement of the correlation between the attosecond pulse duration and HHG efficiency.

To understand this dependence of the attosecond pulse duration on φ_{RB}, the semiclassical calculation of electron trajectories driven by two-color laser fields is performed. The calculation extracts the electron ionization and recombination times within the IR optical cycle (dotted lines in Figure 6.4d-e) and the corresponding field strength at the moment of ionization and

recombination for different φ_{RB} (Figure 6.4c). In the three-step model [64,210], an electron is tunnel-ionized in the first step as the electric field passes through its maximum value. In the quasi-static limit, the ionization rate is given by the ADK model [218], which is proportional to $\exp\left(-\frac{4\sqrt{2m_eE_a^3}}{3e\hbar|E_{ion}|}\right)$, where E_a=15.8 eV is the ionization potential of argon, E_{ion} is the field strength at the moment of ionization, and m_e and e are the mass and charge of an electron, respectively. The values of E_{ion} are directly obtained from the semiclassical calculations and can be controlled by adjusting φ_{RB}. Indeed, by comparing E_{ion} (red dashed line in Figure 6.4b) and the HHG yields obtained from our numerical simulations (red circles in Figure 6.4b), the comparison reveals a direct correlation between the HHG yield and the driving field strength at the moment of ionization. Therefore, within the three-step model of HHG, the efficiency of harmonic emission is dominantly controlled by the total ionization rate at the first step for the two-color driving configuration.

On the other hand, the ionization and recombination of electrons are affected by the symmetry of the two-color fields in the time domain. As shown in Figure 6.4c, when φ_{RB} = 0, the laser field exhibits a single maximum in each IR optical cycle (τ_1^{ion}). The field strength of the second maximum is much lower (~60% of the peak field strength) so that the corresponding electron ionization probability is negligible. As a result, the attosecond EUV burst is only emitted in the corresponding narrow recombination window around τ_1^{emit} as shown by the time-frequency analysis [224] of our simulation results in Figure 6.4d, resulting in the short pulse duration in this situation. In contrast, when φ_{RB} = 0.5π, there exist two maxima with comparable field strength within each IR optical cycle (τ_2^{ion} and τ_3^{ion}) as shown in Figure 6.4c. Both maxima in this situation can induce ionization and the subsequent recombination events (τ_2^{emit} and τ_3^{emit}), which give rise

to HHG emission shown in Figure 6.4e, resulting in the additional attosecond EUV bursts in the time domain (Figure 6.3b).

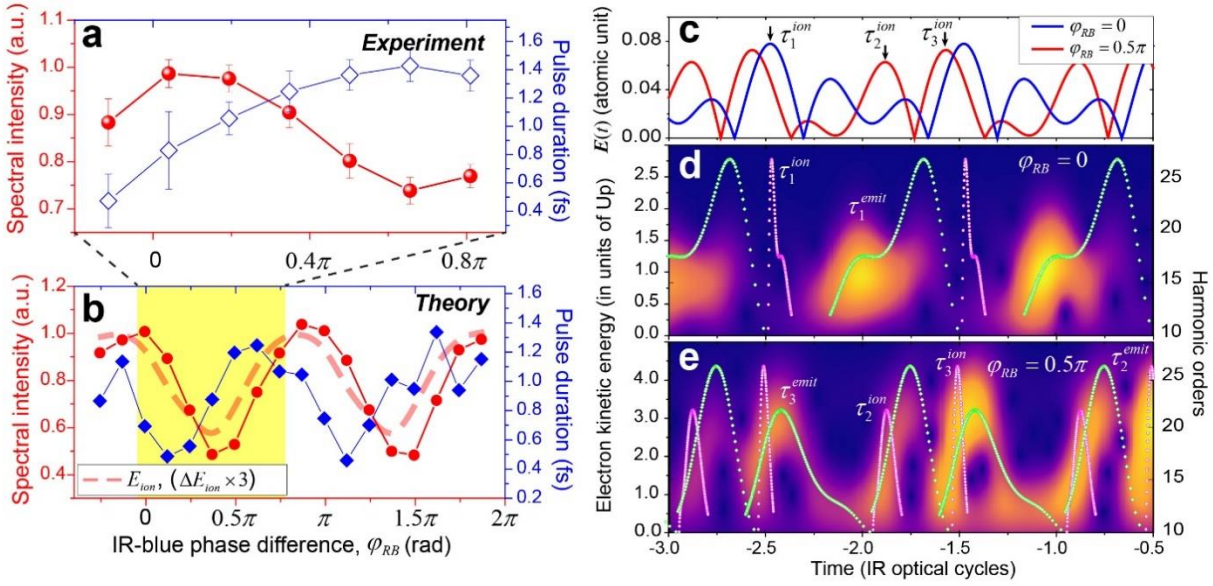

Figure 6.4: Coherent control of attosecond pulses by two-color driving fields. (a) Experimentally measured HHG intensity and FWHM peak-width of the attosecond bursts as a function of φ_{RB}. (b) Same as (a) obtained from the numerical simulation. The yellow-colored section highlights the range of φ_{RB} probed in the experiments as shown in (a). The normalized field strength at the moment of ionization E_{ion} is plotted for comparison (red dashed line). The values E_{ion} are normalized to the maximum value, while the amplitude of the values (ΔE_{ion}) is multiplied by 3 for the convenience of plotting. (c) The time-dependent electric field of the two-color driving field at φ_{RB}=0 and φ_{RB}=0.5π. (d) The time-frequency analysis for the pulse train generated at φ_{RB}=0 obtained from the numerical simulation. The electron ionization (magenta open circles) and recombination times (green open diamonds) are plotted and overlaid on the figure. Clearly, at φ_{RB}=0 electrons recombine and harmonics efficiently generate only in a single time window (τ_1^{emit}) within every IR optical cycle, corresponding to a single ionization time τ_1^{ion} (also see (c)). (e) Same as the (d) for φ_{RB}=0.5π. Different from the situation when φ_{RB}=0, the two-color fields drive electrons to recombine and emit HHG photons in two time windows (τ_2^{emit} and τ_3^{emit}) every IR optical cycle, which corresponds to ionization times τ_2^{ion} and τ_3^{ion}, respectively. This additional ionization and recombination time window leads to additional attosecond temporal structure in the HHG pulse trains driven by two-color laser field as shown in Figure 6.3b.

6.7 Conclusion

In summary, I experimentally investigated the HHG pulse train generated by two-color linearly polarized laser fields. By measuring the HHG phases with interferometric laser-assisted photoelectron spectroscopy, I demonstrated that the temporal structure of the attosecond pulse trains can be coherently controlled in the two-color scheme by adjusting the symmetry of the combined field. It was also found that the phase-matching window for efficient harmonic emission can be significantly reduced when the two-color driving field was used, allowing generation of the quasi-isolated attosecond pulses from the multicycle driving fields. I expect the ability to generate and coherently control short attosecond pulses, as I have demonstrated in the experiments, can make the two-color driven HHG a powerful tool for various attosecond studies.

Chapter 7

Direct Time-Domain Measurement of Attosecond Final-State Lifetimes in Photoemission from Solids

This chapter is adapted, with permission, from:

Z. Tao†, C. Chen†, T. Szilvási, M. Keller, M. Mavrikakis, H. Kapteyn, and M. Murnane, Direct Time-Domain Observation of Attosecond Final-State Lifetimes in Photoemission from Solids. *Scienc*e **353**, 62 (2016) (†These authors contributed equally to this work).

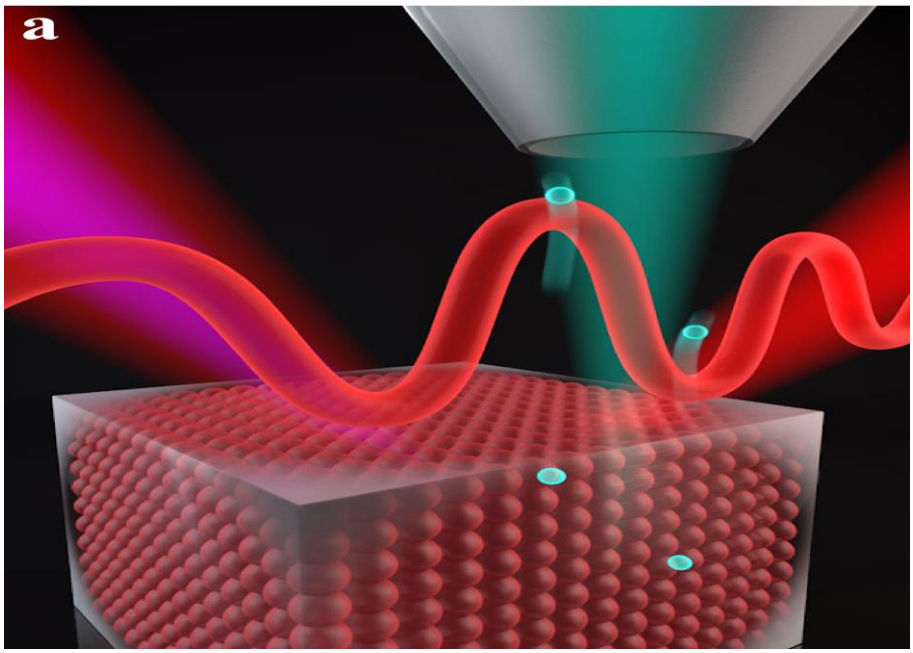

Figure 7.1: Illustration of photoelectron lifetime measurement. (a) High harmonics of a femtosecond laser kick electrons out of a nickel crystal, and the electrons then travel towards the surface. The interaction of the electrons with an infrared laser probe allows us to determine how long electrons linger in excited states before they escape the crystal. Art by Steve Burrows, JILA.

7.1 Abstract

The photoelectric effect represents a fundamental light-matter interaction that has been harnessed to map the band structure of materials with stunning detail. Recently, attosecond spectroscopies have made it possible to measure differences in transport times for photoelectrons from localized core levels and delocalized valence bands. In this work, we use attosecond pulse trains to directly and unambiguously measure the difference in lifetimes for photoelectrons that are born into free-electron-like states compared with those that are excited into unoccupied excited states in the band structure of a material (Ni(111)). A significant increase in lifetime of 212±30 as occurs when the final state coincides with a short-lived excited state. Moreover, a strong dependence of this lifetime on emission angle is directly related to the final-state band dispersion as a function of electron transverse momentum. This finding emphasizes the importance of the material band structure on photoemission response times and corresponding electron escape depths, and represents the shortest lifetime of any state measured to date.

7.2 Introduction

7.2.1 Combing Angle-resolved Photoemission with Tabletop High Harmonic Light

The electronic band structure of materials consists of occupied and unoccupied bands that emerge as the electron wave functions of adjacent atoms in the lattice overlap with each other. In general, valence bands will have more wave function overlap and will therefore be wider than, for example, the core levels. The periodicity of a crystal lattice imposes an energy momentum relation that is described as the dispersion relationship for electrons in each band, making the electronic structure of solids quite complex. Fortunately, angle-resolved photoemission spectroscopy (ARPES) can resolve both the energy and momentum of photoelectrons by probing photoemission

from materials at well-defined angles. This information is directly related to the energy and momentum of electrons in various bands in the material, providing powerful and detailed information about band dispersion and the Fermi surface [148]. Indeed, ARPES is one of the most versatile and powerful tools for studying the electronic structure of materials**.** When combined with ultrafast lasers, time-resolved ARPES makes it possible to capture fast changes in the band structure of materials near the center of the Brillouin zone on picosecond (ps) and femtosecond (fs) time scales [225]. More recently, advances in tabletop high-harmonic generation (HHG) [88,207] have resulted in coherent extreme ultraviolet (EUV) and soft X-ray beams that are ideally suited for ARPES, opening up time-resolved studies over the entire Brillouin zone [171,208]. HHG is emitted as a series of attosecond pulse trains with unique characteristics of good energy resolution (≈100-300 meV), combined with sub-fs time resolution. These new capabilities have made it possible to observe and control the fastest electron dynamics in molecular and material systems [226,227]. Recent work probed how fast a material can change its magnetic or insulating-to-metallic states [208,228], uncovering which microscopic mechanisms were responsible for driving fast phase or state transitions in materials. Other work probed the ≈ 7 fs lifetime of core-excited states of adsorbates on surfaces [112].

7.2.2 Direct Time-domain Measurement of Photoelectron Lifetime

The time delay associated with the photoemission process itself has been probed in isolated atoms and solid-state materials using HHG [42,44,54,56,104,142,229], by taking advantage of laser-assisted photoemission [55]. Although there still exists some discrepancy between experiment and theory [42,136], it is generally agreed that the photoemission time delay from isolated atoms consists of a Wigner time delay due to scattering of photoelectrons in the atomic

potential, convolved with a measurement-induced delay due to propagation of the photoelectrons in the laser field [230]. Compared to the case of isolated atoms, interpreting photoemission time delays from solids is more complicated, because of the complex band structure of materials and various many-body interactions that photoelectrons can experience as they approach the surface. Previous attosecond-streaking studies of a transition-metal W(110) surface revealed a considerable time delay (~110 as) between photoemission from core-level and valence-band states [44]. In contrast, no delay was measured for the free-electron metal Mg, although a similar time delay to W was expected [142]. Various theoretical models have been proposed to explain the photoemission time delay from solids in terms of transport time [138,140], degrees of initial-state localization [138,141], and band-structure effects [143,231], highlighting the complex physics that is not yet well understood. Moreover, the use of isolated attosecond pulses in these experiments is necessarily accompanied by a broad EUV bandwidth, that then gives rise to an integrated broad-band photoemission feature comprised of multiple valence bands of a material [44,56,142]. Other recent work used synchrotron sources to measure the final-state linewidths of photoemission from Cu, and found pronounced variations in the ARPES spectra with small changes in photon energy that could not be assigned to a free-electron final state. This work identified the direct transitions and measured very broad linewidths of >3 eV for final states in the 20 to 150 eV photon energy range [144].

In this work, we directly and unambiguously measure the influence of the band structure of a material on the lifetime of photoelectrons. To accomplish this, we use attosecond pulse trains of well-defined harmonics to measure the photoemission time delays for both free-electron final states as well as final states corresponding to the unoccupied bulk bands of the transition metal Ni(111). We distinguish photoelectron lifetimes from individual valence bands and final states in

Ni(111), with additional help from selection rules for photoemission for EUV fields with different polarizations [148,157]. Our results show that photoelectrons experience an abrupt increase in lifetime by ≈ 212 ± 30 attoseconds when the final-state corresponds to an unoccupied excited state in the Ni band structure. This increase in lifetime can be interpreted physically as a variation of the attenuation length of the final-state wavefunction inside the crystal. Therefore, through a direct time-domain measurement of attosecond photoelectron dynamics, our results provide new insights into the fundamental concepts of photoelectron lifetime, inelastic mean free path and also group velocity. Moreover, we observe large angle- (momentum-) dependent variations in photoemission time delay, which are directly related to the final-state band dispersion. This new capability to probe band-structure effects on photoemission significantly enhances the use of HHG for experimentally accessing quasiparticle lifetimes, electron mean free paths, electron-electron scattering and dynamical screening, all of which represent grand challenges for condensed matter theory.

7.3 Ni(111) Surface Preparation

The Ni(111) single crystal films are prepared by sputtering 200 nm of nickel onto α-Al_2O_3(0001) substrates as described in reference [232]. The sample cleaning is performed in the same UHV chamber for photoemission measurements, with the base pressure $<5\times10^{-10}$ torr. The atomically clean Ni(111) surface is obtained using repeated cycles of Argon ion sputtering (0.5 keV, incidence angle of 60^o) at room temperature (300K) in UHV chamber, followed by annealing to 900 K for 15 minutes. The sample is grounded during all static and dynamic measurements.

7.4 Experimental Setup for Attosecond Photoelectron Lifetime Measurement

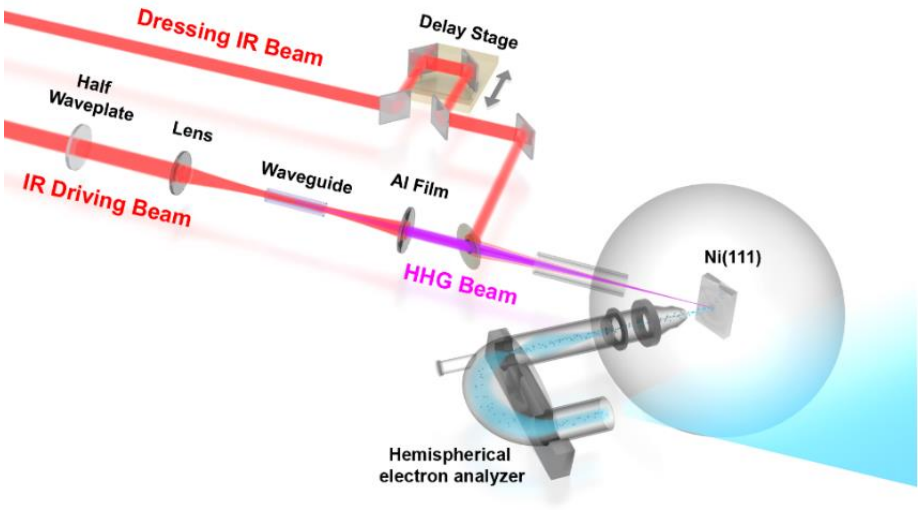

Figure 7.2: Experimental Setup of photoelectron lifetime measurement.

Figure 7.2 illustrates the setup of our experiments. We used a multi-pass Ti:sapphire laser system to generate 26 fs pulses in the near infrared (IR) at a wavelength of ~780 nm ($\hbar\omega_L \approx 1.60$ eV), with pulse energy of 2.4 mJ, and at a repetition rate of 4 kHz. Most of the laser energy (95%) is used for high-harmonic generation, while a small portion (5%, linear polarization) is used to probe (dress) the photoelectrons generated by the attosecond EUV pulse trains. To drive high-order harmonic generation, 95% of the IR beam is focused using a 50 cm focal length lens into a 1-cm-long capillary waveguide, which has an inner diameter of 150 μm. Different gas targets (Xe, Kr, Ar, Ne) are used in order to cover a broad range of harmonic orders or photon energies (11th – 41st spanning from 17 to 66 eV). The corresponding EUV pulse train is comprised of ~200 as [full width at half maximum (FWHM)] bursts with a ~15 fs (FWHM) envelope [32] in the time domain. The EUV light inherits the polarization of the driving laser, which is manipulated by a λ/2 wave plate. The control over EUV photon energy and polarization allows us to selectively

excite photoelectrons from different initial states into different final states (free-electron-like or unoccupied bulk band) and study their individual lifetime (Figure 7.3a). The comb of linearly polarized high-order harmonics are then focused onto an atomically clean Ni(111) surface using a toroidal mirror (coated with B4C or gold depending on HHG orders used) at grazing incidence, to a spot size of ~100 μm FWHM. Any residual laser light is blocked by a 200 nm thick Al filter.

To measure the photoelectron lifetime, the linearly polarized IR probe is recombined collinearly with the high-order harmonics onto an atomically Ni(111) surface using an annular silver mirror (Figure 7.2 and Figure 7.3a). In the presence of both two fields, there are two distinct quantum paths exciting the electrons from an initial state to the same final photoelectron energy (sideband), namely (i) absorption $\hbar\omega_{2n-1} + \hbar\omega_L$ and (ii) emission $\hbar\omega_{2n+1} - \hbar\omega_L$ of an IR photon, as shown in Figure 7.3b. The attosecond beating due to the interference between two quantum pathways modulates the photoelectron spectra as a function of relative delay between the EUV pump and IR probe fields (τ_d). This allows us to extract photoelectron dynamics on attosecond time scales and Å length scales (in a technique called RABBITT) [32,104]. RABBITT and attosecond streaking have been shown to yield the same temporal information about the photoemission process [136,230]. In the experiment, the relative time delay between the HHG pump and IR probe is controlled using an interferometrically-stabilized stepper-motor delay stage (with sub-fs resolution). The FWHM of the IR beam on the sample is ~250 μm, which is larger than the HHG beam to ensure efficient dressing of the photoelectrons. The intensity of the probe IR light is adjusted to be ~3.75 μJ/pulse (peak intensity ~3×10^{11}W/cm^2) using a half wave plate and a linear polarizer. The low intensity of the IR dressing light ensures that the contributions from higher-order sidebands (>1st order) are negligible. The IR probe is fixed to be p-polarized, i.e., perpendicular to the sample surface for all measurements.

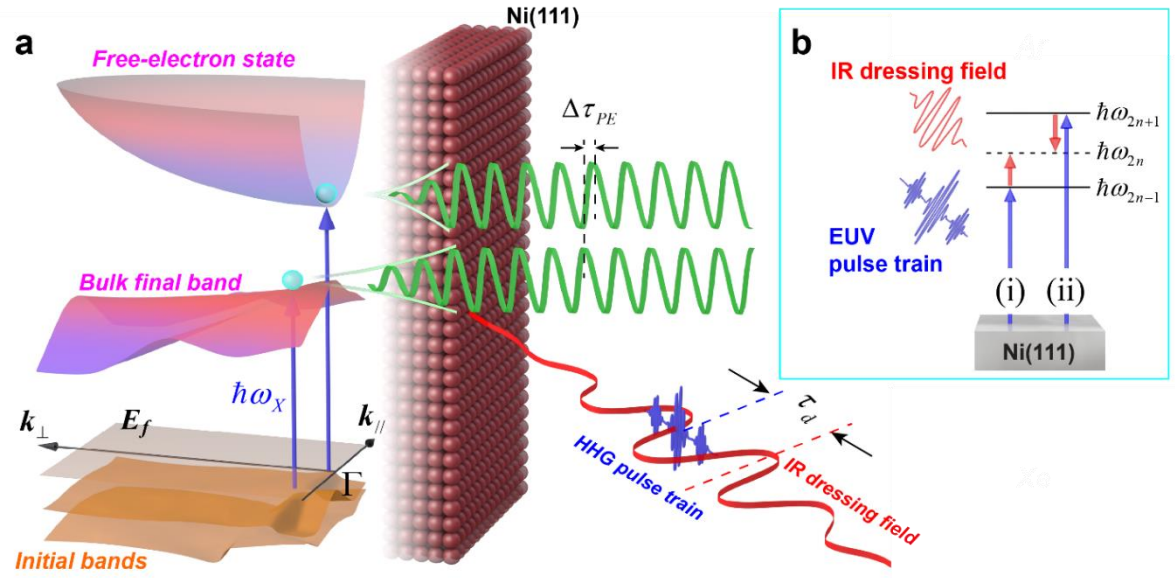

Figure 7.3: Photoemission time delay on and off resonance in the band structure. (a) Using high-order harmonics, different photoelectron final states can be accessed, corresponding to free-electron-like states or excited states in the band structure. The damping length of the final-state wavefunction inside the crystal is significantly increased when the transition coincides with a final-state resonance. (b) Schematic of quantum path interferences from a single initial state using a combined EUV and infrared laser fields.

7.5 Band Structure of Ni(111) along Γ-L Direction

We first probe the electronic band structure of Ni(111) along Γ-L direction by studying the dependence of the static photoelectron spectra on the EUV photon energy and polarization. Under the excitation of EUV harmonic light, photoelectrons with sufficiently large momentum along the surface-normal direction escape the surface and are detected by a hemispherical electron analyzer. In the angle-resolved photoelectron spectrum, the same initial Bloch wavepacket is excited to multiple final states with different kinetic energies by multiple harmonic orders, manifesting itself as a ladder of direct photoemission bands, each separated by twice the fundamental photon energy ($\hbar\omega_L$), as shown in Figure 7.4 (a-b), which are excited by s- and p-polarized EUV harmonics, respectively.

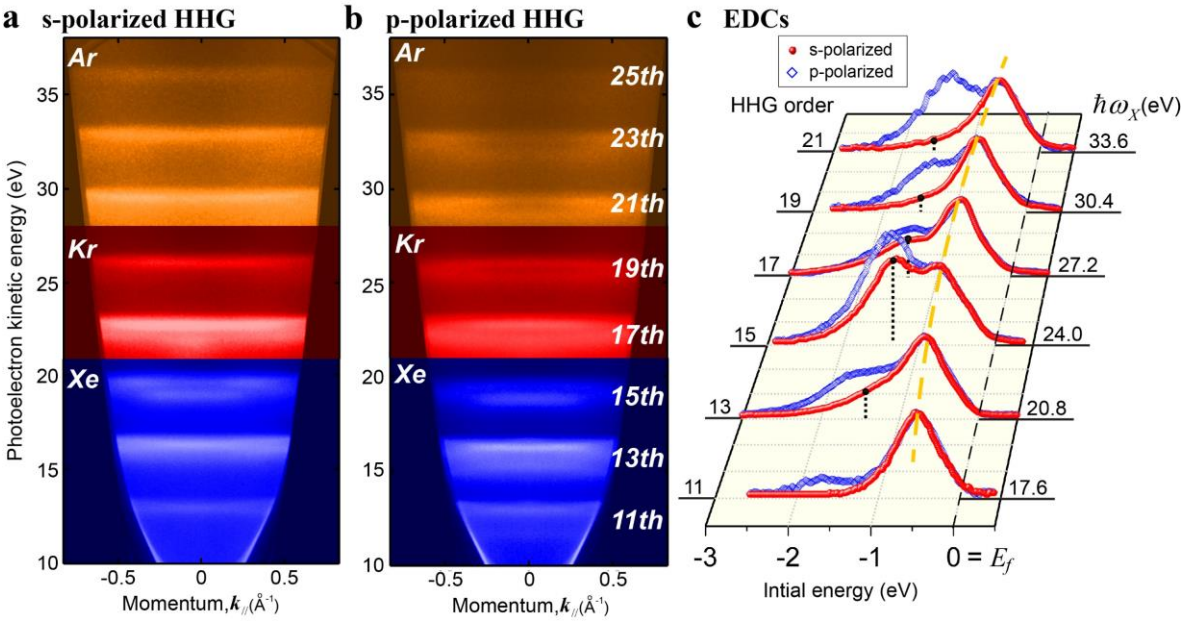

Figure 7.4: Static ARPES spectra of Ni(111) excited by multiple orders of HHG with (a) s- and (b) p- polarization. The energy resolution is ~0.3 eV, which is sufficient to distinguish photoemissions from different initial bands (Λ_3^{α} , Λ_3^{β} and Λ_1 bands). (c) EDC curves excited by s- (red) and p-polarized (blue) HHG in a normal emission geometry (integrated ~±2^o around the Γ point). The position of the Fermi level (black dashed line) is determined from the laser photon energy (~1.6 eV) and analyzer work function (4.25 eV). The orange dashed line shows the shift of the high-energy peak with HHG photon energy, underlining the contribution of bulk-band transitions. The intensity of the Λ_3^{β} band clearly shows a spectral resonance at ~24 eV.

To extract the band dispersion along the Γ- L direction, We first obtain the photoelectron energy distribution curves (EDCs) by integrating the angle-resolved spectra over an angle of ±2^o around the $\bar{\Gamma}$ point and deduct the secondary electron backgroud using the Shirley background subtraction [233], as shown in Figure 7.4c. The energy of Fermi level is determined with the knowledge of the photon energies and the analyzer work function. By utilizing the high energy resolution of attosecnd pulse trains and the photoemission selection rule under polarized (s- and p-) HHG radiation [148,157], we can unambiguously indentify the peaks corresponding to different intial states. According to the DFT band-structure calculation for Ni(111) single crystal, there are three bands along Γ-L contributing to the photoemission spectra: two valence bands with

Λ_3 symmetry (Λ_3^α with lower binding energy of ~0.6 eV and Λ_3^β with higher binding energy of ~1.25 eV) and one deeper valence band with Λ_1 symmetry (~1.7 eV). Since Λ_1 band can only be excited with light field polarized perpendicular to the sample surface, we can assign the two spectral peaks in the EDCs excited by s-polarized HHG light as photoelectrons from Λ_3^α and Λ_3^β bands. We then use double Voight function to fit the EDCs and extract their spectra intensity and binding energy, as shown in Figure 7.5(a-b). The Gaussian linewidths of the Voight function are fixed to the typical experimental resolution of 0.3 eV.

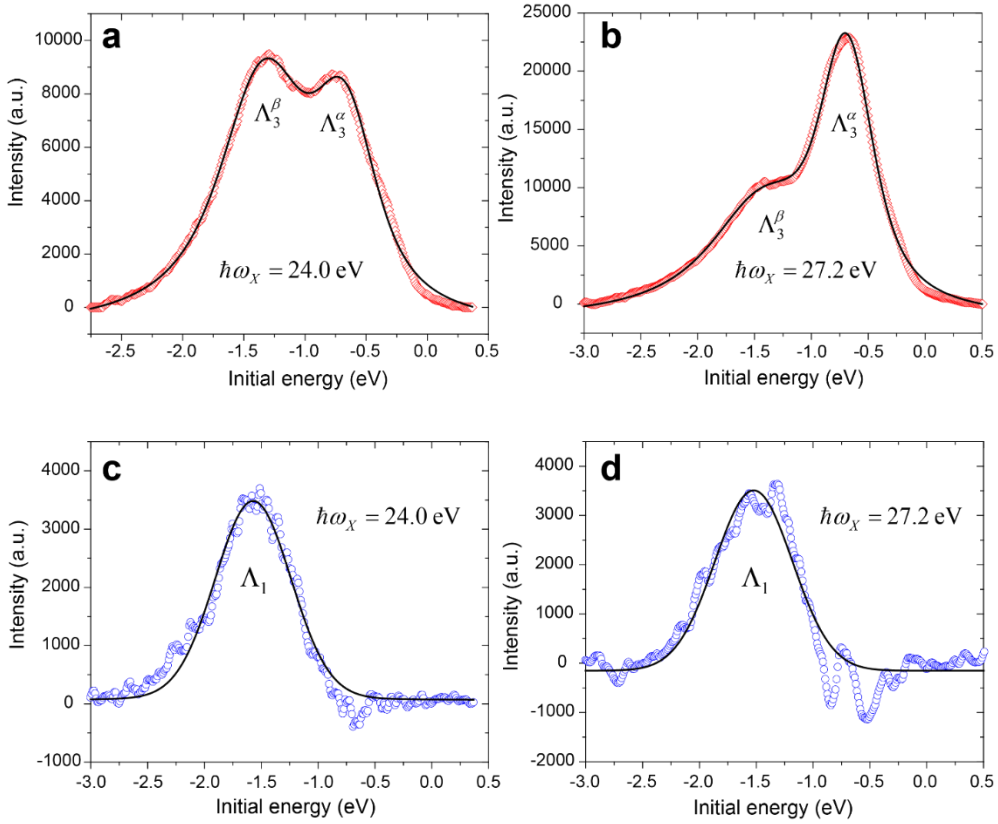

Figure 7.5: Static spectral analysis of Ni(111) exicted by HHG. (a) and (b) Experimentally measured EDCs excited by s-polarized HHG field (red open diamonds). The intensity and binding energies of Λ_3^α and Λ_3^β bands are extracted by fitting the EDCs with double Voigt functions (solid black lines). (c) and (d) The spectral intensity of Λ_1 is extracted by taking the difference spectra between EDCs excited by s- and p-polarized HHG fields (blue open circles). The intensity and binding energies are determined by fitting the EDCs with a single Voigt function (solid black lines).

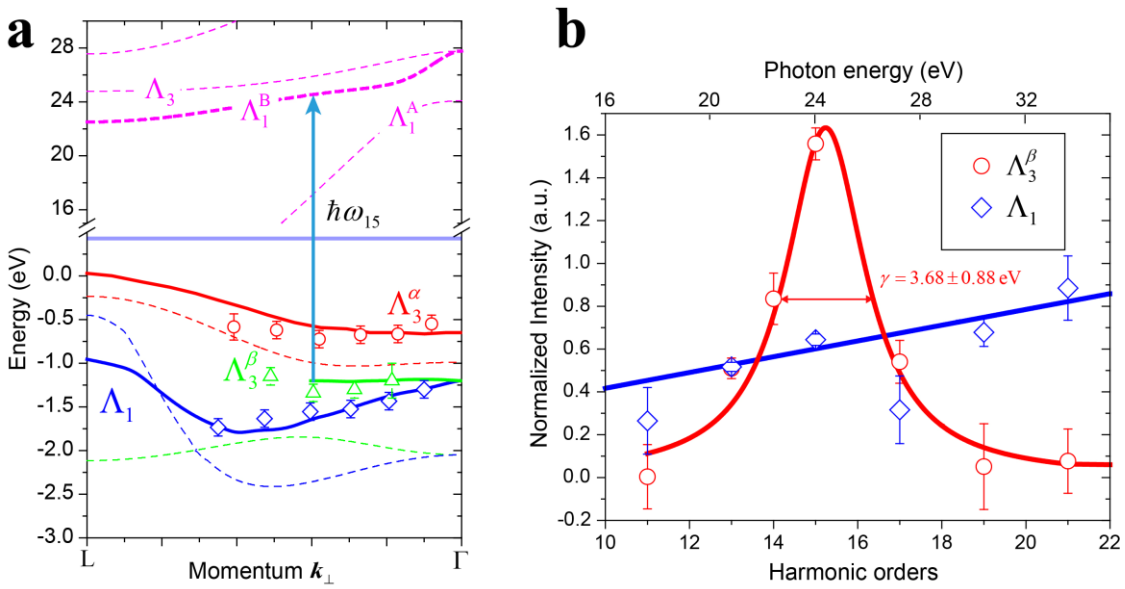

Figure 7.6: Band Mapping of Ni(111). (a) Band structure of Ni(111) along Γ-L (normal to surface). The band structure extracted from our data (open symbols) is compared to previous experiments (solid lines) and DFT calculations (dashed lines). A free-electron final-state in a constant inner potential is assumed and used to map the electron momentum normal to the sample surface $\boldsymbol{k}_\perp$. The final state resonance is highlighted as direct transition from the Λ_3^β initial band to the Λ_1^B final band. (b) Photoemission intensities of Λ_3^β and Λ_1 bands relative to that of Λ_3^α band. The red solid line represents the Lorentzian lineshape fitting to the intensity of Λ_3^β band as a function of photon energy, yielding a linewidth of $\gamma = 3.68$ eV. The blue solid line is a linear fit to the intensity of Λ_1 band.

To obtain the information about the Λ_1 band, the EDCs excited by the same harmonic orders but with different polarizations (s- and p-) are normilized to equalize the intensity of the Λ_3^α band. The additional spectral weight in photoelectron spectra excited by p-polarized HHG is assigned as photoemission from Λ_1 band. We obtain its spectra intensity and binding energy by fitting it with a single Voight function, are shown in Figure 7.5(c-d).

We note that both s- and p-polarized photoemission exhibit peak shifts when excited by different photon energies, which is clear evidence of contributions from bulk-band transitions.

Assuming direct transitions to a free-electron-like final state, we can map the electron momentum in the surface-normal direction $\boldsymbol{k}_{\perp}$ for different photon energies [148,196,234]. The extracted band structure is plotted in Figure 7.6a. The good agreement between our photoelectron spectra with previous studies using synchrotron light covering a similar energy range [234] (see Figure 7.6a) underlines that high harmonics are ideal for capturing electron and band structure dynamics with very high time resolution, good energy resolution, easy manipulation of the photon energy and polarization [30], and perfect synchronization to the driving laser. Note that the calculated valence bands using density functional theory (DFT) are ~0.7 eV deeper than experiment, due to strong correlations present for Ni 3*d* electrons [234–236].

7.6 Spectral-Domain Measurement of Final-State Lifetime in Ni(111)

The most pronounced feature of Figure 7.4 and 5.5 is the enhancement in the intensity of the low-energy spectral peak (~-1.25 eV) when excited by ~24 eV HHG photons (15th order). This resonant feature is clearly shown in the spectra excited by an s-polarized EUV field, indicating that the Λ_3^{β} band is the initial band. Considering the band structure of Ni(111) along Γ-L, we can assign this spectral resonance to direct interband transitions from the Λ_3^{β} initial band to the high-energy Λ_1^{B} final band located at ~24 eV above the Fermi level, as indicated by the blue arrow in Figure 7.6a.

In photoemission theory, the matrix element responsible for photoelectron spectra can be written as $M_{fi} = \langle f | H^{\mathrm{int}} | i \rangle$, where $|i\rangle$ is the initial state, $|f\rangle$ is the final state and $H^{\mathrm{int}} = \boldsymbol{A}_X \cdot \boldsymbol{p} + \boldsymbol{p} \cdot \boldsymbol{A}_X$ represents the interaction Hamiltonian between an electron and EUV electromagnetic radiation with the vector potential $\boldsymbol{A}_X$. The final-state wavefunction can be

represented as a time-reversed low-energy electron diffraction (LEED) state, composed of a free-electron wave arriving at the detector and a damped Bloch wave inside the crystal [148,237], with a characteristic damping length directly related to the inelastic mean free path and photoelectron lifetime. The increase in photoemission intensity as a result of this final-state resonance can be attributed to an increase in lifetime, with associated elongation of the characteristic damping length of the final-state wavefunction, which strongly enhances the spatial overlap between the initial and final-state wave functions - and hence the transition probability.

To determine the coupling of the intial bands to the unoccupied final bands and also the linewidth of the final bands, we need to examine the dependence of indivual band-specific spectral weight on photon energy. To take into account the intensity modulation of the HHG light, we normalize the intensity of the Λ_3^β and Λ_1 bands to the intensity of Λ_3^α band. The relative intensities as a funtion of harmonic orders and photon energies are plotted in Figure 7.6b. The resonant transition from the Λ_3^β band to the unoccupied bulk band Λ_1^B corresponds to an intensity peak around 15th order harmonic. Lorentzian function fit gives the width γ=3.68 ± 0.88 eV centered at 24.40 eV, which is consistent with previous studies [144]. Thus, the characteristic lifetime can be extracted from $\tau_{\text{spec}} = \hbar/\gamma = 179 \pm 43$ as. In contrast, intensity of Λ_1 band varies smoothly across the photon energy range used in our experiments.

7.7 Direct Time-domain Measurement of Final-State Lifetime in Ni(111)

To directly measure the photoelectron lifetime in the time domain, we use the RABBITT method (see Figure 7.3b and section 7.4: experimental step) and measure the photoemission time delay between valence bands of Ni(111) excited to bulk final bands or to free electron final states located in the band-gap region [148,237] (Figure 7.3a). When the relative time delay τ_d between

the HHG pump and the IR probe is changed, the intensity of side bands from a given initial band is modulated as a result of quantum-path interferences [32,104],

$$S_{2n}(\tau_d) = A_0 \sin[2\omega_L(\tau_d - \tau_X - \tau_{PE})], \quad (7.1)$$

where A_0 is the intensity of modulation, $\tau_X = \frac{\phi_{2n+1} - \phi_{2n-1}}{2\omega_L}$ represents a time delay contributed by the phase chirp between neighboring harmonics ($\phi_{2n+1} - \phi_{2n-1}$) and τ_{PE} is the photoemission delay. Simultaneous measurement of two photoelectron wavepackets excited by the same harmonic orders allows us to cancel the influence of attochirp (τ_X). This method was first implemented and validated for isolated atoms [104]. In our experiments, we use the non-resonant photoemission from Λ_3^α band as the timing reference, and determine the relative photoemission delay between the resonant $\tau_{PE}(\Lambda_3^\beta) - \tau_{PE}(\Lambda_3^\alpha)$ and non-resonant $\tau_{PE}(\Lambda_1) - \tau_{PE}(\Lambda_3^\alpha)$. This allows us to compare time delays for comparable photoelectron energies, and cancel effects due to the attochirp or field-induced phase delays.

7.7.1 Time-Resolved Data Collection

To improve the signal-to-noise ratio and minimize the experimental systematic error, the same pump-probe delay sequence from -3 fs to 3 fs in 0.2 fs step is repeated more than 200 times with increasing and decreasing delays alternating between consecutive scans. Each individual photoelectron spectrum in time-resolved measurements is integrated for 4~6 seconds to get sufficient photoelectron counts. To minimize the space charge effects, the overall photoelectron counts are adjusted well below the point where further reduction in HHG light intensity does not shift the spectra. The repetitive scans are analyzed individually and then averaged to obtain the

results of photoemission delays. The error bars are determined by considering the variation of measured time delays in individual scans.

We check the data quality by examining several factors: 1) We confirm that the peak positions in each spectrum corresponding to different initial bands are not altered because of space charge effects, above threshold ionization (ATI) by IR field or the shift in high harmonic photon energies. 2) Each sideband region of interest in every used scan shows a dominant $2\omega_L$ (ω_L is the fundamental laser frequency) oscillation in Fourier analysis. The interferograms shown in Figure 7.7(b-d) and Figure 7.8c are obtained by summing the interferograms of individual scans satisfying the two criteria above.

7.7.2 Photoemission Time Delay between Λ_3^β and Λ_3^α Bands

By utilizing the photoemission selection rules and using s-polarized HHG field in time-resolved measurements [148,157], we can selectively excite Λ_3^β and Λ_3^α bands and unambiguously determine their photoemission time delay [$\tau_{PE}\left(\Lambda_3^\beta\right) - \tau_{PE}\left(\Lambda_3^\alpha\right)$]. To cover as large energy ranges as possible, different noble gases (Xe, Kr, Ar, Ne) are used for high-harmonic generation (Figure 7.7a). The interferograms for τ_d in range of -2 to 2 fs obtained using Xe, Kr and Ar gas targets are plotted in Figure 7.7(b-d). The interferograms were obtained by integrating the photoelectron spectra over ±2.5° around the Γ point and subtracting the background spectrum obtained well before time-zero. We intentionally selected a small angular region to avoid the ambiguities resulting from angle-dependent photoemission time delay (see section 7.8). The side bands around the spectral resonance (SB 14, 16 and 18) can be covered by various gases. The extracted photoemission time delays are consistent between different gases, underlining the robustness of our results. This result indicates that the observed time delay origins from the

material properties and the atto-chirp contributed by HHG process is cancelled out using our method. In the error analysis of experimental data, the deviation of results from different gases are also taken into consideration.

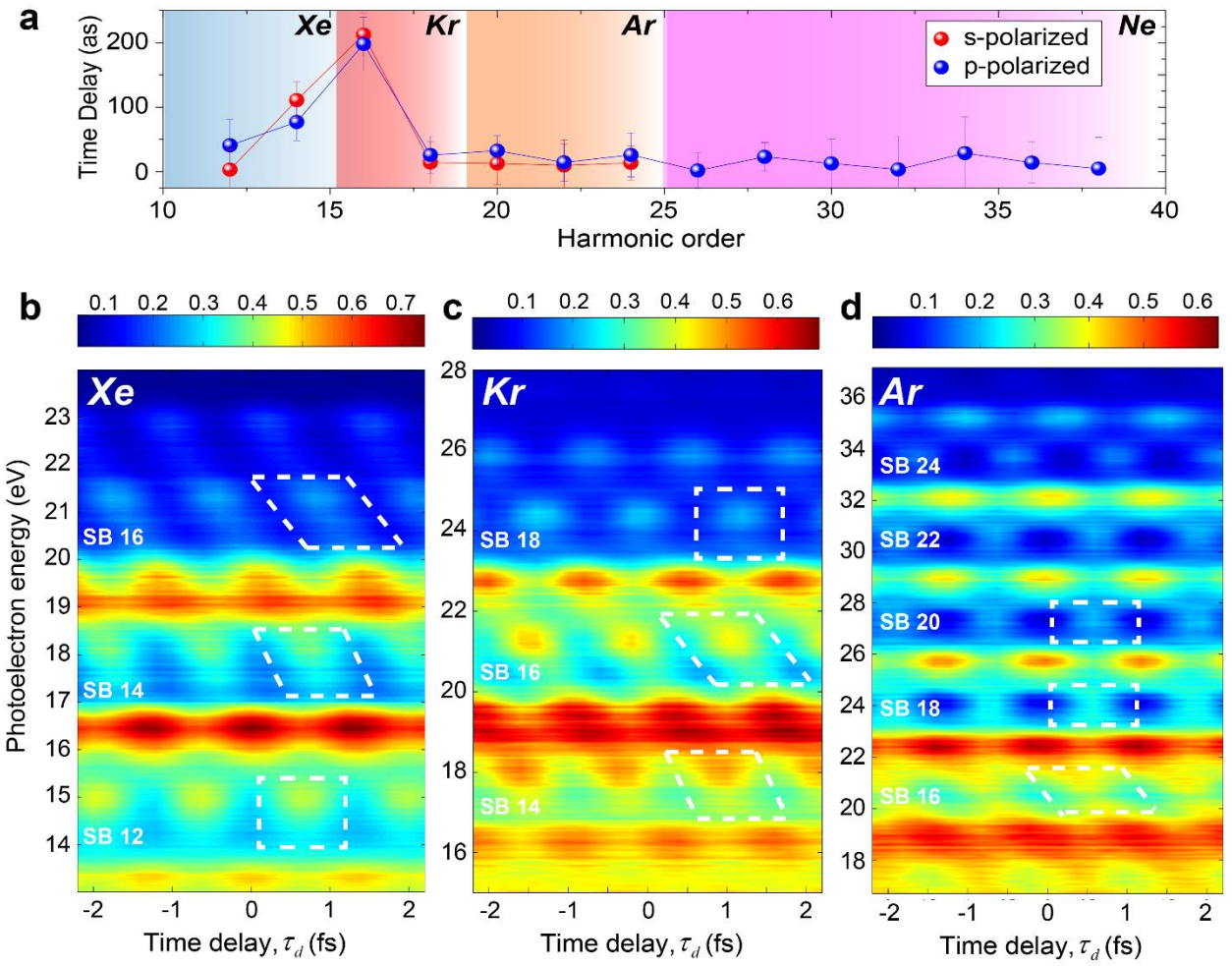

Figure 7.7: Photoemission time delay measurements obtained using different noble gas targets. (a) Photoemission time delays from laser-dressed harmonic sidebands for s- and p-polarized HHG for noble gas targets. A significant delay is introduced at harmonic order 15, due to the > 200 attosecond lifetime of the excited-state in the material band structure. The interferograms covering the resonant energies are obtained by using (b) Xe, (c) Kr and (d) Ar as gas targets for high-harmonic generation process. The photoemission is excited by s-polarized HHG field. 11th to 17th HHG orders are covered by Xe, 13th to 19th by Kr and 15th to 25th by Ar. By using Ne, the EUV probe can cover 23th to 41th HHG orders (not shown here). The oscillation offsets at the side bands corresponding to the spectral resonance are highlighted by white dashed boxes, yielding consistent time delay using different gases.

To better visualize the dependence of photoemission time delay on photon energy, we truncate the interferograms covering different energy regions [Figure 7.7(b-d)] and stitch them together to generate the broad-range interferograms shown in Figure 7.8c. We observe that photoelectrons from the Λ_3^β band are significantly delayed for sideband (SB) 16 (corresponding to a photon energy 25.6 eV), which manifests as a strong oscillation offset in the interferograms. This time delay gradually vanishes at increasing and decreasing photon energies, showing a non-monotonic change of $\tau_{PE}\left(\Lambda_3^\beta\right)-\tau_{PE}\left(\Lambda_3^\alpha\right)$ as a function of photon energies. To extract the 1D lineouts corresponding to the Λ_3^α and Λ_3^β bands in the side-band region, we integrate the photoelectron counts over a spectral window with an energy width of 300 meV and an angle width of ±2.5° centered at $\bar{\Gamma}$ point of the sideband peak corresponding to the band of interest and plot them as a function of the pump-probe delay (τ_d). 1D lineouts of Λ_3^α and Λ_3^β bands are plotted in the panel on the right side of Figure 7.8c, making it possible to determine the precise values of $\tau_{PE}\left(\Lambda_3^\beta\right)-\tau_{PE}\left(\Lambda_3^\alpha\right)$ as a function of photon energy.

To improve the efficiency in the data analysis on the huge dataset of time-resolved measurements, we employed a cross-phase Fourier analysis to extract the relative phases between the oscillations of two bands. The relative phase between two band-dependent 1D lineouts [$x\left(\Lambda_3^\alpha,\tau_d\right)$and $x\left(\Lambda_3^\beta,\tau_d\right)$] can be determined by calculating their cross-correlation function

$$C\left(\Lambda_3^\alpha,\Lambda_3^\beta,\omega\right)=\tilde{x}^*\left(\Lambda_3^\alpha,\omega\right)\tilde{x}\left(\Lambda_3^\beta,\omega\right), \tag{7.2}$$

where $\tilde{x}(\omega)$ is the Fourier transform of $x(\tau_d)$ and $\tilde{x}^*(\omega)$is the complex conjugate of $\tilde{x}(\omega)$. The peak frequency of $\left|C\left(\Lambda_3^\alpha,\Lambda_3^\beta,\omega\right)\right|$is the oscillation frequency shared by both curves and equals to $2\omega_L$, as shown in Figure 7.8c. The averaged phase of $C\left(\Lambda_3^\alpha,\Lambda_3^\beta,\omega\right)$at this peak frequency

corresponds to the relative phase difference between the two oscillations. The extracted time delay is consistent with the values directly extracted by fitting the 1D lineouts with sinusoidal functions.

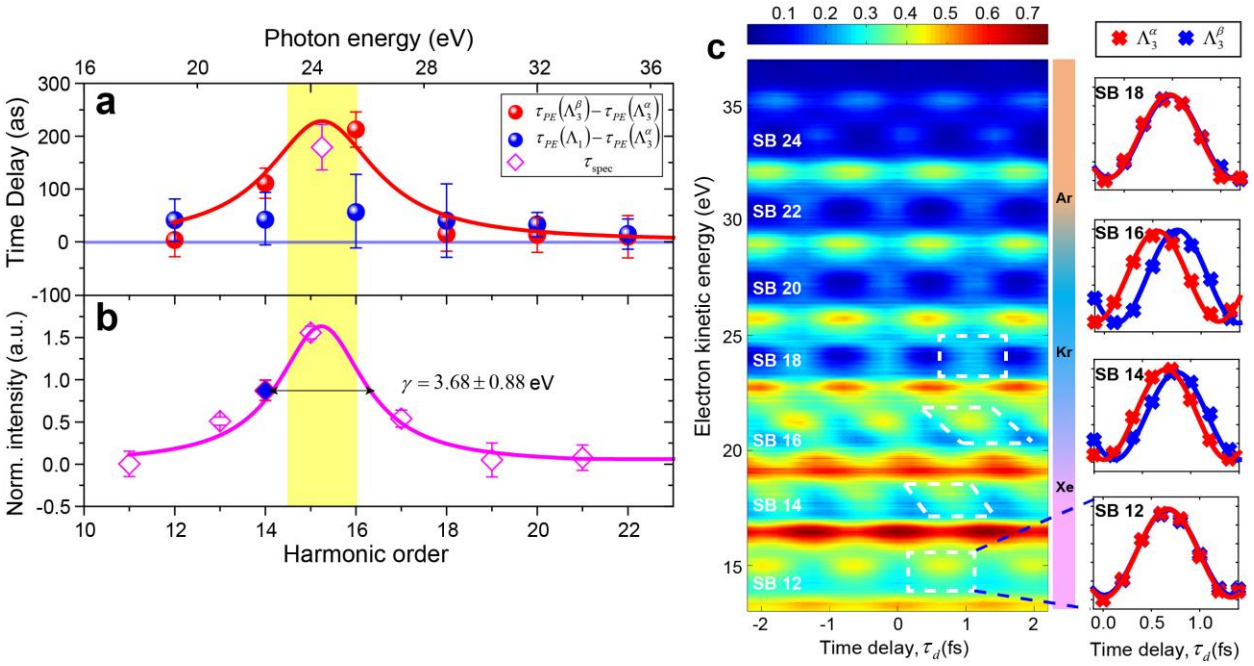

Figure 7.8: Direct time-domain measurement of the final-state lifetime. (a) Photoemission time delays $\tau_{PE}(\Lambda_3^\beta) - \tau_{PE}(\Lambda_3^\alpha)$ and $\tau_{PE}(\Lambda_1) - \tau_{PE}(\Lambda_3^\alpha)$ as a function of photon energy, clearly showing an increase in lifetime by 212 ± 30 as when the final state corresponds to a short-lived excited state in the band structure. (b) Spectral intensity of the Λ_3^β initial band as a function of photon energy. The blue point (14th order) is obtained from 390 nm driven HHG. The pink line represents a Lorentzian fit, yielding a linewidth of $\gamma = 3.68$ eV. (c) 2D map of photoelectron yields as a function of photoelectron energy and pump-probe time delay τ_d, excited by *s*-polarized HHG. To enhance the color contrast, 90% of the ground-state spectrum is subtracted to visualize the interferogram. The relative delays between photoelectrons from the Λ_3^α and Λ_3^β initial bands are manifested as a strong oscillation offset in the side bands (white dashed). 1D lineouts for Λ_3^α and Λ_3^β initial bands in the corresponding regions are plotted in the right panel.

The results are summarized in Figure 7.8a. By comparing this relative photoemission delay with the spectral resonance (Figure 7.8b), we find that the observed maximum in time delay coincides with the spectral resonance at the same photon energy, strongly indicating that the observed photoemission time delay originates from the unoccupied bulk final band Λ_1^{B} of Ni(111). Most importantly, the time delay measured using laser-assisted photoemission, $\tau_{\mathrm{chron}} = 212 \pm 30$ as, agrees with $\tau_{\mathrm{spec}} = 179 \pm 43$ as from the spectral resonance, within error bars.

7.7.3 Photoemission Time Delay between Λ_1 and Λ_3^{α} Bands

To extract the photoemission time delay $\tau_{PE}(\Lambda_1) - \tau_{PE}(\Lambda_3^{\alpha})$, we used p-polarized EUV fields for photoemission. We note that in this situation, the low-energy side-band intensity of the RABBITT oscillations has contributions from both Λ_1 and Λ_3^{β} bands, which is labelled as $\Lambda_3^{\beta} \otimes \Lambda_1$. As a result, the relative time delay we extracted is $\tau_{PE}\left(\Lambda_3^{\beta} \otimes \Lambda_1\right) - \tau_{PE}\left(\Lambda_3^{\alpha}\right)$. Because the quantum paths corresponding to these two oscillations start from different initial bands, we can exclude the interferences between them. Rather, we expect a simple intensity addition of Λ_1 and Λ_3^{β} RABBITT signals. The results of $\tau_{PE}\left(\Lambda_3^{\beta} \otimes \Lambda_1\right) - \tau_{PE}\left(\Lambda_3^{\alpha}\right)$ are plotted in comparison with the values of $\tau_{PE}\left(\Lambda_3^{\beta}\right) - \tau_{PE}\left(\Lambda_3^{\alpha}\right)$ as a function of harmonic order and photon energy in Figure 7.7a. Due to non-negligible contributions of Λ_3^{β} band, large time delays can be observed around the resonant photon energy (~24 eV) when excited by p-polarized field.

In the strong field approximation, the modulation amplitude at SB 2*n* is proportional to the square-root of the spectral intensity product of the two neighboring one-HHG-photon-excited direct photoemission bands which contribute to this side band: $A_{2n} \propto \sqrt{I_{2n+1} I_{2n-1}}$ [34]. The spectral

weight of direct photoemission from the initial Λ_3^β and Λ_1 bands have been determined by the static spectral analysis, as shown in Figure 7.6b. We note that for side band order lower than 14th and higher than 18th, the spectral weight of Λ_3^β band is so low that the time delay $\tau_{PE}(\Lambda_1)-\tau_{PE}(\Lambda_3^\alpha)$ can approximately equal to the time delay directly measured using p-polarized HHG field [$\tau_{PE}(\Lambda_1)-\tau_{PE}(\Lambda_3^\alpha)\approx\tau_{PE}(\Lambda_3^\beta\otimes\Lambda_1)-\tau_{PE}(\Lambda_3^\alpha)$]. The values of $\tau_{PE}(\Lambda_1)-\tau_{PE}(\Lambda_3^\alpha)$ for SB 14, 16 and 18 need to be extracted through a more detailed analysis, where the ratio of the modulation amplitudes between Λ_1 and Λ_3^β bands is given by $P=A_{2n}(\Lambda_1)/A_{2n}(\Lambda_3^\beta)$= 1.0, 0.64 and 0.76, respectively. To extract $\tau_{PE}(\Lambda_1)-\tau_{PE}(\Lambda_3^\alpha)$ of these side bands, we employ the following fitting algorithm:

1) We model the RABBITT oscillation lineout excited by *p*-polarized HHG field by considering the relative contributions from both Λ_3^β and Λ_1 bands:

$$A_{\text{p-pol}}^{\text{model}}(\tau_d)=P\times\sin\{2\omega_L[\tau_d-\tau_{PE}(\Lambda_1)]\}+\sin\{2\omega_L[\tau_d-\tau_{PE}(\Lambda_3^\beta)]\}. \quad (7.3)$$

Here, $\tau_{PE}(\Lambda_3^\alpha)$ is assumed to be zero for simplicity. The parameters *P* and $\tau_{PE}(\Lambda_3^\beta)$ are directly obtained from experimental results, with the latter from the time delays measured using s-polarized HHG field. A modeled lineout with discrete delay points (τ_d) from -3.0 fs to 3.0 fs with 0.2 fs each step can be generated using Equation 7.3.

2) We fit this modeled lineout using a sinusoidal function to extract modeled time delay for p-polarized HHG field, $\tau^{\text{model}}(p-\text{pol})$.

3) By varying the value of $\tau(\Lambda_1)$ in range -200 as to 200 as with 2 as each step, we find the best match of the modeled *p*-polarization time delay $\tau^{\text{model}}(p-\text{pol})$ to experimentally measured one $\tau^{\text{expt}}(p-\text{pol})$ (Figure 7.7a) and hence determine the value of $\tau_{PE}(\Lambda_1)-\tau_{PE}(\Lambda_3^\alpha)$.

The fitting procedure can achieve convergence for the results of SB 14, 16 and 18, yielding the photoemission time delay $\tau_{PE}(\Lambda_1)-\tau_{PE}(\Lambda_3^{\alpha})$ as shown in Figure 7.8a. The error bar is determined by considering the errors of the RABBITT measurements using both s- and p-polarized HHG lights. In strong contrast to the Λ_3^{β} band, photoemission from the Λ_1 band exhibits a very small time delay relative to that from the Λ_3^{α} band and varies smoothly across the photon energy range.

7.7.4 Lifetime of the Unoccupied Bulk Final Band Λ_1^B

The fact that our measured lifetime agrees well with the lifetime extracted from the spectral linewidth indicates that the lifetimes of photoelectrons originating from the Λ_3^{α} band are very small (within experimental error ~±53 as). At the same time, the photoelectron lifetimes corresponding to the Λ_1 band are ≈50 as. Since both bands exhibit a smooth variation in photoemission cross section over the photon energy range used here, it is reasonable to assume their photoelectron lifetimes are slowly varying as a function of photon energies. Thus, the results presented in Figure 7.8a can be interpreted as an abrupt increase of ~212 as in photoelectron lifetime from the Λ_3^{β} band when the direct transition approaches a bulk final band (Λ_1^{B}), resulting in a final-state resonance.

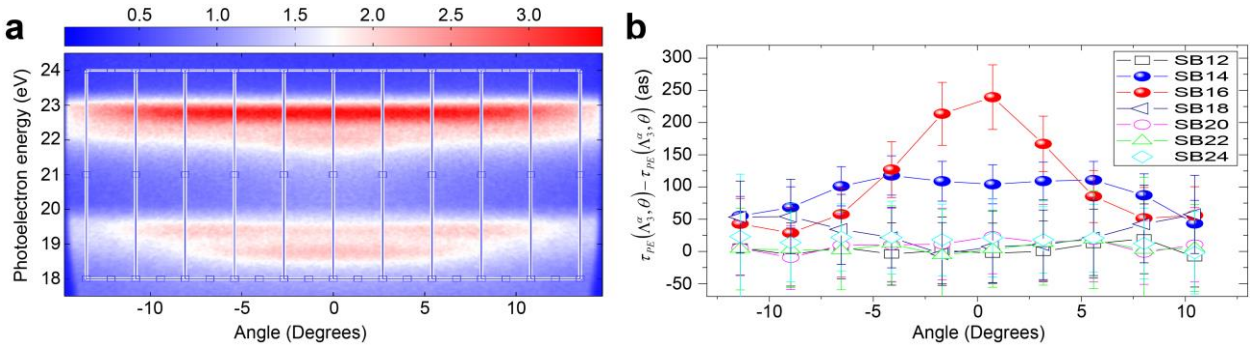

Figure 7.9: Extraction of angle-dependent photoemission time delays. (a) Illustration of the angular regions for integration when extracting the angle-dependent photoemission time delay. The energy region corresponding to SB16 is used as an example here. (b) Angle-dependent photoemission time delays $\tau_{PE}\left(\Lambda_3^{\beta},\theta\right)-\tau_{PE}\left(\Lambda_3^{\alpha},\theta\right)$ at different side bands. The phases of the RABBITT oscillations at different angles [$\tau_{PE}\left(\Lambda_3^{\alpha},\theta\right)$] are used as the timing references for the other band.

7.8 Angle-Dependent Photoemission Time Delay Caused by Final-Band Dispersion

Other important evidence that the band structure of the material strongly influences the photoemission lifetime can be seen from the angle-dependence of the lifetime as a function of electron transverse momentum $\boldsymbol{k}_{//}$. To extract the angle-dependent photoemission time delay, we first divide the angle-resolved photoemission spectra excited by s-polarized EUV light at each side band into ten angular regions, with a ~3° angular span over the entire range of photoelectron emission angle (~±15°), as shown in Figure 7.9a. The photoelectron counts in each region are integrated and plotted as a function of pump-probe time delay τ_d to obtain the angle-dependent RABBITT interferograms. Typical interferograms at the spectral resonance are plotted in Figure 7.10b. In this way, the angle-dependent photoemission time delays for photoelectrons from Λ_3^{α} and Λ_3^{β} bands can be extracted. To cancel any time delays imposed by the incident and reflected laser fields [60,118] and to extract the contribution due to band-structure effects, the RABBITT

oscillations from the Λ_3^α band were used as the timing reference at different emission angles (θ) for each side band. The angle-dependent results of $\tau_{PE}\left(\Lambda_3^\beta,\theta\right)-\tau_{PE}\left(\Lambda_3^\alpha,\theta\right)$ are summarized in Figure 7.9b for SB12 to SB24 (near the resonance). As illustrated in Figure 7.9b, pronounced angle-dependence of photoemission time delays is only observed at the energies around the spectral resonance (SB16 and SB14), while it diminishes at the other sidebands, which strongly supports the band-structure origin of these delays.

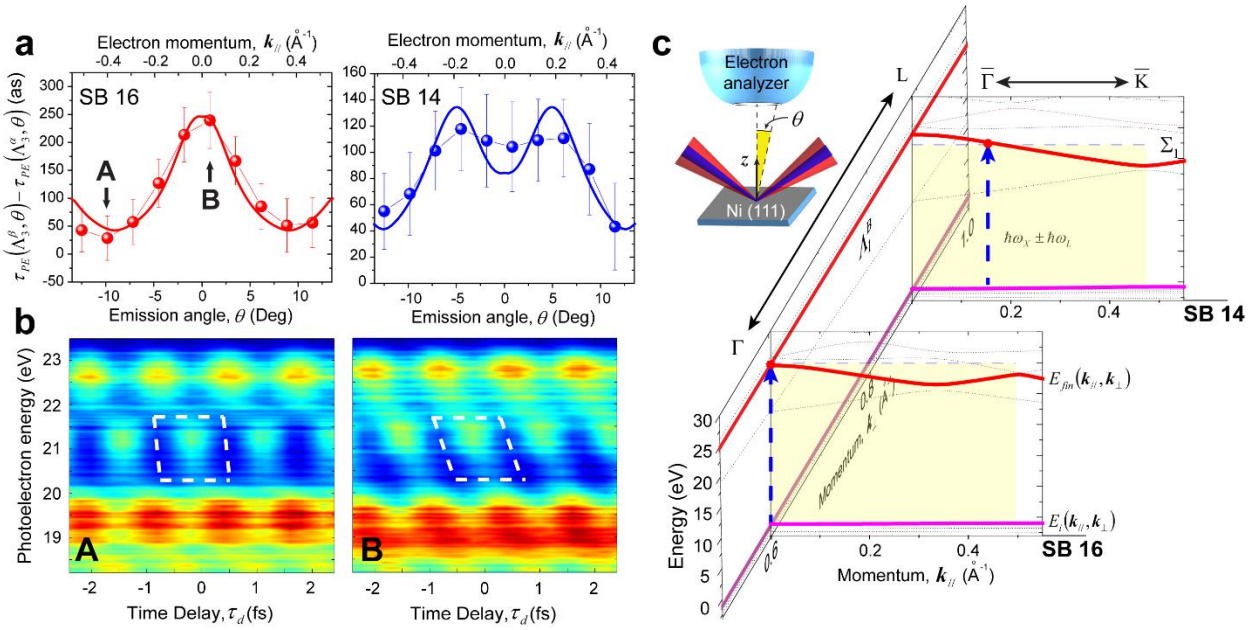

Figure 7.10: Angle-dependent photoemission time delays. (a) Angle-dependent photoemission time delay $\tau_{PE}\left(\Lambda_3^\beta,\theta\right)-\tau_{PE}\left(\Lambda_3^\alpha,\theta\right)$ for SB 16 and 14 obtained using *s*-polarized HHG. The data are points, while the solid lines are a fit to the final-state band structure obtained from our model and DFT calculations. (b) Typical RABBITT interferograms for SB 16 with emission angles [(A) and (B)] labeled in (a). The chirp is highlighted with white dashed boxes. (c) Illustration of direct transitions in the direction $\overline{\Gamma}-\overline{\mathrm{K}}$ for SB 14 and 16. Because different photon energies are used for these two side bands, different $k_\perp$ along the Γ- L direction are assigned according to the band-maps in Figure 7.6a. The initial and final bands are highlighted by thick solid lines and the binding energy of the initial band (pink) is corrected according to the binding energy obtained in our experiments. The transitions are labeled as dashed arrows. Inset: Experimental geometry: IR and HHG beams are focused onto a Ni(111) surface at a 45° incident angle. θ is assigned to the emission angle of photoelectrons relative to the sample normal direction (***z***).

Figure 7.10a shows the individual plots of $\tau_{PE}\left(\Lambda_3^{\beta},\theta\right)-\tau_{PE}\left(\Lambda_3^{\alpha},\theta\right)$ at SB 16 and SB14 to better visualize their angle dependent structure. As illustrated in Figure 7.10a, the time delay $\tau_{PE}\left(\Lambda_3^{\beta},\theta\right)-\tau_{PE}\left(\Lambda_3^{\alpha},\theta\right)$ at SB 16 reaches its maximum value ~220 as at $\overline{\Gamma}$ point (θ=0), while it reduces to ~30 as when the emission angle approaches θ=±15°. The overall trend is symmetric around the $\overline{\Gamma}$ point. Most interestingly, $\tau_{PE}\left(\Lambda_3^{\beta},\theta\right)-\tau_{PE}\left(\Lambda_3^{\alpha},\theta\right)$ exhibits a double-peak shape at SB 14 (Figure 7.10a), as the time delay increases to its maximum on-resonance value at $\theta\approx$±6° and then decreases for larger emission angles.

To understand the band-structure effects on the angle-dependent photoemission time delays shown in Figure 7.9b and Figure 7.10a , our first task is to determine the final band structure along $\bar{\Gamma}$-$\overline{K}$ direction. To do so, we employed DFT calculation to calculate the bulk electronic band structure of Ni(111) up to ~40 eV above the Fermi level, which has shown good agreement to the experimental results along Γ-L momentum direction. The results exhibit that the final band (originally Λ_1^{B} band along Γ-L) evolves into a downward dispersed Σ_1 band, as shown in Figure 7.10c. This conclusion is also supported by the angle-resolved photoemission spectra in our experiments, which exhibit an increment of the probed momentum range of $\boldsymbol{k}_{//}$ when the EUV photon energy approaches lower energies from the resonant photon energy (Figure 7.4a). We believe that the final-band dispersion can lead to a mismatch between the EUV photon energies and the resonant energies at different angles, hence affect the measured angle-dependent photoemission time delays.

To quantify this, we model the photoelectron lifetime as a Lorentzian lineshape, centered at the resonant energy [$E_0(\theta)$] with a linewidth assigned to the resonant spectral linewidth γ (Figure

7.8b). Thus, the photoemission time delay as a function of photon energy $\hbar\omega_X$ and emission angle θ is given by

$$\tau(\omega_X,\theta)=\frac{2M}{\pi}\frac{\gamma}{4\left[\hbar\omega_X-E_0(\theta)\right]^2+\gamma^2}, \tag{7.4}$$

where M is the amplitude coefficient, which determine the maximum time delay at resonance [$\hbar\omega_X = E_0(\theta)$]. The resonant energy $E_0(\theta)$ is directly extracted from the energy difference between the initial and final bands at different transverse momenta $\boldsymbol{k}_{//}$ along $\bar{\Gamma}-\bar{K}$ obtained from DFT calculations. The emission angle θ can be directly related to $\boldsymbol{k}_{//}$ by the well-known relationship $\theta=\arcsin\left(\frac{\hbar k_{//}}{\sqrt{2m_eE_{kin}}}\right)$, where E_{kin} is the photoelectron kinetic energy given by $E_{kin}=\hbar\omega_X-E_B-\Phi$, with E_B and Φ the binding energy and the workfunction, respectively. Because different values of the perpendicular momenta ($\boldsymbol{k}_\perp$) along Γ-L direction are probed by using different EUV photon energies (Figure 7.6a), the dispersion of the initial and final bands along Γ-L direction is also taken into account in this model. Compared to the final Λ_1^B band, the dispersion of initial Λ_3^β band is smaller by one order of magnitude. As a result, we treat the initial Λ_3^β band as a flat band along both $\bar{\Gamma}-\bar{K}$ and Γ-L directions with a binding energy of 1.2 eV, obtained from our experimental results. To determine the structure of final Λ_1^B band, we first determine the values of $\boldsymbol{k}_\perp$ from the band-mapping results in Figure 7.6a for photon energies corresponding to different side bands (e.g., SB14: $\boldsymbol{k}_\perp \approx 0.87$ Å^{-1} and SB 16: $\boldsymbol{k}_\perp \approx 0.61$ Å^{-1}), respectively. Then the final Σ_1 band along $\bar{\Gamma}-\bar{K}$ (Λ_1^B in Γ-L) is extracted from DFT calculation at the corresponding $\boldsymbol{k}_\perp$. We note that the effect of band dispersion along Γ-L is mainly to shift the

energy of the final band, while the band dispersion along $\bar{\Gamma}-\bar{K}$ in the momentum range of interest are approximately the same at different $\boldsymbol{k}_{\perp}$.

With the values of $E_0(\theta)$ determined, we can fit the experimental results for SB 14 and SB 16 by adjusting the value of the amplitude coefficient *M*. We note that *M* is the only fitting parameter used in this model, while the other parameters can be pre-determined by the experimental parameters and DFT calculations, which underlines a very good constrain on this problem. The fitting results for SB 14 and SB 16 are plotted as solid lines in Figure 7.10a. To obtained a good fitting to our experimental results, we find $M\approx1660$ for SB 16 corresponding to a maximum time delay of ~250 as at resonance, while $M \approx 950$ for SB 14 corresponding to a maximum time delay of ~140 as. The choice of different values of *M* at various photon energies might indicate an influence of the band structure along Γ-L on the photoelectron lifetime, which requires further investigations.

Our results show that for SB 16, the HHG photon energy closely matches the resonant excited state at the $\bar{\Gamma}$ point, yielding a maximum time delay for θ=0. Moreover, the time delay monotonically decreases at larger emission angles, since final-state band dispersion causes the transition to be off resonance. On the other hand, for SB 14 where the photon energy is ~3.2 eV lower, the resonant transition is not accessible at the $\bar{\Gamma}$ point, but is on resonance and yields a maximum time delay at a ~ 6° emission angle (Figure 7.10c). The key factor for this agreement is the dispersion of the Σ_1 final band (~ -14 eVÅ$/\hbar$), which determines the slope of the time delay as a function of θ.

7.9 Classical Considerations on Photoemission Time Delay and Screening of IR Field

To understand the experimentally measured time delay, it is helpful to first consider the problem in a classical picture. In a classical model, the drift velocity $\boldsymbol{v}(t)$ of an electron under the effects of IR dressing field with a vector potential $\boldsymbol{A}(t)$ can be determined if we know the velocity ($\boldsymbol{v}_i$) of this electron at a specific time (τ_i), $\boldsymbol{v}(t,\ \tau_i, \boldsymbol{v}_i) = -\frac{e}{m_e}\boldsymbol{A}(t) + \left[\boldsymbol{v}_i + \frac{e}{m_e}\boldsymbol{A}(\tau_i)\right]$. If we measure the energy of this particle at infinitely far away, the first time-dependent term can be ignored at $t \to \infty$, hence we have its final drift velocity $\boldsymbol{v}_f(\tau_i, \boldsymbol{v}_i) = \boldsymbol{v}_i + \frac{e}{m_e}\boldsymbol{A}(\tau_i)$.

Considering the situation when the IR dressing field is applied onto a metal surface and the electron escapes from inside the metal, two consequences are expected: 1) the electron moves faster inside metal than in vacuum, since the workfunction (Φ) is deducted when the electron escapes across the interface; 2) the intensity of the IR dressing field is strongly screened inside metal [60]. So, it is more convenient to consider the electron dynamics inside metal separately. We can take the metal-vacuum interface as the boundary, after which the electron moves as a free particle in the IR dressing field. By knowing the time when the electron arrives right above the metal surface (τ_s) and the escaping velocity ($\boldsymbol{v}_s$), the final drift velocity is given by $\boldsymbol{v}_f(v_s, \tau_s) = \boldsymbol{v}_s + \frac{e}{m_e}\boldsymbol{A}(\tau_s)$. As a result, the measured photoelectron energy is $E_{fin} = \frac{1}{2}m_e\boldsymbol{v}_f^2 \approx \frac{1}{2}m_e\boldsymbol{v}_s^2 + \boldsymbol{v}_s \cdot e\boldsymbol{A}(\tau_s)$, if we assume $\frac{e}{m_e}\boldsymbol{A}(\tau_s) << \boldsymbol{v}_s$ which is valid for most attosecond-streaking or RABBITT experiments. Here we assume the IR dressing field arrives at

t=0, while the EUV photon arrives and excites photoelectrons at t=τ_0, hence the relative pump-probe delay is τ_d = - τ_0.

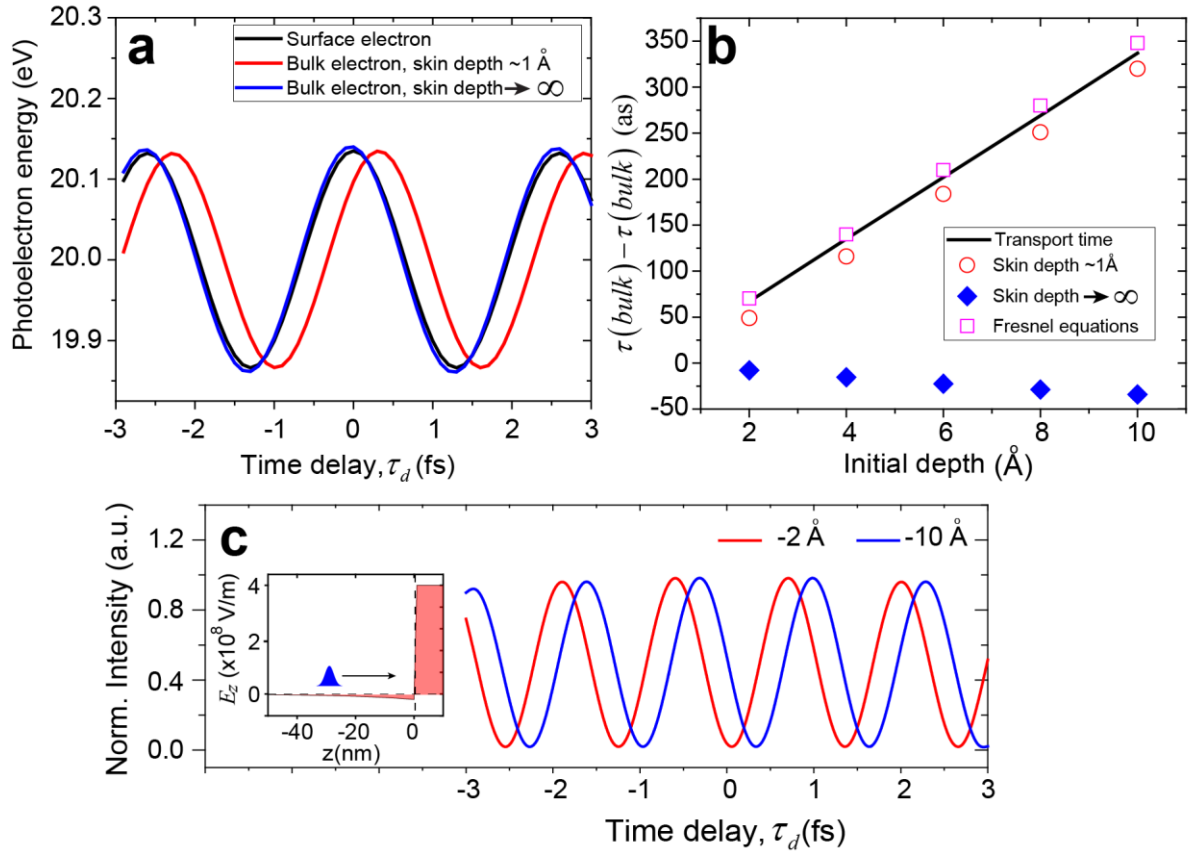

Figure 7.11: Classical model for photoemission time delay. (a) Streaking curves for surface-born photoelectrons (black line) and bulk-emitted electrons at initial depth of 10 Å. Two skin depths of IR fields are considered: l_0~1 Å (red line) and $l_0 \to \infty$ (blue line). The IR field strength is E_{L0} =2x10^{13} V/m with a FWHM pulse duration of 30 fs. (b) Time delay between streaking curves of bulk-emitted and surface-born electrons [$\tau(bulk)-\tau(surface)$] as a function of the initial depth of the bulk-emitted photoelectrons. The results for skin-depth of l_0~1 Å (red open circle), $l_0 \to \infty$ (blue filled diamond) and the IR field distribution calculated using Fresnel equations (pink open square) are plotted. The black solid line represents the transport time delay. (c) Results of 1D semiclassical simulations. Photoelectrons emitted 10 Å below the surface are delayed by 267 as compared to those emitted from 2 Å. Inset: profile of the electric field strength normal to surface (E_z) across the interface.

For an electron born at depth λ inside the metal, the time it arrives the surface is $\tau_s = \tau_0 + \lambda/v_{tr} + \Delta_{IR}$, where v_{tr} is the velocity of this electron in the metal (only considering the direction normal to the surface) and Δ_{IR} is attributed to any time delay induced by the IR dressing field inside metal. If we plot E_{fin} as a function of τ_d, typical attosecond-streaking curves can be reproduced and a time delay ($\Delta t = \lambda/v_{tr} + \Delta_{IR}$) can be observed for this bulk-emitted electron compared to an electron born right above the surface at $t=\tau_0$. In addition, the escape velocity $\boldsymbol{v}_s$ of the bulk-emitted photoelectron can also be affected by the IR dressing field inside the metal, yielding an additional time-dependent distortion to the streaking curve.

It is key to understand the effects of IR dressing field on Δ_{IR} and $\boldsymbol{v}_s$ when the electron is escaping from the metal. To evaluate these effects, we employed a 1D classical model to calculate the electron dynamics inside the metal and to yield the (τ_s , $\boldsymbol{v}_s$) for the bulk-emitted electrons. Another surface-emitted electron is used as a reference to compare the streaking curves. The vector potential of the IR dressing field in the free space above the metal surface is described by an cosine function modulated by an Gaussian envelop with a width of τ_L: $A(t) = A_0 \exp\left(-\frac{t^2}{2\tau_L^2}\right)\cos(\omega_L t)$. The electric field inside the crystal as a function of time and depth (z) is given by $E(t,z) = -\frac{\partial A(t)}{\partial t} \times \exp\left(-\frac{z}{l_0}\right)$ with additional field damping is accounted for by a skin-depth l_0. We assume both electrons (bulk-emitted and surface-born) own the same final energy (E_{fin}) without the IR dressing field. As a result, the initial kinetic energy of the bulk-emitted inside metal is $E_{fin}+\Phi$. The deduction of the workfunction Φ is performed at interface (z=0). For simplicity, we only consider photoelectrons with final energy E_{fin} = 20.0 eV and metal workfunction W= 5.0 eV, which is close to our experimental conditions.

In Figure 7.11a, we plot a comparison of streaking curves for electrons emitted from 10 Å below the surface and a surface-emitted electron. As shown in the figure, when the skin depth $l_0 \sim$ 1 Å, significant time delay can be observed, while this time delay diminishes when $l_0 \to \infty$, leading to a slight advancement in time. In both situations, the measured time delay does not change for IR field strength varying several orders of amplitude. Photoelectrons emitted from different depths are examined using our classical model, as shown in Figure 7.11b. Under this classical model, the measured streaking time delay [τ(bulk) – τ(surface)] is generally in agreement with the transport time of the bulk-emitted electrons, when the skin depth $l_0 \sim$ 1 Å. However, the measured time delay can be significantly different from the electron transport time when $l_0 \to \infty$. From a detailed analysis, it is interesting to see that the effects of the IR dressing field inside the crystal does not contribute significantly to Δ_{IR}, which is typically several attoseconds even when $l_0 \to \infty$. On the other hand, it is the difference in escape velocity $\boldsymbol{v}_s$ that causes the strong deviation of the measured time delay from the transport time.

The analysis above underlines the importance of the skin depth of the IR field to the interpretation of the experimentally measured time delays, which is also noted in recent experimental and theoretical studies [56,60,238]. When the skin depth is long, the measurement-induced time delay cannot be simply canceled by comparing photoelectrons under the influence of the same dressing field. This is different from measurements on isolated atoms, where the measurement-induced delay was shown to be universal. The IR field distribution and phase across the metal-vacuum interface of a Cu(111) surface have been studied in details in recent angle-dependent RABBITT measurements, where the Fresnel equations are found to give a correct description of the IR field at the interface and can account for the observed time delay when the

IR fields is incident at normal and grazing angles. According to the Fresnel equations, the IR field in the direction normal to the surface is given by [239]

$$E_z(z,t)=\begin{cases} -\dfrac{\sin\theta_{in}}{\varepsilon_0^{1/2}}\left[\exp(ik_z z)+r\cdot\exp(-ik_z z)\right]\exp(-i\omega_L t) & (z>0) \\ -\dfrac{\varepsilon_0^{1/2}\sin\theta_{in}}{\varepsilon}\cdot(1+r)\cdot\exp\left[i\dfrac{\omega_L}{c}\left(\varepsilon-\varepsilon_0\sin^2\theta_{in}\right)^{1/2}z\right]\exp(-i\omega_L t) & (z\le 0) \end{cases}, \tag{7.5}$$

where θ_{in} is the incident angle with respect to the surface normal, k_z the wave vector with $k_z=\dfrac{\omega_L}{c}\varepsilon_0^{1/2}\cos\theta_{in}$, r the reflaction coefficient with

$$r=\frac{\left[(\cos\theta_{in})/\varepsilon_0^{1/2}\right]-\left(\varepsilon-\varepsilon_0\sin^2\theta_{in}\right)^{1/2}/\varepsilon}{\left[(\cos\theta_{in})/\varepsilon_0^{1/2}\right]+\left(\varepsilon-\varepsilon_0\sin^2\theta_{in}\right)^{1/2}/\varepsilon}, \tag{7.6}$$

and ε represents the complex dielectric constant of metal. The metal-vacuum interface is defined at z=0, with $z\le 0$ for positions inside the metal and $z>0$ outside the metal. Consider the electric field at the interface (z=0), the ratio of the electric field inside and outside the metal is given by $\left|\dfrac{E_z^{in}(z,t)}{E_z^{out}(z,t)}\right|_{z=0}=\left|\dfrac{\varepsilon_0}{\varepsilon}(1+r)\right|$. Given the dielectric constant of nickel to be $\varepsilon\approx -20+30i$ [240], the ratio is $\left|\dfrac{E_z^{in}(z,t)}{E_z^{out}(z,t)}\right|_{z=0}\approx 0.04$, representing a strong damping of the evanescent wave of the IR dressing field inside metal. The calculated IR field intensity inside nickel is shown in the inset of Figure 7.11c. When this field profile is taken into consideration, the results of the classical model for bulk-emitted electrons are in good agreement with the transport time as shown in Figure 7.11b, because the effects of the IR dressing field are negligible on both Δ_{IR} and $\boldsymbol{v}_s$.

We note that the discontinuity of E_z at the interface could lead to an unrealistic surface charge distribution, which has been noted in previous studies [239,241]. However, with self-consistent calculations where the dynamical charge distributions are taken into considerations

[241], the screening length of E_z has been shown to be ~0.5 Å in metals, consistent with recent experimental results [56]. On the other hand, for dielectric materials with smaller reflection coefficients, the measured time delay will be more suspectible to IR induced phase change, rather than to the electron transport time.

7.10 Semiclassical Model for RABBITT Measurements

To correctly take into account the interference effects in RABBITT measurements, we calculate the accumulated quantum phases of the photoelectrons through scattering on the potentials of IR dressing field and crystal lattice along their 1D trajectories. The transition amplitude for a final state $\left|v_f\right\rangle$ as a function of τ_d is hence given by (atomic units) [34]

$$a\left(v_f,\tau_d\right)=-i\int_{-\infty}^{+\infty}\mathrm{d}t\; e^{i\varphi^{IR}(t)}e^{i\varphi^{C}(t)}\mathbf{d_p}\boldsymbol{E_X}\left(t+\tau_d\right)e^{i\left(\frac{1}{2}v_f^2+\Phi+E_B\right)t}, \tag{7.7}$$

where $\mathbf{d_p}$ is the dipole-matrix element from the ground state to the continuum final state $\left|v_f\right\rangle$, $\boldsymbol{E_X}(t)$ describes the EUV field for photoionization, E_B the binding energy of the initial state and the spectral intensity is given by $\left|a\left(v_f,\tau_d\right)\right|^2$. The phase induced by IR laser field $\varphi^{IR}(t)$ is given by

$$\varphi^{IR}\left(t\right)=\int_t^{+\infty}\mathrm{d}t'\left[\boldsymbol{v}\cdot\boldsymbol{A}\left(z,t'\right)+\boldsymbol{A}^2\left(z,t'\right)/2\right], \tag{7.8}$$

where $\boldsymbol{v}$ is the drift velocity of the electron inside and outside the metal, $z(t')$ describes the photoelectron trajectory and $\boldsymbol{A}(z, t')$ is the IR vector potential acting on the electron along its classical trajectory. The field intensity of the IR field across the metal-vacuum interface is calculated following the Fresnel equations. On the other hand, the phase induced by scattering on the crystal lattice is given by the integration of the crystal potential along the electron trajectory $z(t')$:

$$\varphi^{C}(t) = \int_{t}^{+\infty} \mathrm{d}t' U(z,t'). \tag{7.9}$$

The crystal potential $U(z)$ is defined as Chulkov potential [242] with the parameters for nickel given in Ref. [243]. The Chulkov potential of nickel is plotted in Figure 7.12a with the first atomic layer moved to z=0, defining the metal-vacuum interface. To account for the energy conservation at the interface, the work function Φ is directly deducted from the kinetic energy of photoelectrons when calculating its classical trajectory.

The temporal structure of $\boldsymbol{E}_X(t)$ is given by $E_X(t) = E_{X0}\exp\left(-\frac{t^2}{2\tau_X^2}\right)\sum_i e^{-i\omega_i t}$, where E_{X0} is the field strength, τ_X the width of the Gaussian envelop and ω_i the frequency of ith order of harmonics. By defining $\boldsymbol{E}_X(t)$ in a form of attosecond pulse trains comprised of multiple HHG orders (13th, 15th, 17th and 19th orders in this example) and $\tau_x \approx 6.38$ fs, typical RABBITT interferograms can be generated as shown in Figure 7.12b. The interferogram is obtained by subtracting the ground-state photoelectron spectrum well before time-zero. Similar to experimental data, the time delays can be determined by extracting 1D lineouts at side bands as shown in Figure 7.8c. In this case, we focus on the SB 16 with photoelectron energy ~20.6 eV. On the other hand, when the $\boldsymbol{E}_X(t)$ is modeled as isolated attosecond pulses with a single HHG continuum and $\tau_x \approx 0.43$ fs, the interferogram turns into attosecond-streaking spectrogram as shown in Figure 7.12c. The time delay can be obtained by directly fitting the center of energy (COE) as a function of time delay τ_d, as shown in the figure. For direct comparison with the RABBITT results, we assign the center energy of the isolated EUV pulse at 16th HHG order. In both cases, the phase of IR dressing field is used as timing references.

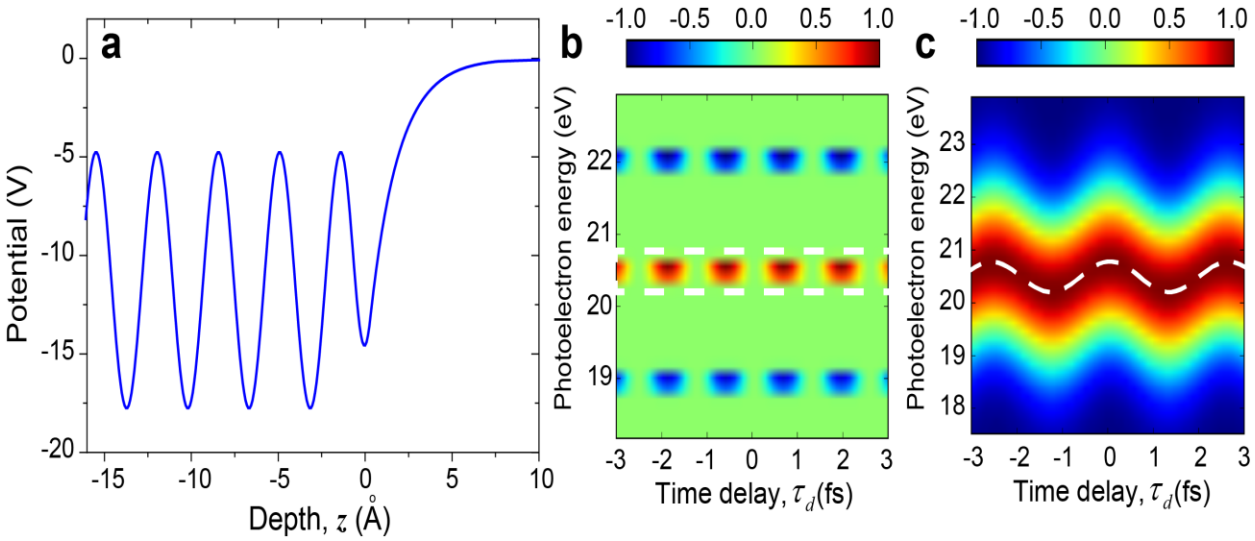

Figure 7.12: Semiclassical simulation results. (a) Chulkov potential of nickel. (b) Typical RABBITT interferogram calculated by semiclassical model when the EUV field $E_X(t)$ is given as an attosecond pulse train. Four harmonic orders (13th, 15th, 17th and 19th) are involved in this simulation and $\tau_x \approx 6.38$ fs. The side band region of 16th order is labeled by dashed white box. (c) Typical atto-streaking spectrogram calculated by the same semiclassical model as (b) with $E_X(t)$ modeled as an isolated EUV pulse. The pulse duration is $\tau_x \approx 0.43$ fs and its center energy is assigned at 16th harmonics for direct comparison with the RABBITT results in (b). A direct fitting of the center of energy (COE) profile is presented as the white dashed line. The field strength of the IR dressing field is 2×10^{14} V/m for both calculations.

Both the RABBITT and attosecond-streaking spectrograms are calculated for photoelectrons emitted from different depths inside metal using our 1D semiclassical model [118]. The results are summarized in Figure 7.13a. As shown in the figure, the time delay extracted from the RABBITT and attosecond-streaking spectrograms are identical for photoelectrons started from different depths. This conclusion is consistent with previous theoretical studies [56,60,238]. More importantly, the extracted time delays from both methods are in good agreement with the transport time of photoelectrons inside the metal, consistent with conclusion obtained from the classical model. This represents direct measurements of photoelectron lifetime of metals using both methods.

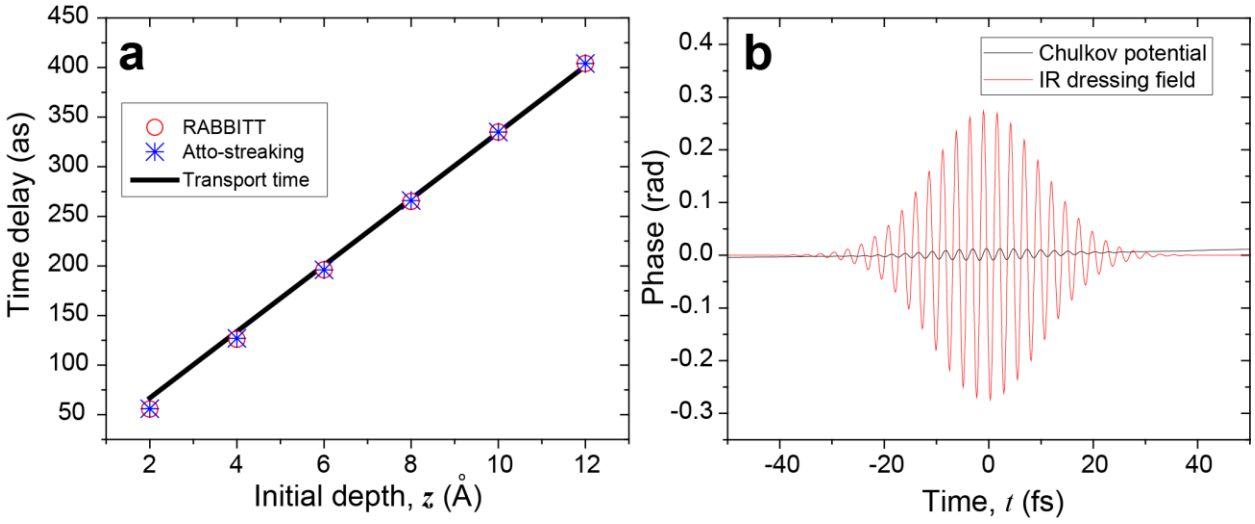

Figure 7.13: Results of the semiclassical model. (a) Time delay extracted from RABBITT and atto-streaking spectrograms for photoelectrons emitted from different initial depths. The solid black line represents the time delay calculated direction from transport model. We note the photoelectron kinetic energy inside metal is 25.6 eV, because the workfunction used in the calculation is 5 eV. (b) The quantum phases of photoelectrons accumulated by scattering on IR dressing field or on Chulkov potential of nickel. The phase from Chulkov potential is shifted by a static phase of ~7 rad for comparison with the phase from laser field. The photoelectron considered in this plot starts from 10 Å below the metal surface with 20.6 eV as its final energy. The pump-probe delay τ_d is fixed to be zero. The horizontal axis represents the variable of integration in Equation 7.6.

We note that the effects of the phase accumulated by scattering on the Chulkov potential (φ^C) on the extracted photoemission time delay is negligible, which is typically ~10 as. This result is consistent with previous studies. However, it is interesting to see that this negligible contribution is not because the absolute value of $\varphi^C(t)$ is small. Instead, it is because the time variation of this phase is much smaller than that from IR laser field [$\varphi^{IR}(t)$]. To illustrate this, we plot $\varphi^C(t)$ and $\varphi^{IR}(t)$ in Figure 7.13b. We note that the $\varphi^C(t)$ is shifted by a static phase ~7 rad for direct comparison with $\varphi^{IR}(t)$. From Equation (5.7), we can see that any static (time-independent) phase shift does not change the calculated photoelectron spectrum $I(v_f, \tau_d) = |a(v_f, \tau_d)|^2$, whereas it is the time-varying components of both phases that contribute to the variation of spectrograms. For $\varphi^C(t)$, the

time-varying component is induced by the change of photoelectron trajectories driven by the IR laser field, which is much smaller than $\varphi^{IR}(t)$ as shown in Figure 7.13b. As a result $\varphi^{C}(t)$ has very limited effects on extracted time delay in solids.

7.11 Inelastic Mean Free Path and Photoelectron Lifetime at High Energies

In photoemission theory, the photoelectron lifetime can be understood as the time taken for the wave function to evolve from a Bloch wave inside thematerial into a free-electron wave function outside the solid. Semiclassically, this is also the time the photoelectron spends moving a distance corresponding to an inelastic mean free paths (IMFP) [237,244]. Figure 7.11c shows that photoelectrons emitted 10 Å below the surface are delayed by 267 as compared with photoelectrons that originate 2 Å below the surface. This allows us to directly relate our time-domain measurements to the lifetimes and (IMFP) of photoelectrons, which determines the surface and bulk contributions [148,237]. The inelastic mean free path is the distance over which a particle travels within its lifetime, but a remaining question is what photoelectron velocity should be used to calculate the inelastic mean free path? In a periodic crystal lattice, the elastic interaction with atoms strongly modifies the electron energy-momentum relationship, giving rise to the electronic band structure. It is generally believed that the velocity of photoelectrons can be represented by the group velocity of the corresponding final bands [44,56,142], which is given by the derivative of the energy with respect to the momentum wave-vector $\boldsymbol{k}_{\perp}$**.** To determine the final-state group velocity, we employed an *ab-initio* calculation for the bulk band-structure of Ni along Γ-L, including the high-energy valence bands (~24 eV). We find the final band involved in the resonant transition (highlighted in Figure 7.6a) has a narrow bandwidth (~4 eV), consistent with our experimental spectra. The corresponding group velocity is given by $\partial E_f / \partial(\hbar \boldsymbol{k}_{\perp}) \approx 3.0$ eVÅ$/\hbar$,

and is significantly smaller than the velocity of a free electron with the same kinetic energy (~19.1 eVÅ$/\hbar$). Using the calculated group velocity, we obtain an inelastic mean free path of at most 1 Å, which is much smaller than values reported in other studies [245,246]. We believe this discrepancy is because the group velocity is not the transport velocity for high-energy photoelectrons. As pointed out in previous studies, high energy (>20 eV) photoelectrons leave the crystal before they feel the influence of the crystal lattice, so they behave more like plane waves with a free-electron dispersion**.** By using the corresponding free-electron velocity in our analysis, we extract a IMFP of ~6 Å for photoelectrons that are emitted on resonance, consistent with previous studies [196]. In contrast, the inelastic mean free paths of photoelectrons from the Λ_3^α and Λ_1 bands, as well as those from the Λ_3^β band away from the spectral resonance, are estimated to be approximately 3 Å, manifesting their surface-emission nature.

The short IMFP of the Λ_3^α and Λ_1 band photoelectrons is not surprising: in the strong-damping region (electron energy from ≈ 20 to 100 eV), many materials have IMFP comparable to the interatomic distances, and the photoelectric current is dominated by the top-most layer. Moreover, the IMFP of Ni was reported to be shorter than in other metals. In a one-step model description, this can be attributed to the fact that the propagation of the final-state wavefunction is strongly damped inside the material in this energy region, because of inelastic electron-electron interactions.

We note that the photon energies used in our experiments are lower compared to previous attosecond-streaking experiments. Indeed for higher photon energies, the density of final bands increases for direct transitions from initial bands in a reduced-zone scheme, and as a result, band-structure (matrix-element) effects become less significant. However, it has been shown in previous photoemission studies that energy- and angle-dependent band-structure effects can still be

observed from noble metals [247–249] and semiconductors [250] even when photon energy is as high as 300 eV**.** For a final band ~100 eV above the Fermi surface, the typical linewidth is ~ 7 eV, corresponding to a lifetime of ~90 as, which could still introduce significant contributions to the photoemission time delay measured.

7.12 Conclusion and Outlook

In conclusion, we directly and unambiguously measure the influence of the final-state band structure on photoelectron lifetime by probing the energy-, angle- and polarization-dependent photoemission time delays from multiple valence bands of Ni(111). We measure a significant increase of photoelectron lifetime when the direct transition coincides with a final-state resonance in the band structure. In the case of angle-dependent measurements, we show that the large variation in the measured photoemission time delay can be explained by the dispersion of the final band. Our results highlight the importance of the material band structure on photoemission time delays, which must also be taken into account even at higher photon energies. In future, this approach can be used to experimentally access quasiparticle lifetimes, electron mean free paths, electron-electron scattering and dynamical screening, all of which represent grand challenges for condensed matter theory. Moreover, other effects, including Cooper minima [251] and Fano resonances [252], could also lead to significant delays, making attosecond studies of metal valence bands a challenging, but also rich and interesting, problem.

Chapter 8

Attosecond Electron-Electron Scattering and Screening in Transition Metals

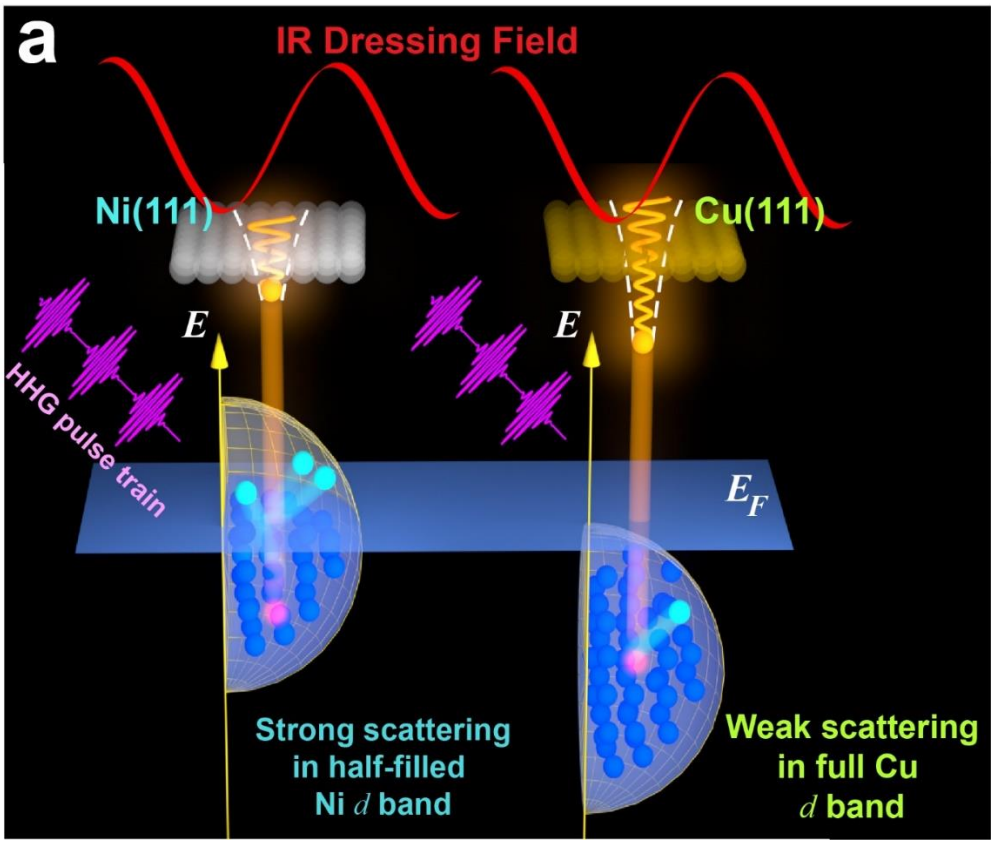

Figure 8.1: Illustration of the photoemission process from Cu(111) and Ni(111) surfaces. (a) Using HHG pulse trains, photoelectrons are excited either from a Cu(111) or Ni(111) surface. Due to the different band structure in these two materials, photoelectrons from Ni(111) experience more electron-electron scattering, which reduces the lifetime of photoelectrons by 100 as compared with Cu(111) as they escape from the material surface. The enhanced scattering also reduces the inelastic mean free path.

8.1 Abstract

Electron-electron interactions are the fastest processes in materials, occurring on femtosecond to attosecond time scales, depending on the electronic band structure of the material and the excitation energy. Such interactions can play a dominant role in light-induced processes such as nano-enhanced plasmonics and catalysis, light harvesting or phase transitions. However, to date it has not been possible to experimentally distinguish fundamental electron interactions such as scattering and screening. Here, we use sequences of attosecond pulses to directly measure electron-electron interactions in different bands of different materials with both simple and complex Fermi surfaces. By extracting the time delays associated with photoemission, we show that the lifetime of photoelectrons from the d band of Cu are longer by ~100 attoseconds compared with those from the same band of Ni, because of enhanced electron-electron scattering in the unfilled d band of Ni. Moreover, we also show that screening influences high-energy photoelectrons (≈20 eV) significantly less than low-energy photoelectrons. As a result, high-energy photoelectrons can serve as a direct probe of spin-dependent electron-electron scattering, yielding information that is directly applicable to quantifying the contribution of screening to low-energy excitations near the Fermi level, and providing valuable information for a host of magnetic materials.

8.2 Introduction

8.2.1 Probing Excited-State Electron Dynamics in Materials

Excited state electron dynamics in materials play a critical role in light-induced phase transitions in magnetic and charge density wave materials, in superdiffusive spin flow, in catalytic processes, and in many nano-enhanced processes. However, to date exploring such dynamics is

challenging both experimentally and theoretically. Using femtosecond lasers in combination with advanced spectroscopies, it is possible to measure the lifetime of excited charges and spins directly in the time domain [253]. To date, such studies have been applied to a wide variety of materials, including noble metals and semiconductors [253–256], ferromagnetic metals [227,257–259], strongly correlated materials [208] and high-T_c superconductors [260,261]. These studies have significantly improved our understanding of the fastest coupled interactions and relaxation mechanisms in matter. However, to date experimental investigations of electron dynamics have been limited to femtosecond time-scale processes in materials with low charge densities [208,260–262] or to Fermi-liquid metals with low excitation energies (<3.0 eV above E_F, where E_F is the Fermi energy) [255–257], due to the visible-to-UV-wavelength photon energies used in these experiments. In this region, two fundamental electron interactions – electron-electron scattering and charge screening due to a rearrangement of adjacent charges - contribute to the signal, making it challenging to independently probe these dynamics. On the theory side, initial studies in the late 1950s were enabled by the seminal Fermi-liquid theory of Landau [263–266]. In exciting recent developments using the self-energy formalism of many-body theory and the random phase approximation, calculations of electron-electron interaction in materials - that include the material band structure - have now become possible [267–272]. Thus, experimental approaches that can distinguish between different electron-electron interactions, particular with band specificity, are very important and timely.

8.2.2 Distinguishing Attosecond Electron-Electron Scattering and Screening

High harmonic generation (HHG) provides attosecond pulses and pulse trains that are perfectly synchronized to the driving laser, and which are ideal for probing the fastest coupled charge and spin dynamics in atoms, molecules, and materials

[32,35,42,54,55,88,104,136,229,273,274]. To date, two approaches have been used to probe attosecond electron dynamics in matter through photoemission, taking advantage of laser-assisted photoemission (LAPE) sidebands [55,273]. For atoms, since the energy separation between different states is large, attosecond streaking using isolated attosecond pulses (with an energy resolution of several eV) has been applied very successfully [42,229]. The same approach has also been used to measure the transit time for a photoelectron to be emitted from the surface of a material. The RABBITT method [32,54,104] (reconstruction of attosecond beating by interference of two-photon transitions) has also been very successfully applied to atomic and material samples, where quantum interferences between neighboring two-photon transition pathways can modulate these sidebands as a function of the relative time delay between the HHG pump and infrared (IR) probe pulses: any time delay in photoemission from different initial or final states will lead to a phase delay in the interferograms [104,136].

In chapter 7, by combining attosecond HHG pulse trains with time- and angle-resolved photoemission (ARPES), I demonstrated the ability to resolve attosecond electron dynamics in different individual final states in materials for the first time, with ≈20 attosecond time resolution. I used attosecond-ARPES to measure a photoelectron lifetime of ~210 as, which was measured for a final-state that coincides with an unoccupied excited state in the band structure of Ni [35,274]. I also showed that the photoelectron lifetime sensitively depends on the band dispersion of the material i.e., the photoelectron emission angle. That work demonstrated that *atto-ARPES can probe intrinsic properties of materials*. A great advantage of atto-ARPES is that it achieves good energy resolution (<0.3 eV), to enable band-selectivity as well as angle-resolved studies, combined with the ability to change the HHG polarization, which are all critical for harnessing photoemission selection rules. This makes it possible, in principle, to selectively capture electron

dynamics in different initial or final bands in many materials, since the typical separation between neighboring valence bands is <1 eV.

Here, we use sequences of attosecond pulses coupled with time-, energy-, polarization-, and angle-resolved photoelectron spectroscopy (atto-ARPES) to distinguish electron-electron interactions for electrons excited from different initial bands during the photoemission process. The high photoelectron energies (E-E_F >20 eV), combined with attosecond time resolution, allows us to independently measure electron-electron scattering in metals with simple and complex Fermi surfaces, without the influence of screening, for the first time. To achieve this, we extract the time delays associated with photoemission from individual valence bands in Ni(111) and Cu(111). We find that the lifetime of photoelectrons from a *d* band of Cu is longer by ~100 attoseconds compared to the lifetime of those from the same band of Ni. We attribute this difference to the fact that the *d* band in Ni is not fully occupied, resulting in enhanced electron-electron scattering and hence a shorter photoelectron lifetime (see Figure 8.1a). Then, using a spin-dependent scattering model to compare electron-electron interactions in Cu and Ni, we show that the photoexcited electron lifetime in Ni involves enhanced electron-electron scattering throughout the energy range from 0.5 eV to 40 eV. Moreover, because screening influences high-energy photoelectrons (≈ 20 eV) significantly less than low-energy photoelectrons [270,272], they can serve as a direct probe of spin-dependent electron-electron scattering. The resulting Coulomb interaction information we extract is applicable across a broad energy range - from the Fermi energy on up – and can separate and quantify the contribution of screening to low-energy excitations, where both screening and scattering contribute to the signal. Our atto-ARPES approach thus makes it possible to independently distinguish the fastest electron-electron scattering and screening dynamics in metals on attosecond time scales, providing valuable information for a host of magnetic materials.

8.3 Sample Surface Preparation

The Cu(111) and Cu(001) samples used in our experiment are commercially available single crystals (Princeton Scientific Corp, diameter 10 mm × thickness 2 mm) with surface polish roughness of <10 nm and orientation accuracy <0.1 deg. Sample cleaning is performed in the same UHV chamber used for the photoemission measurements, with a base pressure $<5\times10^{-10}$ torr. The cleaning procedure for both crystal surfaces follows the same sequence of repeated cycles of Ar ion sputtering (beam energy 0.7 keV) at room temperature and subsequent annealing to 820 K. The sample surface quality is confirmed by monitoring the low energy electron diffraction (LEED) patterns and the sharpness of the static photoemission spectra. For the Cu(111) single crystal, the Shockley surface state can be clearly distinguished for an atomically clean surface. The samples are electrically grounded during all static and dynamic measurements. The preparation of Ni(111) surface is discussed in Section 7.3.

8.4 Static ARPES Spectra of Cu(111) and Cu(001)

The band structure of Cu is plotted in Figure 8.2, which is quite similar to Ni band structure discussed in chapter 7 [35]. According to the theoretical density-functional theory (DFT) calculations, there are three bands along Γ-L that contribute to the photoemission spectra: two valence bands with Λ_3 symmetry (Λ_3^{α} with lower binding energy of ~2.8 eV and Λ_3^{β} with higher binding energy of ~3.5 eV) and one deeper valence band with Λ_1 symmetry (~ 3.8 eV). In our experiments, photoemission from the Cu(100) surface is also measured, whose surface normal corresponds to a band structure along Γ - X direction (Figure 8.2).

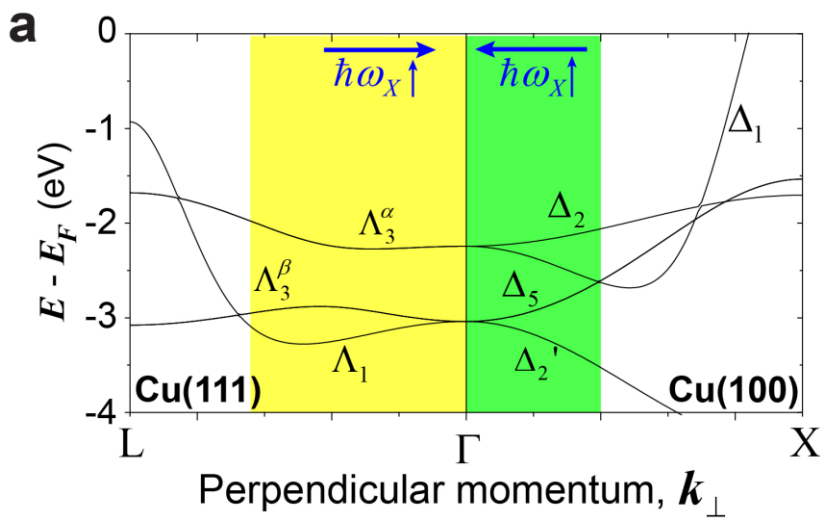

Figure 8.2: Band structure of Cu. (a) Band structure of Cu along the Γ-L direction for Cu(111), and Γ-X for Cu(100), showing the evolution of the Λ bands to Δ bands across the Γ point. Due to the photoemission selection rules [157], transitions from Δ_2 bands are forbidden in the normal emission geometry from Cu(100). The colored areas indicate the perpendicular momentum regions measured in our experiments. Blue arrows indicate the direction in which the HHG photon energy ($\hbar\omega_X$) increases.

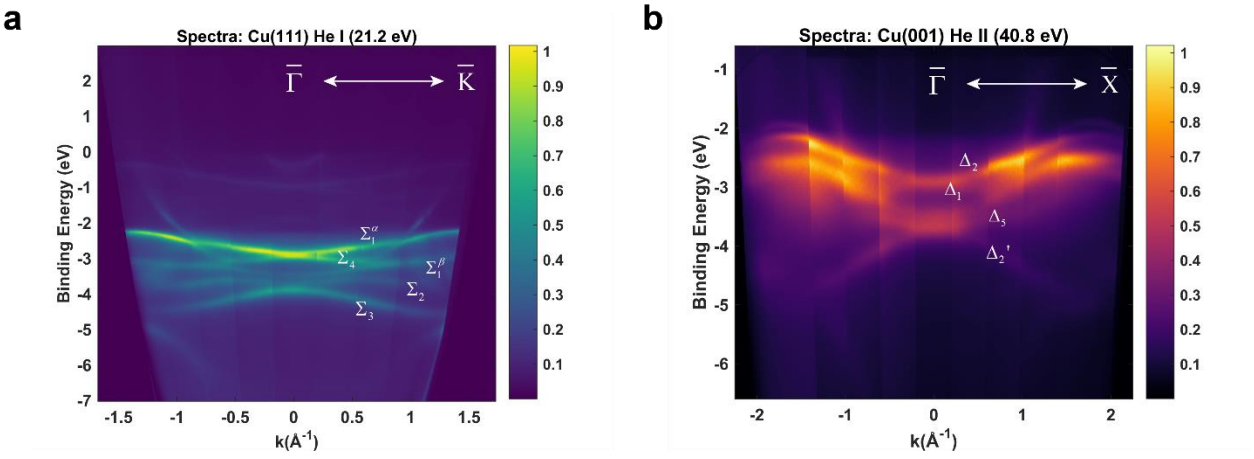

Figure 8.3: Photoelectron spectrum of Cu(111) and Cu(001). (a) ARPES spectrum of Cu(111)along the $\bar{\Gamma}$-$\bar{K}$ direction taken using the He Iα (21.2 eV) line from a He discharge lamp. (b) ARPES spectrum of Cu(001) along the $\bar{\Gamma}$-$\bar{X}$ direction taken using the He II line (40.8 eV) from a He discharge lamp.

We measure the static spectra of the sample at the room temperature using a helium discharge lamp (Specs UVS300, unpolarized radiation). Cu(111) is measured using the He Iα line at 21.2 eV, which can clearly visualize the surface state. The static spectra of Cu(001) surface is obtained using the He II line at 40.8 eV, which is near the HHG photon energy range used in time-resolved experiment on Cu(001). The spectra are recorded with a hemispherical angle-resolved electron analyzer (Specs Phoibos 100, acceptance angle is ±15^o under wide angle mode) and taken along the $\bar{\Gamma}$-$\bar{K}$ direction of the surface Brillouin zone for the Cu(111) surface, and along the $\bar{\Gamma}$-$\bar{X}$ direction for the Cu(001) surface. During the measurement, the sample is mounted on a XYZ manipulator with azimuthal angle adjustment so that the crystal orientation and position of the pump and probe beams can be adjusted.

Figure 8.3a shows the band structure of Cu(111) along $\bar{\Gamma}$-$\bar{K}$ measured using the He Iα source. The Cu(111) single crystal features a Shockey surface state at ~0.4 eV below the Fermi surface. In terms of the bulk bands, all the original Λ bands along the Γ-L direction evolve into Σ bands along the $\bar{\Gamma}$-$\bar{K}$ direction. The Λ_3^α band with a binding energy ~2.8 eV splits into $\sum_1^\alpha$ and Σ_4 bands. The lower Λ_3^β and Λ_1 bands with binding energies around 3.6 eV evolve into $\sum_1^\beta$, Σ_2 and Σ_3 bands. Due to the wave-function symmetry of these bands, they can be selectively excited with polarized HHG light [157].

The band structure of Cu(001) along $\bar{\Gamma}$-$\bar{X}$ measured using a He II line is plotted in Figure 8.3b. Since emission from the Γ-point of the bulk band structure in Cu(001) occurs at photon energy around 41 eV, which is close to the He II 40.8eV photon energy, Figure 8.3b manifests the transition along the Δ axis of the bulk Brillouin zone [144,275]. The two degenerate upper bands at the Γ-point with binding energy ~2.9 eV are Δ_1 and Δ_2 bands. The lower two bands crossing at the Γ-point with binding energy ~3.7 eV are $\Delta_{2'}$ and Δ_5 bands. These two lower bands both exhibit

double components due to spin-orbit splitting. In the normal emission geometry, photoemission from bands with a Δ_2 geometry is forbidden because of selection rules, allowing us to unambiguously extract the photoemission delay between the Δ_1 and Δ_5 bands.

8.5 Experimental Setup

The experimental setup (Figure 8.4) is similar to the one described in section 7.4. Most of the output of a near infrared (IR) femtosecond laser is used to generate high harmonics in various noble gases (Xe, Kr and Ar), which are then focused onto single crystal Cu(111) and Ni(111) surfaces. In the spectral domain, these harmonics span ~15-45 eV (corresponding to 11ω - 27ω), each with a linewidth of ~0.3 eV, and separated by $2\omega_L \approx 3.2$ eV, where ω_L is the frequency of the driving infrared (IR) laser. The residual phase-locked laser field is used to simultaneously irradiate the material together with a high harmonic field, which induces sidebands of the photoelectron peaks corresponding to the absorption or emission of an IR laser photon. The photoelectron spectrum is then collected using a hemispherical photoelectron analyzer (Specs Phoibos 100). Note that it has already been shown that RABBITT and attosecond-streaking yield the same temporal information about the photoemission process [136], while ARPES adds significant advantages of band-specificity [35]. Moreover, by simultaneously measuring two photoelectron wavepackets from different initial states excited by the same harmonic orders, we can eliminate the influence of the HHG phase [104].

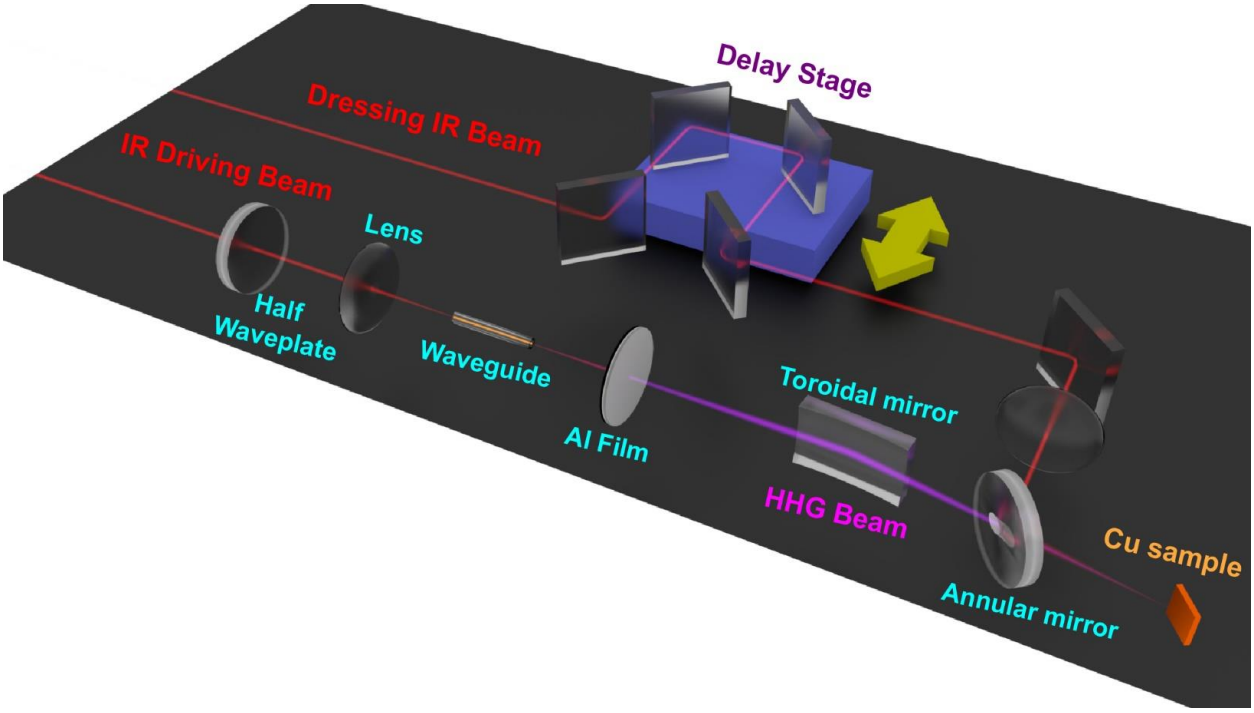

Figure 8.4: Experimental setup.

8.6 Static HHG Photoelectron Spectra Analysis of Cu(111)

Experimentally, the band dispersions of Cu(111) along the Γ-L direction are extracted from the HHG-excited photoelectron spectra in a normal emission geometry. As shown in Figure 8.5(a-b), photoemission dipole transitions couple different initial and final states (bands) of Cu(111) that can be selected using different harmonic orders and polarizations. By utilizing the good energy resolution of attosecond pulse trains and photoemission selection rules for s- and p-polarized HHG beams, we can unambiguously identify the peaks corresponding to different initial states [35,38]. Since the Λ_1 band can only be excited by light fields polarized perpendicular to the sample surface [148,157], we can assign the two spectral peaks excited by s-polarized HHG light as photoelectrons from Λ_3^{α} and Λ_3^{β} bands. We first obtain the photoelectron energy distribution curves (EDCs) corresponding to surface normal (Γ-L) emission by integrating the angle-resolved

spectra over an angle of ±2° around the $\bar{\Gamma}$ point and deduct the secondary electron background using the Shirley background subtraction [250]. The energy of the Fermi level of each EDC is determined with the knowledge of the photon energies and the analyzer work function. We then use a double Voigt function to fit the EDCs and extract their spectra intensity and binding energy, as shown in Figure 8.6(a-b). The Gaussian linewidths of the Voigt function are set to the experimental resolution of ≈0.3 eV.

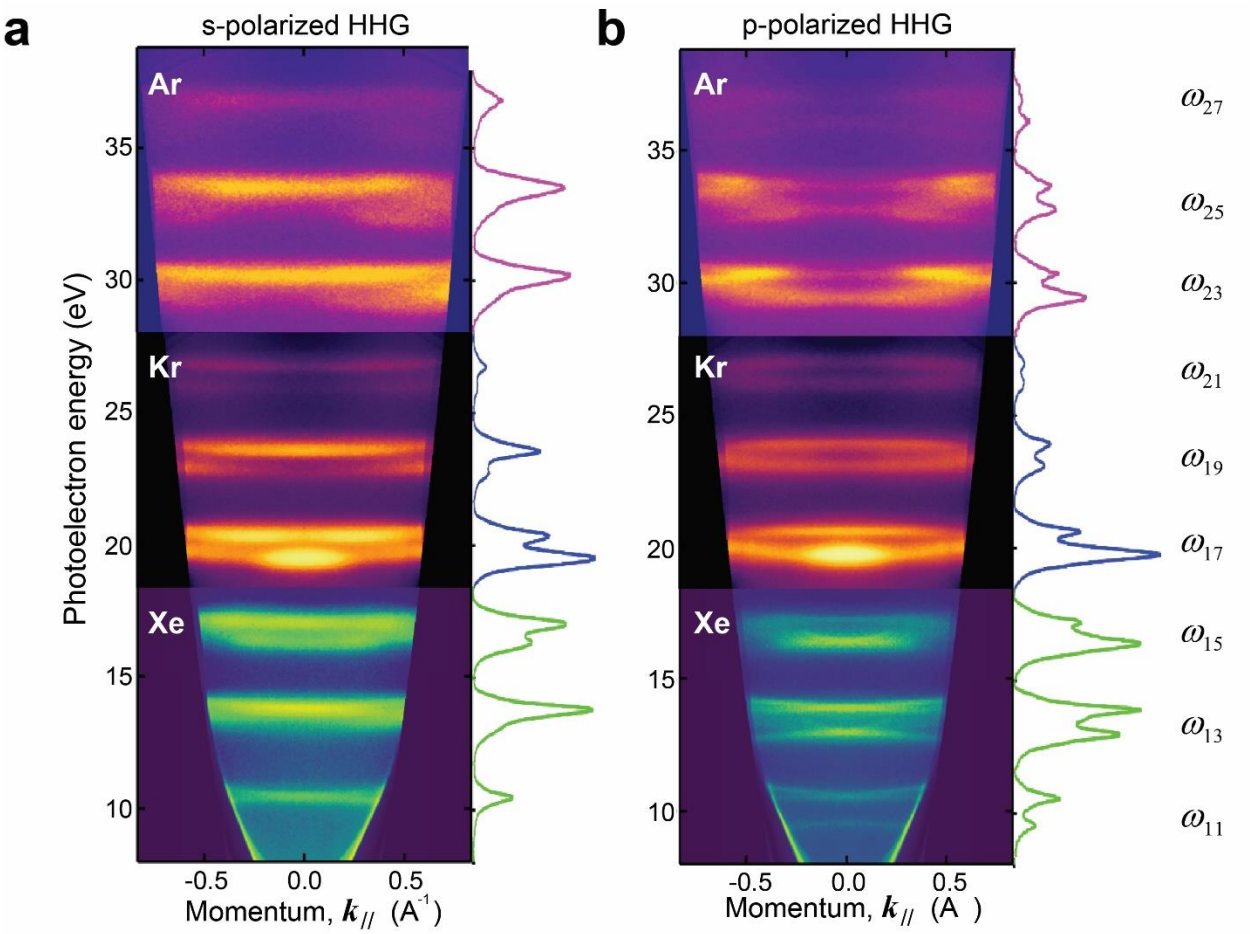

Figure 8.5: **HHG-excited photoelectron spectra of Cu(111).** Static ARPES spectra excited by s-polarized (a) and p-polarized (b) HHG field, generated using different noble gases (Xe, Kr and Ar).

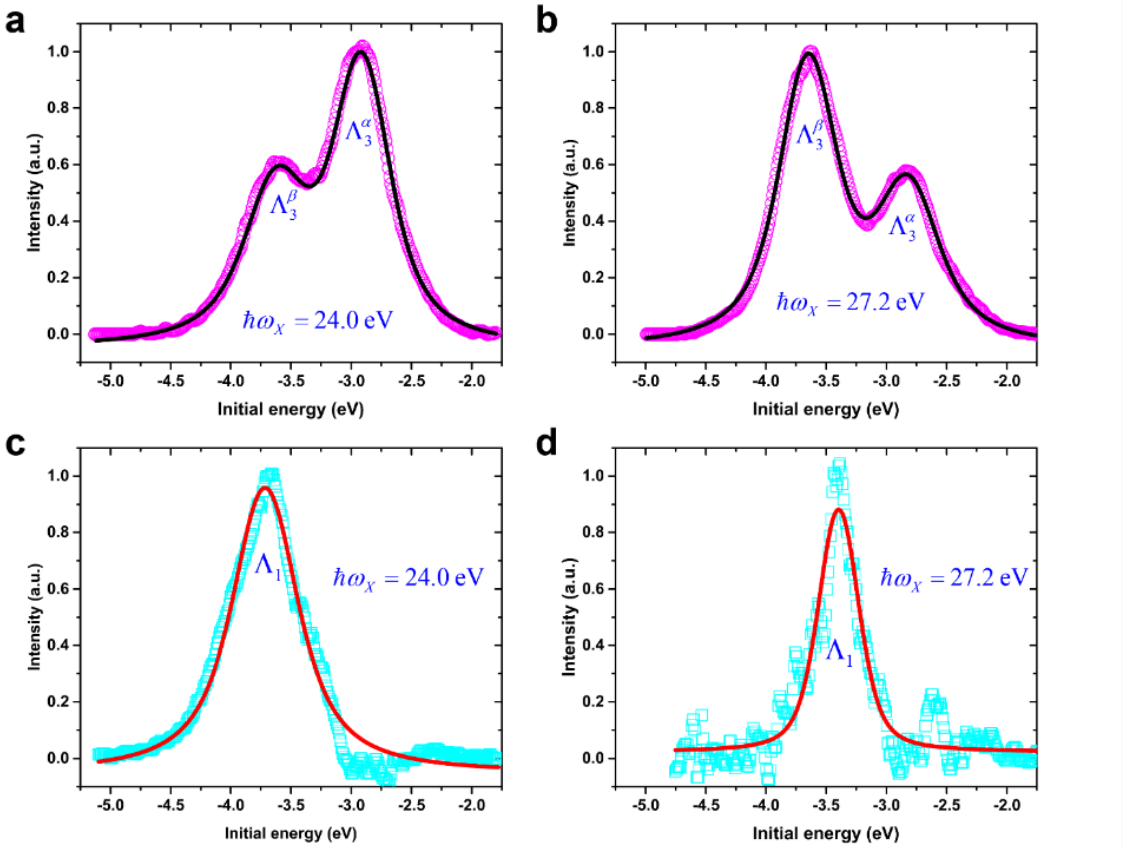

Figure 8.6: Static spectral analysis of photoemission from Cu(111) surface. (a) and (b) Experimentally measured EDCs excited by s-polarized HHG field (magenta open circles). The intensity and binding energies of Λ_3^α and Λ_3^β bands are extracted by fitting the EDCs with double Voigt functions (solid black lines). (c) and (d) The spectral intensity of Λ_1 is extracted by taking the difference spectra between EDCs excited by s- and p-polarized HHG fields (cyan open squares). The intensity and binding energies are determined by fitting the EDCs with a single Voigt function (solid red lines).

To extract information about the Λ_1 band, the EDCs excited by the same harmonic orders but with different polarizations (s- and p-) are normalized to equalize the intensity of the Λ_3^α band. The additional spectral weight in the photoelectron spectra excited by p-polarized HHG is assigned as photoemission from the Λ_1 band. We obtain its spectral intensity and binding energy by fitting it with a single Voigt function, as shown in Figure 8.6(c-d).

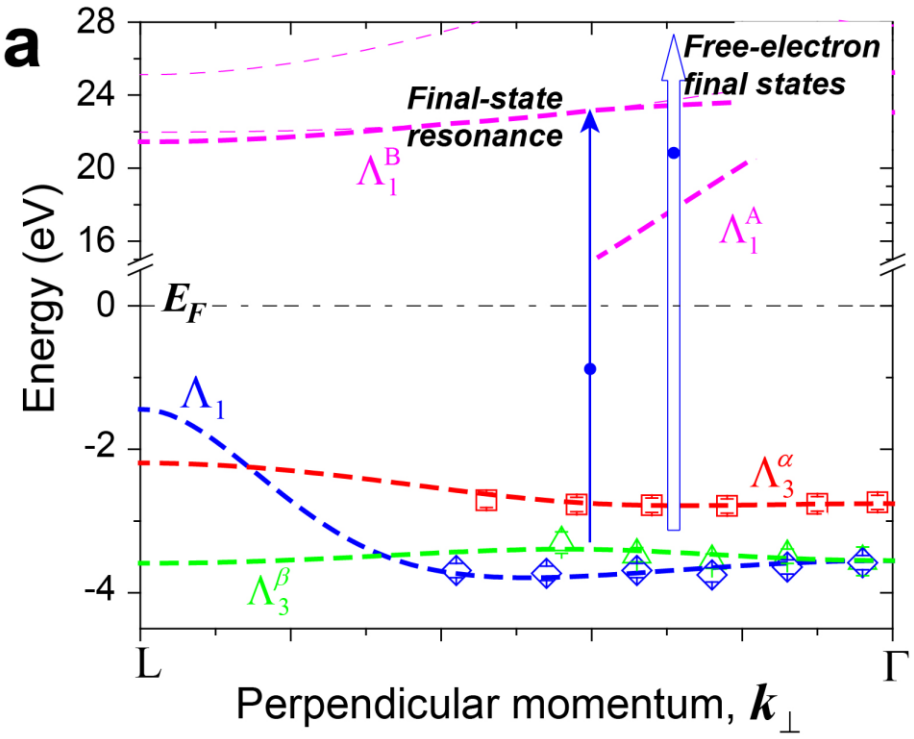

Figure 8.7: Band mapping of Cu(111). Band structure of Cu(111) along the Γ-L direction from DFT calculation (dashed lines), compared with experimental results of band mapping. The interband transition $\Lambda_3^\beta \rightarrow \Lambda_1^B$ is highlighted by the blue arrow, which corresponds to the spectral enhancement of the photoelectron spectrum at harmonic orders ω_{15} and ω_{17} as shown in Figure 8.5.

The band-mapping results using s- and p-polarized HHG light are plotted in Figure 8.7, showing good agreement with the band structure obtained from DFT calculations. The inner potential of Cu(111) is 8.6 eV according to previous photoemission studies [276]. We observe a strong dispersion of the photoemission peaks as a function of photon energy, indicating that photoemission from bulk states contributes to the signal.

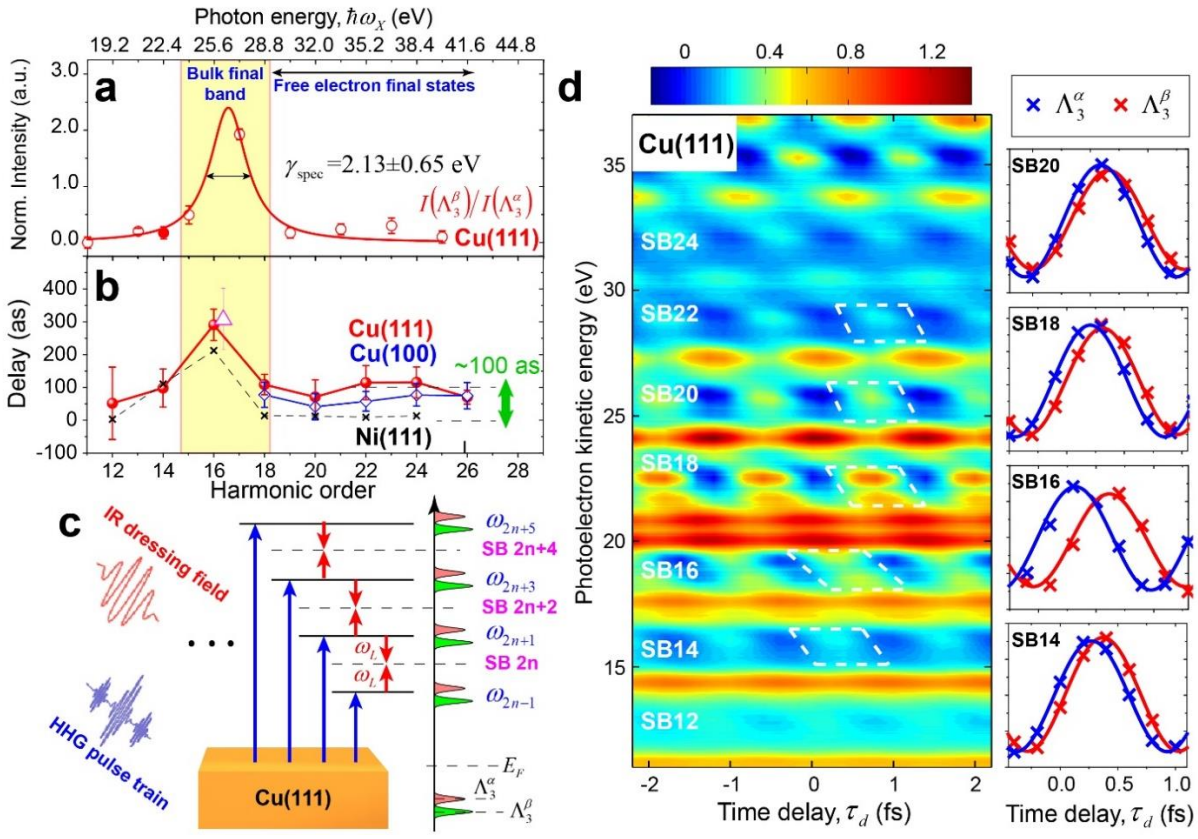

Figure 8.8: Comparison of photoelectron lifetimes in Cu(111) and Ni(111). The comparison includes photoelectron lifetimes for photoemission either into excited-states (on resonance, ≈ 25 eV) or into free-electron states (off resonance). (a) Normalized spectral intensity of the Cu(111) Λ_3^β band as a function of photon energy. The filled symbol (14th order) is obtained from HHG driven by 390-nm laser field. The red solid line represents the Lorentzian fitting to the spectral intensity, which yields a linewidth of 2.13±0.65 eV. (b) Photoemission time delay $\tau_{PE}(\Lambda_3^\beta) - \tau_{PE}(\Lambda_3^\alpha)$ as a function of photon energy for both Cu(111) and Ni(111) surfaces. The time delay $\tau_{PE}(\Delta_5) - \tau_{PE}(\Delta_1)$ measured for a Cu(100) surface is also plotted for comparison. The open triangle represents the lifetime derived from the linewidth in (a). (c) Illustration of the quantum-path interference in RABBITT measurements. Electrons from two initial states (Λ_3^α and Λ_3^β) are excited by multiple harmonic orders into different final states. By absorbing and emitting one additional IR photon (ω_L), quantum-path interference causes spectral modulation at the side bands (SB) in between neighboring harmonic orders. (d) Two-dimensional map of photoelectron spectral intensity as a function of photoelectron energy and HHG-laser field time delay τ_d. The relative time delay between photoelectrons from Λ_3^β and Λ_3^α initial bands are highlighted as large offsets in oscillations in the sideband region by white dashed boxes. Right panel: 1D lineouts for the spectral modulations with angular integration of ±2.5° around the Γ point of photoelectrons from Λ_3^β and Λ_3^α initial bands in the selected side-band region.

8.7 Final-State Resonance in Cu(111)

To distinguish the influence of wavefunction localization (excited bulk states vs. free-electron final states) as well as the influence of the fundamental electron interactions on the photoelectron lifetimes, we first identify where the final-state resonances occur in Cu(111). The spectral intensity of Λ_3^β band photoelectrons excited by the s-polarized HHG field is plotted in Figure 8.8a. A strong enhancement of the spectral intensity peaked around the 15th order at the resonant photon energy of ~26 eV can be observed, which can be attributed to the interband transition from the Λ_3^β initial band to the excited Λ_1^B final band (Figure 8.7). The Lorentzian linewidth is γ_{spec}=2.13±0.65 eV (Figure 8.8a), which is consistent with the linewidth recently obtained using high-resolution photoemission at a synchrotron radiation source [144]. The predicted final-state lifetime is therefore given by $\tau_{spec} = \hbar/\gamma_{spec}$ = 309±94 as.

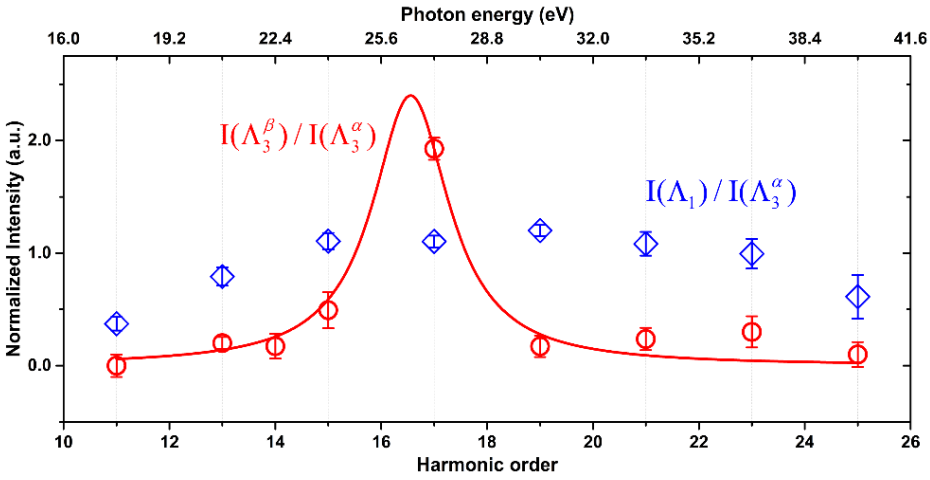

Figure 8.9: Spectral intensity of Λ_3^β and Λ_1 bands. Photoemission intensities of the Λ_3^β (red open circle) and Λ_1 (blue open diamond) bands relative to that of the Λ_3^α band. The red solid line represents the Lorentzian lineshape fit to the intensity of the Λ_3^β band as a function of photon energy, which yields a linewidth of 2.13±0.65eV (Figure 8.8a).

The photoemission time delay $\tau_{PE}\left(\Lambda_3^{\beta}\right)-\tau_{PE}\left(\Lambda_3^{\alpha}\right)$ at the Γ point can be extracted from the RABBITT interferogram (Figure 8.8d) and is summarized in Figure 8.8b. The quantum paths involved in RABBITT interference are illustrated in Figure 8.8c. These interferograms (Figure 8.8d) were obtained by integrating the photoelectron spectra over ±2.5° around the Γ point (normal-emission direction). Comparing Figures 8.8a and 8.8b, we find that $\tau_{PE}\left(\Lambda_3^{\beta}\right)-\tau_{PE}\left(\Lambda_3^{\alpha}\right)$ at the Γ point reaches its maximum value τ_{chron}=291±48 as at the resonant photon energy for the interband transition $\Lambda_3^{\beta}\rightarrow\Lambda_1^{\text{B}}$ (Figure 8.7), which is in good agreement with $\tau_{\text{spec}}\approx$ 309±94 as. This agreement indicates that the lifetime of photoelectrons emitted from the initial Λ_3^{α} band ($\tau_{PE}\left(\Lambda_3^{\alpha}\right)$) is short at the Γ point. Considering the fact that the spectral intensity of Λ_3^{α} is a smooth function of photon energy (Figure 8.9), it allows us to directly assign the measured time delay to the lifetime of photoelectrons from the Λ_3^{β} band. Compared to Ni(111) results in chapter 7 [35], the resonant linewidth from the initial Λ_3^{β} band in Cu is narrower, which is consistent with the longer lifetime measured in the time domain (291±48 as for Cu vs. 212±30 as for Ni).

8.8 Momentum Dispersion of Photoelectron Lifetime

To extract the angle-dependent photoemission time delay, we first divide the angle-resolved photoemission spectra into 16 angular regions at each side band, with a ~1.8° angular span over the entire range of photoelectron emission angle (-15°< θ <15°), as shown in Figure 8.10a. The photoelectron counts in each region are integrated and plotted as a function of pump-probe time delay τ_d to obtain the angle-dependent RABBITT interferograms. Typical interferograms at the spectral resonance are plotted in Figure 8.10(b-c). In this way, the angle-

dependent photoemission time delays for photoelectrons originating from different bands [$\tau_{PE}\left(\Lambda,\theta\right)$] can be extracted.

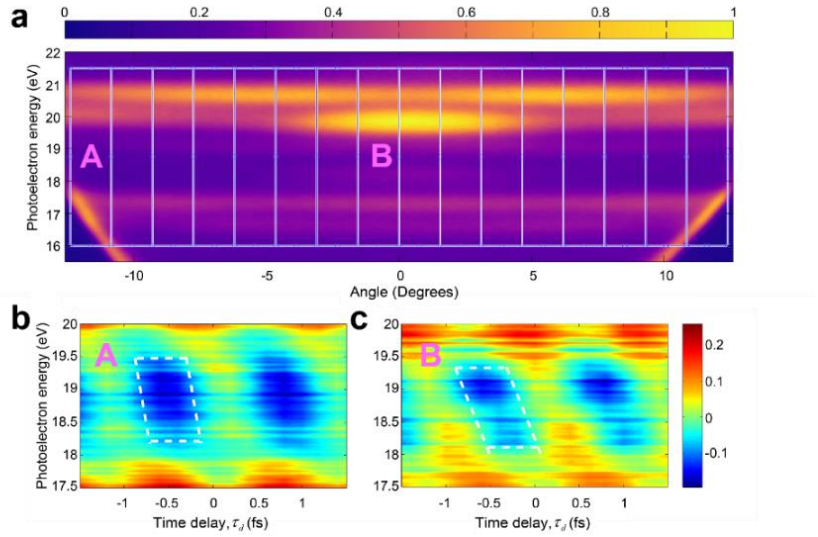

Figure 8.10: Extraction of angle-dependent photoemission time delay. (a) Illustration of the angular regions for integration when extracting the angle-dependent photoemission time delay. The energy region corresponding to SB16 is used as an example here. (b-c) Typical RABBITT interferograms for SB16 with emission angles [(A) and (B)] labeled in (a). The offset is highlighted with white dashed boxes.

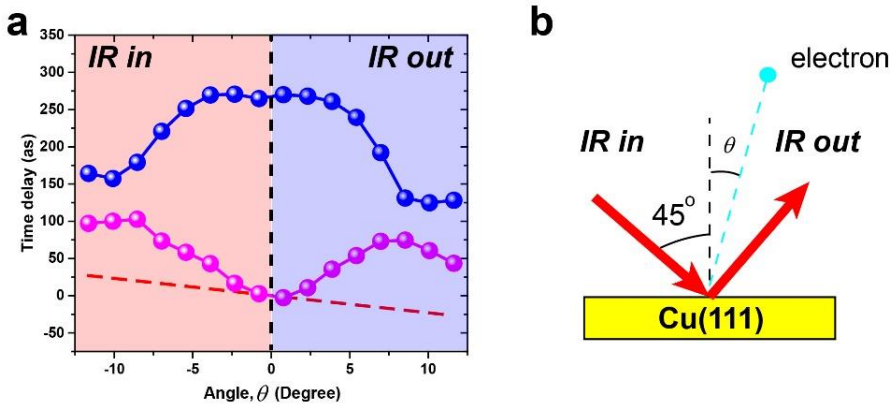

Figure 8.11: Angle-dependent photoemission time delay. (a) Angle-resolved photoemission time delay at the resonant photon energy (SB16) of photoelectrons from both the Λ_3^{α} and Λ_3^{β} initial bands (s-polarized HHG fields) are plotted as blue and magenta symbolled lines. The photoemission delay of Λ_3^{α} band photoelectrons at θ=0 ($\tau_{PE}\left(\Lambda_3^{\alpha},0\right)$) is used as the timing reference. The red dashed line indicates the angle dependent delay imposed by the IR dressing field. (b) Experimental geometry of laser excitation and photoelectron detection.

The angle-dependent time delay due to band-structure effect alone should be symmetric with respect to the Γ point. However, as shown in Figure 8.11a, when we use the phase corresponding to the Λ_3^α band at the Γ point [$\tau_{PE}\left(\Lambda_3^\alpha,0\right)$] as the timing reference, the time delays extracted from the two equivalent regions on the two sides of the Γ point are different. This is also observed in other side-band regions (both resonant and non-resonant). The photoemission time delay induced by IR probing field can be simulated using the semiclassical model (details presented in Ref. [60,118]). The IR field distribution is calculated using the Fresnel equations with the optical parameters of Cu extracted from Ref. [240]. The simulation results are plotted in Figure 8.11a as the red dashed line. The results show that the photoelectrons emitted from IR incident side is relatively delayed to those emitted from the IR exit side. The delay depends linearly on the electron emission angle θ (Figure 8.11b) with a slope of ~2.15 as/deg. This slope is quantitatively consistent with the background delay of the experimentally measured angle-dependent photoemission time delay (Figure 8.11a) and is also qualitatively consistent with the field effects reported before [60,118]. We note that because the binding energies of Cu(111) Λ_3^α and Λ_3^β band are very similar ($\Delta E \approx 0.7$ eV), the IR-laser induced angular dependence of time delay are very similar for photoemission from both bands. This allows us to cancel the laser-induced time delay by subtracting the photoemission time delay of one band from the other ($\tau_{PE}\left(\Lambda_3^\beta,\theta\right)-\tau_{PE}\left(\Lambda_3^\alpha,\theta\right)$).

8.9 Lifetime of Photoelectrons from Λ_1 Band

The relative photoemission time delays between L_1 and Λ_3^α bands [$\tau_{PE}\left(\Lambda_1\right)-\tau_{PE}\left(\Lambda_3^\alpha\right)$] can be extracted from experimental results of both s- and p-polarized HHG fields. The time delay $\tau_{PE}\left(\Lambda_3^\beta\otimes\Lambda_1\right)-\tau_{PE}\left(\Lambda_3^\alpha\right)$ is the result obtained with p-polarized HHG field, where the low-energy

photoemission peak has the convoluted contributions from both Λ_1 and Λ_3^β bands. The retrieval algorithm was described in detail in Chapter 7. The retrieved photoemission time delay $\tau_{PE}\left(\Lambda_1\right)-\tau_{PE}\left(\Lambda_3^\alpha\right)$ is plotted in Figure 8.12. The error bar is determined by considering the errors of the RABBITT measurements using both s- and p-polarized HHG lights. We note that for Cu(111) surface, $\tau_{PE}\left(\Lambda_1\right)-\tau_{PE}\left(\Lambda_3^\alpha\right)$ exhibits a discontinuity and abrupt change in sign at SB 18. This is due to the contribution of surface state excited by p-polarized HHG field. We also note that it does not affect our conclusion, which was based on the results measured using s-polarized HHG field.

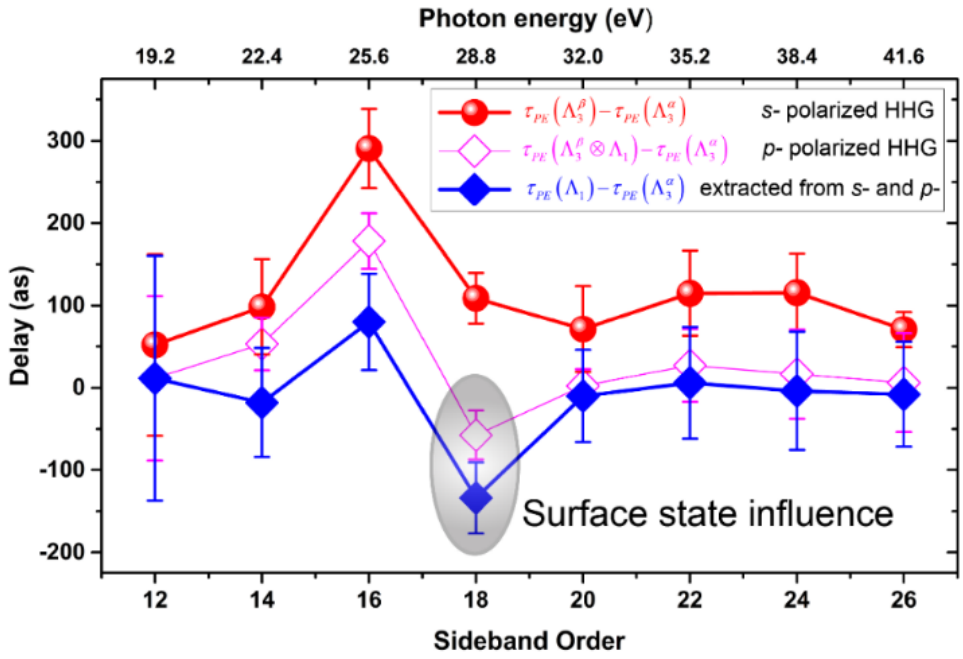

Figure 8.12: Photoemission time delay of Λ_3^β and Λ_1 bands relative to the Λ_3^α band. Time delays $\tau_{PE}\left(\Lambda_3^\beta\right)-\tau_{PE}\left(\Lambda_3^\alpha\right)$ and $\tau_{PE}\left(\Lambda_3^\beta\otimes\Lambda_1\right)-\tau_{PE}\left(\Lambda_3^\alpha\right)$ as a function of photon energy are obtained by exciting photoemission using p-polarized HHG fields, respectively. $\tau_{PE}\left(\Lambda_1\right)-\tau_{PE}\left(\Lambda_3^\alpha\right)$ is extracted by combining the s- and p-polarized delay and the relative photoemission intensity of Λ_1 and Λ_3^α bands in Figure 8.9. The ellipse marks the contribution of surface state to the RABBITT interferogram at sideband 18.

8.10 Photoelectron Lifetime Difference between Cu and Ni

For photoemission through free-electron final states (away from any final-state resonances, >25 eV in Figure 8.13a), we find that the photoelectron lifetime from the Λ_3^β band of Cu(111) is ~100 as in the normal-emission geometry. Moreover, this lifetime is a smooth function of the final-state energy (Figure 8.13a). The associated time delay can be clearly seen in the experimentally measured interferograms of Cu(111) as an obvious phase shift in the oscillations of the RABBITT quantum interferences (Figure 8.13b), which interestingly is absent in Ni(111) for free-electron final states [35].

We note that we can exclude the possibility that the finite photoelectron lifetime in this energy range in Cu(111) is caused by another final-state resonance because we did not observe any photoelectron yield enhancement in this energy range (Figure 8.8a), and because that it exhibits little momentum (angle) dispersion - unlike the lifetime on resonance (Figure 8.13c). To further reinforce this conclusion, we also measured the photoemission time delay between the Δ_5 and Δ_1 bands along the Γ-X direction for Cu(100) as the two Λ_3 bands cross the Γ point of the Brillouin zone (Figure 8.4). As shown in Figure 8.8b, a similar lifetime difference between Δ_5 and Δ_1 band photoelectrons was observed on the Cu(100) surface when there is no spectral resonance. Excluding final-state effects, the ~100 as lifetime difference of photoelectrons from the Λ_3^β band for Cu(111) and Ni(111) must be attributed to differences in the fundamental electron-electron interactions experienced by the high-energy photoexcited electrons during photoemission from these two materials.

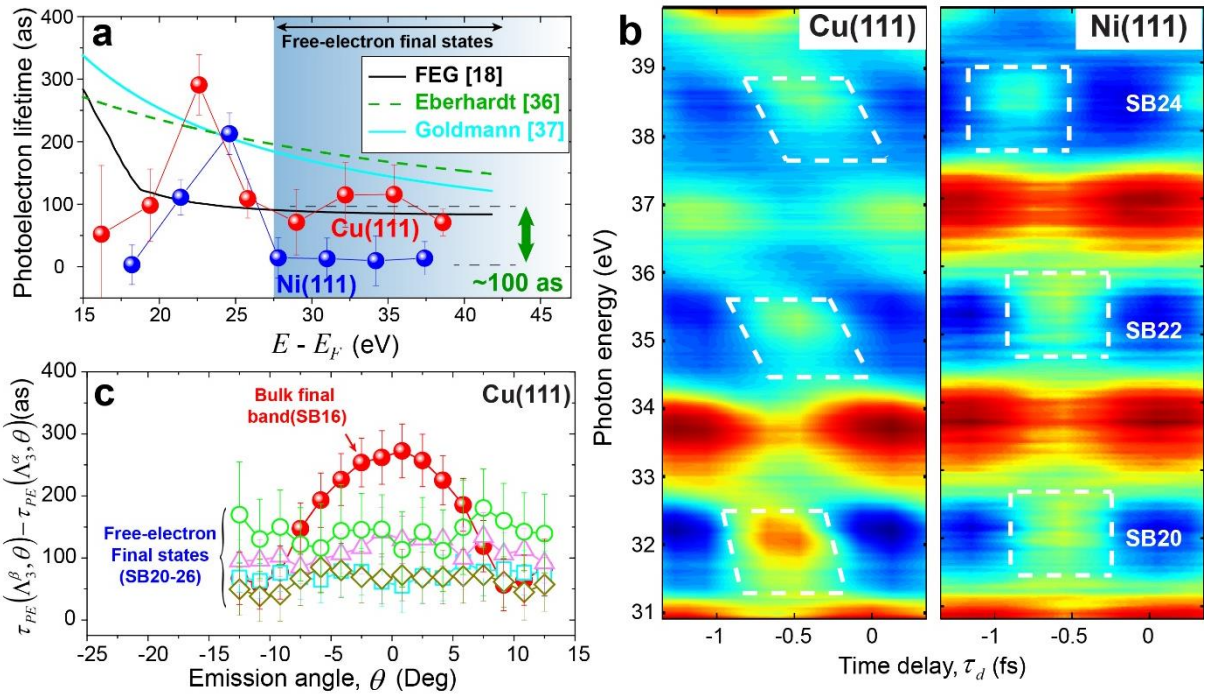

Figure 8.13. Origin of different photoelectron lifetimes for photoemission into free-electron final states for Cu and Ni. (a) Photoelectron lifetime emitted from Λ_3^β band measured using atto-ARPES as a function of the final-state energy (E-E_F) for both Cu(111) and Ni(111), in comparison with the FEG model (black) [268], Goldmann *et al.* (cyan) [277] and Eberhardt and coworkers (green dashed) [144] models. The lifetime corresponding to free-electron final states are highlighted in the colored region. (b) Interferograms for sidebands 20-24 (off-resonance, away from final-band resonance) measured from Cu(111) and Ni(111) [35] surfaces. Large offsets in the side band regions can be observed in the Cu(111) data, as highlighted by the white dashed boxes. Such offsets are absent for Ni(111). (c) Angle-dependent photoemission time delay of $\tau_{PE}\left(\Lambda_3^\beta,\theta\right)-\tau_{PE}\left(\Lambda_3^\alpha,\theta\right)$ measured on Cu(111), which clearly shows the difference between a resonant transition to a bulk final band (side band 16) and those to free-electron final states (side band 20: square; sideband 22: triangle; sideband 24: circle; and sideband 26: diamond).

8.11 Dynamic Screening and Inelastic Electron-Electron Scattering

The photoexcited electron lifetime for free-electron final states is mainly determined by the competition between dynamic screening and inelastic electron-electron scattering during the photoemission process [268]. This is because for highly excited electronic states (>20 eV), other

decay channels including scattering with photoholes, phonons and impurities are expected to have negligible contributions.

8.11.1 Absence of Electron Screening

In Figure 8.13a, we compare our measured photoelectron lifetime from the Λ_3^β band of Cu to two empirical models (Goldmann *et al*. [277] and Eberhardt and coworkers [144]) that are based on bulk excited-state linewidths, as well as a free-electron gas (FEG) model with r_s=2.67 for Cu [268], where r_s is the electron-density parameter defined for an electron density n by $n = 3/\left(4\pi r_s^3\right)$. As shown in Figure 8.13a, both empirical models agree well with the photoelectron lifetime on resonance (SB16) as expected; however, they overestimate the photoelectron lifetime off-resonance. This is not surprising – the Goldmann and Eberhardt models are derived from a linewidth analysis of photoemission and inverse photoemission experiments [144,277], that are mainly based on contributions from resonant (bulk final state) excitations. Compared to steady-state photoemission and inverse photoemission studies, our time-domain approach has unique advantages that allows us to measure the intrinsic high-energy photoelectron lifetime at arbitrary energies (including transitions both on and off final-state resonance). Note that the FEG model cannot reproduce the photoelectron lifetime on resonance, which is also not surprising since it does not account for the real band structure of the material. Most interestingly, the FEG model matches the off-resonance (i.e., free-electron final-state) lifetime measured on Cu(111) very well, but not for Ni(111), which is ~100 as shorter. Note that this trend is very different from the hot-electron lifetimes measured at low energy (<3 eV above E_F), which exhibit a strong deviation from the FEG model due to the added presence of screening of *d*-band electrons [267,269].

The absence of electron screening effects in high-energy photoemission can be understood by considering two different aspects. First, screening of *d* band electrons can be estimated by considering an effective dielectric constant $\varepsilon_d = 1 + \delta\varepsilon_d$ that is induced by the polarizable background of *d* electrons. At low energies, the corrected lifetime is larger than the value predicted by the FEG model by $\sqrt{\varepsilon_d}$ [278–280]. As pointed out by Quinn [281,282], $\delta\varepsilon_d$ reduces as a function of excitation photon energy. As a result, the variation of the photoelectron lifetime due to *d*-electron screening is estimated to be only a few percent of the FEG lifetime at energies >20 eV. Second, on ~100 attosecond time scales, we also need to consider the dynamics of electron screening in metals. As shown in previous theoretical studies, the buildup of charge screening in metals is not instantaneous, but takes approximately half of a plasma period to fully develop [283], which corresponds to ~200 as in both Cu and Ni. Because the off-resonance photoelectron lifetimes are much less than this, it appears that photoelectrons from Cu (and Ni) escape before dynamic screening can influence the photoelectron lifetime in this energy range. As a result, dynamic electron screening has negligible influence on the photoelectron lifetimes at energies > 20 eV.

8.11.2 Influence of Inelastic Electron-Electron Scattering

On the other hand, the ~100 as lifetime difference between photoelectrons from the *d* bands of Cu and Ni can be attributed to the differences in the band structure of these materials, which results in different electron-electron scattering rates between photoelectrons and other electrons in the conduction bands during photoemission. The scattering rate between photoelectrons and unexcited bulk electrons is calculated using Fermi's Golden rule, following the formulas presented in Refs. [258,284,285]. Because the unoccupied states above E_F in Ni are electronic states with

minority spins ($\downarrow$), spin-dependent electron-electron scattering needs to be taken into account. Here, we consider a high-energy photoexcited electron with energy E above E_F. This electron decays into a lower energy state E' by exciting one of the other electrons in the band (a scattering partner) from its original state ε into an unoccupied state above E_F, $\varepsilon+\Delta$, where $\Delta=E-E'$ is the energy transfer (see Figure 8.14a). We note that the scattering process illustrated in Figure 8.14a is responsible for removing photoelectron signal from our measurement. Thus, the experimentally measured photoelectrons are those that escape without scattering; nevertheless, the lifetimes of these electrons are influenced by scattering within the occupied bands, and experience different phase shifts in our RABBITT measurement.

The two-electron scattering processes presented in Figure 8.14a can be either a spin-conserving or a spin-flipping process for the photoexcited electron. In order to calculate the total probability of inelastic scattering between two electrons as shown in Figure 8.14a, the full quantum states of the two-particle initial and final states need to be taken into consideration. The Coulomb matrix element is given by $M^{Ek\sigma,\varepsilon k_1\sigma_1}_{E'k'\sigma',\varepsilon'k_2\sigma_2} \equiv \langle Ek\sigma,\varepsilon k_1\sigma_1|V|E'k'\sigma',\varepsilon'k_2\sigma_2\rangle$, where ($E$, k, σ) and (E', k', σ') are the initial and final states of the photoexcited electron and (ε, k_1, σ_1) and (ε', k_2, σ_2) are the initial and final states of the scattering partner. V is the screened electron-electron interaction. The spin indices σ_1, σ' and σ_2 either equal to σ or are opposite to σ ($\bar{\sigma}$). Specifically, when $\sigma'=\sigma$ the scattering is a spin-conserving process for the photoelectron, while if $\sigma'=\bar{\sigma}$, it is a spin-flipping one. The scattering process conserves the total spin-angular momentum of the two-electron system.

In principle, the matrix element $M^{Ek\sigma,\varepsilon k_1\sigma_1}_{E'k'\sigma',\varepsilon'k_2\sigma_2}$ can be calculated by considering the momentums of different states if the wave functions and selection rules are known. However, in general this information is not available allowing accurate calculations in materials. Here, we

assume the matrix element is independent to the momenta (k) of both electrons involved in the scattering process (random-$\boldsymbol{k}$ approximation) in order to investigate the effects of electron-electron scattering on the photoelectron lifetime. Indeed, as shown in Figure 8.13c, we verified experimentally that the assumption of a momentum-averaged Coulomb matrix element M is valid. The random-$\boldsymbol{k}$ approximation was first used by Berglund and Spicer to calculate the photoemission from Cu and Ag [149] and was later used to calculate electron-electron scattering probability in different materials [258,286–288]. It has been shown that with a proper choice of the momentum-independent matrix element, the results obtained from the random-$\boldsymbol{k}$ approximation can be in good agreement with more sophisticated calculations [289,290]. By considering the random-$\boldsymbol{k}$ approximation we can evaluate the electron-electron scattering rate by including the appropriate densities of states (DOS) and Fermi functions. As a result, we can write an averaged matrix element as $M^{E\beta\sigma,\varepsilon\alpha\sigma_1}_{E'\beta\sigma',\varepsilon'\alpha\sigma_2} \equiv \langle E\beta\sigma,\varepsilon\alpha\sigma_1 | V | E'\beta\sigma',\varepsilon'\alpha\sigma_2 \rangle$, where the energy ($E$), spin ($\sigma$) and orbital character (α, β) of the initial and final states are taken into consideration.

The spin-conserving processes scatter the photoexcited electron from an original state (E, σ) into an unoccupied state (E', σ), and can be formulated as -

$$\Gamma^{1)}(E\sigma,E'\sigma)=\frac{\pi}{\hbar}\sum_{\beta=s,p,d}\int_{E_F}^{E}dE'\,\rho_\sigma^{\beta,>}(E')\Bigg[\underbrace{\sum_{\alpha=s,p,d}\int_{E_F-\Delta}^{E_F}d\varepsilon\Big[\rho_\sigma^{\alpha,<}(\varepsilon)\rho_\sigma^{\alpha,>}(\varepsilon+\Delta)\Big|M^{E\beta\sigma,\varepsilon\alpha\sigma}_{E'\beta\sigma,\varepsilon'\alpha\sigma}-M^{E\beta\sigma,\varepsilon\alpha\sigma}_{\varepsilon'\alpha\sigma,E'\beta\sigma}\Big|^2}_{\mathrm{I}}, \quad (8.1)$$
$$+\underbrace{\rho_{\bar\sigma}^{\alpha,<}(\varepsilon)\rho_{\bar\sigma}^{\alpha,>}(\varepsilon+\Delta)\Big|M^{E\beta\sigma,\varepsilon\alpha\bar\sigma}_{E'\beta\sigma,\varepsilon'\alpha\bar\sigma}\Big|^2}_{\mathrm{II}}\Big]$$

where

$$\rho_\sigma^{\alpha,>}(E)=[1-f(E)]\rho_\sigma^{\alpha}(E)$$
$$\rho_\sigma^{\alpha,<}(E)=f(E)\rho_\sigma^{\alpha}(E), \quad (8.2)$$

where $f(E)$ is the Fermi-Dirac distribution function, and $\rho_{\sigma}^{\alpha}(E)$ is the spin-dependent density of states (DOS) of the α orbital that is obtained from a DFT calculation (see the inset of Figure 8.14c). $\Delta = E - E'$ is the energy transfer between the two electrons and σ_1 can be either σ (same to) or $\overline{\sigma}$ (opposite to photoexcited electron). The first term (I) in the integrand describes the scattering between a photoexcited electron with spin σ and an unexcited electron with the same spin. The fact that electrons are indistinguishable particles is taken into account. The second term (II) describes scattering between the photoexcited electron and an electron with opposite spin ($\overline{\sigma}$). We first neglect the interference term after expanding the modulus square of the matrix elements [287]. Then, following Ref. [258], we do not further distinguish between *s*, *p* and *d* states for the matrix element and assume *M* is energy-independent. As a result, we only have matrix elements for scattering between electrons with the same spins ($M^{\sigma\sigma}$) and opposite spins ($M^{\sigma\overline{\sigma}}$).We however note that energy-dependent matrix element (*M*) is obviously observed in current work and other studies, which we will illustrate by using different (but constant throughout energy) values of *M* to make agreement with low-energy and high-energy results obtained in experiments. Beyond the approach in Ref. [258], we assumed that the wavefunction character (*s*, *p* or *d*) of the initial and final states of an electron are the same during the scattering process. This was suggested by a recent all-electron *ab initio* calculations showing that the scattering rate between two electrons will be vanishingly small if the wave-function characters of the initial and final states are different [269]. For simplicity, we only distinguish between different wave functions for the scattering partner in the DOS assignment, but do not further distinguish it for the photoexcited electrons. As a result, the DOS used for the final state of photoexcited electrons is the total DOS, $\sum_{\beta=s,p,d} \rho_{\sigma}^{\beta,>}(E)$.With the considerations above, the Equation 8.1 is reduced to -

$$\Gamma^{1)}(E\sigma,E'\sigma)=\frac{\pi}{\hbar}\int_{E_F}^{E}dE'\sum_{\beta=s,p,d}\rho_{\sigma}^{\beta,>}(E')\sum_{\alpha=s,p,d}\int_{E_F-\Delta}^{E_F}d\varepsilon\left[\rho_{\sigma}^{\alpha,<}(\varepsilon)\rho_{\sigma}^{\alpha,>}(\varepsilon+\Delta)2\left|M^{\sigma\sigma}\right|^2+\rho_{\bar{\sigma}}^{\alpha,<}(\varepsilon)\rho_{\bar{\sigma}}^{\alpha,>}(\varepsilon+\Delta)\left|M^{\sigma\bar{\sigma}}\right|^2\right]\cdot \tag{8.3}$$

Similarly, the scattering rate for the spin-flip process is given by -

$$\Gamma^{2)}\left(E\sigma,E'\bar{\sigma}\right)=\frac{\pi}{\hbar}\int_{E_F}^{E}dE'\sum_{\beta=s,p,d}\rho_{\bar{\sigma}}^{\beta,>}(E')\sum_{\alpha=s,p,d}\int_{E_F-\Delta}^{E_F}d\varepsilon\,\rho_{\bar{\sigma}}^{\alpha,<}(\varepsilon)\rho_{\sigma}^{\alpha,>}(\varepsilon+\Delta)\left|M^{\sigma\bar{\sigma}}\right|^2\cdot \tag{8.4}$$

Note that in this process, the photoexcited electron must scatter with an unexcited electron with opposite spin in order to conserve spin-angular momentum in the process. The total scattering rate (which will correspond to the inverse of the lifetime τ_σ) is hence given by

$$\frac{1}{\tau_\sigma(E)}=\sum_{\sigma'=\sigma,\bar{\sigma}}\Gamma\left(E\sigma,E'\sigma'\right)=\Gamma^{1)}\left(E\sigma,E'\sigma\right)+\Gamma^{2)}\left(E\sigma,E'\bar{\sigma}\right), \tag{8.5}$$

which yields

$$\begin{aligned}\frac{1}{\tau_\sigma(E)}=\frac{\pi}{\hbar}\int_{E_F}^{E}dE'\Bigg\{&\sum_{\beta=s,p,d}\rho_{\sigma}^{\beta,>}(E')\sum_{\alpha=s,p,d}\int_{E_F-\Delta}^{E_F}d\varepsilon\left[\rho_{\sigma}^{\alpha,<}(\varepsilon)\rho_{\sigma}^{\alpha,>}(\varepsilon+\Delta)2\left|M^{\sigma\sigma}\right|^2+\rho_{\bar{\sigma}}^{\alpha,<}(\varepsilon)\rho_{\bar{\sigma}}^{\alpha,>}(\varepsilon+\Delta)\left|M^{\sigma\bar{\sigma}}\right|^2\right]\\&+\sum_{\beta=s,p,d}\rho_{\bar{\sigma}}^{\beta,>}(E')\sum_{\alpha=s,p,d}\int_{E_F-\Delta}^{E_F}d\varepsilon\,\rho_{\bar{\sigma}}^{\alpha,<}(\varepsilon)\rho_{\sigma}^{\alpha,>}(\varepsilon+\Delta)\left|M^{\sigma\bar{\sigma}}\right|^2\Bigg\}.\end{aligned} \tag{8.6}$$

We note that because the unoccupied states above the Fermi energy in Ni are dominated by electronic states with minority-spin polarization ($\downarrow$), spin-dependent scattering needs to be taken into account, which results in spin-dependent excited-electron lifetime in the ferromagnetic materials such as Ni [257,258,285]. Assuming $\rho_\uparrow=\rho_\downarrow=\rho$ and $M^{\uparrow\uparrow}=M^{\uparrow\downarrow}=M$, Equation (8.6) is simply reduced to $\frac{1}{\tau(E)}=\frac{2\pi}{\hbar}\rho^3\left|M\right|^2(E-E_F)^2$, which is the well-known $(E-E_F)^{-2}$ scaling of hot electron lifetimes excited close to the E_F [149].

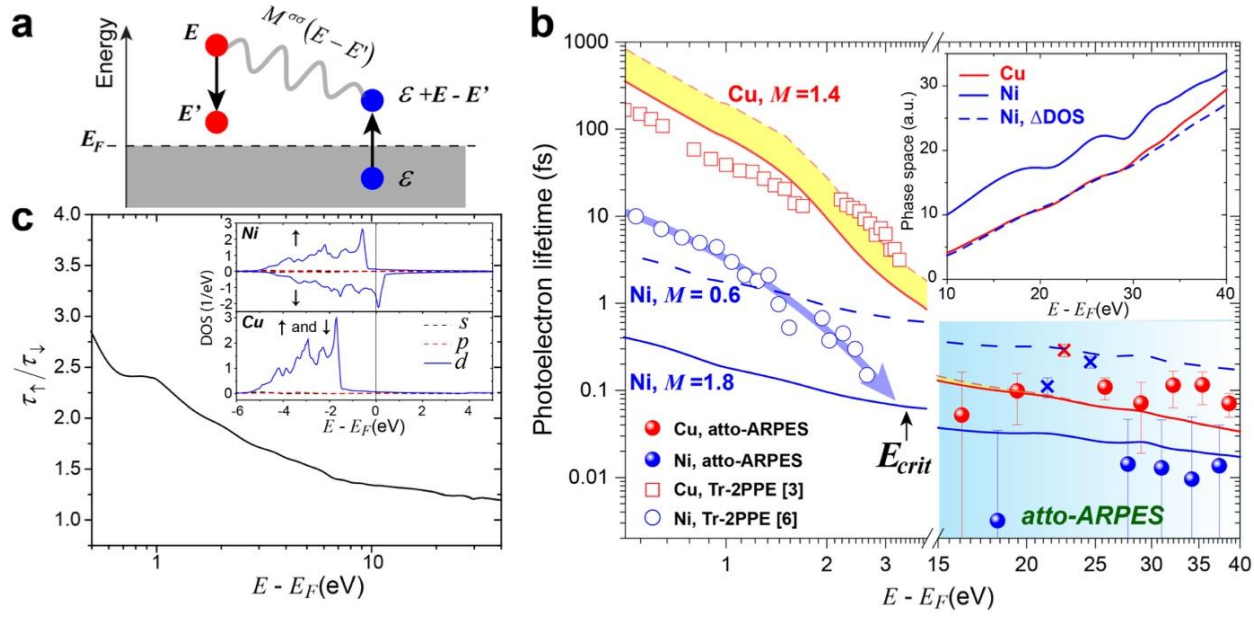

Figure 8.14: Spin-dependent model of electron-electron scattering. (a) Illustration of the electron-electron scattering process described by Equation (8.1). The photoexcited electron (red circle) can decay by exciting another unexcited electron (blue circle) to a state above E_F. $M^{\sigma\sigma}(E-E')$ is the Coulomb matrix element, which we find is mostly constant for Cu (at 1.4) across a broad energy range, but varies for Ni due to stronger screening at low energies. (b) Comparison between the spin-dependent scattering model (red (Cu) and blue (Ni)) and the experimentally measured lifetime of photoexcited electrons in Cu and Ni. The low-energy data (0.5-3 eV) are measured using Tr-2PPE method, extracted from Ref. [255] for Cu and from Ref. [258] for Ni. The high-energy data (15 - 40 eV) are directly measured in our experiment using atto-ARPES. The data that overlap final-state resonances in both materials are represented by crosses to distinguish them from the off-resonant results of interest here. The yellow-area estimates *d*-electron screening effects by considering the optical constants of Cu [291]. The experimentally measured low-energy electron lifetime approaches the bare electron-electron scattering limit (solid blue line, M=1.8 for Ni) at an energy $E_{crit} \approx 3$eV. Inset: the phase space of the two materials calculated from Equation (8.1), assuming $M^{\uparrow\uparrow} = M^{\uparrow\downarrow} = 1.0$. The blue dashed line (Ni, ΔDOS) is the results with the DOS of Ni downshifted by 1.8 eV. (c) Lifetime ratio $\tau_\uparrow/\tau_\downarrow$ as a function of excited electron energy (E-E_F) for Ni obtained using Equation (8.1). Inset: spin and orbital-dependent DOS of Ni and Cu obtained from DFT calculations.

We first evaluate the influence of the DOS on the available phase space for scattering by assuming $M^{\uparrow\uparrow} = M^{\uparrow\downarrow} = 1.0$ in Equation (8.6). As shown in the inset of Figure 8.14b, the phase space increases monotonically as a function of the photoexcited electron energy above E_F for both Ni and Cu, and indeed, the phase space of Ni is larger than Cu in the energy range of our experiments, indicating that a higher scattering rate and a shorter photoelectron lifetime would indeed be expected. The additional phase space of Ni is dominated by the unoccupied DOS above E_F, as evidenced by the fact that the available phase space of Ni moves closer to Cu as its DOS is down-shifted by 1.8 eV to artificially remove the peaked unoccupied DOS (dashed line in the inset of Figure 8.14b). Figure 8.14b plots the experimentally measured and theoretically calculated lifetimes of photoexcited electrons from 0.5 to 40 eV. Although the focus of this work is on photoelectron lifetimes in the high energy >20 eV region, a comparison with Tr-2PPE data allows us to gain valuable physical insights. In general, electron-electron Coulomb interactions are energy-dependent due to different screening properties at different energies in a material [149]. Here, for convenience, we assume the Coulomb matrix element M is a constant, and select values by fitting to the experimental data. For example, to further determine the Coulomb matrix element, we compare the photoexcited electron lifetimes measured using spin-integrated Tr-2PPE on Cu [255] and Ni [258] with our atto-ARPES results and models. For Cu, we have $M^{\uparrow\uparrow} = M^{\uparrow\downarrow} = M$, because the DOS for electrons with majority ($\uparrow$) and minority ($\downarrow$) spins are the same. For Ni, as shown in the inset of Figure 8.14c, there are spin-dependent DOS differences, so we assume $\left|M^{\uparrow\uparrow}/M^{\uparrow\downarrow}\right| = 0.5$ and $M = \sqrt{\frac{\left|M^{\uparrow\uparrow}\right|^2 + \left|M^{\uparrow\downarrow}\right|^2}{2}}$ in order to get agreement with the spin-dependent electron lifetime measured at low energies [258]. The spin-averaged excited electron lifetime

$\tau = \frac{2\tau_\uparrow \tau_\downarrow}{\tau_\uparrow + \tau_\downarrow}$ is plotted in Figure 8.14b as solid lines for Cu and Ni, while Figure 8.14c plots the ratio between spin-up and spin-down electron lifetimes ($\tau_\uparrow / \tau_\downarrow$). Most interestingly, we find that the photoexcited-electron lifetime in Cu can be explained by a mostly energy-independent Coulomb matrix element (M=1.4) throughout the entire energy range from 0.5 to 40 eV. The presence of the *d*-band screening in the low energy range (<3 eV) is well known for Cu, which increases the lifetime by approximately a factor of 2.5 [267,291]. In stark contrast, our atto-ARPES measurements suggest a stronger energy dependence of the Coulomb matrix element in Ni: M=1.8 is best for high energy photoelectrons and is close to that observed in Cu, while M=0.6 is best for low energy photoelectrons - that are influenced by both screening and scattering.

Considering that electron screening does not have a strong influence on the photoelectron lifetime in the high energy range [270,272], we can extract the influence of the bare electron-electron Coulomb interactions (no screening) at high energies and extend the corresponding matrix element to the low energy range (the solid blue line in Figure 8.14b). The measured lifetime at low energy in Ni is more than one order of magnitude longer than the bare electron-electron scattering limit, as shown in Figure 8.14b. Most interestingly, we find that the experimentally measured low-energy excited electron lifetime in Ni gradually approaches the bare electron-electron scattering limit (solid blue line in Figure 8.14b) defined by our atto-ARPES measurement at an energy E_{crit} ~ 3 eV above E_F. This further corroborates our findings, since screening is expected to diminish at these higher energies [272]. Comparing Cu and Ni, our results strongly suggest the presence of enhanced electron screening in Ni at low energies, which can be attributed to the high DOS at the Fermi energy based on our DFT calculations (see Figure 8.14c inset) [258]. From the above, we conclude that atto-ARPES can extend measurements of photoexcited-electron lifetimes to higher energies (>20 eV) to distinguish and quantify fundamental electron interactions such as electron

scattering and screening, as well as the influence of resonant interband transitions. Compared to other approaches, atto-ARPES also has the unique ability to distinguish band-specific electron-electron scattering for direct comparison with theory, and can exclude other contributions such as hot electrons and intermediate-state refilling [227,258,292].

8.11.3 Spin-Dependent Electron-Electron Scattering

Finally, we note that spin-dependent electron-electron scattering in ferromagnetic materials is responsible for many interesting phenomena, including laser-induced demagnetization [227], superdiffusive spin transport, and giant magnetoresistance [293]. Low-energy spin-dependent electron lifetimes have been studied, providing much valuable information [257,258]. However, to date it is not possible to experimentally isolate electron-electron scattering, because of strong contributions to the measured lifetimes from electron screening from localized *d* and *f* band electrons, as well as contributions from other interactions e.g., phonons and impurities. By probing high-energy photoelectron lifetimes, where electron screening becomes negligible, spin-resolved atto-ARPES could probe spin-dependent electron-electron scattering, which could help uncover fundamental magnetic properties.

8.12 Atto-ARPES as a Probe of High-Energy Final States and Matrix Element Effect in Photoemission

We note that when photoexcitation is on-resonance with an excited bulk band final state, the photoemission time delay strongly varies as a function of the electron transverse momentum, i.e., photoelectron emission angle θ, which is a consequence of the final-band dispersion [35]. This allows us to clearly understand what transitions are involved, and when we are observing lifetimes of bulk final bands. To extract the final (excited) state time delay, we simulated and subtracted the

angular dependence of the time delay imposed by the incident and reflected laser fields [60,118] . The angle-dependent photoemission time delays ($\tau_{PE}\left(\Lambda_3^{\beta},\theta\right)-\tau_{PE}\left(\Lambda_3^{\alpha},0\right)$ and $\tau_{PE}\left(\Lambda_3^{\alpha},\theta\right)-\tau_{PE}\left(\Lambda_3^{\alpha},0\right)$) excited with an s-polarized HHG field are plotted in Figure 8.15a. Most interestingly, we find the time delay disperses oppositely around Γ point as a function of θ for Λ_3^{α} and Λ_3^{β} band photoelectrons. Using the model presented in Ref. [35], and the band structure along the $\overline{\Gamma}$-$\overline{\mathrm{K}}$ direction obtained from density-functional theory (DFT) calculations (Figure 8.15b), we model the lifetime dispersion of Λ_3^{β} band photoelectrons, as shown by the red-solid line in Figure 8.15a. The maximum time delays at θ≈5° (**A**) and θ≈16° (**B**) corresponds well to the features on Σ_1^{B} final band (Λ_1^{B} band along Γ-L direction) as shown in Figure 8.15b, which corroborates the contribution of the Σ_1^{B} final band in this resonant transition.

In contrast, we find that the dispersion of the measured time delay $\tau_{PE}\left(\Lambda_3^{\alpha},\theta\right)-\tau_{PE}\left(\Lambda_3^{\alpha},0\right)$ is in good agreement with the shape of the Σ_1^{A} band (Λ_1^{A} band along the Γ-L direction), as shown by our model results (pink curve) in Figure 8.15a. The maximum delay (**C**) at θ≈8° corresponds to the peak in the Σ_1^{A} band shown in Figure 8.15b. More interestingly, by adjusting the polarization of the HHG field from s to p, we can tune the transition from Λ_3^{α} initial band to out of the resonance with the Σ_1^{A} final band and directly into a free-electron-like final state as illustrated by the non-dispersive feature of the time delay $\tau_{PE}\left(\Lambda_3^{\alpha},\theta\right)-\tau_{PE}\left(\Lambda_3^{\alpha},0\right)$ in Figure 8.15a. We believe this result is due to photoemission selection rules, which determine the allowed transitions for different polarizations. Indeed, we find different initial bands are excited with s- and p-polarized HHG fields (Σ_1^{α} by *s*-pol and Σ_4 by *p*-pol), as clearly evidenced by the different dispersion in the photoelectron spectra (Figure 8.15c).

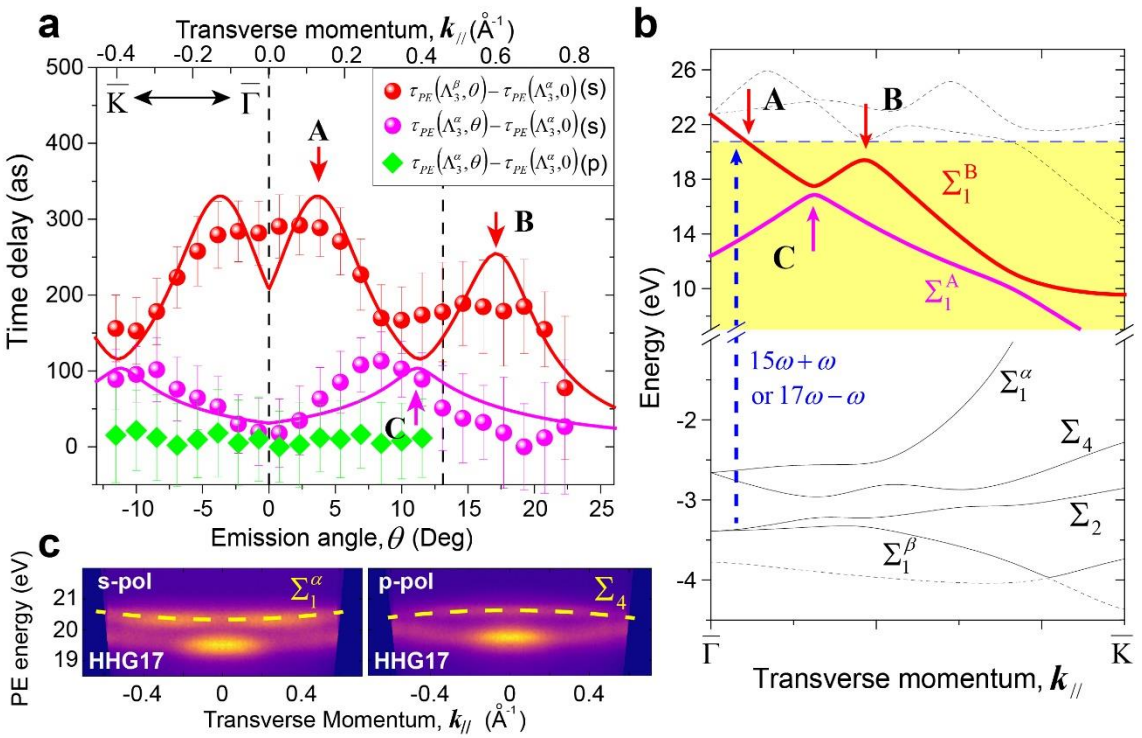

Figure 8.15: Extracting final-state effects in photoemission. (a) Angle-resolved photoemission time delay at the resonant photon energy (side band 16) of photoelectrons from both the Λ_3^α and Λ_3^β initial bands (both s- and p-polarized HHG fields, for a Λ_3^α initial band). The photoemission delay of Λ_3^α band photoelectrons at θ=0 ($\tau_{PE}\left(\Lambda_3^\alpha,0\right)$) is used as the timing reference. The solid lines plot the theoretical lifetime dispersion considering two interband transitions ($\Lambda_3^\beta \rightarrow \Sigma_1^B$ and $\Lambda_3^\alpha \rightarrow \Sigma_1^A$). The peaks of the lifetime dispersion curves are labeled (**A**, **B** and **C**). The vertical dashed line at θ=13° represents the angle limit of our hemispherical analyzer. To measure the time delays at larger angles, the sample was rotated by 12°. (b) Band structure of Cu(111) along the $\bar{\Gamma}-\bar{K}$ transverse momentum ($\boldsymbol{k}_{//}$) direction obtained by DFT calculations. The perpendicular momentum $\boldsymbol{k}_\perp$ is determined by the band-mapping results of Figure 8.7b. The labeled band structure features (**A**, **B** and **C**) correspond to the labels in (a). (c) ARPES spectra obtained using the 17th order harmonic for both s- and p-polarizations. The dispersion of the upper band is obviously opposite in both cases, as highlighted by the yellow dashed lines, indicating that different initial states (Σ_1^α and Σ_4) are selectively excited by HHG fields with different polarizations.

High-energy final states are very important and represent one of the major difficulties in interpreting photoemission spectra [144,148,294], which has been extensively studied by two-photon photoemission [295,296], inverse photoemission [148,297] and very-low-energy electron diffraction (VLEED) techniques [298]. Here, through angle- and polarization-dependent photoemission time delay measurements at the resonant energy, we show that our method can be a very sensitive tool to measure the selectivity of dipole transitions between different initial and final states.

8.13 Conclusion and Outlook

In conclusion, we show that attosecond electron interactions in metals can be studied using energy-, polarization-, and angle-resolved atto-ARPES, allowing us to distinguish the contributions of occupied and unoccupied bands to the photoelectron lifetimes. Strong electron-electron scattering in the unfilled *d* band of Ni decreases the lifetime of photoelectrons by ~100 as relative to the photoelectrons emitted from the same band of Cu. Most interestingly, we find that dynamical screening influences high-energy photoelectrons much less than low-energy photoelectrons, and is different for Cu and Ni due to the difference in material band structure. As a result, spin-dependent atto-ARPES with high-energy excitation is a unique tool to exclusively study the fundamental processes of spin-dependent electron-electron scattering in magnetic materials, and also quantify the contributions of scattering and screening for low-energy excitations. In the future, atto-ARPES can also be used to extract valuable information about fundamental electron-electron interactions in a host of materials including strongly correlated materials and modern quantum materials.

Chapter 9

Conclusion and Outlook

9.1 Conclusion

The work presented in this thesis demonstrated interferometric laser-assisted photoemission (I-LAPE) as a quantitative technique to study both the attosecond pulses and the attosecond electron dynamics in solids with unprecedented temporal and spatial resolution. Within the pursued metrology approach, photoelectron wave packets are launched inside the solid through excitation by extreme ultraviolet (EUV) attosecond pulse trains. The generated photoelectrons are subsequently probed by their interactions with an infrared laser pulse perfectly phase-locked to the attosecond excitation. The presence of IR field induces the absorption and stimulated emission of IR photons for photoelectrons, forming sidebands around the direct photoemission peak. Quantum path interference modulates the sideband intensities at twice the frequency of the IR field, with the oscillation phase related to the arrival time of photoelectrons into the laser field. There are two factors determining the instant of photoelectron release: 1) the timing (phase) of the EUV photons and 2) the photoemission time. Therefore, the I-LAPE technique (i.e., RABBITT) can serve as a probe of the attosecond pulse structure as well as the photoelectron lifetime. To summarize the primary results of the thesis:

- Tomographic reconstruction of the circularly polarized harmonic field have revealed the 3D structure of the circular attosecond pulse train produced by bi-chromatic counter-rotating

driving fields. It was demonstrated experimentally that the circular harmonics generated through this method was composed of three linear burst within one optical cycle of the IR field, with each burst rotated 120^{o} from the previous one, collaborating with the theoretical calculations. This represent the first *ex-situ* spatial-temporal (4D) reconstruction of attosecond pulses. It was enabled by the capability to rotate the circular attosecond pulse train and the polarization sensitivity in surface photoemission. The full temporal characterization also provides a universal way to measure the ellipticity of circular harmonics.

- Linearly polarized high harmonic radiation generated by two-color field consisting of the fundamental IR laser (ω) and its second harmonic (2ω) is an attractive attosecond light source because it has broader spectral coverage and the pulse train structure can be controlled by tuning the relative delay between two drivers. We fully characterized the evolution of the attosecond pulse structure as a function of the ω-2ω delay. We found that the delay corresponding to the highest overall harmonic yield also results in the shortest attosecond pulse train.

- Attosecond RABBITT experiments performed on Ni(111) surface confirm the influence of material bandstructure on the photoelectron lifetime. In particular, there is an abrupt increase in photoelectron lifetime when the photoexcitation resonantly couples the bound electron with an unoccupied final band, resulting in a photoemission time delay for the resonant excitation compared to non-resonant excitations. This lifetime elongation peaks at the resonant photon energy and decreases at higher or lower photon energies. A strong emission-angle-dependent photoelectron lifetime was observed, which perfectly tracks the dispersion of the final band. This serves as a strong proof for the final band effect on the photoemission time delay.

- After identifying the unoccupied final band effect, we move forward to investigate how the occupied initial band influence the photoelectron lifetime. The pinpoint of the final bands allows

us the select the photon energies to excite the electron wave packets into free electron final states instead of coupling to a final bulk band. We found that for the same free electron final states, photoelectrons in Cu(111) has a longer lifetime than Ni(111). Unlike the resonance case, this delay is non-dispersive, exempting the final state as an origin. Combined with a numerical simulation, we show that the longer photoelectron lifetime in Cu(111) is due to lower scattering cross section as a result of its fully occupied *d* band. We also found that distinct from the lower excited states probed by two-photon photoemission, the high energy photoelectrons escape so fast that the dynamical screening has a negligible influence on it.

- As a bonus of the final state effect on the angular dispersion of the photoelectron lifetime, attosecond metrology can act as a sensitive probe of the coupling between different initial and final states. This is a peek into the mysterious “black box” of transition dipole matrix in photoemission. The results will inform the theoretical effects to shed light on this problem.

The outlook is very bright for using attosecond metrology in combination with angle-resolved photoemission spectroscopy to study the material systems. Since only electronic systems are evolving on the attosecond time scale while the lattice is essentially frozen, attosecond spectroscopy provides a powerful tool to study the electron-electron many-body interactions adiabatically. This avenue holds great potential in solving the central mysteries in condensed matter physics such as superconductivity, nano-plasma, ultrafast demagnetization and photoinduced metal-insulator phase transition.

9.2 Ongoing Experiment

We have investigated two transition metal surfaces Ni and Cu in the thesis. In the immediate future, we will expand our study to more metallic systems to answer several important

questions: 1) how the localization of the valence band impacts the photoemission time? 2) Is it possible to find a system with photoelectron lifetime comparable to the time scale of dynamical screening to investigate the interaction between two processes? 3) It is reported that the surface state of metal has a varying mean free path depending on photon energy. Can we directly measure it in the time-domain? Is surface state emission really from "surface"? Besides the valence bands of meal single crystals, we are also investigating the following dynamics.

9.2.1 Time-Domain Study of Fano Resonance in Solid-State Materials

Spectral phase measurement of Fano resonance has been performed on gas phase argon atoms using RABBITT technique. In the proximity of the $3s^2 3p^6 \rightarrow 3s^1 3p^6 4p$ autoionizing resonance, the oscillation phase of the nearest sideband to this resonance strongly depends on the harmonic photon energy relative to the resonant energy. This phase variation reflects the interaction between the continuum $[3p^{-1}\epsilon s, d]$ and quasi-bound $[3s^{-1}4p]$ states.

Same Fano type resonance was also observed in photoemission from nickel [252,299,300]. It was first reported by Guillot *et al.* in 1977 [252], followed by a detailed analysis by Barth *et al.* in 1979 [299]. They observed that $M_{2,3}VV$ Auger electrons peaked around 6 eV started to emerge and increased dramatically when the photon energy passed through the *3p* threshold at about 66 eV. The dependence of Auger spectral intensity on photon energy showed a typical Fano type asymmetric line shape with a minimum at 66 eV and a maximum at 71 eV. More interestingly, it was demonstrated that not only the Auger peak but also the Ni 3*d* band photoemission was coupled to the 3p excitation. Furthermore, this *3p*-*3d* interaction differs from the top to the bottom part of the *d* band.

The investigation of photoelectron lifetime in Ni(111) are mainly focused on valence bands at photon energies < 60 eV in thesis. Since bright high harmonic source can reach wavelength all the way to 13 nm using the current laser system, time-domain study of Fano resonances in Ni(111) can be achieved. It could shed light on the influence of core-level excitation to valence band, which is scarcely addressed before.

9.2.2 Doped Metal and Surface-Adsorbate Systems

The RABBITT experiments so far have been mainly performed on metallic samples. In these experiments, the dressing IR field can be assumed to be substantially screened in the interior of the solid, which is a result of the optical properties of metals. This assumption is proved to be valid in multiple publications [56,60]. This assumption simplifies the interpretation of streaking and RABBITT measurements because the liberation of photoelectrons inside the metal can be separated from their subsequent interaction with the dressing field in vacuum.

Conversely, the screening effect is less pronounced in semiconductors and dielectrics. This gives rise to the complication in determining when the photoelectrons are “streaked” or “dressed” by the IR field. For dielectrics, the refractive index is close to unity. The IR field can efficiently penetrate into the material. It was proposed that the photoelectrons from dielectric were immediately accelerated by the dressing field and could serve as the reference to measure the “absolute” photoemission time in metals [301]. The approach to implement this scheme is to absorb certain dielectric layers on top of metal surface. Nepple *et al.* studied the solid state Xe/W(110) system and concluded that the absolute timing measurement relied on an improved understanding of the photoemission time from isolated atoms, which is not yet achieved [301].

Another interesting problem is how the orbital hybridization changes the excited-state lifetime. In chemisorbed system like O_2/metal and CO/metal, the electrons are transferred between the molecular HOMO/LUMO and the conduction bands of metal [302,303]. Even in physisorbed noble atoms on metal surface, the electrons that are resonantly excited to the autoionization state can transfer into the metal surfaces [304]. This charge transfer can influence the Auger electron and autoionization state lifetime and has been a hot topic for static and time-resolved photoemission. Chemisorbed molecules can also induce changes on the final states of metals and impact the photoelectron lifetime.

It has been observed that the asymmetric molecular potential will lead to the dependence of Wigner time delay on photoelectron emission angle. For chemisorbed systems like CO/Ni(111) [121], the molecular potential is perturbed by the surface and photoemission can only occur on one side. Attosecond photoemission can be a sensitive probe to map the potential change. Furthermore, collective nuclear motion such as the vibrational, rotational and stretching mode of the molecule can be excited by IR laser. The impact of these dynamics on photoionization time will shed light on the surface-adsorbate interactions.

We have successfully fabricated single-layer and double-layer graphene on Ni(111) surface in our setup using chemical vapor deposition (CVD) growth method [151,305]. Their band structures have been mapped using linearly polarized harmonics. We also added alkali Na atoms to modify the electronic structure of Graphene/Ni(111) system. The ARPES spectra reveal distinct spectral change during the course of atomic Na absorption onto and intercalation into Graphene/Ni(111). Subsequent oxygen exposure of adsorbed/intercalated surface shows that the on-top Na atoms that are not “protected” under the graphene layer can be oxidized and form sodium oxide layer.

This manipulation of oxygen-sodium-graphene-nickel layered system gives us the access to a wide range of photoionization dynamics. 1) For double-layer graphene grown on nickel, the first layer is strongly hybridized with nickel but the second layer is almost free-standing [306]. It is therefore a candidate system to study the photoelectron lifetime of hybridized states. 2) The study of transport time difference for Na on top of graphene and intercalated under graphene will give information on electron transport through a single layer graphene. 3) During the oxygen exposure, metallic sodium on top of graphene will be oxidized into dielectric sodium oxide. This metal to dielectric transitions might lead to different interactions between photoelectrons with the dressing field.

9.3 Future Opportunities

Within the past three years, time-resolve photoemission spectroscopy benefit from two developments in high harmonic generation. 1) Narrow bandwidth harmonics driven by 2ω light substantially improved the energy-resolution and photon flux for high harmonic-based photoemission experiments [171]. 2) Different methods of circularly polarized high harmonic generation were demonstrated [30,68–70]. In terms of the detection of photoelectrons, spin-resolved photoemission can add unique information especially for itinerant magnetic systems. Recently spin detector based on very low-energy electron scattering from an oxygen-passivated epitaxial Fe film improved the efficiency of spin-detection by a factor 20 compared to previous Mott- or spin polarized lower energy electron diffraction (SPLEED-) based detectors. It has been demonstrated that the combination of spin-resolved detector with high-flux 2ω–driven high harmonic sources can be used to track the band stricture evolution during ultrafast ferromagnetic to paramagnetic phase transitions in cobalt. Our results show that the phase transition in cobalt

cannot be explained by a collapse of exchange splitting in spin-polarized bands, but instead shows rapid band mirroring after excitation.

Similar experimental setup can be used to study spin-dependent photoemission time in solids. In Chapter 8 of the thesis, we have shown through simulation that the photoelectron lifetime in Ni(111) is spin-dependent due to electron-electron scattering. The experimental measurement of such dynamics will shed light on influence of spin on electron correlations.

Bibliography

[1] P. H. Bucksbaum, "The future of attosecond spectroscopy," *Science* **317**, 766–769 (2007).

[2] H. Mashiko, K. Oguri, T. Yamaguchi, A. Suda, and H. Gotoh, "Petahertz optical drive with wide-bandgap semiconductor," *Nat. Phys.* **12**, 741–746 (2016).

[3] M. Garg, M. Zhan, T. T. Luu, H. Lakhotia, T. Klostermann, A. Guggenmos, and E. Goulielmakis, "Multi-petahertz electronic metrology," *Nature* **538**, 359–363 (2016).

[4] H. Hartridge and F. J. W. Roughton, "A Method of Measuring the Velocity of Very Rapid Chemical Reactions," *Proc. R. Soc. A* **104**, 376–394 (1923).

[5] B. Chance, "The accelerated flow method for rapid reactions," *J. Franklin Inst.* **229**, 613–640 (1940).

[6] R. G. W. Norrish, F.R.S, G. Porter, and B. A. Thrush, "Studies of the explosive combustion of hydrocarbons by kinetic spectroscopy. II. Comparative investigations of hydrocarbons and a study of the continuous absorption spectra," *Proc. R. Soc. London A Math. Phys. Eng. Sci.* **227**, 423–433 (1955).

[7] M. Eigen, "Immeasurably fast reactions," *Nobel Lect.* (1967).

[8] P. Krehl and S. Engemann, "August Toepler - The first who visualized shock waves," *Shock Waves* **5**, 1–18 (1995).

[9] P. P. Sorokin and J. R. Lankard, "Stimulated emission observed from an organic dye, chloro-aluminum phthalocyanine," *IBM J. Res. Dev.* **10**, 162–163 (1966).

[10] R. L. Fork, B. I. Greene, and C. V. Shank, "Generation of optical pulses shorter than 0.1 psec by colliding pulse mode locking," *Appl. Phys. Lett.* **38**, 671–672 (1981).

[11] J.-C. Diels, W. Dietel, J. J. Fontaine, W. Rudolph, and B. Wilhelmi, "Analysis of a mode-locked ring laser: chirped-solitary-pulse solutions," *J. Opt. Soc. Am. B* **2**, 680–686 (1985).

[12] R. L. Fork, O. E. Martinez, and J. P. Gordon, "Negative dispersion using pairs of prisms," *Opt. Lett.* **9**, 150–152 (1984).

[13] W. Dietel, J. J. Fontaine, and J.-C. Diels, "Intracavity pulse compression with glass: a new method of generating pulses shorter than 60 fsec," *Opt. Lett.* **8**, 4–6 (1983).

[14] R. L. Fork, C. H. Cruz, P. C. Becker, and C. V. Shank, "Compression of optical pulses to six femtoseconds by using cubic phase compensation," *Opt. Lett.* **12**, 483–485 (1987).

[15] U. Keller, K. J. Weingarten, F. X. Kärtner, D. Kopf, B. Braun, I. D. Jung, R. Fluck, C. Hönninger, N. Matuschek, et al., "Semiconductor saturable absorber mirrors (SESAM's) for femtosecond to nanosecond pulse generation in solid-state lasers," *IEEE J. Sel. Top. Quantum Electron.* **2**, 435–451 (1996).

[16] D. H. Sutter, G. Steinmeyer, L. Gallmann, N. Matuschek, F. Morier-Genoud, U. Keller, V. Scheuer, G. Angelow, and T. Tschudi, "Semiconductor saturable-absorber mirror-assisted Kerr-lens mode-locked Ti: sapphire laser producing pulses in the two-cycle regime," *Opt. Lett.* **24**, 631–633 (1999).

[17] D. E. Spence, P. N. Kean, and W. Sibbett, "60-fsec pulse generation from a self-mode-locked Ti:sapphire laser," *Opt. Lett.* **16**, 42–44 (1991).

[18] F. Salin, J. Squier, and M. Piché, "Mode locking of Ti:Al(2)O(3) lasers and self-focusing: a Gaussian approximation," *Opt. Lett.* **16**, 1674–1676 (1991).

[19] U. Keller, G. W. 'tHooft, W. H. Knox, and J. E. Cunningham, "Femtosecond pulses from

a continuously self-starting passively mode-locked Ti:sapphire laser," *Opt. Lett.* **16**, 1022–1024 (1991).

[20] A. H. Zewail, "Femtochemistry: Atomic-scale dynamics of the chemical bond using ultrafast lasers (Nobel lecture)," in *Angew. Chemie Int. Ed.* **39** (2000).

[21] J. D. Bonlie, F. Patterson, D. Price, B. White, and P. Springer, "Production of > 10^(21) W/cm2 from a large-aperture Ti:sapphire laser system," *Appl. Phys. B* **70**, S155–S160 (2000).

[22] T. Popmintchev, M.-C. Chen, D. Popmintchev, P. Arpin, S. Brown, S. Ališauskas, G. Andriukaitis, T. Balčiunas, O. D. Mücke, et al., "Bright coherent ultrahigh harmonics in the keV X-ray regime from mid-infrared femtosecond lasers," *Science* **336**, 1287–1291 (2012).

[23] C. Hernández-García, J. A. Pérez-Hernández, T. Popmintchev, M. M. Murnane, H. C. Kapteyn, A. Jaron-Becker, A. Becker, and L. Plaja, "Zeptosecond high harmonic keV X-ray waveforms driven by midinfrared laser pulses," *Phys. Rev. Lett.* **111**, 33002 (2013).

[24] P. Lan, P. Lu, W. Cao, and X. Wang, "Attosecond and zeptosecond x-ray pulses via nonlinear Thomson backscattering," *Phys. Rev. E* **72**, 66501 (2005).

[25] Y. Xiang, Y. Niu, Y. Qi, R. Li, and S. Gong, "Single zeptosecond pulse generation from muonic atoms with nonlinear chirped laser pulses," *J. Mod. Opt.* **57**, 385–389 (2010).

[26] S. Gordienko, A. Pukhov, O. Shorokhov, and T. Baeva, "Relativistic doppler effect: universal spectra and zeptosecond pulses," *Phys. Rev. Lett.* **93**, 115002 (2004).

[27] A. Ipp, C. H. Keitel, and J. Evers, "Yoctosecond photon pulses from quark-gluon plasmas," *Phys. Rev. Lett.* **103**, 152301 (2009).

[28] A. Wirth, M. T. Hassan, I. Grguraš, J. Gagnon, A. Moulet, T. T. Luu, S. Pabst, R. Santra,

Z. A. Alahmed, et al., “Synthesized light transients,” *Science* **334**, 195–200 (2011).

[29] P. Tzallas, D. Charalambidis, N. A. Papadogiannis, K. Witte, and G. D. Tsakiris, “Direct observation of attosecond light bunching,” *Nature* **426**, 267–271 (2003).

[30] C. Chen, Z. Tao, C. Hernández-García, P. Matyba, A. Carr, R. Knut, O. Kfir, D. Zusin, C. Gentry, et al., “Tomographic reconstruction of circularly polarized high-harmonic fields: 3D attosecond metrology,” *Sci. Adv.* **2**, e1501333 (2016).

[31] M. Chini, K. Zhao, and Z. Chang, “The generation, characterization and applications of broadband isolated attosecond pulses,” *Nat. Photonics* **8**, 178–186 (2014).

[32] P. M. Paul, E. S. Toma, P. Breger, G. Mullot, F. Augé, P. Balcou, P. M. Paul, E. S. Toma, P. Breger, et al., “Observation of a train of attosecond pulses from high harmonic generation,” *Science* **292**, 1689–1692 (2001).

[33] M. Lucchini, S. A. Sato, A. Ludwig, J. Herrmann, M. Volkov, L. Kasmi, Y. Shinohara, K. Yabana, L. Gallmann, et al., “Attosecond dynamical Franz-Keldysh effect in polycrystalline diamond,” *Science* **353**, 916–919 (2016).

[34] Y. Mairesse and F. Quéré, “Frequency-resolved optical gating for complete reconstruction of attosecond bursts,” *Phys. Rev. A* **71**, 011401(R) (2005).

[35] Z. Tao, C. Chen, T. Szilvási, M. Keller, M. Mavrikakis, H. Kapteyn, and M. Murnane, “Direct time-domain observation of attosecond final-state lifetimes in photoemission from solids,” *Science* **353**, 62–67 (2016).

[36] M. Schultze, K. Ramasesha, C. D. Pemmaraju, S. A. Sato, D. Whitmore, A. Gandman, J. S. Prell, L. J. Borja, D. Prendergast, et al., “Attosecond band-gap dynamics in silicon,” *Science* **346**, 1348–1352 (2014).

[37] M. Drescher, M. Hentschel, R. Kienberger, M. Uiberacker, V. Yakovlev, A. Scrinzi, T.

Westerwalbesloh, U. Kleineberg, U. Heinzmann, et al., “Time-resolved atomic inner-shell spectroscopy,” *Nature* **419**, 803–807 (2002).

[38] H. Niikura, H. J. Wörner, D. M. Villeneuve, and P. B. Corkum, “Probing the spatial structure of a molecular attosecond electron wave packet using shaped recollision trajectories,” *Phys. Rev. Lett.* **107**, 93004 (2011).

[39] A. Baltus, T. Udem, M. Uiberacker, M. Hentschel, E. Goulielmakis, C. Gohle, R. Holzwarth, V. S. Yakovlev, A. Scrinzi, et al., “Attosecond control of electronic processes by intense light fields,” *Nature* **421**, 611–615 (2003).

[40] M. Schultze, E. M. Bothschafter, A. Sommer, S. Holzner, W. Schweinberger, M. Fiess, M. Hofstetter, R. Kienberger, V. Apalkov, et al., “Controlling dielectrics with the electric field of light,” *Nature* **493**, 75–78 (2013).

[41] K. T. Kim, C. Zhang, A. D. Shiner, S. E. Kirkwood, E. Frumker, G. Gariepy, A. Naumov, D. M. Villeneuve, and P. B. Corkum, “Manipulation of quantum paths for space-time characterization of attosecond pulses,” *Nat. Phys.* **9**, 159–163 (2013).

[42] M. Schultze, M. Fiess, N. Karpowicz, J. Gagnon, M. Korbman, M. Hofstetter, S. Neppl, a. L. Cavalieri, Y. Komninos, et al., “Delay in photoemission,” *Science* **328**, 1658–1662 (2010).

[43] F. Calegari, D. Ayuso, A. Trabattoni, L. Belshaw, S. De Camillis, S. Anumula, F. Frassetto, L. Poletto, A. Palacios, et al., “Ultrafast electron dynamics in phenylalanine initiated by attosecond pulses,” *Science* **346**, 336–339 (2014).

[44] A. L. Cavalieri, N. Müller, T. Uphues, V. S. Yakovlev, A. Baltus, B. Horvath, B. Schmidt, L. Blümel, R. Holzwarth, et al., “Attosecond spectroscopy in condensed matter,” *Nature* **449**, 1029–1032 (2007).

[45] B. Förg, J. Schötz, F. Süßmann, M. Förster, M. Krüger, B. Ahn, W. A. Okell, K. Wintersperger, S. Zherebtsov, et al., "Attosecond nanoscale near-field sampling," *Nat. Commun.* **7**, doi: 10.1038/ncomms11717 (2016).

[46] S. A. Beznosyuk, Y. V. Terentyeva, O. A. Maslova, M. S. Zhukovsky, and D. A. Volkov, "Attosecond nanotechnology: quantum dots of nanoelectromechanical systems of CuIn(x)Ga(1 – x)Se(2) compounds," *AIP Conf. Proc.* **1783**, 20015 (2016).

[47] W. Li, X. Zhou, R. Lock, S. Patchkovskii, A. Stolow, H. C. Kapteyn, and M. M. Murnane, "Time-resolved dynamics in N2O4 probed using high harmonic generation," *Science* **322**, 1207–1211 (2008).

[48] D. Shafir, H. Soifer, B. D. Bruner, M. Dagan, Y. Mairesse, S. Patchkovskii, M. Y. Ivanov, O. Smirnova, and N. Dudovich, "Resolving the time when an electron exits a tunnelling barrier," *Nature* **485**, 343–346 (2012).

[49] C. Vozzi, M. Negro, F. Calegari, G. Sansone, M. Nisoli, S. De Silvestri, and S. Stagira, "Generalized molecular orbital tomography," *Nat. Phys.* **7**, 822–826 (2011).

[50] D. Shafir, Y. Mairesse, D. M. Villeneuve, P. B. Corkum, and N. Dudovich, "Atomic wavefunctions probed through strong-field light–matter interaction," *Nat. Phys.* **5**, 412–416 (2009).

[51] F. Lindner, M. G. Schätzel, H. Walther, A. Baltuška, E. Goulielmakis, F. Krausz, D. B. Milošević, D. Bauer, W. Becker, et al., "Attosecond double-slit experiment," *Phys. Rev. Lett.* **95**, 40401 (2005).

[52] M. Meckel, D. Comtois, D. Zeidler, A. Staudte, D. Pavičić, H. C. Bandulet, H. Pépin, J. C. Kieffer, R. Dörner, et al., "Laser-induced electron tunneling and diffraction," *Science* **320**, 1478–1482 (2008).

[53] M. Spanner, O. Smirnova, P. B. Corkum, and M. Y. Ivanov, “Reading diffraction images in strong field ionization of diatomic molecules,” *J. Phys. B At. Mol. Opt. Phys.* **37**, L243 (2004).

[54] R. Locher, L. Castiglioni, M. Lucchini, M. Greif, L. Gallmann, J. Osterwalder, M. Hengsberger, and U. Keller, “Energy-dependent photoemission delays from noble metal surfaces by attosecond interferometry,” *Optica* **2**, 405–410 (2015).

[55] L. Miaja-Avila, C. Lei, M. Aeschlimann, J. L. Gland, M. M. Murnane, H. C. Kapteyn, and G. Saathoff, “Laser-assisted photoelectric effect from surfaces,” *Phys. Rev. Lett.* **97**, 113604 (2006).

[56] S. Neppl, R. Ernstorfer, A. L. Cavalieri, C. Lemell, G. Wachter, E. Magerl, E. M. Bothschafter, M. Jobst, M. Hofstetter, et al., “Direct observation of electron propagation and dielectric screening on the atomic length scale,” *Nature* **517**, 342–346 (2015).

[57] A. N. Pfeiffer, C. Cirelli, M. Smolarski, D. Dimitrovski, M. Abu-samha, L. B. Madsen, and U. Keller, “Attoclock reveals natural coordinates of the laser-induced tunnelling current flow in atoms,” *Nat. Phys.* **8**, 76–80 (2012).

[58] P. Eckle, A. N. Pfeiffer, C. Cirelli, A. Staudte, R. Dörner, H. G. Muller, M. Büttiker, and U. Keller, “Attosecond ionization and tunneling delay time measurements in helium,” *Science* **322**, 1525–1529 (2008).

[59] M. Kotur, D. Guénot, Á. Jiménez-Galán, D. Kroon, E. W. Larsen, M. Louisy, S. Bengtsson, M. Miranda, J. Mauritsson, et al., “Spectral phase measurement of a Fano resonance using tunable attosecond pulses,” *Nat. Commun.* **7**, 10566 (2016).

[60] M. Lucchini, L. Castiglioni, L. Kasmi, P. Kliuiev, A. Ludwig, M. Greif, J. Osterwalder, M. Hengsberger, L. Gallmann, et al., “Light-matter interaction at surfaces in the

spatiotemporal limit of macroscopic models," *Phys. Rev. Lett.* **115**, 137401 (2015).

[61] O. D. Mücke, "Petahertz electronics: pick up speed," *Nat. Phys.* **12**, 724–725 (2016).

[62] L. V. Keldysh, "Ionization in the field of a strong electromagnetic wave," *Sov. Phys. JETP* **20**, 1307–1314 (1965).

[63] P. B. Corkum, "Plasma perspective on strong field multiphoton ionization," *Phys. Rev. Lett.* **71**, 1994–1997 (1993).

[64] K. J. Schafer, B. Yang, L. F. DiMauro, and K. C. Kulander, "Above threshold ionization beyond the high harmonic cutoff," *Phys. Rev. Lett.* **70**, 1599–1602 (1993).

[65] J. B. Bertrand, H. J. Wörner, P. Salières, D. M. Villeneuve, and P. B. Corkum, "Linked attosecond phase interferometry for molecular frame measurements," *Nat. Phys.* **9**, 174–178 (2013).

[66] B. Manschwetus, N. Lin, J. Rothhardt, R. Guichard, T. Auguste, A. Camper, P. Breger, J. Caillat, M. Géléoc, et al., "Self-probing spectroscopy of the SF6 molecule: a study of the spectral amplitude and phase of the high harmonic emission," *J. Phys. Chem. A* **119**, 6111–6122 (2015).

[67] B. E. Schmidt, A. D. Shiner, M. Giguère, P. Lassonde, C. A. Trallero-Herrero, J.-C. Kieffer, P. B. Corkum, D. M. Villeneuve, and F. Légaré, "High harmonic generation with long-wavelength few-cycle laser pulses," *J. Phys. B At. Mol. Opt. Phys.* **45**, 74008 (2012).

[68] A. Fleischer, O. Kfir, T. Diskin, P. Sidorenko, and O. Cohen, "Spin angular momentum and tunable polarization in high-harmonic generation," *Nat. Photonics* **8**, 543–549 (2014).

[69] O. Kfir, P. Grychtol, E. Turgut, R. Knut, D. Zusin, D. Popmintchev, T. Popmintchev, H. Nembach, J. M. Shaw, et al., "Generation of bright phase-matched circularly-polarized extreme ultraviolet high harmonics," *Nat. Photonics* **9**, 99–105 (2015).

[70] T. Fan, P. Gychtol, R. Knut, C. Hernández-garcía, D. Hickstein, C. Gentry, C. Hogle, D. Zusin, K. Dorney, et al., "Bright circularly polarized soft X-Ray high harmonics for X-Ray magnetic circular dichroism," *CLEO Postdeadline Pap.* **JTh5C.1** (2015).

[71] D. Milošević, W. Becker, and R. Kopold, "Generation of circularly polarized high-order harmonics by two-color coplanar field mixing," *Phys. Rev. A* **61**, 63403 (2000).

[72] J. Mauritsson, P. Johnsson, E. Gustafsson, A. L'Huillier, K. J. Schafer, and M. B. Gaarde, "Attosecond pulse trains generated using two color laser fields," *Phys. Rev. Lett.* **97**, 13001 (2006).

[73] H. Eichmann, a. Egbert, S. Nolte, C. Momma, B. Wellegehausen, W. Becker, S. Long, and J. K. McIver, "Polarization-dependent high-order two-color mixing," *Phys. Rev. A* **51**, 3414–3417 (1995).

[74] Y. Mairesse, A. de Bohan, L. J. Frasinski, H. Merdji, L. C. Dinu, P. Monchicourt, P. Breger, M. Kovacev, R. Taïeb, et al., "Attosecond synchronization of high-harmonic soft X-rays," *Science* **302**, 1540–1543 (2003).

[75] M. G. Pullen, B. Wolter, A.-T. Le, M. Baudisch, M. Hemmer, A. Senftleben, C. D. Schröter, J. Ullrich, R. Moshammer, et al., "Imaging an aligned polyatomic molecule with laser-induced electron diffraction," *Nat. Commun.* **6** (2015).

[76] C. I. Blaga, J. Xu, A. D. Dichiara, E. Sistrunk, K. Zhang, P. Agostini, T. A. Miller, L. F. Dimauro, and C. D. Lin, "Imaging ultrafast molecular dynamics with laser-induced electron diffraction," *Nature* **483**, 194–197 (2012).

[77] B. Wolter, M. G. Pullen, A.-T. Le, M. Baudisch, K. Doblhoff-Dier, A. Senftleben, M. Hemmer, C. D. Schröter, J. Ullrich, et al., "Ultrafast electron diffraction imaging of bond breaking in di-ionized acetylene," *Science* **354**, 308–312 (2016).

[78] Y. Huismans, A. Rouzée, A. Gijsbertsen, J. H. Jungmann, A. S. Smolkowska, P. S. W. M. Logman, F. Lépine, C. Cauchy, S. Zamith, et al., "Time-resolved holography with photoelectrons," *Science* **331**, 61–64 (2011).

[79] M. Meckel, A. Staudte, S. Patchkovskii, D. M. Villeneuve, P. B. Corkum, and M. Spanner, "Signatures of the continuum electron phase in molecular strong-field photoelectron holography," *Nat. Phys.* **10**, 594–600 (2014).

[80] D. B. Miloševic, G. C. Paulus, D. Bauer, and W. Becker, "Above-threshold ionization by few-cycle pulses," *J. Phys. B At. Mol. Opt. Phys.* **39**, R203–R262 (2006).

[81] G. G. Paulus, F. Grasbon, H. Walther, P. Villoresi, M. Nisoli, S. Stagira, E. Priori, and S. De Silvestri, "Absolute-phase phenomena in photoionization with few-cycle laser pulses," *Nature* **414**, 182–184 (2001).

[82] G. G. Paulus, F. Lindner, H. Walther, A. Baltuška, E. Goulielmakis, M. Lezius, and F. Krausz, "Measurement of the phase of few-cycle laser pulses," *Phys. Rev. Lett.* **91**, 253004 (2003).

[83] A. L'Huillier, L. A. Lompre, G. Mainfray, and C. Manus, "Multiply charged ions induced by multiphoton absorption in rare gases at 0.53 μm," *Phys. Rev. A* **27**, 2503–2512 (1983).

[84] D. Zeidler, A. Staudte, A. B. Bardon, D. M. Villeneuve, R. Dörner, and P. B. Corkum, "Controlling attosecond double ionization dynamics via molecular alignment," *Phys. Rev. Lett.* **95**, 203003 (2005).

[85] P. Eckle, M. Smolarski, P. Schlup, J. Biegert, A. Staudte, M. Schöffler, H. G. Muller, R. Dörner, and U. Keller, "Attosecond angular streaking," *Nat. Phys.* **4**, 565–570 (2008).

[86] A. N. Pfeiffer, C. Cirelli, M. Smolarski, X. Wang, J. H. Eberly, R. Dörner, and U. Keller, "Breakdown of the independent electron approximation in sequential double ionization,"

New J. Phys. **13**, 93008 (2011).

[87] L. Torlina, F. Morales, J. Kaushal, I. Ivanov, A. Kheifets, A. Zielinski, A. Scrinzi, H. G. Muller, S. Sukiasyan, et al., "Interpreting attoclock measurements of tunnelling times," *Nat. Phys.* **11**, 503–509 (2015).

[88] A. Rundquist, C. G. Durfee III, Z. Chang, C. Herne, S. Backus, M. M. Murnane, and H. C. Kapteyn, "Phase-matched generation of coherent soft X-rays," *Science* **280**, 1412–1415 (1998).

[89] T. Popmintchev, M.-C. Chen, P. Arpin, M. M. Murnane, and H. C. Kapteyn, "The attosecond nonlinear optics of bright coherent X-ray generation," *Nat. Photonics* **4**, 822–832 (2010).

[90] E. Goulielmakis, M. Schultze, M. Hofstetter, V. S. Yakovlev, J. Gagnon, M. Uiberacker, A. L. Aquila, E. M. Gullikson, D. T. Attwood, et al., "Single-cycle nonlinear optics," *Science* **320**, 1614–1617 (2008).

[91] M. Kovacev, Y. Mairesse, E. Priori, H. Merdji, O. Tcherbakoff, P. Monchicourt, P. Breger, E. Mével, E. Constant, et al., "Temporal confinement of the harmonic emission through polarization gating," *Eur. Physicsal J. D* **26**, 79–82 (2003).

[92] G. Sansone, E. Benedetti, F. Calegari, C. Vozzi, L. Avaldi, R. Flammini, L. Poletto, P. Villoresi, C. Altucci, et al., "Isolated single-cycle attosecond pulses," *Science* **314**, 443–446 (2006).

[93] K. Ramasesha, S. R. Leone, and D. M. Neumark, "Real-time probing of electron dynamics using attosecond time-resolved spectroscopy," *Annu. Rev. Phys. Chem.* **67**, 41–63 (2016).

[94] T. Pfeifer, L. Gallmann, M. J. Abel, D. M. Neumark, and S. R. Leone, "Single attosecond

pulse generation in the multicycle-driver regime by adding a weak second-harmonic field," *Opt. Lett.* **31**, 975–977 (2006).

[95] X. Feng, S. Gilbertson, H. Mashiko, H. Wang, S. D. Khan, M. Chini, Y. Wu, K. Zhao, and Z. Chang, "Generation of isolated attosecond pulses with 20 to 28 femtosecond lasers," *Phys. Rev. Lett.* **103**, 183901 (2009).

[96] H. Mashiko, S. Gilbertson, C. Li, S. D. Khan, M. M. Shakya, E. Moon, and Z. Chang, "Double optical gating of high-order harmonic generation with carrier-envelope phase stabilized lasers," *Phys. Rev. Lett.* **100**, 130906 (2008).

[97] Z. Chang, "Controlling attosecond pulse generation with a double optical gating," *Phys. Rev. A* **76**, 051403(R) (2007).

[98] M. J. Abel, T. Pfeifer, P. M. Nagel, W. Boutu, M. J. Bell, C. P. Steiner, D. M. Neumark, and S. R. Leone, "Isolated attosecond pulses from ionization gating of high-harmonic emission," *Chem. Phys.* **366**, 9–14 (2009).

[99] T. Pfeifer, A. Jullien, M. J. Abel, P. M. Nagel, L. Gallmann, D. M. Neumark, and S. R. Leone, "Generating coherent broadband continuum soft-x-ray radiation by attosecond ionization gating," *Opt. Express* **15**, 17120–17128 (2007).

[100] M.-C. Chen, C. Mancusoa, C. Hernández-García, F. Dollar, B. Galloway, D. Popmintchev, P.-C. Huang, B. Walker, L. Plaja, et al., "Generation of bright isolated attosecond soft X-ray pulses driven by multicycle midinfrared lasers," *Proc. Natl. Acad. Sci.* **111**, E2361–E2367 (2014).

[101] K. T. Kim, C. Zhang, T. Ruchon, J.-F. Hergott, T. Auguste, D. M. Villeneuve, P. B. Corkum, and F. Quéré, "Photonic streaking of attosecond pulse trains," *Nat. Photonics* **7**, 651–656 (2013).

[102] E. Goulielmakis, V. S. Yakovlev, A. L. Cavalieri, M. Uiberacker, V. Pervak, A. Apolonski, R. Kienberger, U. Kleineberg, and F. Krausz, "Attosecond control and measurement: lightwave electronics," *Science* **317**, 769–775 (2007).

[103] C.-H. Zhang and U. Thumm, "Effect of wave-function localization on the time delay in photoemission from surfaces," *Phys. Rev. A* **84**, 65403 (2011).

[104] K. Klünder, J. M. Dahlström, M. Gisselbrecht, T. Fordell, M. Swoboda, D. Guénot, P. Johnsson, J. Caillat, J. Mauritsson, et al., "Probing single-photon ionization on the attosecond time scale," *Phys. Rev. Lett.* **106**, 143002 (2011).

[105] F. Lépine, M. Y. Ivanov, and M. J. J. Vrakking, "Attosecond molecular dynamics: fact or fiction?," *Nat. Photonics* **8**, 195–204 (2014).

[106] F. Krausz and M. Ivanov, "Attosecond physics," *Rev. Mod. Phys.* **81**, 163–234 (2009).

[107] E. Goulielmakis, Z.-H. Loh, A. Wirth, R. Santra, N. Rohringer, V. S. Yakovlev, S. Zherebtsov, T. Pfeifer, A. M. Azzeer, et al., "Real-time observation of valence electron motion," *Nature* **466**, 739–743 (2010).

[108] A. R. Beck, B. Bernhardt, E. R. Warrick, M. Wu, S. Chen, M. B. Gaarde, K. J. Schafer, D. M. Neumark, and S. R. Leone, "Attosecond transient absorption probing of electronic superpositions of bound states in neon : detection of quantum beats," *New J. Phys.* **16**, 113016 (2014).

[109] D. J. Kane, "Recent progress toward real-time measurement of ultrashort laser pulses," *IEEE J. Quantum Electron.* **35**, 421–431 (1999).

[110] L. B. Madsen, "Strong-field approximation in laser-assisted dynamics," *Am. J. Phys.* **73**, 57–62 (2005).

[111] M. Chini, S. Gilbertson, S. D. Khan, and Z. Chang, "Characterizing ultrabroadband

attosecond lasers," *Opt. Express* **18**, 13006–13016 (2010).

[112] L. Miaja-Avila, G. Saathoff, S. Mathias, J. Yin, C. La-o-vorakiat, M. Bauer, M. Aeschlimann, M. M. Murnane, and H. C. Kapteyn, "Direct measurement of core-level relaxation dynamics on a surface-adsorbate system using ultrafast X-rays," *Phys. Rev. Lett.* **101**, 46101 (2008).

[113] L. Miaja-Avila, "Laser-assisted dynamics on metallic surfaces by using ultrafast X-Rays," in *Ph.D. Thesis* (2009).

[114] A. Ferré, C. Handschin, M. Dumergue, F. Burgy, A. Comby, D. Descamps, B. Fabre, G. A. Garcia, R. Géneaux, et al., "A table-top ultrashort light source in the extreme ultraviolet for circular dichroism experiments," *Nat. Photonics* **9**, 93–98 (2015).

[115] G. Lambert, B. Vodungbo, J. Gautier, B. Mahieu, V. Malka, S. Sebban, P. Zeitoun, J. Luning, J. Perron, et al., "Towards enabling femtosecond helicity-dependent spectroscopy with high-harmonic sources," *Nat. Commun.* **6**, 6167 (2015).

[116] N. Dudovich, O. Smirnova, J. Levesque, Y. Mairesse, M. Y. Ivanov, D. M. Villeneuve, and P. B. Corkum, "Measuring and controlling the birth of attosecond XUV pulses," *Nat. Phys.* **2**, 781–786 (2006).

[117] J. B. Bertrand, H. J. Wörner, H.-C. Bandulet, É. Bisson, M. Spanner, J.-C. Kieffer, D. M. Villeneuve, and P. B. Corkum, "Ultrahigh-order wave mixing in noncollinear high harmonic generation," *Phys. Rev. Lett.* **106**, 23001 (2011).

[118] M. Lucchini, A. Ludwig, L. Kasmi, L. Gallmann, and U. Keller, "Semi-classical approach to compute RABBITT traces in multi-dimensional complex field distributions," *Opt. Express* **23**, 8867–8879 (2015).

[119] A. Sommer, E. M. Bothschafter, S. A. Sato, C. Jakubeit, T. Latka, O. Razskazovskaya, H.

Fattahi, M. Jobst, W. Schweinberger, et al., “Attosecond nonlinear polarization and light–matter energy transfer in solids,” *Nature* **534**, 86–90 (2016).

[120] M. . T. Hassan, T. T. Luu, A. Moulet, O. Raskazovskaya, P. Zhokhov, M. Garg, N. Karpowicz, A. M. Zheltikov, V. Pervak, et al., “Optical attosecond pulses and tracking the nonlinear response of bound electrons,” *Nature* **530**, 66–70 (2016).

[121] L. Cattaneo, J. Vos, M. Lucchini, C. Cirelli, and U. Keller, “Asymmetric Wigner time delay in CO photoionization,” *Int. Conf. Ultrafast Phenom.* **UM2B.3** (2016).

[122] C. Chen, Z. Tao, A. Carr, T. Szilvási, M. Keller, M. Mavrikakis, H. Kapteyn, and M. Murnane, “Direct time-domain observation of attosecond photoelectron lifetimes and attosecond electron dynamics in occupied bands in solids,” in *Int. Conf. Ultrafast Phenom.* **UTh5A.1**, (2016).

[123] A. Kaldun, A. Blättermann, V. Stooß, S. Donsa, H. Wei, R. Pazourek, S. Nagele, C. Ott, C. D. Lin, et al., “Observing the ultrafast buildup of a Fano resonance in the time domain,” *Science* **354**, 738–741 (2016).

[124] V. Gruson, L. Barreau, Á. Jiménez-Galan, F. Risoud, J. Caillat, A. Maquet, B. Carré, F. Lepetit, J.-F. Hergott, et al., “Attosecond dynamics through a Fano resonance: Monitoring the birth of a photoelectron,” *Science* **354**, 734–738 (2016).

[125] U. Fano, “Sullo spettro di assorbimento dei gas nobili presso il limite dello spettro d’arco,” *Nuovo Cim.* **12**, 154–161 (1935).

[126] L. R. Moore, M. A. Lysaght, J. S. Parker, H. W. Van Der Hart, and K. T. Taylor, “Time delay between photoemission from the 2p and 2s subshells of neon,” *Phys. Rev. A* **84**, 061404(R) (2011).

[127] J. Feist, O. Zatsarinny, S. Nagele, R. Pazourek, J. Burgdörfer, X. Guan, K. Bartschat, and

B. I. Schneider, “Time delays for attosecond streaking in photoionization of neon,” *Phys. Rev. A* **89**, 33417 (2014).

[128] A. S. Kheifets and I. A. Ivanov, “Delay in atomic photoionization,” *Phys. Rev. Lett.* **105**, 233002 (2010).

[129] W. Domcke and D. R. Yarkony, “Role of conical intersections in molecular spectroscopy and photoinduced chemical dynamics,” *Annu. Rev. Phys. Chem.* **63**, 325–352 (2012).

[130] M. N. R. Ashfold, B. Cronin, A. L. Devine, R. N. Dixon, and M. G. D. Nix, “The role of πσ* excited states in the photodissociation of heteroaromatic molecules,” *Science* **312**, 1637–1640 (2006).

[131] F. Calegari, G. Sansone, S. Stagira, C. Vozzi, and M. Nisoli, “Advances in attosecond science,” *J. Phys. B At. Mol. Opt. Phys.* **49**, 62001 (2016).

[132] G. Sansone, F. Kelkensberg, J. F. Pérez-Torres, F. Morales, M. F. Kling, W. Siu, O. Ghafur, P. Johnsson, M. Swoboda, et al., “Electron localization following attosecond molecular photoionization,” *Nature* **465**, 763–766 (2010).

[133] M. Huppert, I. Jordan, D. Baykusheva, A. Von Conta, and H. J. Wörner, “Attosecond delays in molecular photoionization,” *Phys. Rev. Lett.* **117**, 93001 (2016).

[134] S. Pisana, M. Lazzeri, C. Casiraghi, K. S. Novoselov, A. K. Geim, A. C. Ferrari, and F. Mauri, “Breakdown of the adiabatic Born–Oppenheimer approximation in graphene,” *Nat. Mater.* **6**, 198–201 (2007).

[135] Q. Liao and U. Thumm, “Attosecond time-resolved photoelectron dispersion and photoemission time delays,” *Phys. Rev. Lett.* **112**, 23602 (2014).

[136] C.-H. Zhang and U. Thumm, “Electron-ion interaction effects in attosecond time-resolved photoelectron spectra,” *Phys. Rev. A* **82**, 43405 (2010).

[137] Q. Liao and U. Thumm, "Attosecond time-resolved streaked photoemission from Mg-covered W(110) surfaces," *Phys. Rev. A* **92**, 031401(R) (2015).

[138] C.-H. Zhang and U. Thumm, "Attosecond photoelectron spectroscopy of metal surfaces," *Phys. Rev. Lett.* **102**, 123601 (2009).

[139] U. Thumm, Q. Liao, E. M. Bothschafter, F. Süßmann, M. F. Kling, and R. Kienberger, "Attosecond Physics: attosecond streaking spectroscopy of atoms and solids," in *Fundam. Photonics Phys.*, D. L. Andrew, Ed. (2015).

[140] C. Lemell, B. Solleder, K. Tőkési, and J. Burgdörfer, "Simulation of attosecond streaking of electrons emitted from a tungsten surface," *Phys. Rev. A* **79**, 62901 (2009).

[141] A. K. Kazansky and P. M. Echenique, "One-electron model for the electronic response of metal surfaces to subfemtosecond photoexcitation," *Phys. Rev. Lett.* **102**, 177401 (2009).

[142] S. Neppl, R. Ernstorfer, E. M. Bothschafter, A. L. Cavalieri, D. Menzel, J. V. Barth, F. Krausz, R. Kienberger, and P. Feulner, "Attosecond time-resolved photoemission from core and valence states of magnesium," *Phys. Rev. Lett.* **109**, 87401 (2012).

[143] A. G. Borisov, D. Sánchez-Portal, A. K. Kazansky, and P. M. Echenique, "Resonant and nonresonant processes in attosecond streaking from metals," *Phys. Rev. B* **87**, 12110(R) (2013).

[144] F. Roth, C. Lupulescu, E. Darlatt, A. Gottwald, and W. Eberhardt, "Angle resolved photoemission from Cu single crystals: Known facts and a few surprises about the photoemission process," *J. Electron Spectros. Relat. Phenomena* **208**, 2–10 (2016).

[145] L. Cattaneo, J. Vos, M. Lucchini, L. Gallmann, C. Cirelli, and U. Keller, "Comparison of attosecond streaking and RABBITT," *Opt. Express* **24**, 29060–29076 (2016).

[146] W. A. OKell, T. Witting, D. FAbris, C. A. Arrell, J. Hengster, S. Ibrahimkutty, A. Seiler,

M. Barthelmess, S. Stankov, et al., “Temporal broadening of attosecond photoelectron wavepackets from solid surfaces,” *Optica* **2**, 383–387 (2015).

[147] D. Guénot, K. Klünder, C. L. Arnold, D. Kroon, J. M. Dahlström, M. Miranda, T. Fordell, M. Gisselbrecht, P. Johnsson, et al., “Photoemission-time-delay measurements and calculations close to the 3s-ionization-cross-section minimum in Ar,” *Phys. Rev. A* **85**, 53424 (2012).

[148] S. Hüfner, *Photoelectron spectroscopy: principles and applications*, in *Springer Sci. Bus. Media* (2013).

[149] C. N. Berglund and W. E. Spicer, “Photoemission studies of copper and silver: experiment,” *Phys. Rev.* **136**, 1044–1064 (1964).

[150] M. P. Seah and W. A. Dench, “Quantitative electron spectroscopy of surfaces: A standard data base for electron inelastic mean free paths in solids,” *Surf. Interface Anal.* **1**, 2–11 (1979).

[151] A. V. Carr, “Ultrafast investigations of materials using angle-resolved photoemission spectroscopy with high harmonic generation,” in *Ph.D thesis* (2015).

[152] R. Schlaf, “Calibration of photoemission spectra and work function determination,” *http://rsl.eng.usf.edu/Documents/Tutorials/PEScalibration.pdf*, 2014.

[153] A. Damascelli, “Probing the electronic structure of complex systems by ARPES,” *Phys. Scr.* **T109**, 61–74 (2004).

[154] H. Ibach, *Physics of surfaces and interfaces* (2006).

[155] Y. Cao, “Exploring orbital physics with angle-resolved photoemission spectroscopy,” in *Ph.D thesis* (2014).

[156] A. Damascelli, Z. Hussain, and Z. Shen, “Angle-resolved photoemission studies of the

cuprate superconductors," *Rev. Mod. Phys.* **75**, 473–541 (2003).

[157] J. Hermanson, "Final-state symmetry and polarization effects in angle-resolved photoemission spectroscopy," *Solid State Commun.* **22**, 9–11 (1977).

[158] T. Pfeifer, C. Spielmann, and G. Gerber, "Femtosecond x-ray science," *Reports Prog. Phys.* **69**, 443–505 (2006).

[159] A. Mcpherson, G. Gibson, H. Jara, U. Johann, T. S. Luk, I. A. Mcintyre, K. Boyer, and C. K. Rhodes, "Studies of multiphoton production of vacuum-ultraviolet radiation in the rare gases," *J. Opt. Soc. Am. B* **4**, 595–601 (1987).

[160] M. Ferray, A. L'Huillier, X. F. Li, L. A. Lompre, G. Mainfray, and C. Manus, "Multiple-harmonic conversion of 1064 nm radiation in rare gases," *J. Phys. B At. Mol. Opt. Phys.* **21**, L31–L35 (1988).

[161] S. Backus, C. G. Durfee III, M. M. Murnane, and H. C. Kaptey, "High power ultrafast lasers," *Rev. Sci. Instrum.* **69**, 1207–1223 (1998).

[162] Z. Chang, P. B. Corkum, and S. R. Leone, "Attosecond optics and technology: progress to date and future prospects [Invited]," *J. Opt. Soc. Am. B* **33**, 1081–1097 (2016).

[163] E. Constant, D. Garzella, P. Breger, E. Mével, C. Dorrer, C. Le Blanc, F. Salin, and P. Agostini, "Optimizing high harmonic generation in absorbing gases: model and experiment," *Phys. Rev. Lett.* **82**, 1668–1671 (1999).

[164] E. J. Takahashi, T. Kanai, K. L. Ishikawa, Y. Nabekawa, and K. Midorikawa, "Coherent water window X Ray by phase-matched high-order harmonic generation in neutral media," *Phys. Rev. Lett.* **101**, 253901 (2008).

[165] C. G. I. Durfee, A. R. Rundquist, S. Backus, C. Herne, M. M. Murnane, and H. C. Kapteyn, "Phase matching of high-order harmonics in hollow waveguides," *Phys. Rev.*

Lett. **83**, 2187–2190 (1999).

[166] M.-C. Chen, P. Arpin, T. Popmintchev, M. Gerrity, B. Zhang, M. Seaberg, D. Popmintchev, M. M. Murnane, and H. C. Kapteyn, "Bright, coherent, ultrafast soft X-ray harmonics spanning the water window from a tabletop light source," *Phys. Rev. Lett.* **105**, 173901 (2010).

[167] P. Emma, R. Akre, J. Arthur, R. Bionta, C. Bostedt, J. Bozek, A. Brachmann, P. Bucksbaum, R. Coffee, et al., "First lasing and operation of an ångstrom-wavelength free-electron laser," *Nat. Photonics* **4**, 641–647 (2010).

[168] J. Amann, W. Berg, V. Blank, F.-J. Decker, Y. Ding, P. Emma, Y. Feng, J. Frisch, D. Fritz, et al., "Demonstration of self-seeding in a hard-X-ray free-electron laser," *Nat. Photonics* **6**, 693–698 (2012).

[169] J. D. Koralek, J. F. Douglas, N. C. Plumb, Z. Sun, A. V. Fedorov, M. M. Murnane, H. C. Kapteyn, S. T. Cundiff, Y. Aiura, et al., "Laser based angle-resolved photoemission, the sudden approximation, and quasiparticle-like spectral peaks in Bi 2 Sr 2 CaCu 2 O 8 + δ," *Phys. Rev. Lett.* **96**, 17005 (2006).

[170] S. Mathias, M. Bauer, M. Aeschlimann, L. Miaja-avila, H. C. Kapteyn, and M. M. Murnane, "Time-Resolved Photoelectron Spectroscopy at Surfaces Using Femtosecond XUV Pulses," in *Dyn. Solid State Surfaces Interfaces Curr. Dev.* **1**, M. W. Uwe Bovensiepen, Hrvoje Petek, Ed. (2010).

[171] S. Eich, a. Stange, a. V. Carr, J. Urbancic, T. Popmintchev, M. Wiesenmayer, K. Jansen, a. Ruffing, S. Jakobs, et al., "Time- and angle-resolved photoemission spectroscopy with optimized high-harmonic pulses using frequency-doubled Ti:Sapphire lasers," *J. Electron Spectros. Relat. Phenomena* **195**, 231–236 (2014).

[172] S. Mathias, S. Eich, J. Urbancic, S. Michael, A. V. Carr, S. Emmerich, A. Stange, T. Popmintchev, T. Rohwer, et al., "Self-amplified photo-induced gap quenching in a correlated electron material," *Nat. Commun.* **7**, 12902 (2016).

[173] T. Popmintchev, M. Chen, A. Bahabad, M. Gerrity, P. Sidorenko, O. Cohen, I. P. Christov, M. M. Murnane, and H. C. Kapteyn, "Phase matching of high harmonic generation in the soft and hard X-ray regions of the spectrum," *Proc. Natl. Acad. Sci. United States* **106**, 10516–10521 (2009).

[174] J. Tate, T. Auguste, H. G. Muller, P. Salières, P. Agostini, and L. F. DiMauro, "Scaling of wave-packet dynamics in an intense midinfrared field," *Phys. Rev. Lett.* **98**, 13901 (2007).

[175] J. Vura-Weis, C. Jiang, C. Liu, H. Gao, J. M. Lucas, F. M. F. de Groot, P. Yang, A. P. Alivisatos, and S. R. Leone, "Femtosecond M2,3-edge spectroscopy of transition-metal oxides: Photoinduced oxidation state change in α-Fe2O3," *J. Phys. Chem. Lett.* **4**, 3667–3671 (2013).

[176] Z. Zeng, Y. Cheng, X. Song, R. Li, and Z. Xu, "Generation of an extreme ultraviolet supercontinuum in a two-color laser field," *Phys. Rev. Lett.* **98**, 203901 (2007).

[177] J. Schmidt, A. Guggenmos, M. Hofstetter, S. H. Chew, and U. Kleineberg, "Generation of circularly polarized high harmonic radiation using a transmission multilayer quarter waveplate," *Opt. Express* **23**, 33564–33578 (2015).

[178] B. Vodungbo, A. B. Sardinha, J. Gautier, G. Lambert, C. Valentin, M. Lozano, G. Iaquaniello, F. Delmotte, S. Sebban, et al., "Polarization control of high order harmonics in the EUV photon energy range," *Opt. Express* **19**, 4346–4356 (2011).

[179] X. Zhou, R. Lock, N. Wagner, W. Li, H. C. Kapteyn, and M. M. Murnane, "Elliptically polarized high-order harmonic emission from molecules in linearly polarized laser fields,"

Phys. Rev. Lett. **102**, 73092 (2009).

[180] D. D. Hickstein, F. J. Dollar, P. Grychtol, J. L. Ellis, R. Knut, C. Hernández-García, D. Zusin, C. Gentry, J. M. Shaw, et al., "Non-collinear generation of angularly isolated circularly polarized high harmonics," *Nat. Photonics* **9**, 743–750 (2015).

[181] X. Zhou, P. Ranitovic, C. W. Hogle, J. H. D. Eland, H. C. Kapteyn, and M. M. Murnane, "Probing and controlling non-Born–Oppenheimer dynamics in highly excited molecular ions," *Nat. Phys.* **8**, 232–237 (2012).

[182] C. Boeglin, E. Beaurepaire, V. Halté, V. López-Flores, C. Stamm, N. Pontius, H. A. Dürr, and J.-Y. Bigot, "Distinguishing the ultrafast dynamics of spin and orbital moments in solids," *Nature* **465**, 458–461 (2010).

[183] T. Muraoka, K. Kinbara, and T. Aida, "Mechanical twisting of a guest by a photoresponsive host," *Nature* **440**, 512–515 (2006).

[184] K. S. Budil, P. Salières, M. D. Perry, and A. L'Huillier, "Influence of ellipticity on harmonic generation," *Phys. Rev. A* **48**, 3437–3440 (1993).

[185] V. V. Strelkov, A. A. Gonoskov, I. A. Gonoskov, and M. Y. Ryabikin, "Origin for ellipticity of high-order harmonics generated in atomic gases and the sublaser-cycle evolution of harmonic polarization," *Phys. Rev. Lett.* **107**, 43902 (2011).

[186] S. Long, W. Becker, and J. K. McIver, "Model calculations of polarization-dependent two-color high-harmonic generation," *Phys. Rev. A* **52**, 2262–2278 (1995).

[187] D. B. Milošević and W. Becker, "Attosecond pulse trains with unusual nonlinear polarization," *Phys. Rev. A* **62**, 11403 (2000).

[188] T. Zuo and A. D. Bandrauk, "High-order harmonic generation in intense laser and magnetic fields," *J. Nonlinear Opt. Phys. Mater.* **4**, 533–546 (1995).

[189] A. D. Bandrauk and H. Lu, “Controlling harmonic generation in molecules with intense laser and static magnetic fields: Orientation effects,” *Phys. Rev. A* **68**, 43408 (2003).

[190] C. A. Mancuso, D. D. Hickstein, P. Grychtol, R. Knut, O. Kfir, X.-M. Tong, F. Dollar, D. Zusin, M. Gopalakrishnan, et al., “Strong-field ionization with two-color circularly polarized laser fields,” *Phys. Rev. A* **91**, 31402 (2015).

[191] M. Hentschel, R. Kienberger, C. Spielmann, G. A. Reider, N. Milosevic, T. Brabec, P. Corkum, U. Heinzmann, M. Drescher, et al., “Attosecond metrology,” *Nature* **414**, 509–513 (2001).

[192] L. Medišauskas, J. Wragg, H. van der Hart, and M. Y. Ivanov, “Generating isolated elliptically polarized attosecond pulses using bichromatic counter rotating circularly polarized laser fields,” *Phys. Rev. Lett.* **115**, 153001 (2015).

[193] D. B. Milošević, “Generation of elliptically polarized attosecond pulse trains,” *Opt. Lett.* **40**, 2381–2384 (2015).

[194] D. B. Milošević, “Circularly polarized high harmonics generated by a bicircular field from inert atomic gases in the <math> <mi>p</mi> </math> state: A tool for exploring chirality-sensitive processes,” *Phys. Rev. A* **92**, 43827 (2015).

[195] T. Ruchon and A. Camper, “Notes on attosecond pulse profile measurements with the RABBIT technique,” in *UVX 2012-11e Colloq. sur les Sources Cohérentes Incohérentes UV, VUV X; Appl. Développements Récents*, (2013).

[196] J. A. Knapp, F. J. Himpsel, and D. E. Eastman, “Experimental energy band dispersions and lifetimes for valence and conduction bands of copper using angle-resolved photoemission,” *Phys. Rev. B* **19**, 4952–4964 (1979).

[197] M. Rhudy, B. Bucci, J. Vipperman, J. Allanach, and B. Abraham, “Microphone array

analysis methods using cross-correlations," in *ASME 2009 Int. Mech. Eng. Congr. Expo.*, (2009).

[198] D. Whitley, "A genetic algorithm tutorial," *Stat. Comput.* **4**, 65–85 (1994).

[199] J. A. Pérez-Hernández and L. Plaja, "Quantum description of the high-order harmonic generation in multiphoton and tunneling regimes," *Phys. Rev. A* **76**, 23829 (2007).

[200] V. P. Krainov, "Ionization rates and energy and angular distributions at the barrier-suppression ionization of complex atoms and atomic ions," *J. Opt. Soc. Am. B* **14**, 425–431 (1997).

[201] E. Clementi and C. Roetti, "Roothaan-Hartree-Fock atomic wavefunctions: basis functions and their coefficients for ground and certain excited states of neutral and ionized atoms, Z ≤ 54," *At. Data Nucl. Data Tables* **14**, 177–478 (1974).

[202] E. Pisanty, S. Sukiasyan, and M. Ivanov, "Spin conservation in high-order-harmonic generation using bicircular fields," *Phys. Rev. A* **90**, 43829 (2014).

[203] D B Milošević, "High-order harmonic generation by a bichromatic elliptically polarized field: conservation of angular momentum," *J. Phys. B At. Mol. Opt. Phys.* **48**, 171001 (2015).

[204] K. Schafer and K. Kulander, "High harmonic generation from ultrafast pump lasers," *Phys. Rev. Lett.* **78**, 638–641 (1997).

[205] I. P. Christov, M. M. Murnane, and H. C. Kapteyn, "High-harmonic generation of attosecond pulses in the 'single-cycle' regime," *Phys. Rev. Lett.* **78**, 1251–1254 (1997).

[206] F. Kelkensberg, W. Siu, J. F. Pérez-Torres, F. Morales, G. Gademann, A. Rouzée, P. Johnsson, M. Lucchini, F. Calegari, et al., "Attosecond control in photoionization of hydrogen molecules," *Phys. Rev. Lett.* **107**, 43002 (2011).

[207] D. Popmintchev, C. Hernández-García, F. Dollar, C. Mancuso, J. A. Pérez-Hernández, M.-C. Chen, A. Hankla, X. Gao, B. Shim, et al., "Ultraviolet surprise: efficient soft x-ray high-harmonic generation in multiply ionized plasmas," *Science* **350**, 1225–1231 (2015).

[208] S. Hellmann, T. Rohwer, M. Kalläne, K. Hanff, C. Sohrt, a. Stange, a. Carr, M. M. Murnane, H. C. Kapteyn, et al., "Time-domain classification of charge-density-wave insulators," *Nat. Commun.* **3**, 1069 (2012).

[209] J. Miao, T. Ishikawa, I. K. Robinson, and M. M. Murnane, "Beyond crystallography: Diffractive imaging using coherent x-ray light sources," *Science* **348**, 530–535 (2015).

[210] P. B. Corkum, "Plasma perspective on strong-field multiphoton ionization," *Phys. Rev. Lett.* **71**, 1994–1997 (1993).

[211] I. J. Kim, C. M. Kim, H. T. Kim, G. H. Lee, Y. S. Lee, J. Y. Park, D. J. Cho, and C. H. Nam, "Highly efficient high-harmonic generation in an orthogonally polarized two-color laser field," *Phys. Rev. Lett.* **94**, 243901 (2005).

[212] R. López-Martens, K. Varjú, P. Johnsson, J. Mauritsson, Y. Mairesse, P. Salières, M. B. Gaarde, K. J. Schafer, A. Persson, et al., "Amplitude and phase control of attosecond light pulses," *Phys. Rev. Lett.* **94**, 33001 (2005).

[213] X. He, J. M. Dahlström, R. Rakowski, C. M. Heyl, A. Persson, J. Mauritsson, and A. L'Huillier, "Interference effects in two-color high-order harmonic generation," *Phys. Rev. A* **82**, 33410 (2010).

[214] E. J. Takahashi, P. Lan, O. D. Mücke, Y. Nabekawa, and K. Midorikawa, "Infrared two-color multicycle laser field synthesis for generating an intense attosecond pulse," *Phys. Rev. Lett.* **104**, 233901 (2010).

[215] W. Holgado, C. Hernández-García, B. Alonso, M. Miranda, F. Silva, L. Plaja, H. Crespo,

and I. J. Sola, “Continuous spectra in high-harmonic generation driven by multicycle laser pulses,” *Phys. Rev. A* **93**, 13816 (2016).

[216] C. Hernández-García, J. A. Pérez-Hernández, J. Ramos, E. C. Jarque, L. Roso, and L. Plaja, “High-order harmonic propagation in gases within the discrete dipole approximation,” *Phys. Rev. A* **82**, 33432 (2010).

[217] C. Hernández-García, T. Popmintchev, M. M. Murnane, H. C. Kapteyn, L. Plaja, A. Becker, and A. Jaron-Becker, “Group velocity matching in high-order harmonic generation driven by mid-infrared lasers,” *New J. Phys.* **18**, 73031 (2016).

[218] M. V. Ammosov, N. B. Delone, and V. P. Kraĭnov, “Tunnel ionization of complex atoms and of atomic ions in an alternating electromagnetic field,” *Sov. Phys. JETP* **64**, 1191 (1986).

[219] G. Laurent, W. Cao, I. Ben-Itzhak, and C. L. Cocke, “Attosecond pulse characterization,” *Opt. Express* **21**, 16914–16927 (2013).

[220] G. Laurent, W. Cao, H. Li, Z. Wang, I. Ben-Itzhak, and C. L. Cocke, “Attosecond control of orbital parity mix interferences and the relative phase of even and odd harmonics in an attosecond pulse train,” *Phys. Rev. Lett.* **109**, 83001 (2012).

[221] I. Thomann, A. Bahabad, X. Liu, R. Trebino, M. M. Murnane, and H. C. Kapteyn, “Characterizing isolated attosecond pulses from hollow-core waveguides using multi-cycle driving pulses,” *Opt. Express* **17**, 4611–4633 (2009).

[222] B. L. Henke, E. M. Gullikson, and J. C. Davis, “X-Ray interactions: photoabsorption, scattering, transmission, and reflection at E = 50-30,000 eV, Z = 1-92,” *At. Data Nucl. Data Tables* **54**, 181–342 (1993).

[223] L. Rego, J. S. Román, A. Picón, L. Plaja, and C. Hernández-García, “Nonperturbative

twist in the generation of extreme-ultraviolet vortex beams," *Phys. Rev. Lett.* **117**, 163202 (2016).

[224] P. Antoine, B. Piraux, and A. Maquet, "Time profile of harmonics generated by a single atom in a strong electromagnetic field," *Phys. Rev. A* **51**, R1750–R1753 (1995).

[225] F. Schmitt, P. S. Kirchmann, U. Bovensiepen, R. G. Moore, L. Rettig, M. Krenz, J.-H. Chu, N. Ru, L. Perfetti, et al., "Transient electronic structure and melting of a charge density wave in TbTe3," *Science* **321**, 1649–1652 (2008).

[226] W. Li, A. A. Jaroń-Becker, C. W. Hogle, V. Sharma, X. Zhou, A. Becker, H. C. Kapteyn, and M. M. Murnane, "Visualizing electron rearrangement in space and time during the transition from a molecule to atoms," *Proc. Natl. Acad. Sci.* **107**, 20219–20222 (2010).

[227] S. Mathias, C. La-O-Vorakiat, P. Grychtol, P. Granitzka, E. Turgut, J. M. Shaw, R. Adam, H. T. Nembach, M. E. Siemens, et al., "Probing the timescale of the exchange interaction in a ferromagnetic alloy," *Proc. Natl. Acad. Sci.* **109**, 4792–4797 (2012).

[228] E. Turgut, C. La-O-vorakiat, J. M. Shaw, P. Grychtol, H. T. Nembach, D. Rudolf, R. Adam, M. Aeschlimann, C. M. Schneider, et al., "Controlling the competition between optically induced ultrafast spin-flip scattering and spin transport in magnetic multilayers," *Phys. Rev. Lett.* **110**, 197201 (2013).

[229] R. Pazourek, S. Nagele, and J. Burgdörfer, "Attosecond chronoscopy of photoemission," *Rev. Mod. Phys.* **87**, 765–802 (2015).

[230] J. M. Dahlström, D. Guénot, K. Klünder, M. Gisselbrecht, J. Mauritsson, A. L'Huillier, A. Maquet, and R. Taïeb, "Theory of attosecond delays in laser-assisted photoionization," *Chem. Phys.* **414**, 53–64 (2013).

[231] E. E. Krasovskii, "Attosecond spectroscopy of solids: Streaking phase shift due to lattice

scattering," *Phys. Rev. B* **84**, 195106 (2011).

[232] D. L. Miller, M. W. Keller, J. M. Shaw, A. N. Chiaramonti, and R. R. Keller, "Epitaxial (111) films of Cu, Ni, and CuxNiy on α−Al2O3 (0001) for graphene growth by chemical vapor deposition," *J. Appl. Phys.* **112**, 64317 (2012).

[233] D. A. Shirley, "High-resolution X-ray photoemission spectrum of the valence bands of gold," *Phys. Rev. B* **5**, 4709–4714 (1972).

[234] F. J. Himpsel, J. A. Knapp, and D. E. Eastman, "Experimental energy-band dispersions and exchange splitting for Ni," *Phys. Rev. B* **19**, 2919–2927 (1979).

[235] A. Liebsch, "Effect of self-energy corrections on the valence-band photoemission spectra of Ni," *Phys. Rev. Lett.* **43**, 1431–1434 (1979).

[236] D. E. Eastman, F. J. Himpsel, and J. A. Knapp, "Experimental band structure and temperature-dependent magnetic exchange splitting of nickel using angle-resolved photoemission," *Phys. Rev. Lett.* **40**, 1514–1517 (1978).

[237] B. Feuerbacher and R. F. Willis, "Photoemission and electron states at clean surfaces," *J. Phys. C Solid State Phys.* **9**, 169–216 (1976).

[238] Q. Liao and U. Thumm, "Initial-state, mean-free-path, and skin-depth dependence of attosecond time-resolved IR-streaked XUV photoemission from single-crystalline magnesium," *Phys. Rev. A* **89**, 33849 (2014).

[239] K. L. Kliewer, "Electromagnetic effects at metal surfaces; A nonlocal view," *Surf. Sci.* **101**, 57–83 (1980).

[240] A. D. Rakić, A. B. Djurišić, J. M. Elazar, and M. L. Majewski, "Optical properties of metallic films for vertical-cavity optoelectronic devices," *Appl. Opt.* **37**, 5271–5283 (1998).

[241] A. T. Georges, “Calculation of surface electromagnetic fields in laser-metal surface interaction,” *Opt. Commun.* **188**, 321–331 (2001).

[242] E. V Chulkov, V. M. Silkin, and P. M. Echenique, “Image potential states on metal surfaces: binding energies and wave functions,” *Surf. Sci.* **437**, 330–352 (1999).

[243] N. Armbrust, J. Gudde, and U. Höfer, “Formation of image-potential states at the graphene/metal interface,” *New J. Phys.* **17**, 103043 (2015).

[244] J. S. Dolado, V. M. Silkin, M. A. Cazalilla, A. Rubio, and P. M. Echenique, “Lifetimes and mean-free paths of hot electrons in the alkali metals,” *Phys. Rev. B* **64**, 195128 (2001).

[245] C. J. Powell, “Attenuation lengths of low-energy electrons in solids,” *Surf. Sci.* **44**, 29–46 (1974).

[246] D. E. Eastman, J. A. Knapp, and F. J. Himpsel, “Direct determination of lifetime and energy dispersion for the empty Δ1 conduction band of copper,” *Phys. Rev. Lett.* **41**, 825–828 (1978).

[247] I. Lindau, P. Pianetta, K. Y. Yu, and W. E. Spicer, “Photoemission of gold in the energy range 30-300 eV using synchrotron radiation,” *Phys. Rev. B* **13**, 492–495 (1976).

[248] J. Stöhr, P. S. Wehner, R. S. Williams, G. Apai, and D. A. Shirley, “Bulk versus surface effects in normal photoemission from Cu(110) in the range $32 \leq h\nu \leq 160$eV,” *Phys. Rev. B* **17**, 587–590 (1978).

[249] J. Stöhr, G. Apai, P. S. Wehner, F. R. McFeely, R. S. Williams, and D. A. Shirley, “Angle-resolved photoemission from valence bands of Cu and Au single crystals using 32-200-eV synchrotron radiation,” *Phys. Rev. B* **14**, 5144–5155 (1976).

[250] T.-C. Chiang, J. A. Knapp, M. Aono, and D. E. Eastman, “Angle-resolved photoemission, valence-band dispersions E(k), and electron and hole lifetimes for GaAs,” *Phys. Rev. B*

21, 3513–3522 (1980).

[251] G. Rossi, I. Lindau, L. Braicovich, and I. Abbati, “Cooper-minimum effects in the photoionization cross sections of 4d and 5d electrons in solid compounds,” *Phys. Rev. B* **28**, 3031–3042 (1983).

[252] C. Guillot, Y. Ballu, J. Paigné, J. Lecante, K. P. Jain, P. Thiry, R. Pinchaux, Y. Pétroff, and L. M. Falicov, “Resonant photoemission in nickel metal,” *Phys. Rev. Lett.* **39**, 1632–1935 (1977).

[253] R. Haight, “Electron dynamics at surfaces,” *Surf. Sci. Rep.* **21**, 275–325 (1995).

[254] T. Hertel, E. Knoesel, M. Wolf, and G. Ertl, “Ultrafast electron dynamics at Cu(111): response of an electron gas to optical excitation,” *Phys. Rev. Lett.* **76**, 535–538 (1996).

[255] M. Bauer, A. Marienfeld, and M. Aeschlimann, “Hot electron lifetimes in metals probed by time-resolved two-photon photoemission,” *Prog. Surf. Sci.* **90**, 319–376 (2015).

[256] C. A. Schmuttenmaer, M. Aeschlimann, H. E. Elsayed-Ali, R. J. D. Miller, D. A. Mantell, J. Cao, and Y. Gao, “Time-resolved two-photon photoemission from Cu(100): Energy dependence of electron relaxation,” *Phys. Rev. B* **50**, 8957–8960 (1994).

[257] M. Aeschlimann, M. Bauer, S. Pawlik, W. Weber, R. Burgermeister, D. Oberli, and H. C. Siegmann, “Ultrafast spin-dependent electron dynamics in fcc Co,” *Phys. Rev. Lett.* **79**, 5158–5161 (1997).

[258] R. Knorren, K. H. Bennemann, R. Burgermeister, and M. Aeschlimann, “Dynamics of excited electrons in copper and ferromagnetic transition metals: Theory and experiment,” *Phys. Rev. B* **61**, 9427–9440 (2000).

[259] D. Rudolf, C. La-O-Vorakiat, M. Battiato, R. Adam, J. M. Shaw, E. Turgut, P. Maldonado, S. Mathias, P. Grychtol, et al., “Ultrafast magnetization enhancement in

metallic multilayers driven by superdiffusive spin current," *Nat. Commun.* **3**, 1037 (2012).

[260] W. Nessler, S. Ogawa, H. Nagano, H. Petek, J. Shimoyama, Y. Nakayama, and K. Kishio, "Femtosecond time-resolved study of the energy and temperature dependence of hot-electron lifetimes in Bi2Sr2CaCu2O8+δ," *Phys. Rev. Lett.* **81**, 4480–4483 (1998).

[261] L. Perfetti, P. A. Loukakos, M. Lisowski, U. Bovensiepen, H. Eisaki, and M. Wolf, "Ultrafast electron relaxation in superconducting Bi2Sr2CaCu2O8+δ by time-resolved photoelectron spectroscopy," *Phys. Rev. Lett.* **99**, 197001 (2007).

[262] R. Huber, F. Tauser, A. Brodschelm, M. Bichler, G. Abstreiter, and A. Leitenstorfer, "How many-particle interactions develop after ultrafast excitation of an electron-hole plasma," *Nature* **414**, 286–289 (2001).

[263] C. Mathieu, B. Lalmi, T. O. Mentes, E. Pallecchi, A. Locatelli, S. Latil, R. Belkhou, and A. Ouerghi, "Effect of oxygen adsorption on the local properties of epitaxial graphene on SiC (0001)," *Phys. Rev. B* **86**, 35435 (2012).

[264] J. J. Quinn and R. A. Ferrell, "Electron self-energy approach to correlation in a degenerate electron gas," *Phys. Rev.* **112**, 812–827 (1958).

[265] L. D. Landau, "The theory of a Fermi liquid," *Sov. Phys. Jetp-Ussr* **3**, 920–925 (1957).

[266] L. D. Landau, "Oscillations in a Fermi liquid," *Sov. Phys. JETP-USSR* **5**, 101–108 (1957).

[267] I. Campillo, J. M. Pitarke, A. Rubio, E. Zarate, and P. M. Echenique, "Inelastic lifetimes of hot electrons in real metals," *Phys. Rev. Lett.* **83**, 2230–2233 (1999).

[268] P. M. Echenique, J. M. Pitarke, E. V. Chulkov, and A. Rubio, "Theory of inelastic lifetimes of low-energy electrons in metals," *Chem. Phys.* **251**, 1–35 (2000).

[269] F. Ladstädter, U. Hohenester, P. Puschnig, and C. Ambrosch-Draxl, "First-principles calculation of hot-electron scattering in metals," *Phys. Rev. B* **70**, 235125 (2004).

[270] F. Aryasetiawan, M. Imada, A. Georges, G. Kotliar, S. Biermann, and A. I. Lichtenstein, "Frequency-dependent local interactions and low-energy effective models from electronic structure calculations," *Phys. Rev. B* **70**, 195104 (2004).

[271] F. Aryasetiawan, K. Karlsson, O. Jepsen, and U. Schönberger, "Calculations of Hubbard U from first-principles," *Phys. Rev. B* **74**, 125106 (2006).

[272] M. Springer and F. Aryasetiawan, "Frequency-dependent screened interaction in Ni within the random-phase approximation," *Phys. Rev. B* **57**, 4364–4368 (1998).

[273] C.-H. Zhang and U. Thumm, "Laser-assisted photoemission from adsorbate-covered metal surfaces: Time-resolved core-hole relaxation dynamics from sideband profiles," *Phys. Rev. A* **80**, 32902 (2009).

[274] U. Bovensiepen and M. Ligges, "Timing photoemission—Final state matters," *Science* **353**, 28–29 (2016).

[275] F. J. Himpsel and W. Eberhardt, "High energy final bands in Cu," *Solid State Commun.* **31**, 747–749 (1979).

[276] P. Thiry, D. Chandesris, J. Lecante, C. Guillot, R. Pinchaux, and Y. Pétroff, "E vs k and inverse lifetime of Cu(110)," *Phys. Rev. Lett.* **43**, 82–85 (1979).

[277] A. Goldmann, W. Altmann, and V. Dose, "Experimental widths of excited electron states in metals," *Solid State Commun.* **79**, 511–514 (1991).

[278] I. G. Gurtubay, J. M. Pitarke, and P. M. Echenique, "Exchange and correlation effects in the relaxation of hot electrons in noble metals," *Phys. Rev. B* **69**, 245106 (2004).

[279] J. Kliewer, R. Berndt, E. V. Chulkov, V. M. Silkin, P. M. Echenique, and S. Crampin, "Dimensionality effects in the lifetime of surface states," *Science* **288**, 1399–1402 (2000).

[280] A. García-Lekue, J. M. Pitarke, E. V. Chulkov, A. Liebsch, and P. M. Echenique, "Role of

occupied d bands in the dynamics of excited electrons and holes in Ag," *Phys. Rev. B* **68**, 45103 (2003).

[281] J. J. Quinn, "The range of hot electrons and holes in metals," *Appl. Phys. Lett.* **2**, 167–169 (1963).

[282] J. J. Quinn, "Range of excited electrons in metals," *Phys. Rev.* **126**, 1453–1457 (1962).

[283] A. Borisov, D. Sánchez-Portal, R. D. Muiño, and P. M. Echenique, "Building up the screening below the femtosecond scale," *Chem. Phys. Lett.* **387**, 95–100 (2004).

[284] D. R. Penn, S. P. Apell, and S. M. Girvin, "Theory of spin-polarized secondary electrons in transition metals," *Phys. Rev. Lett.* **55**, 518–521 (1985).

[285] E. Zarate, P. Apell, and P. M. Echenique, "Calculation of low-energy-electron lifetimes," *Phys. Rev. B* **60**, 2326–2332 (1999).

[286] W. F. Krolikowski and W. E. Spicer, "Photoemission studies of the noble metals. I. Copper," *Phys. Rev.* **185**, 882–900 (1969).

[287] D. R. Penn, S. P. Apell, and S. M. Girvin, "Spin polarization of secondary electrons in transition metals: theory," *Phys. Rev. B* **32**, 7753–7768 (1985).

[288] E. O. Kane, "Electron scattering by pair production in Silicon," *Phys. Rev.* **159**, 624–631 (1967).

[289] V. P. Zhukov, F. Aryasetiawan, E. V Chulkov, and P. M. Echenique, "Lifetimes of quasiparticle excitations in 4d transition metals: Scattering theory and LMTO-RPA-GW approaches," *Phys. Rev. B* **65**, 115116 (2002).

[290] V. P. Zhukov and E. V Chulkov, "Lifetimes of low-energy electron excitations in metals," *J. Phys. Condens. Matter* **14**, 1937–1947 (2002).

[291] H. Ehrenreich and H. R. Philipp, "Optical properties of Ag and Cu," *Phys. Rev.* **128**,

1622–1629 (1962).

[292] R. Knorren, G. Bouzerar, and K. H. Bennemann, “Dynamics of excited electrons in copper: The role of Auger electrons,” *Phys. Rev. B* **63**, 94306 (2001).

[293] M. N. Baibich, J. M. Broto, A. Fert, F. N. Van Dau, F. Petroff, P. Eitenne, G. Creuzet, A. Friederich, and J. Chazelas, “Giant magnetoresistance of (001)Fe/(001)Cr magnetic superlattices,” *Phys. Rev. Lett.* **61**, 2472–2475 (1988).

[294] V. N. Strocov, “Intrinsic accuracy in 3-dimensional photoemission band mapping,” *J. Electron Spectros. Relat. Phenomena* **130**, 65–78 (2003).

[295] J. A. Sobota, S.-L. Yang, A. F. Kemper, J. J. Lee, F. T. Schmitt, W. Li, R. G. Moore, J. G. Analytis, I. R. Fisher, et al., “Direct optical coupling to an unoccupied Dirac surface state in the topological insulator Bi2Se3,” *Phys. Rev. Lett.* **111**, 136802 (2013).

[296] D. Niesner, T. Fauster, S. V. Eremeev, T. V. Menshchikova, Y. M. Koroteev, A. P. Protogenov, E. V. Chulkov, O. E. Tereshchenko, K. A. Kokh, et al., “Unoccupied topological states on bismuth chalcogenides,” *Phys. Rev. B* **86**, 205403 (2012).

[297] J. B. Pendry, “New probe for unoccupied bands at surfaces,” *Phys. Rev. Lett.* **45**, 1356–1358 (1980).

[298] V. N. Strocov, “Very low-energy electron diffraction as a method of band structure investigations: Applications in photoelectron spectroscopy,” *Phys. Solid State* **42**, 1973–1989 (2000).

[299] J. Barth, G. Kalkoffen, and C. Kunz, “Resonance enhancement of the nickel d-band photoemission,” *Phys. Lett. A* **74**, 360–362 (1979).

[300] G. van der Laan, M. Surman, M. A. Hoyland, C. F. J. Flipse, B. T. Thole, Y. Seino, H. Ogasawara, and A. Kotani, “Resonant photoemission at the Ni 2p core level as a probe of

electron correlation effects in nickel," *Phys. Rev. B* **46**, 9336–9340 (1992).

[301] S. Neppl, "Attosecond time-resolved photoemission from surfaces and interfaces," in *Ph.D* (2012).

[302] A. Föhlisch, M. Nyberg, J. Hasselström, O. Karis, L. G. M. Pettersson, and A. Nilsson, "How carbon monoxide adsorbs in different sites," *Phys. Rev. Lett.* **85**, 3309–3312 (2000).

[303] M. Bauer, C. Lei, K. Read, R. Tobey, J. Gland, M. M. Murnane, and H. C. Kapteyn, "Direct observation of surface chemistry using ultrafast soft-X-ray pulses," *Phys. Rev. Lett.* **87**, 25501 (2001).

[304] W. Wurth and D. Menzel, "Ultrafast electron dynamics at surfaces probed by resonant Auger spectroscopy," *Chem. Phys.* **251**, 141–149 (2000).

[305] P. Matyba, A. Carr, C. Chen, D. L. Miller, G. Peng, S. Mathias, M. Mavrikakis, D. S. Dessau, M. W. Keller, et al., "Controlling the electronic structure of graphene using surface-adsorbate interactions," *Phys. Rev. B* **92**, 041407(R) (2015).

[306] T. Ohta, A. Bostwick, J. L. Mcchesney, T. Seyller, K. Horn, and E. Rotenberg, "Interlayer interaction and electronic screening in multilayer graphene investigated with angle-resolved photoemission spectroscopy," *Phys. Rev. Lett.* **98**, 206802 (2007).